DYNAMIC RESPONSE OF FREE-STANDING DRY STORAGE CASKS AND ITS VARIATION UNDER LONG RETURN PERIOD SEISMIC EVENTS

by

Sharad Dangol

A dissertation submitted to the faculty of
The University of Utah
in partial fulfillment of the requirements for the degree of

Doctor of Philosophy

Department of Civil and Environmental Engineering

The University of Utah

August 2017

The University of Utah Graduate School

STATEMENT OF DISSERTATION APPROVAL

The dissertation of **Sharad Dangol**

has been approved by the following supervisory committee members:

Luis F. Ibarra	, Chair	**05/02/2017** Date Approved
Chris P. Pantelides	, Member	**05/02/2017** Date Approved
David H. Sanders	, Member	**05/24/2017** Date Approved
Steven F. Bartlett	, Member	**05/02/2017** Date Approved
Brittany Coats	, Member	**05/02/2017** Date Approved

and by **Michael E. Barber** , Chair of

the Department of **Civil and Environmental Engineering**

and by David B. Kieda, Dean of The Graduate School.

ABSTRACT

Dry storage casks (DSCs) store spent nuclear fuel (SNF) at sites contiguous to nuclear power plants (NPPs), known as Interim Spent Fuel Storage Installations (ISFSIs). DSCs can be stored in concrete bunkers, or designed as free-standing or anchored structures. The primary focus of this study is to investigate response of free-standing DSCs under seismic excitation. Recent consideration of DSCs as a potential midterm solution may increase the operating period (initially 20 years) up to 300 years and requires response reevaluation. A longer compliance period results in larger accelerations, and larger vertical-to-horizontal spectral acceleration ratios that could have destabilizing effects on the cask response.

The response of free-standing DSCs under seismic excitations is highly nonlinear, especially under concurrent sliding and rocking motion triggered by multidirectional seismic excitations. It depends on parameters such as aspect ratio, coefficient of friction between cask and foundation pad, and ground motion characteristics, among other factors.

This research presents the investigation on the response of free-standing DSCs under long return period seismic events. Dynamic experimental tests were performed on a 6-degree-of-freedom shake table at the University of Nevada, Reno. Ground motions used for the tests were spectrally matched to spectral acceleration for seismic events of 10,000- and 30,000-year return periods. Experimental results were used to validate finite element (FE) models. The validated models were then be used to study casks' response under full intensity long-term seismic event, tip-over spectrum under sinusoidal excitation and soil structure interaction (SSI).

The research also addresses whether the response of DSCs is repeatable under identical ground motions. If the cask response has a relatively large variation (nonrepeatable), the analytical and FE models cannot directly capture this variation. Experimental tests on repeated ground motions showed that the dynamic response is not repeatable, which is the first indicator of chaos or extreme sensitivity to initial conditions. Numerical techniques for chaotic analysis were then implemented, for harmonic excitation, to show that DSCs' motion is in fact chaotic for certain excitation conditions. This sensitivity was studied in FE models and analytical simulations by varying input parameters by ±1%. This small change resulted in large variation in the response.

Dedicated to my mother, Gita Dangol;

and to my siblings Sarina Dangol and Sameer Dangol.

TABLE OF CONTENTS

Chapters

Appendices

ACKNOWLEDGEMENTS

The author would like to express his sincere gratitude towards his advisor and mentor Dr. Luis Ibarra for his continuous guidance and support he provided through each and every step. It has been the author’s honor and a privilege to learn under his tutelage.

The author would also like to express sincere thanks to Prof. Chris Pantelides, Prof. David Sander, Prof. Steven Bartlett and Associate Prof. Brittany Coats on his supervisory committee. Without their valuable insights, support and suggestions, this work would have not been possible.

Fellow graduate students and friends, Joel Parks, Ahmed Maree (UNR) and Taylor Nielsen (UNR), who are also the part of the research group. They contributed towards the design, build, instrumentation and experimental testing of specimens. Their contribution in every step of this research project has to be mentioned. Their work and support is greatly acknowledged. The author also wishes to thank Raul Uribe, fellow graduate student, for his help in running countless simulations and data processing.

Patrick Laplace, manager of large scale structures laboratory (Earthquake Engineering Laboratory) and his team at University of Nevada, Reno (UNR); Mark Bryant, manager of structure laboratory and Trevor Nye at The University of Utah deserve great appreciation.

Support and encouragement from friends Yuandong (Matt) Wang, Catherine Tucker, Sulcohan Dhungel, Elmar Eidelpes, MJ Ameli Renani (MJ), Anurag Upadhyay and Andrew Wu are also greatly acknowledged by the author.

Last but not the least; author owes huge thanks towards his mom, Gita Dangol; his sister: Sarina Dangol and brother: Sameer Dangol. Without their support and patience this endeavor would not have been possible.

This material is based upon work supported under a Department of Energy Nuclear Energy University Programs. This research project was a joint project between The University of Utah, University of Nevada, Reno and Oregon State University. Any opinions, findings, conclusions or recommendations expressed in this publication are those of the authors and do not necessarily reflect the views of the Department of Energy Office of Nuclear Energy.

CHAPTER 1

INTRODUCTION

Dry Storage Casks (DSCs) store spent nuclear fuel (SNF) at sites contiguous to nuclear power plants (NPPs), known as Interim Spent Fuel Storage Installations (ISFSIs). The SNF at NPPs is initially stored in pools for at least five years to control the temperature of the fuel assemblies, and prevent melting of their cladding. Thereafter, the SNF is transferred to DSCs. The regulations for these storage systems 10 CFR Part 72 [1] are designed to ensure adequate passive heat removal and radiation shielding during normal operations, off-normal events, and accident scenarios. Vertically stored DSCs can be designed as free-standing structures resting on a reinforced concrete foundation pad (Figure 1.1), or casks anchored to a foundation pad (e.g., Diablo Canyon ISFSI). The casks can also be designed to be placed in concrete bunkers in horizontal or vertical position (e.g., San Onofre and Humboldt Bay, respectively). This study will focus on the seismic response of free-standing DSCs.

The DSCs can be divided into: i) bare-fuel dry-storage, and ii) canister based systems. In bare-fuel cask systems, fuel-rod assemblies are placed in a vertical position directly into a fuel basket integrated into the cask. The basket supports the fuel assemblies and fixed neutron absorbers for criticality control. In the case of canister based storage systems, spent-fuel assemblies are placed into baskets integrated into a thin-wall stainless steel cylinder (Figure 1.2). This cylinder is usually called multipurpose canister (MPC), although, currently it only has two functions: store and transport SNF. Originally canisters would also be used for disposal.

DSCs have been considered as a temporary storage solution, and usually are licensed for 20 years, although they can be relicensed for operating periods up to 60 years. Recently, DSCs have been reevaluated as a potential midterm solution, in which the operating period may be extended for up to 300 years [2]. Consideration of DSC longer compliance period results in larger accelerations, and larger vertical-to-horizontal spectral acceleration ratios, which could have destabilizing effects on the cask response. This study evaluates the seismic performance of free-standing canisterized DSCs subjected to such large seismic accelerations in two horizontal and one vertical directions simultaneously.

Nuclear regulatory commission (NRC) prescribes performance goals of DSCs and ISFSIs in 10 CFR Part 72 [1]. The guideline requires consideration of the most severe of natural phenomena and combination of the effects of normal and accident condition. It also requires DSCs and ISFSIs to be designed to prevent collapse or failure of systems and components important to safety. This includes ventilation systems that ensures adequate heat removal and radiation shielding. Excessive movement of casks relative to pad, potential overturning and excessive movement relative to each other may impact the heat removal system even if the system is undamaged to cause radiation leakage. All these requirements are usually assessed using numerical simulations. However, the response of such free-standing DSCs is usually considered to be deterministic and response sensitivity and existence of chaotic response are not generally considered.

1.1 Objectives

The study's main objective is to evaluate the response of free-standing DSCs under seismic events of long return period. To achieve this, experimental tests on 1:2.5 scaled DSCs were performed on a six degree-of-freedom (6DOF) shake table at the University of Nevada, Reno (UNR). In addition, FE models developed mainly using the explicit FE code LS-DYNA [3]. Data from experimental tests were also used to validate these FE models. The validated models were then used to obtain the response under full intensity long-term seismic event (10,000- and 30,000-years). The validated FE models were also used for parametric studies on casks' response, including overturning spectrum under sinusoidal excitation and soil structure interaction (SSI).

The study also addresses the repeatability of the response free-standing DSCs, given that nonrepeatability is an indicator of chaotic response. Investigations on the existence of chaotic response are also performed in this study. If the cask response has a relatively large variation to minute changes in initial and boundary conditions the analytical and FE models cannot easily capture this variation because they cannot account for the minute differences in the field conditions responsible for this chaotic behavior. Finally, Monte Carlo simulations are implemented to study the variation in the response of a free-standing body when the input parameters have small variations.

1.2 Research Outline

This research is one of the most comprehensive investigations to date on the response of free-standing DSCs under long return period seismic events. The consideration of DSC as a potential midterm solution led to a seismic reevaluation under stronger seismic events.

This dissertation covers the description of the studied specimens, including scaling and similitude law, as well as a summary of experimental tests. The selection of ground motions and development of design basis response spectra used in the study are also covered.

Several DSC specimens were tested under repeat conditions during the experimental tests to assess the potential lack of repeatability in the response. These tests showed that the response is not repeatable. The experimental results are also used to study the response of DSCs subjected ground motions with near field and far field characteristics. Near field motions exhibit one or two major pulses, while far field motions have multiple lesser magnitude pulses. The models are used to study DSC response under full intensity 10,000- and 30,000-year return period ground motions. Finite element (FE) models are also used to study the parameters affecting the response of the casks like frequency and amplitude of excitation. Fundamental behavior under harmonic excitation is also studied and overturning (tip-over) spectra under single cycle sinusoidal excitation are obtained. The FE models are also used to study the effect of the pulse duration (i.e., the ground motion frequency content on the response).

Full scale cask-pad-soil FE models are used to study the effect of soil on the response of free-standing DSCs. Deconvolution and convolution analyses are performed to include the effect of soil on the considered ground motions. The convolved motions recovered at the level of soil-column depth are then applied to the FE model to obtain DSC response. The results show that softening of soil shifts the predominant period of ground motion to longer period region while muting the high frequency accelerations. This effect caused larger rocking of DSCs and is unfavorable for stability of free-standing structures.

The chaotic DSC response was observed in experimental results, as well as FE and analytical models that showed extreme sensitivity to minor changes in initial conditions. The chaotic behavior was first detected for DSCs under horizontal and vertical sinusoidal excitations. Thereafter, the variation in the maximum rocking angle of simple 2D rocking free-standing body under actual ground motions was investigated. The variation parameters obtained like coefficient of variation (cov) and β (standard deviation of natural logarithm of values) of rocking angle could be used to provide a confidence interval on maximum rocking angle to be expected. This was achieved by varying input parameters by ±1%, a small change that resulted in large response variation when implementing a Monte Carlo simulation 10,000 realizations. The coefficient of variation and standard deviation for the maximum rocking angle was obtained based on a log-normal distribution. These parameters can be useful in determining the upper and lower bound for response of free-standing bodies under the considered ground motions with 10,000- and 30,000-year return period.

(a) (b)

Figure 1.1. ISFSI facilities. (a) Freestanding vertical DSCs on a concrete pad, (b) Horizontal DSC in a concrete vault [4] (This item appears courtesy of IASMiRT at iasmirt.org.)

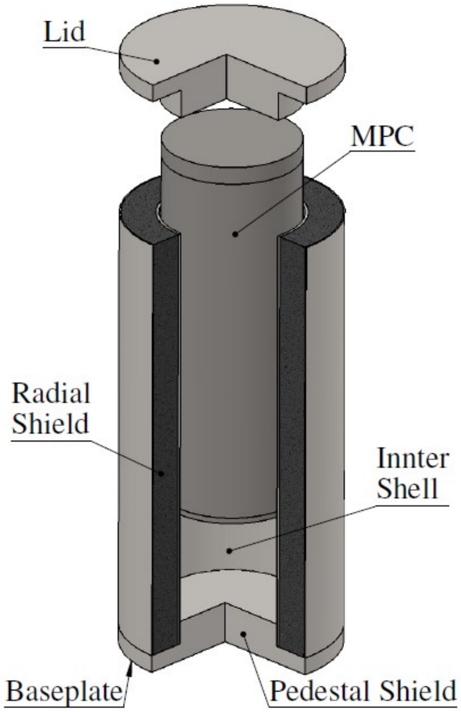

Figure 1.2. Example of canister-based DSC (generic)

CHAPTER 2

LITERATURE REVIEW

The response of a free-standing body subjected to horizontal base excitation was first studied by Housner [5] in 1963. Housner along with other recent researchers [6–13] simplified the problem by considering only planar free-standing bodies (2D). The problem was further simplified by considering either sliding only, or rocking response only [11–13], and few studies consider simultaneously sliding and rocking [6,8,14]. The response when rocking and sliding occurs becomes complex, even for 2D rigid block type structures. Note that 2D models cannot model out of plane motion and, therefore, there is no difference between the response of rectangular prismatic and cylindrical bodies. The response of free-standing or unanchored bodies like casks is highly nonlinear, and its response depends on several factors [10,12]. The DSC performance is mainly influenced by cask geometry (radius-to-centroidal height ratio, or aspect ratio, r/h_{cg}); friction between cask and pad; and ground motion characteristics such as frequency content, number of pulses, amplitude, and duration.

Studies have also analytically modelled three-dimensional (3D) free-standing bodies. Koh and Mustafa (1990) [15] initially modelled free rocking of cylindrical structures, without including the energy dissipation mechanism of the rocking system. Later, Koh and Hsiung in 1991 [16] included such energy dissipation mechanism in their rocking model of cylindrical free-standing bodies. However, sliding was still not included in the rocking only model. Recently studies have also attempted to analytically model the response of 3D free-standing blocks [17,18]. The Chatzis and Smyth [18] model considers sliding and rocking together, but it is only applicable to square or rectangular prismatic blocks. Although the model can possibly be extended to a cylindrical free-standing bodies like DSCs, the application of such model is complicated, particularly when there are multiple interacting bodies other than the foundation pad and the base of free-standing body. For instance, the DSCs under investigation include an overpack that interacts with an internal MPC and the foundation concrete pad.

Another drawback of analytical models is that DSC stresses and strains are not easily computed. For these reason, finite element (FE) models can be a better alternative as they can simulate multiple complex interactions between the bodies. FE models can also estimate stress and strain under tip-over and/or collision, and have been used to simulate DSC seismic response [19–24]. These studies have shown that the response of free-standing DSCs are highly nonlinear and depend on various factors, other than the peak ground accelerations (PGAs) of the input ground motion. For instance, tip-over has been detected for horizontal PGAs as low as 0.6 g's [19], while other studies show no tip-over for horizontal accelerations of up to 1.3 g [20]. Also, these studies usually disregard the effect of vertical accelerations, or consider vertical accelerations as a fraction of horizontal acceleration. However, the vertical accelerations may be of the same order, or even larger, than the horizontal acceleration, especially for records of long return period earthquakes close to the fault [25].

Few experimental tests of free-standing bodies have been carried out. Shirai et al.

(2003) performed one of these few experimental tests on a 1:3 scaled cask, but only selected results were published. Even fewer attempts have been made to investigate whether the response of free-standing bodies is repeatable under identical random ground motion [27,28]. As the response of free-standing structures under seismic excitations is highly nonlinear (especially under concurrent sliding and rocking motion triggered by multidirectional seismic excitations), minute changes in the initial condition or boundary condition may result in a very different body movement. Although the lack of repeatability in the response of free-standing bodies has been known since the 1980s [14,29–34], few studies address this lack in repeatability either in experiments [27,28,30], FE models or analytical evaluations.

Soil structure interaction (SSI) also influences the response of free-standing casks. SSI is particularly important when lateral dimension of foundation pad is very big compared to its thickness [35,36]. For instance, the largest lateral dimension of a typical ISFSI pad can be more than 50 times [19] larger than its thickness. This allows bending of the foundation pad, which would have been considered as relatively rigid in bending if the pad was shorter. The flexibility of the pad may lead to a change in the frequency and magnitude of the motion experienced by the cask compared to the reference free-field ground motion.

CHAPTER 3

DESCRIPTION OF SYSTEM CONSIDERED

This chapter describes the geometric characteristics (dimensions, weight, etc.) of scaled DSCs used in this study, development of evaluation basis spectra and ground motions considered for such ground motions, and the experimental test performed to obtain the coefficient of friction between steel and concrete used in this study. This chapter also presents the scaling or similitude law that should be followed when dynamic tests have to be performed on a scaled specimen to represent response of full scale prototype.

3.1 DSC Characteristics

A free-standing body under static loading is presented in Figure 3.1. The body has a cross-section of a free-standing cylinder with radius r, height of center-of-gravity h_{cg}, and mass m. The parameter g is the gravity acceleration; a_h and a_v are the horizontal and vertical accelerations, respectively; and μ is the friction coefficient. Based on this static equilibrium configuration, sliding occurs when the horizontal seismic force exceeds the friction force:

$$\mu(mg - ma_v) < ma_h \tag{3.1}$$

which leads to Equation (3.2) as follows:

$$\mu < \frac{a_h}{g - a_v} \tag{3.2}$$

Similarly, tip-over occurs when the stabilizing moment at point O is smaller than the moment created by the horizontal force at point O:

$$(mg - ma_v)r < ma_h h_{cg} \tag{3.3}$$

Rendering,

$$\frac{r}{h_{cg}} < \frac{a_h}{g - a_v} \tag{3.4}$$

Equations (3.2) and (3.4) show that μ and r / h_{cg} play a crucial role in the response of unanchored bodies. To study the two main response mechanisms (i.e., sliding and rocking) of freestanding casks, two DSC prototypes with aspect ratios r / h_{cg} of 0.55 (FS.55) and 0.43 (FS.43) were mainly used in this project. 'FS' in the nomenclature stands for 'free-standing' and '.43 or .55' represents the aspect ratio of the specimen. The slender cask with aspect ratio, $r / h_{cg} = 0.43$ is more likely to exhibit large rotations, whereas the squat cask with $r / h_{cg} = 0.55$ is more likely to show sliding displacements. These aspect ratios roughly correspond to the lower bound and average aspect ratios of Nuclear Regulatory Commission (NRC) approved casks [19]. Although the main physical characteristics of these generic DSCs are based on NRC list, the detailed dimensions of the overpack and multipurpose canister (MPC) do not correspond to commercially available casks.

Scaled (1:2.5) DSC prototypes were used due to physical constraints of the 6-degree-of-freedom (DOF) shake table used in the study. The similitude law parameters between the scaled and prototype casks are given in Table 3.1, whereas Figure 3.2a shows the overpack of the scaled prototype DSC. The overpack and canister cavity (Figures 3.2c 3.2d) were filled with lead units (Figure b) to compensate for the additional mass necessary to satisfy the similitude law [37,38]. To prevent pounding of the lead units and the cylindrical shell, the leftover space of MPC and overpack cavity was filled with sand. Table 3.2 presents MPC and overpack dimensions for both squat and slender casks, and Figure 3.3 shows a sectional elevation of FS.43 overpack.

The original FS.55 and FS.43 shared the same MPC. Two additional specimens of aspect ratio 0.39 and 0.62 (Table 3.2) were also tested. The first specimen consisted of the MPC only, and was named FS.39. The cask with aspect ratio of 0.62 (FS.62) corresponds to the empty overpack of the FS.55 system (without the additional mass filling and MPC). The last two specimens represented extreme free-standing cask's aspect ratios. Also, because of their relative light weight, larger seismic accelerations could be applied during testing without the risk of exceeding the table's capacity. However, the last two specimens do not meet scaling and similitude requirements.

3.2 Development of Evaluation Basis Earthquakes

For a 20-year compliance period, ISFSIs are usually designed for a Design Bases Earthquake (DBE) associated to a return period, $T =$ 2,000 years [39], corresponding to a probability of exceedance $\upsilon = 1/T =$ 1/ (5 × 10^{-4})/year. To obtain the probability of exceeding the DBE in 20 years (probability of occurrence), a Poisson distribution can be used [40], given in Equation (3.5):

$$P(x > 0) = 1 - P(x = 0) = 1 - e^{-\upsilon \cdot t} \tag{3.5}$$

In Equation (3.5), t is time in years, and $\upsilon \cdot t$ is the expected number of occurrences in a given interval. Then, the probability of exceeding the DBE $[P(x > 0)]$ in 20 years is 1%. To obtain the same probability of exceedance of 1% in 300 years, Equation (3.5) indicates that a return period $T \geq 29{,}850$ years needs to be considered in the calculations ($\upsilon \leq 3.3 \times 10^{-5}$/year) [41]. For this reason, the ground motion records used in the study were spectrally matched to earthquake events of 10,000- and 30,000-year return periods [42,43]. The target spectra developed using NUREG 6728 [42] guidelines were for Western US (WUS) rock sites. Thereafter, two ground motion sets were used as FE model dynamic input.

Two ground motion sets were selected and spectrally matched [43] to the seismic hazard level or spectral accelerations of respective return periods: i) Near-Field (NFGM) and ii) Far-Field ground motions (FFGM) sets. An NFGM is characterized by one or two big pulses due to forward directivity effects, while an FFGM exhibits a series of multiple large pulses. For NFGMs, events with magnitude M = 6 and distance R = 2 km were considered, while FFGM included events with M = 8 and R = 20 km. Each set had 15 candidate earthquakes (Tables 3.3 and 3.4) selected from FEMA P695 [44] and Alavi and Krawinkler [45]. All the original ground motions of Tables 3.3 and 3.4 were obtained from the PEER database [46]. The process of developing the target response spectrum and spectral matching of the ground motion sets is as follows:

i. Select the evaluation earthquake cases
    - Near Field (R = 0-10 km and M = 6)
    - Far Field ($R \geq$ 10 km and M = 8)

ii. Select the appropriate response at the hazard level: The two hazard levels used in this study are 10,000- and 30,000-year return period levels. Hazard curves for PGA, 10 Hz and 1 Hz are selected from NUREG 6728 [42]. Values are then read from the curves for each return period. For example, the values for 10,000-year return period are shown in Figure 3.4.

iii. Develop and scale rock spectral shapes from NUGREG 6728: Equation 4-8 of NUREG 6728 [42] was used to develop response spectra shapes.

$$\ln\left[\frac{SA(f)}{PGA}\right] = \frac{C_1}{\cosh(C_2 f^{C_3})} + C_4\left[\frac{\exp(C_5 f)}{f^{C_6}}\right] \tag{3.6}$$

where, $SA(f)$ = spectral acceleration for a given frequency

PGA = peak ground acceleration

f = frequency (Hz)

C_1 = 1.8197

C_2 = 0.30163

$C_3 = 0.47498 + 0.034356M + 0.0057204\ln(R+1)$

$C_4 = -12.650 + M\{2.4796 - 0.14732M + 0.034605\ln(0.040762R+1)\}$

C_5 = -0.25746

$C_6 = 0.29784 + 0.010723M - 0.0000133R$

M = Moment magnitude

R = Fault Distance

Coefficients (C_1, C_2, C_3, C_4, C_5 and C_6) are obtained from Table 4-3 of NUREG 6728 for Western United States (WUS), California site.

- For Near Field spectra, the PGA was adjusted until spectrum matched the target value at 10 Hz.
- For Far Field spectra, the PGA was adjusted until spectrum matched the target value at 1 Hz.
- Then vertical-to-horizontal (V/H) spectral ratios from Table 4-4 of NUREG 6728 were used to determine vertical spectra. Figure 3.5 shows the V/H ratios used to determine vertical response spectra for this study. The final target spectrum is presented in Figure 3.6.

iv. The two horizontal components of ground motions (Tables 3.3 and 3.4) were rotated to find the major and minor principal components of the time history. The technique employed minimizes the cross-correlation between the horizontal components by reducing the covariance of the components to zero. This is achieved by transforming the horizontal components of the motion (say X and Y axes) are transformed into new set of orthogonal axes (X' and Y') with rotation angle θ_1. The transformed accelerations are given by Equation (3.7) with the covariance between them shown by Equation (3.8) [47].

$$\begin{aligned} ax'(t) &= ax(t)\cos\theta_1 + ay(t)\sin\theta_1 \\ ay'(t) &= -ax(t)\sin\theta_1 + ay(t)\cos\theta_1 \end{aligned} \tag{3.7}$$

$$\eta_{xy} = \frac{1}{t_d}\int_0^{t_d}\left[ax(t) - \overline{ax(t)}\right]\cdot\left[ay(t) - \overline{ay(t)}\right]dt \tag{3.8}$$

In Equation (3.8), $\overline{ax(t)}$ and $\overline{ay(t)}$ represents average values. Substituting x' and y' for x and y in the Equation (3.8) yields the corresponding covariance for $ax'(t)$ and $ay'(t)$

components. When this function is minimized (to be zero), by changing rotation angle (θ_1), major and minor principal components are found.

v. Finally the ground motion sets were spectrally matched to the developed target response spectra (Figure 3.6) using the program RSPMATCH [43]. In addition to the spectral matching, baseline correction using a software called SeismoSignal [48].

3.3 Main Ground Motions Selected for Experimental Tests

Two representative spectrally matched ground motions were selected as the input for the seismic excitation tests from the above ground motion sets. The chosen records had the desired NFGM and FFGM characteristics and showed larges cask horizontal displacement and rocking response in the initial FE simulations. The CHY101 station of the Chi-Chi Taiwan, 1999 earthquake was chosen to represent a FFGM earthquake. The absolute peak accelerations of the Chi-Chi original ground motion are 0.353 g's in the x-direction, 0.440 g's in the y-direction, and 0.165 g's in the vertical direction. The Erzican, Turkey earthquake of 1992's time histories was selected to represent a NFGM earthquake for testing. This ground motion exhibits NF forward directivity effects, as inferred from a couple of large pulses in the velocity and displacement time histories. The Erzican original PGAs are 0.496 g's in the x-direction, 0.515 g's in the y-direction, and 0.248 g's in the vertical direction. The Pacoima Dam station of the 1971 San Fernando earthquake (SFPD) was also selected for the experiments. The SFPD original PGAs are 1.220 g's in the x-direction, 1.240 g's in the y-direction, and 0.687 g's in the vertical direction.

Table 3.5 presents the main characteristics of the above ground motions used as input for the test and PGA for the 10,000- and 30,000-year return periods. Figure 3.7 shows the acceleration time histories (ATHs) for spectrally matched motions (10,000-year return period), whereas Figure 3.8 presents the ATHs for ground motions spectrally matched to 30,000-year target spectra. Figures 3.7 and 3.8 also show the significant duration for the ground motions based on Arias intensity, which represents the strong shaking duration based on a timespan associated to a specified amount of dissipated energy. In this case, this timespan corresponds to the occurrence of 5% and 95% of the total Arias intensity. For the selected FFGM, the significant duration is approximately three times (about 30 s.) larger than that of the NFGM. The two representative motions (one from each set) were selected based on a preliminary FE simulations in ABAQUS [49]. Figure 3.9 presents velocity time history (VTH) of Erzikan and Chi-Chi, spectrally matched to 10,000-year target spectra, which illustrates the difference in pulse content for NFGM and FFGM events. The ATHs for the original San Fernando motion are presented in Figure 3.10.

3.4 Test for Coefficient of Friction

An experiment was performed at the University of Utah to measure the steel-concrete friction coefficient to provide more accurate parameters for the simulation. Figures 3.11 and 3.12 present the experimental setup to measure the steel-concrete friction coefficient, considering a relatively smooth concrete surface.

3.4.1 Test Description and Result

An actuator was attached to the pad and the cask was held in place by attaching it to the reaction frame. A load cell was attached to the link connecting the cask to the reaction frame. The actuator was used to monotonically push the pad at varying displacement rates to cause the cask to slide. As the cask slid with respect to the concrete pad, the friction force generated at the interface was measured by the load cell. The coefficient of friction is then calculated as:

$$\mu = \frac{F_{LC}}{F_N} = \frac{F_{LC}}{W_C} \tag{3.9}$$

where, μ = coefficient of friction; F_{LC} = force recorded by the load cell; W_C = weight of the cask = 5108 lbs.

3.4.2 Test Results

Figure 3.13 plots the resulting friction coefficient with respect to the relative displacement at various displacement rates. The data show that the average static coefficient of friction between the cask and the pad is 0.55. As observed, the difference between static and kinematic friction coefficient was not significant. Hence the kinematic friction coefficient was also approximated as 0.55. Table 3.6 presents the summary of data obtained from seven tests. NUREG 6865 [19] presents a large range in the coefficient of friction at the steel-concrete interface. The values presented in Table 3.6 are within the range presented in [19].

Table 3.1. Similarity law for scaled specimens

Parameter	Notation	Dimension	Similarity Ratio		
			General Form*	N =	N =
Length	L	L	$L_s/L_p = 1/N$	½.5	1/3.5
Time	T	T	$T_s/T_p = 1/N^{1/2}$	0.6325	0.5345
Acceleration	a	LT^{-2}	$a_s/a_p = 1$	1	1
Angle	θ	---	$\theta_s/\theta_p = 1$	1	1
Mass	M	M	$M_s/M_p = \gamma(1/N^3)$	0.16	0.0816
Mass Moment of	I	ML^2	$I_s/I_p =$	0.0256	0.0067
Equivalent Cross	A	L^2	$A_s/A_p = 1/N^2$	0.16	0.0816
Bottom Stress	σ	$ML^{-1}T^{-2}$	$\sigma_s/\sigma_p = (M_s a_s/A_s)/$	1	1
Friction	μ	---	$\mu_s/\mu_p = 1$	1	1
(*) Suffix (p) refers to generic prototype, and suffix (s) refers to scaled model specimens γ = correction factor = N					

Table 3.2. Dimensions of scaled cask spcimens

DSC Specimen	**Component**	**Diameter (mm.)**	**Height (h, mm.)**	**Weight (ton)**	**Scale**
FS.55 (r/h_{cg}= 0.55)	MPC	660	1765	4.8	1:2.5
	Overpack	670 (inside) 1156 (outside)	1786 (cavity) 2223 (total)	11.96	
FS.43 (r/h_{cg}= 0.43)	MPC	660	1867	5.05	1:2.5
	Overpack	670 (inside) 1054 (outside)	1880 (cavity) 2426 (total)	9.72	
FS.39 (r/h_{cg}=0.39)	MPC	660	1765	4.8	1:3.5
FS.62 (r/h_{cg}= 0.62)	Empty overpack only	1156 (outside)	2223 (total)	3.39	1:3.5

Table 3.3. Near-field record set (pulse records subset)

No.	Earthquake Name	Year	Station	Fault Type	M	R (km)	PGA (g)			PGV (m/s)		
							X	Y	Vert.	X	Y	Vert.
1	Imperial Valley-06	1979	El Centro Array #6	Strike-Slip	6.5	0.0	0.410	0.439	1.655	0.649	1.098	0.569
2	Imperial Valley-06	1979	El Centro Array #7	Strike-Slip	6.5	0.6	0.338	0.463	0.544	0.476	1.093	0.263
3	Irpinia, Italy-01	1980	Struno	Normal	6.9	6.8	0.251	0.358	0.260	0.370	0.527	0.260
4	Morgan Hill	1984	Coyote Lake Dam (SW Abutment)	*	6.2	0.1	0.711	1.298	0.388	0.516	0.808	0.156
5	Loma Prieta	1989	Saratoga Aloha Ave	Strike-Slip	6.9	7.6	0.512	0.324	0.389	0.412	0.426	0.268
6	**Erzikan, Turkey**	**1992**	**Erzican**	**Stike-Slip**	**6.7**	**0.0**	**0.496**	**0.515**	**0.248**	**0.643**	**0.839**	0.184
7	Kobe, Japan	1995	JMA	*	6.9	0.6	0.821	0.599	0.343	0.813	0.744	0.383
8	Landers	1992	Lucerne	Strike-Slip	7.3	2.2	0.727	0.789	0.818	1.465	0.324	0.460
9	Northridge-01	1994	Rinaldi Receiving Sta	Thrust	6.7	0.0	0.825	0.487	0.834	1.601	0.745	0.435
10	Northridge-01	1994	Sylmar - Olive View	Thrust	6.7	1.7	0.843	0.604	0.535	1.294	0.781	0.188
11	Kocaeli, Turkey	1999	Izmit	Strike-Slip	7.5	3.6	0.152	0.220	0.146	0.226	0.298	0.131
12	Chi-Chi, Taiwan	1999	TCU065	Thrust	7.6	0.6	0.814	0.603	0.272	1.262	0.788	0.771
13	Chi-Chi, Taiwan	1999	TCU102	Thrust	7.6	1.5	0.298	0.169	0.189	1.125	0.772	0.562
14	Duzce, Turkey	1999	Duzce	Stike-Slip	7.1	0.0	0.348	0.535	0.357	0.600	0.835	0.226
15	Kobe, Japan	1995	Takatori	*	6.9	1.5	0.611	0.616	0.272	1.272	1.207	0.160
$\sigma_{\ln PGA}$ (standard deviation of natural log of PGAs) =							0.520	0.494	0.631			
Median PGA =							0.512	0.515	0.357			

* From Table 2.1 of [38]

M: Moment Magnitude

R: Site-Source Distance (Joyner-Boore)

PGA: Peak Ground Acceleration

PGV: Peak Ground Velocity

Table 3.4. Far-field record set

No.	Earthquake Name	Year	Station	Fault Type	M	R (km)	PGA (g)			PGV (m/s)		
							X	Y	Vert.	X	Y	Vert.
1	Duzce, Turkey	1999	Bolu	Strike-Slip	7.1	12.0	0.728	0.822	0.203	0.564	0.621	0.173
2	Hector Mine	1999	Hector	Strike-Slip	7.1	10.4	0.266	0.337	0.150	0.286	0.417	0.120
3	Kocaeli, Turkey	1999	Duzce	Strike-Slip	7.5	13.6	0.312	0.358	0.229	0.589	0.464	0.204
4	Kocaeli, Turkey	1999	Arcelik	Strike-Slip	7.5	10.6	0.219	0.150	0.086	0.177	0.396	0.086
5	Landers	1992	Yermo Fire Station	Strike-Slip	7.3	23.6	0.152	0.245	0.136	0.297	0.514	0.128
6	Landers	1992	Coolwater	Strike-Slip	7.3	19.7	0.283	0.417	0.174	0.256	0.423	0.099
7	Manjil, Iran	1990	Abhar	Strike-Slip	7.4	12.6	0.132	0.209	0.077	0.207	0.552	0.075
8	Cape Mendocino	1992	Rio Dell Overpass	Thrust	7.0	7.9	0.549	0.385	0.195	0.419	0.438	0.105
9	**Chi-Chi, Taiwan**	**1999**	**CHY101**	**Thrust**	**7.6**	**10.0**	**0.353**	**0.440**	**0.165**	**0.707**	**0.150**	**0.280**
10	Chi-Chi, Taiwan	1999	TCU045	Thrust	7.6	26.0	0.474	0.512	0.361	0.367	0.391	0.215
11	Kobe, Japan	1995	Nishi-Akashi	Strike-Slip	6.9	7.1	0.509	0.503	0.371	0.373	0.366	0.173
12	Kobe, Japan	1995	Shin-Osaka	Strike-Slip	6.9	19.1	0.243	0.212	0.059	0.378	0.279	0.064
13	Loma Prieta	1989	Capitola	Strike-Slip	6.9	8.7	0.529	0.443	0.541	0.350	0.292	0.177
14	Loma Prieta	1989	Gilroy Array #3	Strike-Slip	6.9	12.2	0.555	0.367	0.338	0.357	0.447	0.155
15	Northridge	1994	Beverly Hill-Mulhol	Thrust	6.7	9.4	0.617	0.444	0.314	0.407	0.301	0.140
$\sigma_{\ln PGA}$ (standard deviation of natural log of PGAs) =							0.522	0.428	0.632			
Median PGA =							0.353	0.385	0.195			

M: Moment Magnitude

R: Site-Source Distance (Joyner-Boore)

PGA: Peak Ground Acceleration

PGV: Peak Ground Velocity

Table 3.5. Peak Ground Accelerations (PGAs) of target spectra

Earthquake Name	**Year**	**Station**	**Target Spectrum**		**Peak Ground Acceleration (PGA), g**		
					Original	**10,000 yr. return period**	**30,000 yr. return period**
Erzican, Turkey	1992	Erzican	NFGM	Horizontal	EW 0.496, NS 0.515	1.053	1.412
				Vertical	0.248	1.127	1.511
Chi-Chi, Taiwan	1999	CHY101	FFGM	Horizontal	EW 0.353, NS 0.440	0.640	0.918
				Vertical	0.165	0.685	0.982
San Fernando	1971	Pacoima Dam	---	Horizontal	EW 1.220, NS 1.240	---	---
				Vertical	0.687	---	---

Table 3.6. Coefficient of friction between steel and concrete (different displacement rate)

Test No.	**Applied Displacement Rate**		**Coefficient of Friction(μ)**
	in./min	**in./s (mm/s)**	
1	1	0.017 (0.432)	0.57
2	1	0.017 (0.432)	0.54
3	1	0.017 (0.432)	0.50
4	2	0.033 (0.838)	0.56
5	4	0.067 (1.702)	0.54
6	12	0.200 (5.080)	0.53
7	12	0.200 (5.080)	0.60
		Average	**0.55**

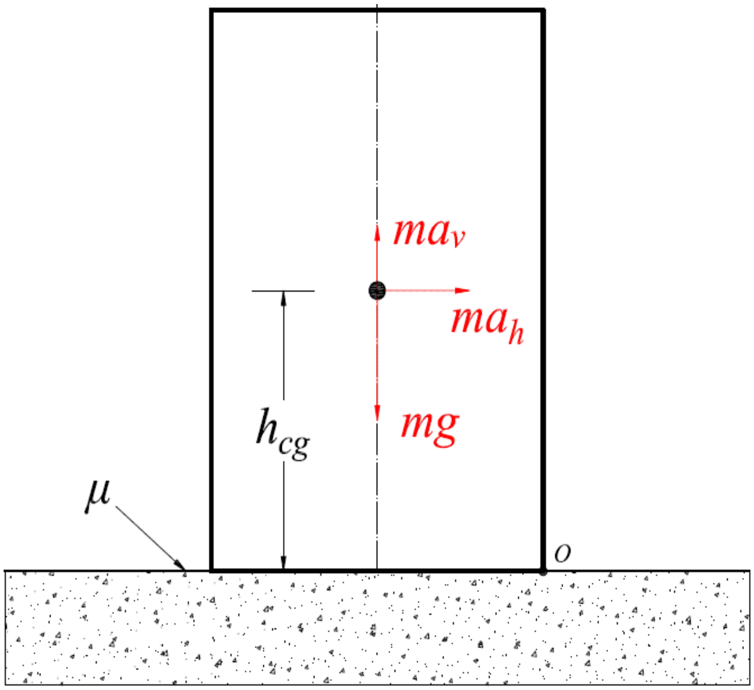

Figure 3.1. Static loading forces of free-standing body

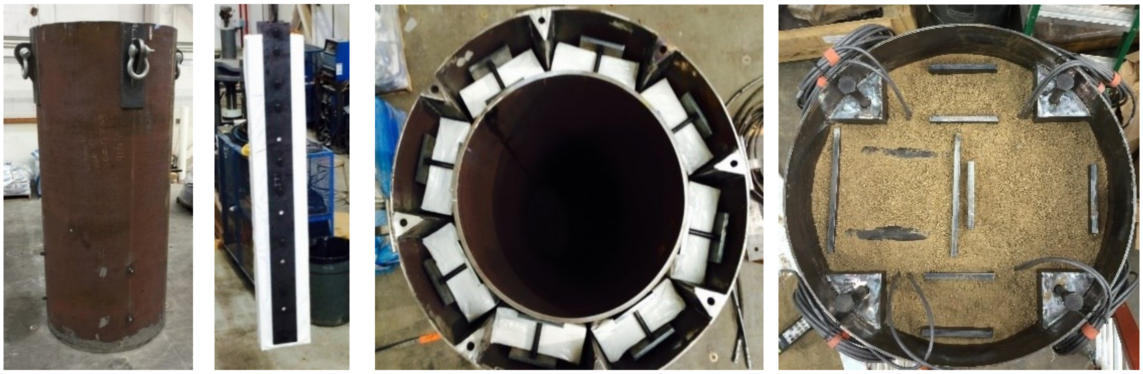
(a) (b) (c) (d)

Figure 3.2. Assembly process of DSC: (a) FS.43’s overpack, (b) Assembly of lead units in one panel, (c) overpack cavity filled with lead, and (d) MPC filled with lead and sand

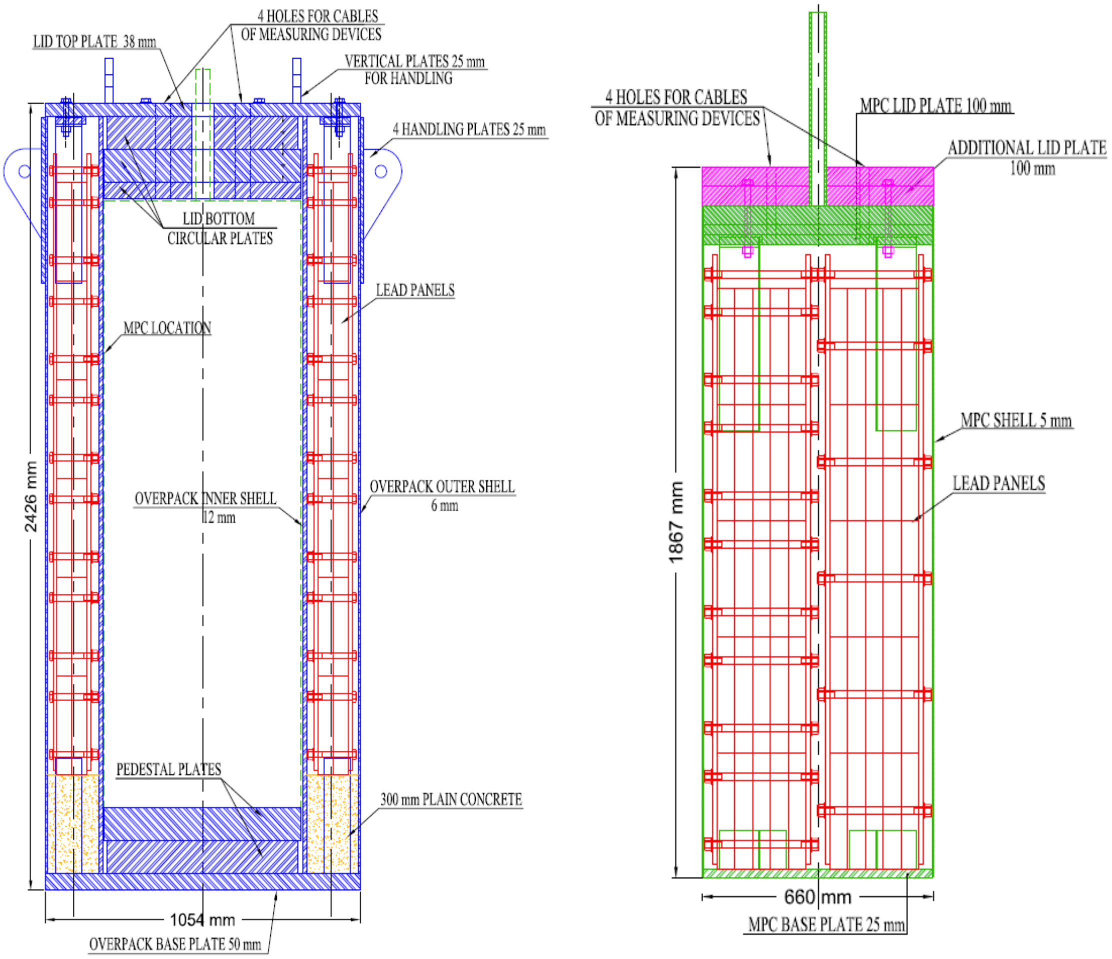

(a) (b)

Figure 3.3. Sectional elevation (a) overpack of FS.43, (b) MPC

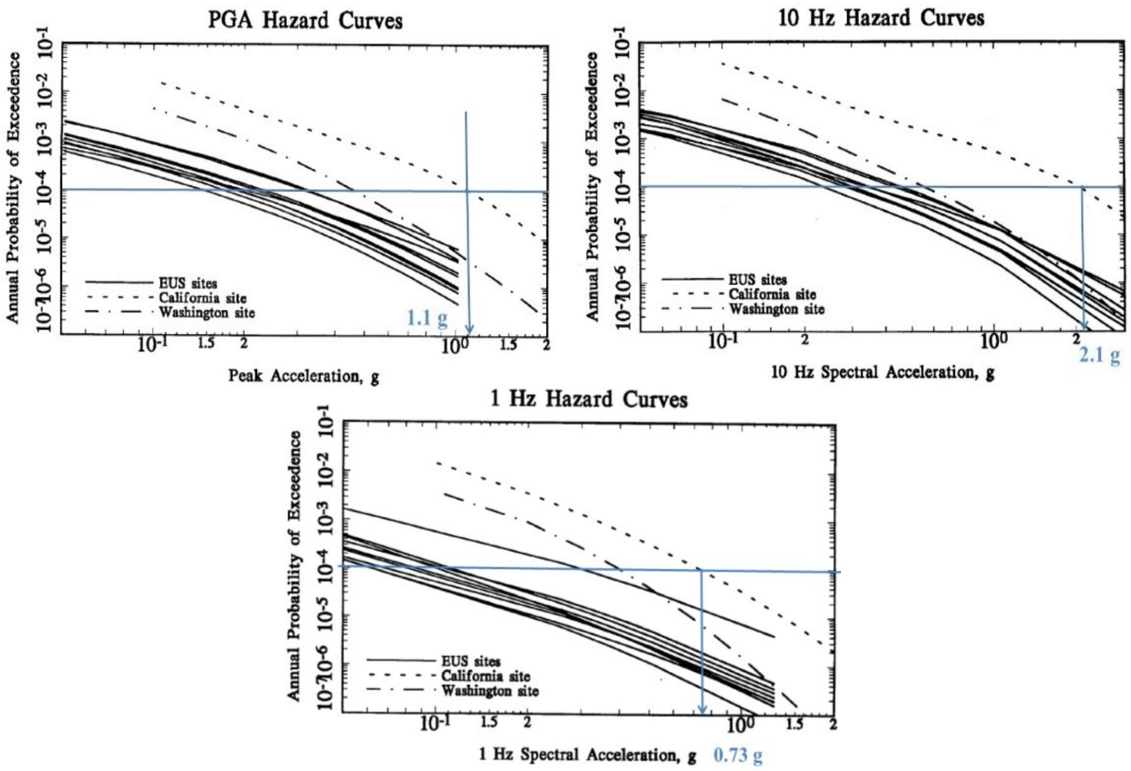

Figure 3.4. Hazard level values for 10,000-year return period event (NUREG 6728) [42]

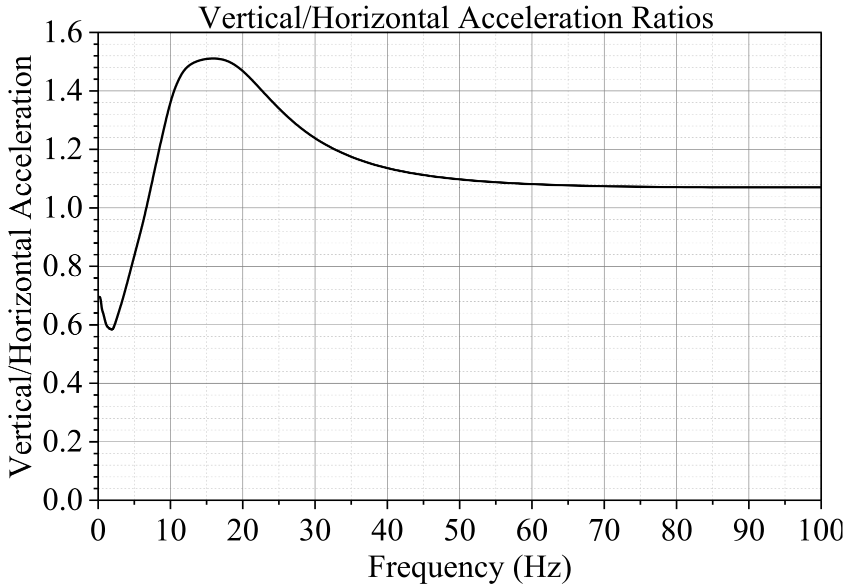

Figure 3.5. Vertical to horizontal (V/H) ratios (from Table 4-4 of NUREG 6728) for accelerations exceeding 0.5 g

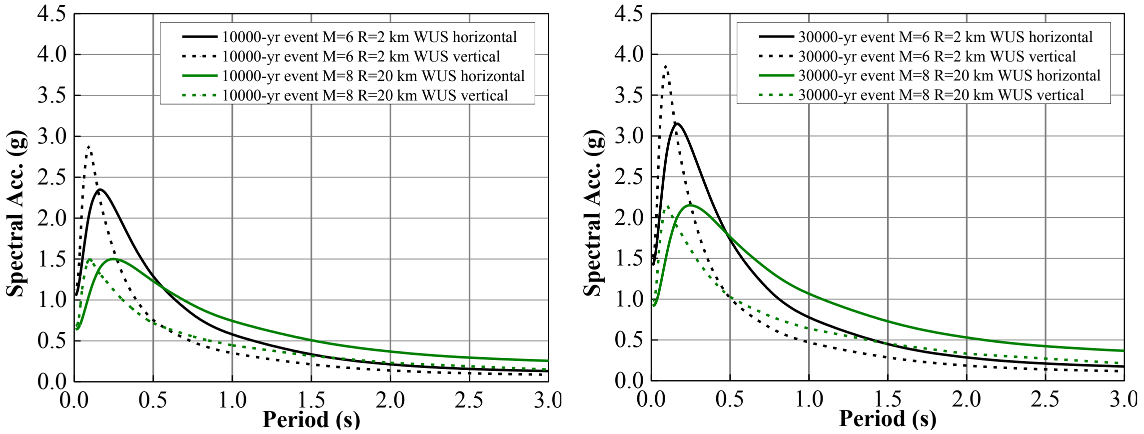

(a) (b)

Figure 3.6. Target response spectra (Western US rock): (a) 10,000-year event, (b) 30,000-year event

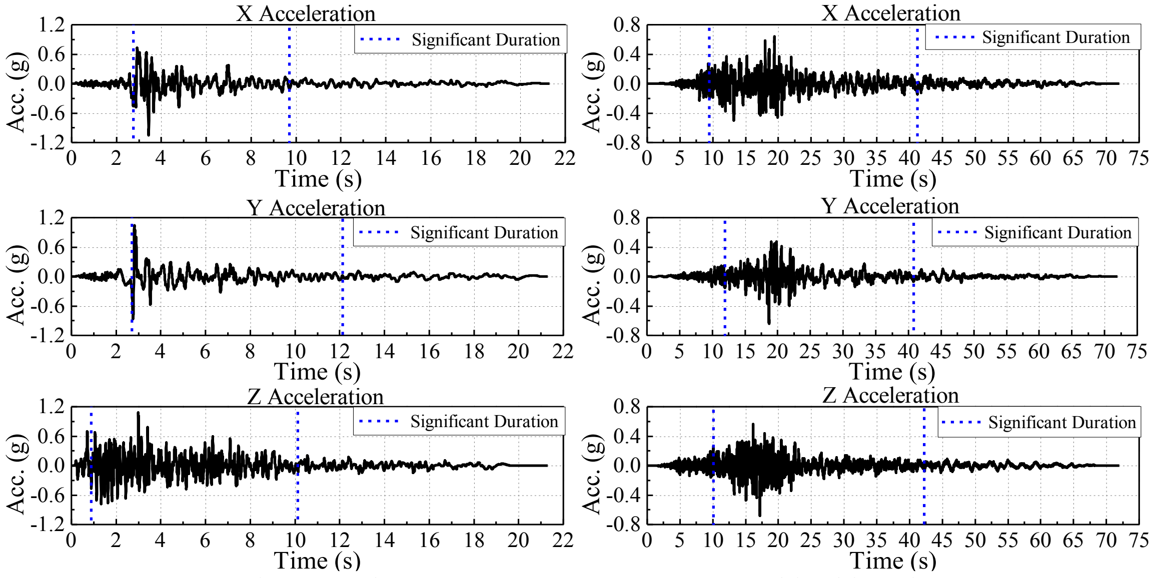

Erzican, Turkey Chi-Chi, Taiwan

Figure 3.7. Time histories of input ground motions spectrally matched to 10,000-year return period

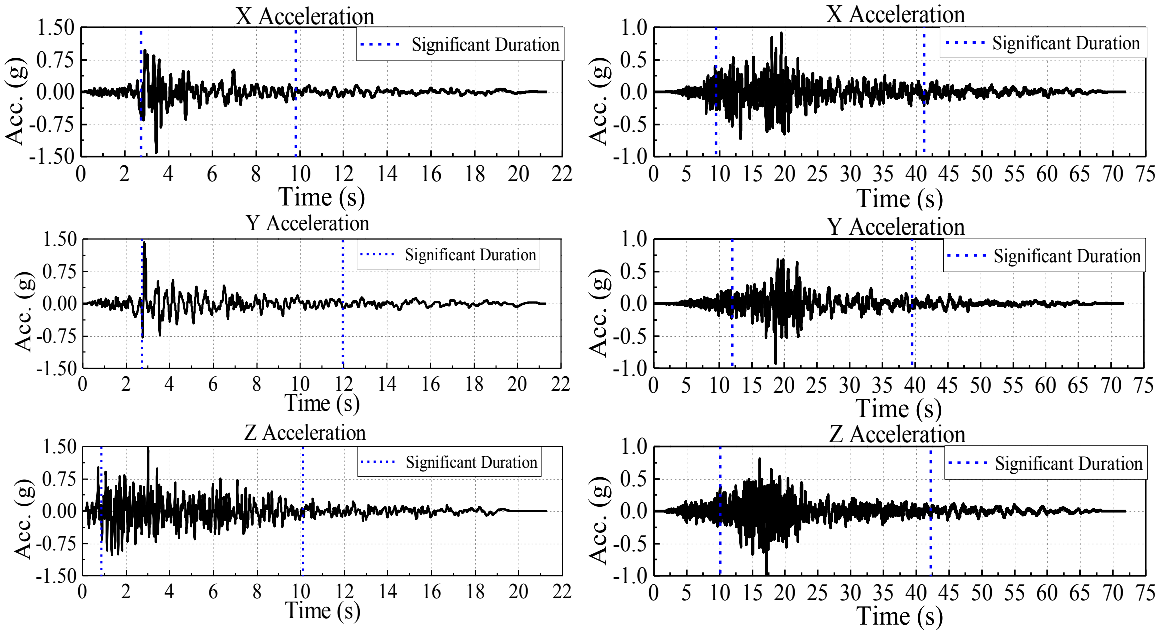

Erzican, Turkey

Chi-Chi, Taiwan

Figure 3.8. Time histories of input ground motions spectrally matched to 30,000-year return period

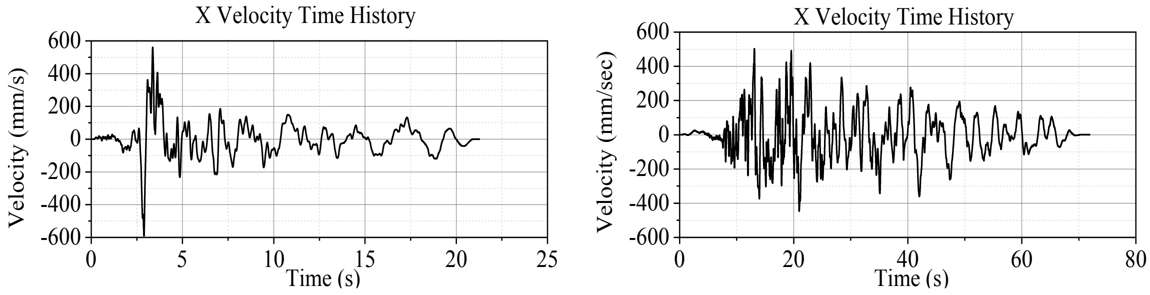

Erzikan, Turkey

Chi-Chi, Taiwan

Figure 3.9. Velocity time history (VTH), horizontal (X) component

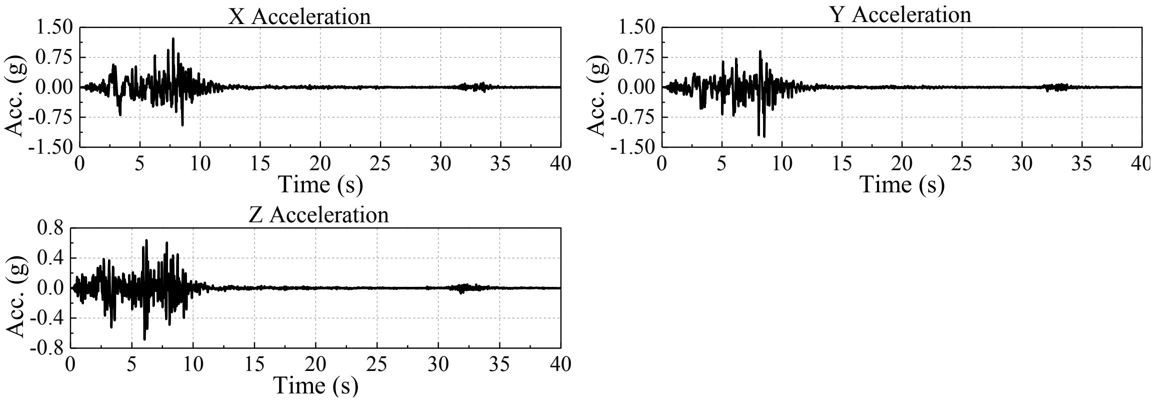

Figure 3.10. Time history of original San Fernando, Pacoima Dam (1971)

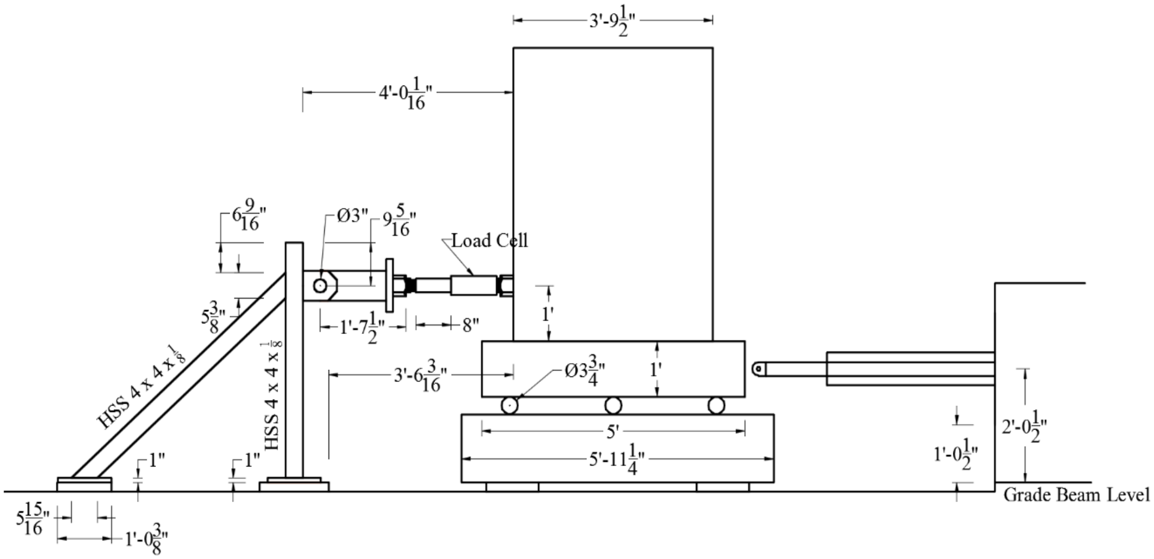

Figure 3.11. Experimental test setup for friction test

Figure 3.12. Experimental setup for friction coefficient test

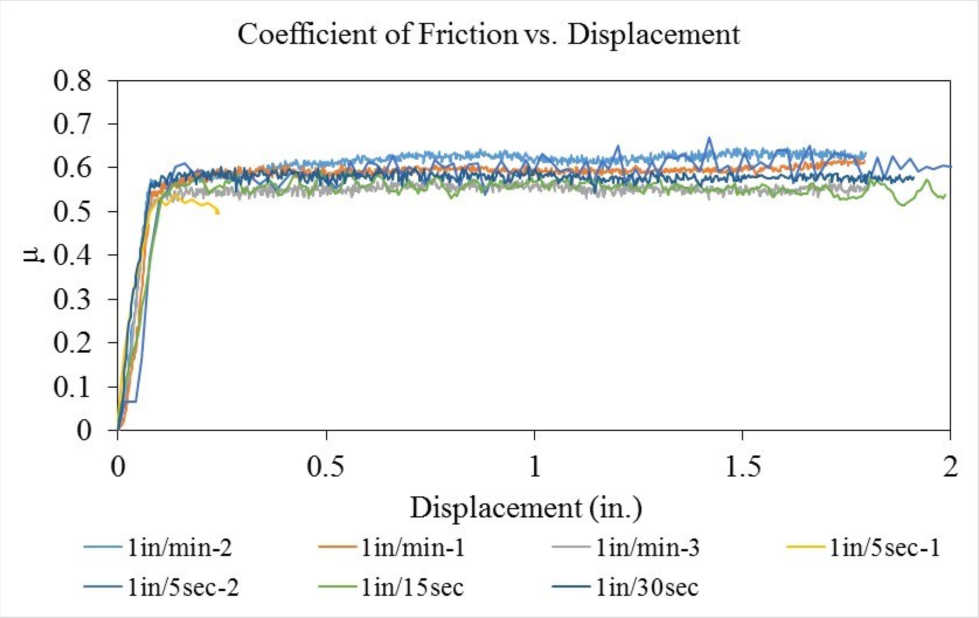

Figure 3.13. Coefficient of friction Test 1 data plots

CHAPTER 4

METHODS OF ANALYSES

4.1 Experimental Testing

The dynamic experimental tests were carried out at the University of Nevada, Reno (UNR) six-degree-of-freedom shaking table. Figure 4.1 shows one of the experimental setups of the cask FS.43, on top of the concrete pad (2,134 mm × 2,134 mm × 354 mm). The pad was anchored to the shaking table, while the cask was free-standing on top of the concrete pad. To prevent damage due to possible tip-over, a cable safety system was implemented during the tests. The figure also shows part of the instrumentation, which includes 12 string-pots to measure horizontal displacements at top and bottom surface points of the cask, 4 LVDTs to measure vertical displacement at four edge points at base of cask, 8 accelerometers to measure overpack acceleration response, and 10 accelerometers for MPC response accelerations. Eight strain gages were also used in the overpack shell. More details on the experimental tests and all the realizations carried out can be found in [50–54].

During the experimental tests, the ground motions presented by Figures 3.7-3.9 were applied to the scaled casks at different magnitude incremental steps, until the shake table was automatically stopped when the impact accelerations exceeded the allowable load capacity of the vertical actuators. Because of the scaled casks, time step of ground motions was scaled according to Tables 3.1 and 3.2. To study the variability in response of DSCs, some experimental realizations were repeated several times.

4.2 FE Analyses

4.2.1 Finite Element Model for Scaled Casks (Cask-Pad Only)

FE simulations for cask-pad models were started in the explicit code ABAQUS [49]. Preliminary simulations showed the solution was extremely sensitive not only to input parameters in the model, but to computer characteristics, and number of CPU cores used to run the simulations. This variation in response of FE models only occurred when rocking was induced in the system. However, if rocking was prevented by assigning low coefficient of friction, the extreme sensitivity was not present. Figures 4.2 and 4.2 demonstrate this variation when rocking was present, as well as absence of variation when only sliding was present.

This variation in the response for the same input file led to consideration of another FE code: LS-DYNA [3]. The advantage of using LS-DYNA was that a consistency flag could be introduced by defining negative number of CPUs in the input keyword file. This consistency flag, according LS-DYNA user's manual is recommended to control parallel processing. When the consistency flag is "turned on," the solver assembles the global vector assembly consistently, and provides identical results when the same input file is run multiple times, or different number of CPUs is used. This eliminated the solution variation due to computational inaccuracies (like round-off errors, etc.). However, the convergence of the model to a unique DSC solution does not guarantee that this is the only possible solution, as was shown later in the investigation.

Three-dimensional (3D) FE models for all free-standing specimens (Table 3.2) were created in LS-DYNA [3]. The models consisted of a free-standing cask on a square concrete pad. Figure 4.4 shows the cask-pad model built for $r/h_{cg} = 0.43$ cask (FS.43). The cask model included overpack and MPC containers for the base models. Alternatively, some models included an empty overpack only, or MPC only, to represent the last two specimens tested on the shake table. All parts in the model were hexahedral solid elements. However, to preserve the aspect ratio and weight of the cask specimen, the overpack wall and MPC were divided into two equal halves and their density was defined according to the target aspect ratio. Table 4.1 summarizes the material properties used in the FE models.

Contact was defined between the overpack and pad, and between the overpack and MPC, using "automatic_surface_to_surface" contact definition with a baseline concrete pad-steel overpack friction coefficient $\mu_s = \mu_k = 0.55$ (Section 3.4). The friction coefficient between overpack and MPC was assumed as 0.74, as expected in steel-to-steel friction surfaces [55]. The contact definition used in the model adopts a penalty contact algorithm. This is similar to introducing stiff springs between the two interacting surfaces to prevent penetration between slave and master surfaces. Global damping, as well as a scale factor for vertical damping, were determined by trial and error to account for energy loss, that is, coefficient of restitution during impact. The response of surfaces interacting through frictional contact can be highly nonlinear; therefore explicit time integration schemes were used to analyze the model. An explicit code was implemented because of its capability to solve highly nonlinear problems. Acceleration input was applied at the base of the concrete pad.

4.2.2 FE Model for Cask-Pad-Soil Simulation (Full Scale)

To study the effect of soil in the casks response, a fully coupled Cask-Pad-Soil model was created in LS-DYNA[3]. The model consists of a concrete pad on top of 152.4 m (500 ft.) of soil column, divided in 28 layers (Figure 4.5). The diameter of soil column was set to 15 times the diagonal of the pad with the pad's dimension: 29.41 × 9.45 × 0.61 m (158 × 372 × 24 in.). This large soil dimension is necessary to approximate semi-infinite soil, and to minimize the effects of reflected waves within the soil. Multiple iterations were carried out to determine most suitable soil dimensions for this study.

The nodes at the outer ring of each layer were constrained together to have the same node displacements. This is represented by a white ring in the top layer of Figure 4.5. The process was repeated multiple times for each layer except bottom edge nodes. This technique allows for the soil column to behave globally as a one-dimensional soil column, while allowing for local disturbances and movement [19,20].

Soil layer properties were defined as the strain compatible properties obtained from the convolution analysis performed in DEEPSOIL [56] using an equivalent linear approach. The details of deconvolution and convolution analyses and soil properties used in the model, including parameters for Rayleigh damping will be presented in the following chapter. The concrete pad was tied to the soil surface at the top to simulate any embedment of pad into the soil. Figure 4.5 shows a full scale model of four casks with aspect ratio r/h_{cg} = 0.43 placed in the middle section of the pad, while the rest of the pad was loaded with equivalent cask surface loads, as shown in Figure 4.6. A similar model for casks with aspect ratio 0.55, with dimensions of cask and surface load is given by Figure 4.7. The summary of calculations for weight of a cask and surface load is presented in Table 4.2.

4.3 Analytical Model

This research also utilized the analytical 2D analytical model to compare and contrast the analytical response with that obtained from 3D FE model. In addition running a large number of simulations in FE to perform response sensitivity analysis is computationally expensive. However, using analytical model for 2D body does not necessarily capture all the sources of variation like sliding and 3D motion in FE model.

Free-standing body's response is usually idealized as a 2D rigid body problem. In this investigation a cylindrical free-standing body like DSCs was idealized as a 2D planar body. One of the disadvantages of using planar bodies is that the 2D equations cannot make a distinction between a "block type" body with a rectangular base and a cylindrical structure. However, the corresponding analytical models are not computationally expensive and are useful for studying chaotic response, parametric studies, and comparing 3D FE response to that of classical 2D approach. Thus, the simplest idealization of 2D rocking only was considered. When a free-standing body is idealized as a 2D rigid system and only pure rocking is considered (Figure 4.8), the governing equation of motion [57] for such a body can be expressed by Equation (4.1).

$$\ddot{\theta} = -p^2 \left\{ \sin[\alpha * \mathrm{sgn}(\theta(t)) - \theta(t)] \left(1 + \frac{\ddot{v}_g}{g} \right) + \frac{\ddot{u}_g}{g} \cos[\alpha * \mathrm{sgn}(\theta(t)) - \theta(t)] \right\} \tag{4.1}$$

where, sgn(x) is a signum function; $\ddot{u}_g$ and $\ddot{v}_g$ are the horizontal and vertical accelerations, and α = $\tan^{-1}(r/h_{cg})$ is the critical angle. The distance from c.g. to rocking pole is, $R = \sqrt{r^2 + h_{cg}^2}$; the frequency parameter (rad/s) is $p = \sqrt{mgR/I}$; and $I = I_O + mR^2$ = mass moment of inertia about rocking pole.

Equation (4.1) was solved with the explicit fourth order Runge-Kutta method using a time step $dt < 0.001$ s (from 10^{-3} to 10^{-4} s). Figure 4.9 shows the implemented algorithm to obtain the rocking response. During the solution of Equation (4.1), the impact condition ($\theta_i \cdot \theta_{i+1} < 0$) was monitored at each time step. If the condition was satisfied, a subroutine checked if the rocking angle (θ_i) was within the required precision ($\leq 10^{-6}$). Otherwise the time step was reduced one order of magnitude. When this condition was satisfied, impact or contact was assumed to have occurred and the velocity after impact ($\dot{\theta}_{i+1}$) was modified using Equation (4.2) to account for energy loss during impact (i.e., damping).

$$\dot{\theta}_{i+1} = e * \dot{\theta}_i \tag{4.2}$$

In Equation (4.2), e is the coefficient of restitution, conventionally estimated by Equation (4.3) [5,10,12,29,30,57]. The energy loss equation can be derived from the principle of conservation of angular momentum immediately before and after impact. The main assumptions for Equations (4.1) and (4.3) are that the body and base are rigid, no bouncing or complete lifting off of the body, and there is no sliding between body and base.

$$e = 1 - \frac{2mR^2}{I}\sin^2\alpha \tag{4.3}$$

However, previous experiments have consistently shown that Equation (4.3) under-predicts e [58]. Elgawady et al. [59] in 2011 presented a relationship to determine e from experimentally obtained rocking angle time history given by Equation (4.4). In Equation (4.4) θ_n and θ_{n-1} is rocking angle after n^{th} and $(n-1)^{\text{th}}$ impact, respectively.

$$e = \frac{\dot{\theta}_n}{\dot{\theta}_{n-1}} = \sqrt{\frac{\cos(\alpha - \theta_n) - \cos(\alpha)}{\cos(\alpha - \theta_{n-1}) - \cos(\alpha)}} \tag{4.4}$$

In one of the experimental realizations for the FS.43 specimen [50–54] the shake table aborted, due to high impact acceleration, after initiation of rocking. The DSC then experienced free-rocking after the shake table stopped. Figure 4.10 shows rocking angle time history for the experimental realization. The average value of e determined from Equation (4.4) was found to be 0.872, 14.5% larger than the theoretical value of 0.761 obtained using Equation (4.3) (for the FS.43 DSC with $\alpha = 0.41$, $R = 1.33$ m. and $p = 2.37$ rad/s, Table 4.3). This value of e (= 0.872 for FS.43) will be used, particularly in Chapter 8.

Table 4.1. Material properties of FE models of DSCs

Specimen	Parts	Material Properties		
		Young's modulus, E (kN/m^2)	Poisson's ratio, ν	Density, ρ (kg/m^3)
FS.55	Top and bottom plates	2.00×10^8	0.3	7.83×10^3
	Overpack	2.00×10^8	0.3	8.11×10^3 (bottom half) 6.26×10^3 (top half)
	MPC	2.00×10^8	0.3	8.67×10^3 (bottom half) 7.19×10^3 (top half)
FS.43	Top and bottom plates	2.00×10^8	0.3	7.83×10^3
	Overpack	2.00×10^8	0.3	6.03×10^3 (bottom half) 7.01×10^3 (top half)
	MPC	2.00×10^8	0.3	8.65×10^3 (bottom half) 7.15×10^3 (top half)
	Concrete Pad	2.78×10^7	0.2	2.29×10^3
Coefficient of friction		0.55 ($\mu_s = \mu_k$)		

Table 4.2. Weight of full scale casks and surface load calculations

Description	**Full Scale Cask r/h_{cg} = 0.43**	**Full Scale Cask r/h_{cg} = 0.55**
Area (A) [m^2]	5.457	6.560
Bottom Stress [kPa] *	166.29	160.30
Weight [kN]	907.44	1051.50
Weight of 4 Casks [kN]	3629.75	4206.10
Surface Load [kPa]	35.8	44.6
Note: * - Bottom stress is same as that of scaled casks		

Table 4.3. Geometric properties of idealized 2D free-standing DSCs

Parameters		**Specimen**	
Name, Symbol	**Units**	**Squat Cask FS.55**	**Slender Cask FS.43**
Aspect ratio, r/h_{cg}	-	0.55	0.43
Mass, **m**	kg [kip]	17.10×10^3 [37.70]	14.75×10^3 [32.51]
Radius, r	mm [in]	577.85 [22.75]	527.05 [20.75]
Total height, h	mm [in]	2223	2426
Centroidal height, h_{cg}	mm [in]	1055.62 [41.56]	1219.96 [48.03]
Critical rocking angle, $\alpha = \tan^{-1}\{r/h_{cg}\}$	Radian	0.50	0.41
Mass Moment of Inertia about c.g., I_o	Kg-m^2 [lb/g-in^2]	8,347 [73,814]	8,260 [73,044]
Distance of c.g. from rocking point, R	mm [in]	1203.43 [47.38]	1334.21 [52.26]
Frequency Parameter, p	rad/s	2.47	2.37

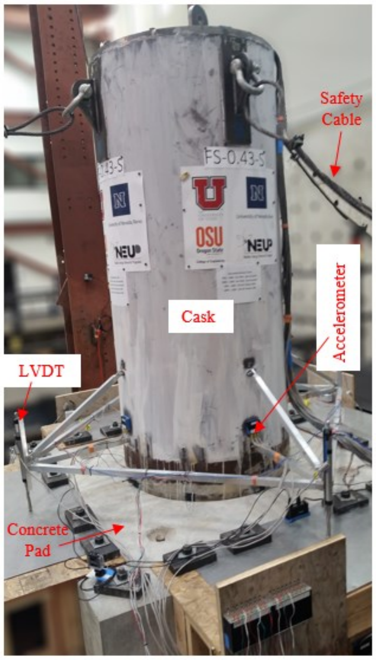

Figure 4.1. Experimental test setup of free-standing cask

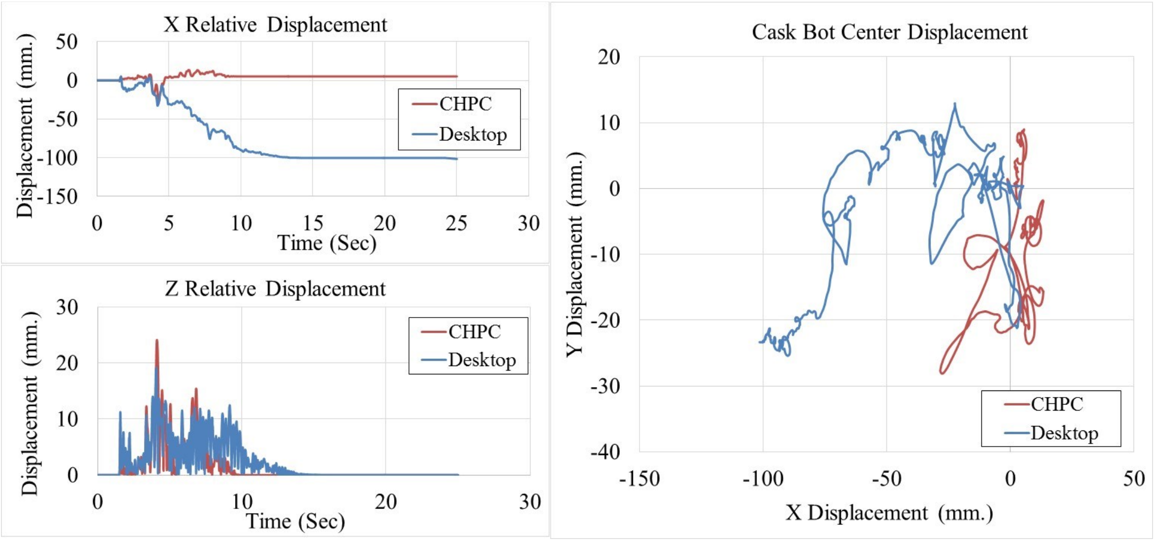

Figure 4.2. Variation in FE model solution: same input file, different computers (rocking present) [CHPC and Desktop – different computers]

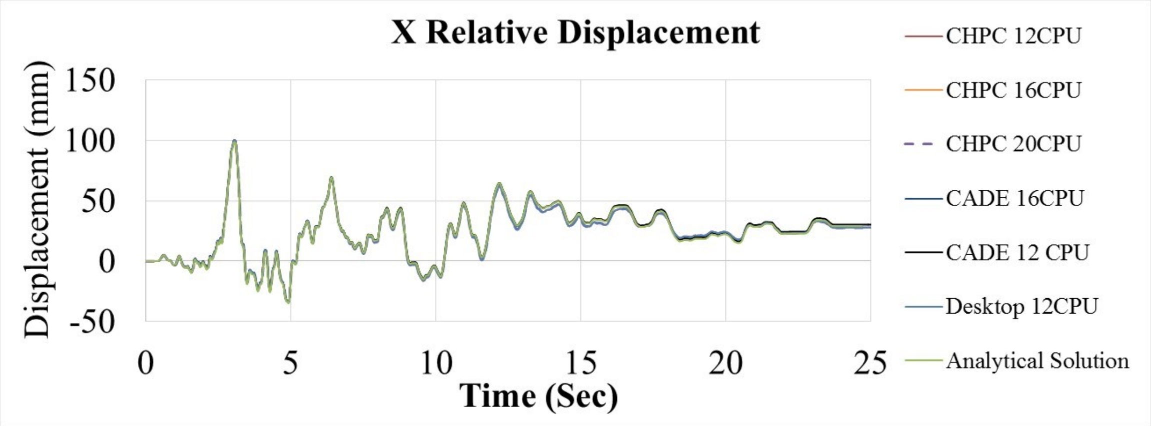

Figure 4.3. No variation in FE model solution: same input file, different computers (μ = 0.1, sliding only, no rocking) [CHPC, CADE, Desktop – different computers; 12, 16, 20CPU –number of central processing unit used for parallel processing]

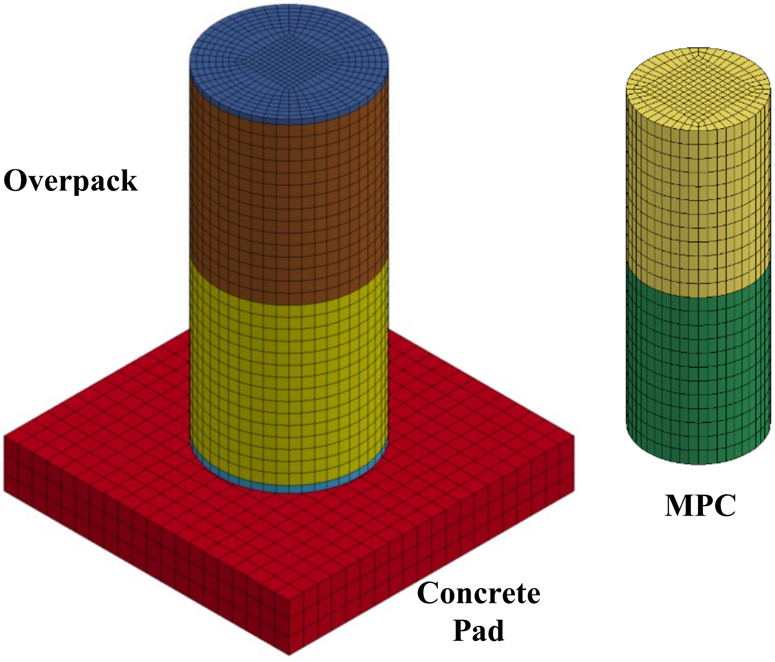

(a) (b)

Figure 4.4. FE model of free-standing specimen: (a) Cask-Pad assembly, (b) MPC

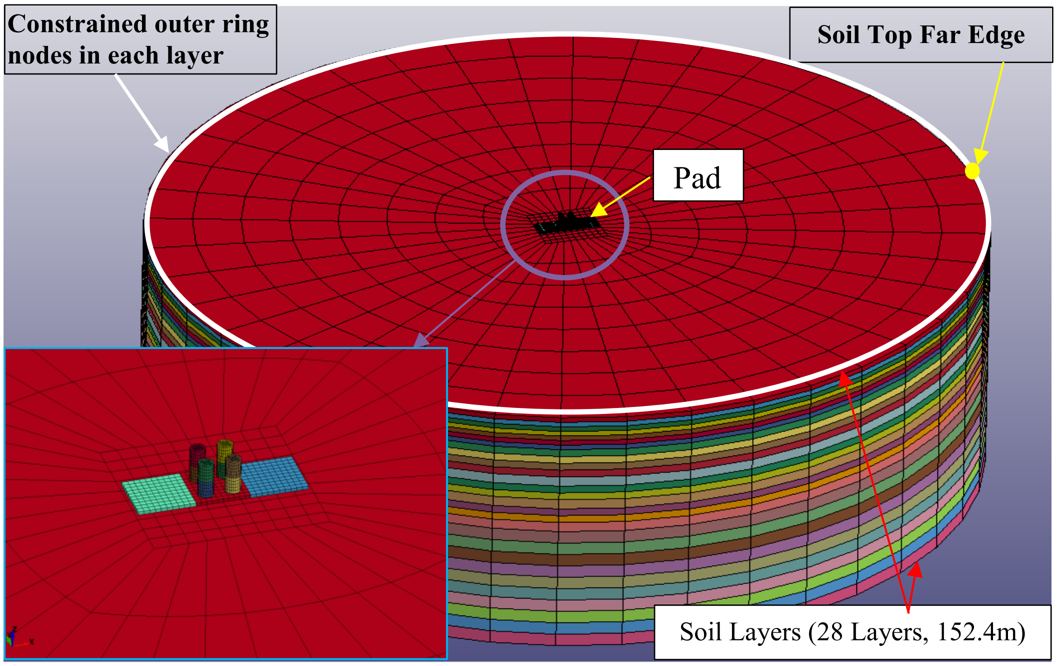

Figure 4.5. FE model for cask-pad-soil full scale model

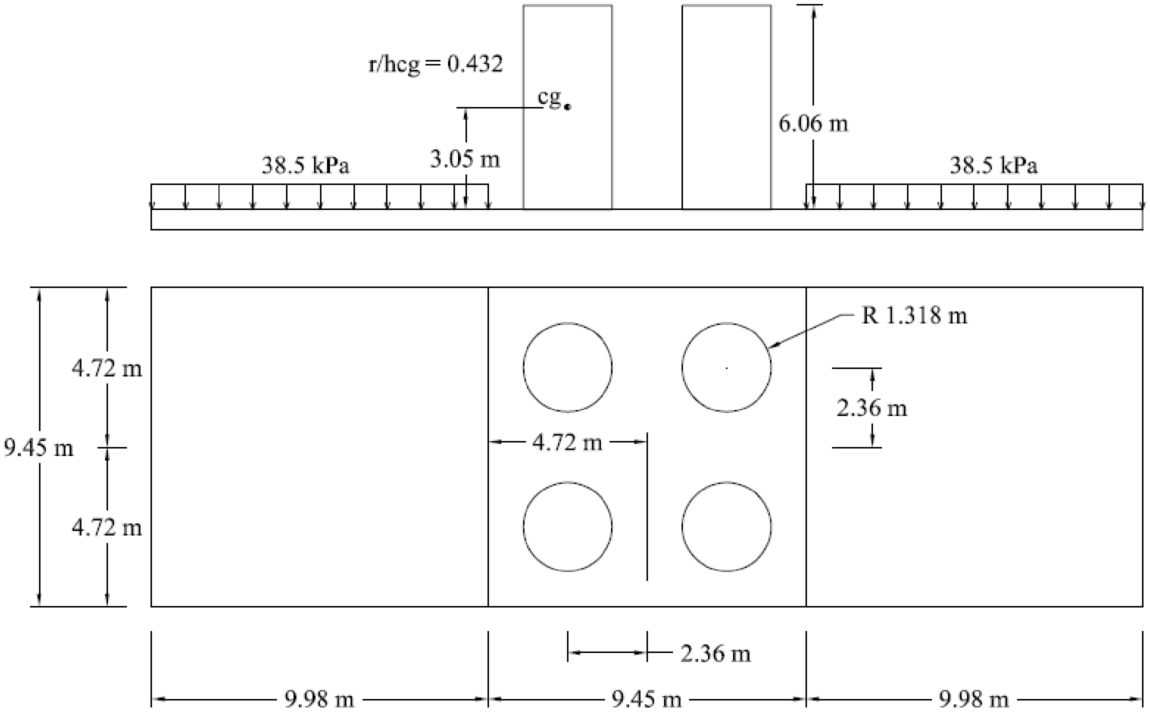

Figure 4.6. Schematics of casks and pad for full-scale (Cask $r/h_{cg} = 0.43$)

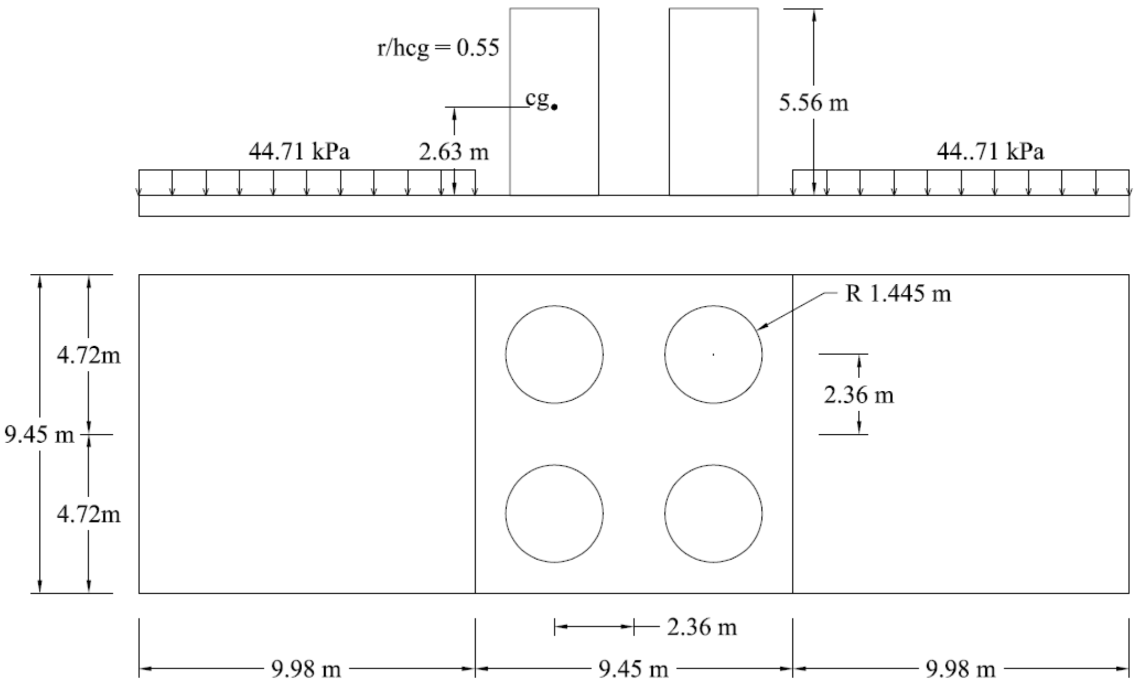

Figure 4.7. Schematics of casks and pad for full-scale (Cask $r/h_{cg} = 0.55$)

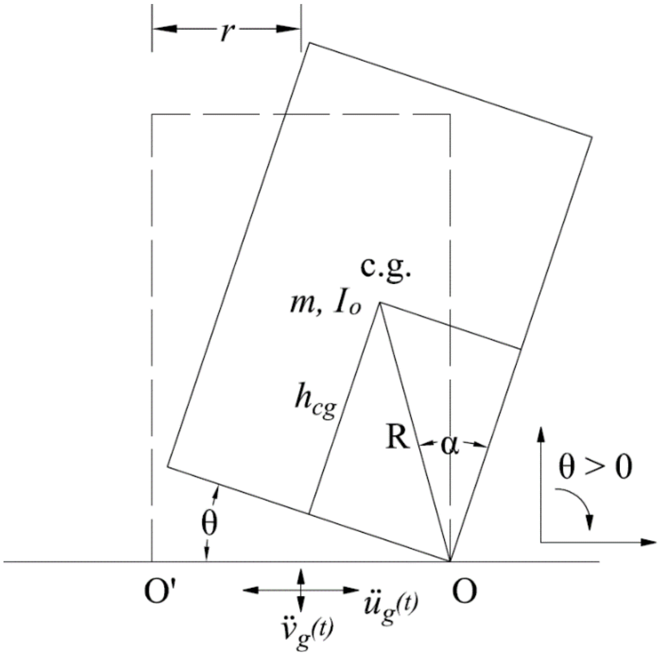

Figure 4.8. Cross-section of a cylindrical free-standing body, idealized rocking state

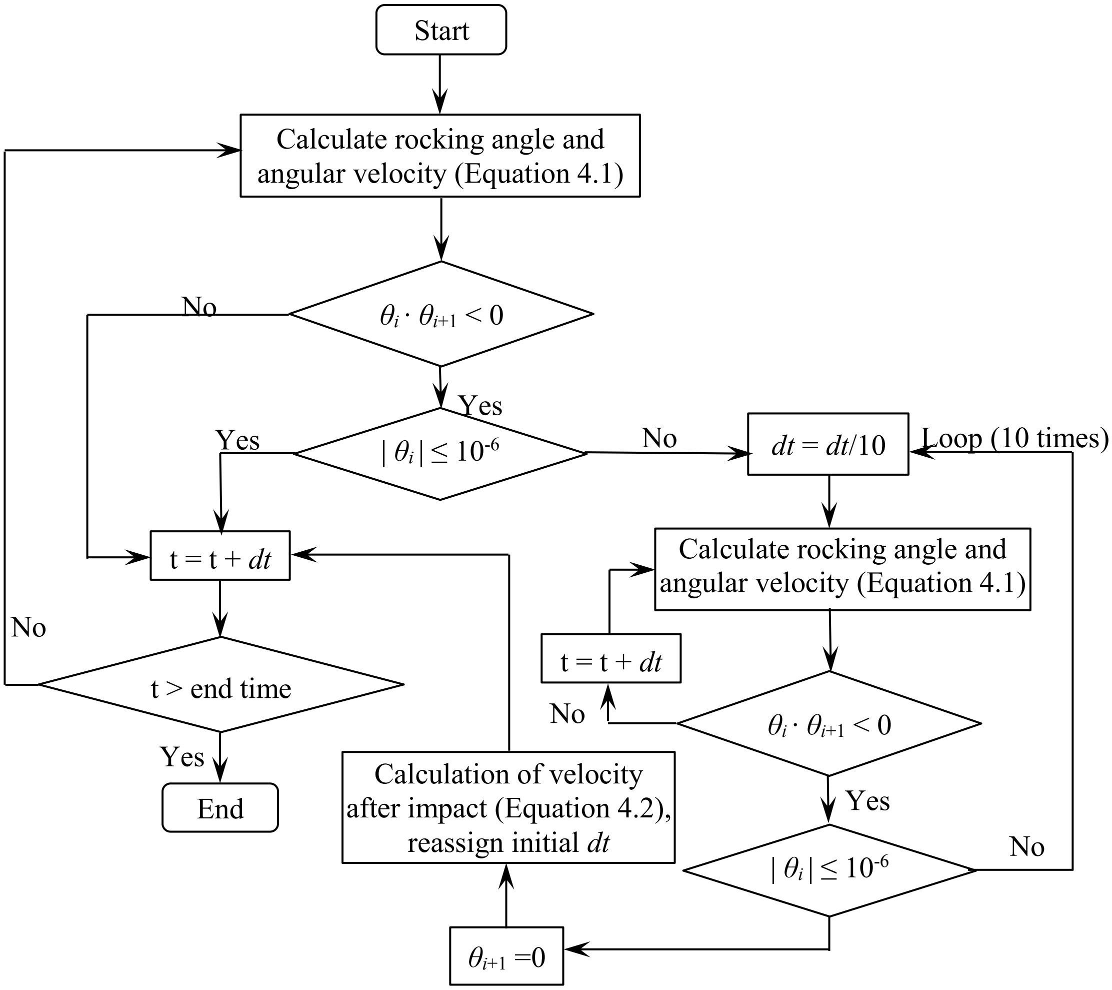

Figure 4.9. Rocking response analysis algorithm

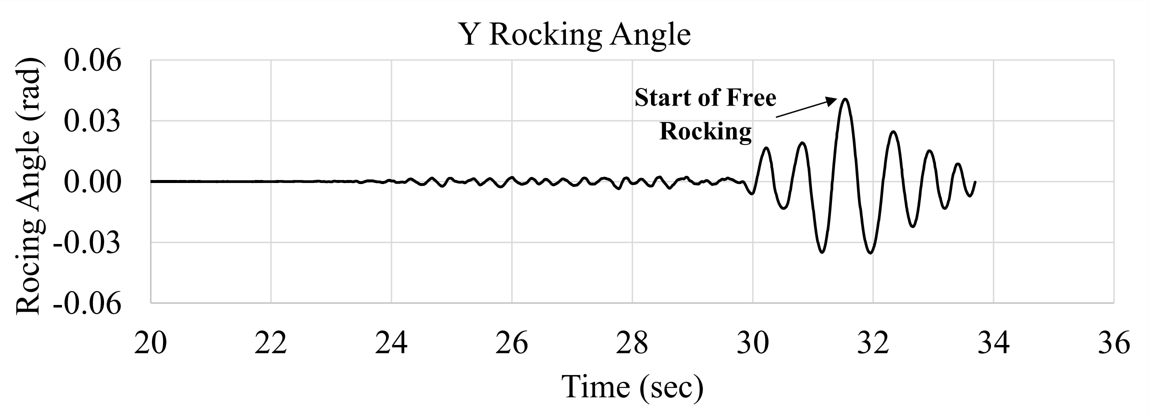

Figure 4.10. Rocking angle time history of the FS.43 DSC from experiment

CHAPTER 5

RESULTS FROM EXPERIMENTS

The ground motions presented in Figures 3.7-3.9 were applied to the scaled cask at different magnitude incremental steps, until the shake table was automatically stopped when the impact forces exceeded the allowable load capacity of the vertical actuators, or the vertical displacements at the edge of the cask exceeded 102 mm (4 in.).

Dynamic experimental tests were performed for four free-standing DSC specimens (FS.55, FS.43, FS.39 and FS.62). The details about the specimens can be found in Table 3.2. The maximum intensity of ground motions that could be applied during the testing of FS.55 and FS.43 are given in Table 5.1. The cask FS.55 did not show significant movement because of the low accelerations of the maximum applied ground motions that could be applied. Hence experimental results for FS.55 are not presented in this dissertation. Specimens FS.39 and FS.62 were tested in a similar way. However, due to their relative light weight, larger ground motion accelerations were successfully applied. Maximum input motions for FS.39 are given in Table 5.1, which also presents the maximum intensity of ground motions applied for the test of FS.62.

Results from experimental realizations with multiple repeats were used to study the repeatability of the response under similar (repeated) ground motions. The experimental test results are also used to compare the response between Erzican having only one major pulse and Chi-Chi that has multiple pulses (i.e., NFGM vs. FFGM response, respectively).

5.1 Repeatability Study under Repeated Motions

Figure 5.1 compares the results of FS.43 casks under repeated motions. Figures 5.2 and 5.3 present similar realizations for the FS.39 cask. Lastly, Figure 5.4 presents the response comparison for the five repeat tests for FS.62. Table 5.2 shows the peak and residual values for FS.62 response under 100% of 10,000-year Chi-Chi (Figure 5.4), as well as the standard deviation and coefficient of variation for the data obtained from five repeats. Note that five data point is considered to be statistically insufficient, but it provides an estimate of dispersion from experimental tests.

The results shown in Figures 5.1-5.4 suggest that the response of free-standing cask is not repeatable. These results are consistent with similar observations of previous studies [14,27–30]. The response variation is particularly significant for the lateral displacement of the cask, and to a lesser degree on the rocking response of the cask. In Figures 5.1 and 5.2 the variation in rocking angle is not significant. However variation in the displacement is clearly visible. These cases were exceptions rather than the norm as shown in Figures 5.3 and 5.4. In these cases the differences in displacement as well as rocking angle are more evident. Figure 5.3 describes the response of FS.39 (same specimen as Figure 5.2) under 75% of 10,000-year Chi-Chi instead of original San Fernando motion. Chi-Chi, as mentioned earlier, is a far field motion while original San Fernando has near field characteristics. For this reason, Chi-Chi resulted in large variation in rocking angle, more than two times for one realization compared to other repeats of same motion.

The coefficients of variation shown in Table 5.2, obtained from Figure 5.4, confirm these trends. The variation on the response appears to be caused by small changes in initial conditions. This change in the initial position, which exists during rocking results in difference boundary condition at any given instance of movement.

Specimens FS.39 and FS.62, were also tested under repeated bidirectional and unidirectional excitations. Figures 5.5-5.7 present the response of FS.39 under unidirectional (X only) and bidirectional (X and Y; X and Z) components, respectively, under 75% of 10,000-year Chi-Chi. Figures 5.8 and 5.9 present the response of FS.62 unidirectional (X only) and bidirectional (X and Z) components, respectively, for 100% of 10,000-year Chi-Chi. The results show the lack of repeatability on the response, even for unidirectional and bidirectional excitations. Note that significant out-of-plane motion was recorded for cases where only one horizontal component is applied. A similar out-of-plane displacement was observed for realizations with one horizontal and vertical excitation. These figures show that tridirectional excitation is not necessary for response variation. When an actual ground motion is applied, response may vary even for unidirectional and bidirectional horizontal excitation, where vertical excitation is not present, the response is not repeatable.

5.2 Response under Near Field and Far Field Motion

Figure 5.10 shows the response of FS.43 for 50% of 10,000-year Erzican and 75% of 10,000-year Chi-Chi. Note that 10,000-year Chi-Chi at 75% had the smaller PGA of the two motions, but it led to the higher peak lateral displacements and rocking angle, possibly because this FFGM contains multiple pulses and it is able to sustain rocking and nutation motion of the cask. In this type of motion, the cask rolls or travels around its edge. During prolonged rocking and nutation, it is easier for cask to move around, producing larger displacements.

The experimental responses of FS.39 for 75% of 10,000-year Erzican and 75% of 10,000-year Chi-Chi are shown in Figure 5.11, indicating that rocking angle response increases as the aspect ratio decreases (i.e., as the cask becomes slender). The results again indicate that sustained rocking and nutation motion are undesirable as they facilitate large lateral displacements. PGA for the applied 10,000-year Erzican motion was about 1.63 times larger than that for 10,000-year Chi-Chi (Table 5.1). That resulted in larger rocking for the NFGM (Erzican). However, Chi-Chi motion still produced lateral displacements comparable to those obtained for Erzican. The response for FS.62 under 100% of 10,000-year Erzican and 100% of 10,000-year Chi-Chi is presented in Figure 5.12, whereas the response of 75% of 30,000-year Erzican and 100% of 30,000-year Chi-Chi is shown in Figure 5.13. These results suggest that FFGM with multiple pulses produce larger rocking and displacements than NFGMs, under similar seismic intensity measures (e.g., PGA).

5.3 Discussion of Results from Experiments

5.3.1 Repeatability Study

Scaled free-standing casks were subjected to multidirectional earthquake motions to study the response of DSCs under long-term seismic events. The specimens used in this study have aspect ratios of 0.62, 0.55, 0.43 and 0.39. Repeat tests were performed to investigate the potential variation on the dynamic cask response. The main findings are summarized below:

i. Repeated tests under identical ground motions lead to large variation on the dynamic response of free-standing DSCs. A small change in initial conditions causes large variations in the response.

ii. The variation in response under seismic motions, not only exists when accelerations are applied in three orthogonal directions, but also under bidirectional and unidirectional excitations.

iii. While most of the previous studies focus on block type structures (2D or 3D), this study investigated response of 3D cylindrical free-standing DSCs. The fact that DSCs have a circular base increases the likelihood of motions along the cask edge, resulting in tumbling or nutation motion. Any minute differences at any instance of DSC's response, while on its edge, propagate in the following time steps and the response diverges.

iv. Response variation was also observed on rocking displacements, particularly for free-standing bodies with lower aspect ratios (slender bodies).

v. The fact that the seismic response can be drastically different due to small changes in initial conditions is an important finding because it indicates the potential for a chaotic response. Anchoring the cask to the concrete foundation could be a solution to avoid such unpredictable response. Such systems can also help in reducing the possibility of extreme events like cask overturning or excessive movement, but they require the additional anchor design, a thicker foundation base, and there may a possibility of sliding of the entire foundation pad.

5.3.2 NFGM vs. FFGM Response

Ground motions used for the study have near field and far field characteristics. The experimental results show that FFGM with multiple pulses leads to larger rocking and lateral displacements compared to NFGM with a one or two large pulses. The series of pulses in FFGMs increases rocking and tumbling motion of the free-standing bodies, as the input motion unfolds. Early pulses cause the free-standing casks to rock or tumble, making it easier for the casks to move (lateral or rocking motion) when subsequent pulses occur. Despite the fact of having varied cask response, the DSCs' response under FFGMs consistently shows larger displacements, because of the multiple pulses.

Table 5.1. Intensity of ground motion applied during experimental tests

Specimen	**Ground Motion**	**Return Period (years)**	**Applied Intensity (%)**	**Target Scaled PGA (g)**		
				X	**Y**	**Vert. (Z)**
FS.55	Erzican	10,000	30	0.316	0.316	0.338
	Chi-Chi	10,000	50	0.320	0.320	0.343
FS.43	Erzican	10,000	50	0.527	0.527	0.564
	Chi-Chi	10,000	75	0.480	0.480	0.514
FS.39	Erzican	10,000	75	0.790	0.790	0.845
	Chi-Chi	10,000	75	0.480	0.480	0.514
FS.62	Erzican	10,000	100	1.053	1.053	1.127
	Chi-Chi	10,000	100	0.640	0.640	0.685
	Erzican	30,000	75	1.059	1.059	1.133
	Chi-Chi	30,000	100	0.918	0.918	0.982

Table 5.2. Peak and residual values of FS.62 response (100% of 10,000-year Chi-Chi)

Description		**Run 1**	**Run 2**	**Run 3**	**Run 4**	**Run 5**	**Std. Dev**[a]	**cov**[b]
X Displacement (mm)	Peak	65.03	15.31	-18.89	22.48	-30.92	20.14	0.66
	Residual	51.92	-7.70	-17.95	12.14	-21.15	17.42	0.79
Y Displacement (mm)	Peak	34.06	-54.29	28.06	-33.16	30.17	10.53	0.29
	Residual	13.88	-49.85	15.78	-26.45	-5.24	17.18	0.77
Z Displacement (mm)	Peak	26.06	19.01	17.53	17.53	22.99	3.78	0.18
X Rocking Angle (rad)	Abs Max[c]	0.030	0.034	0.027	0.028	0.032	0.003	0.10
Y Rocking Angle (rad)	Abs Max[c]	0.043	0.014	0.021	0.020	0.029	0.011	0.44

[a] Std. Dev: Standard Deviation, calculated using absolute values

[b] cov: Coefficient of Variation, calculated using absolute values

[c] Abs Max: Absolute Maximum

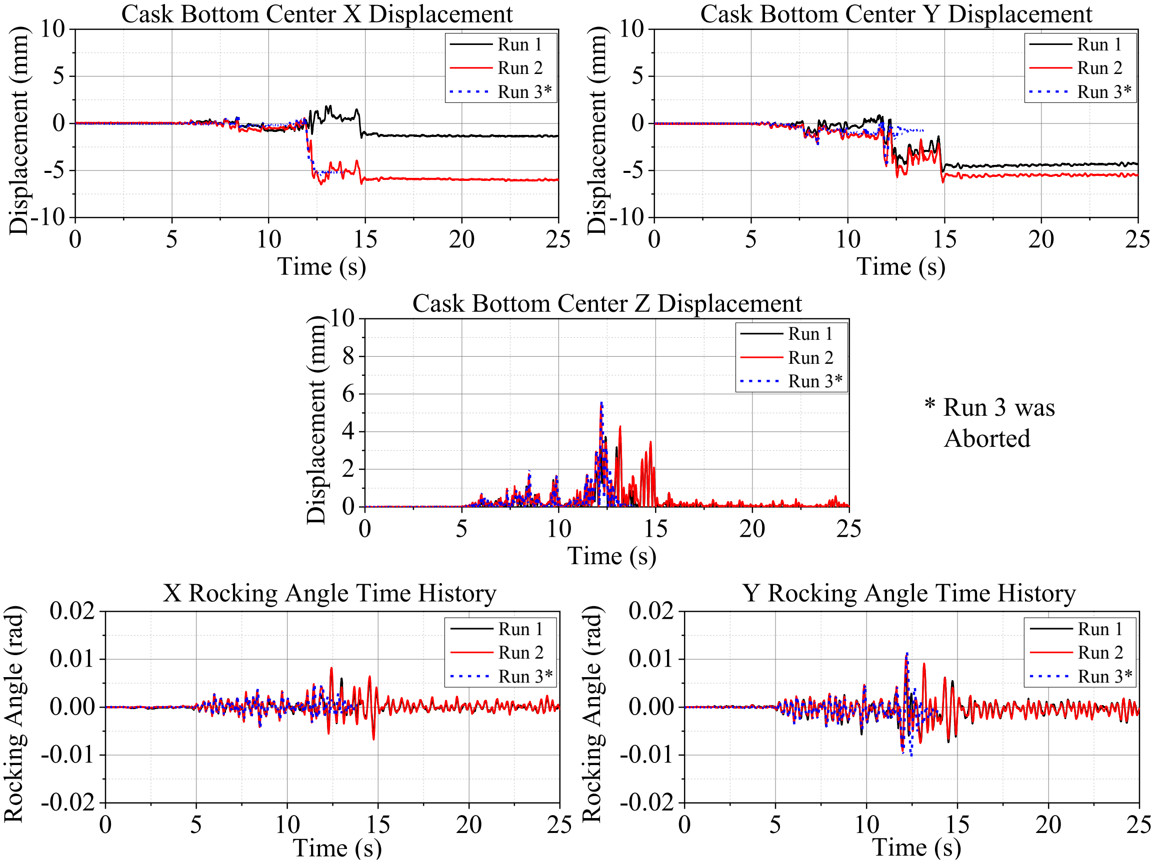

Cask Bottom Center X Displacement

Cask Bottom Center Y Displacement

Cask Bottom Center Z Displacement

X Rocking Angle Time History

Y Rocking Angle Time History

* Run 3 was
Aborted

Figure 5.1. Response of FS.43 under repeated 75% of 10,000-year Chi-Chi

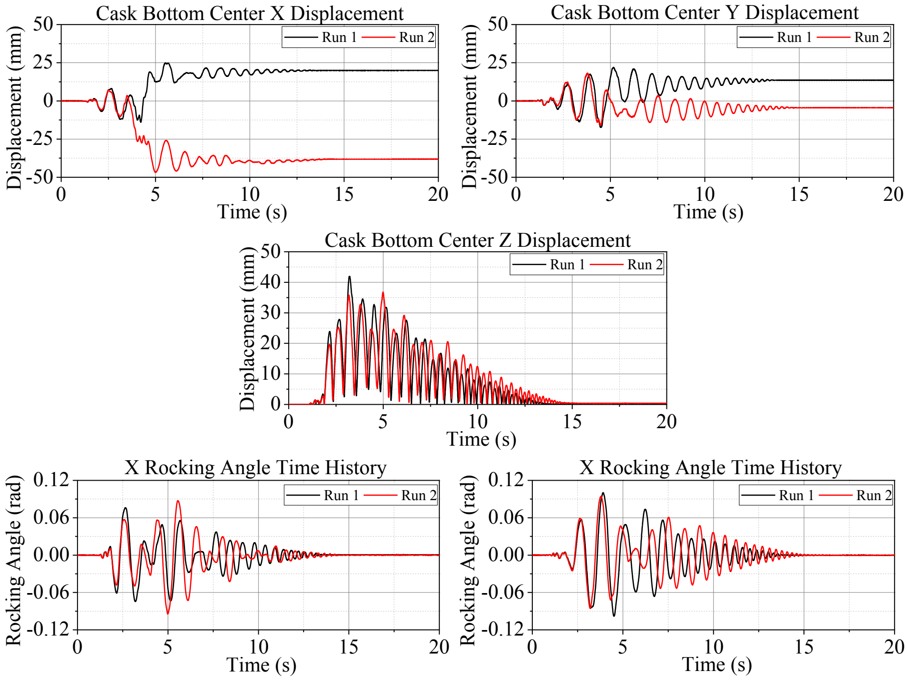

Figure 5.2. Response of FS.39 under repeated 75% of Original San Fernando

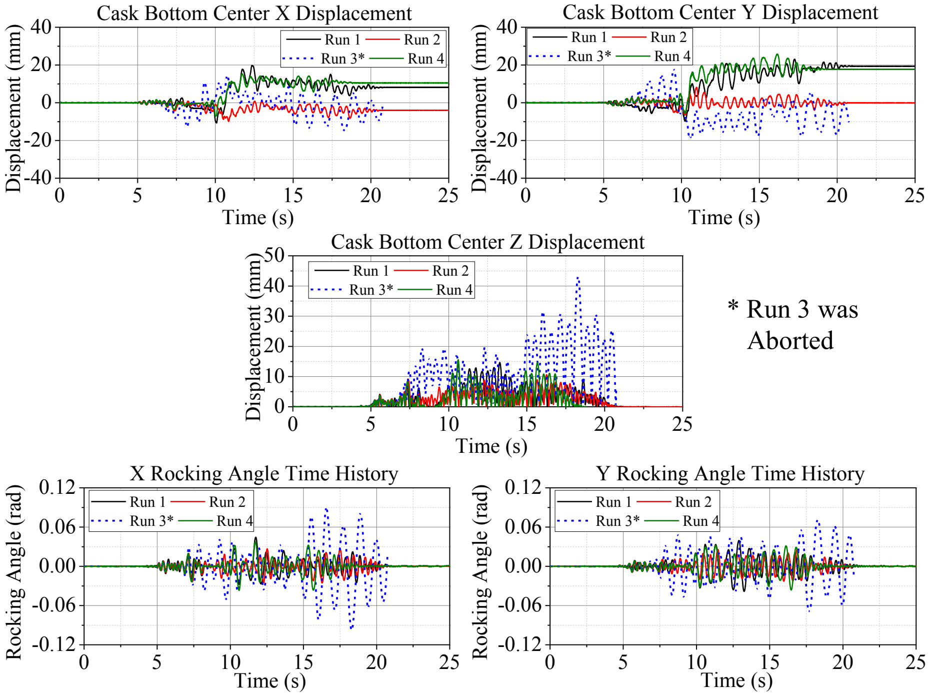

* Run 3 was Aborted

Figure 5.3. Response of FS.39 under repeated 75% of 10,000-year Chi-Chi

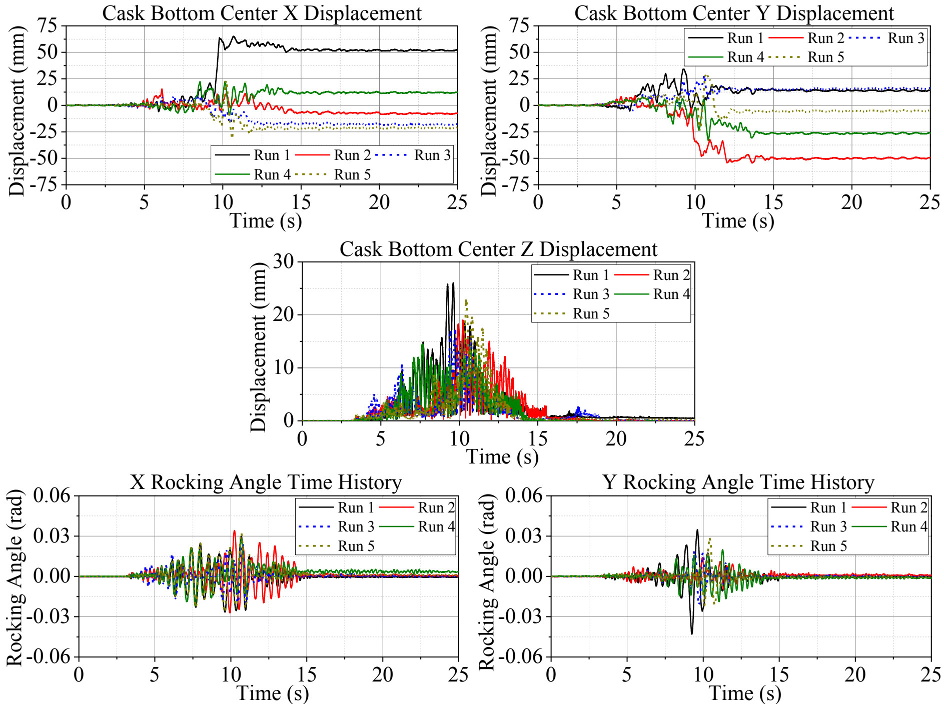

Figure 5.4. Response of FS.62 under repeated 100% of 10,000-year Chi-Chi

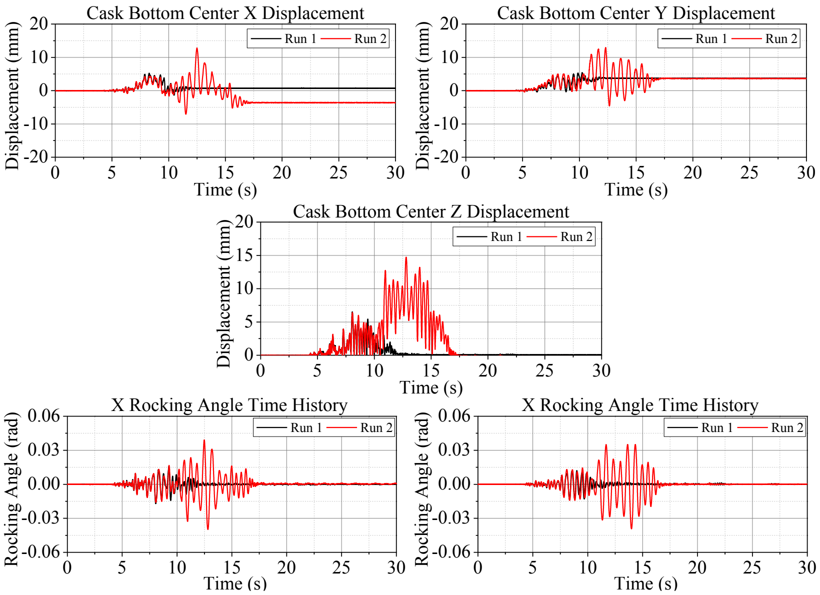

Figure 5.5. Response of FS.39 under repeated 75% of 10,000-year Chi-Chi (X only)

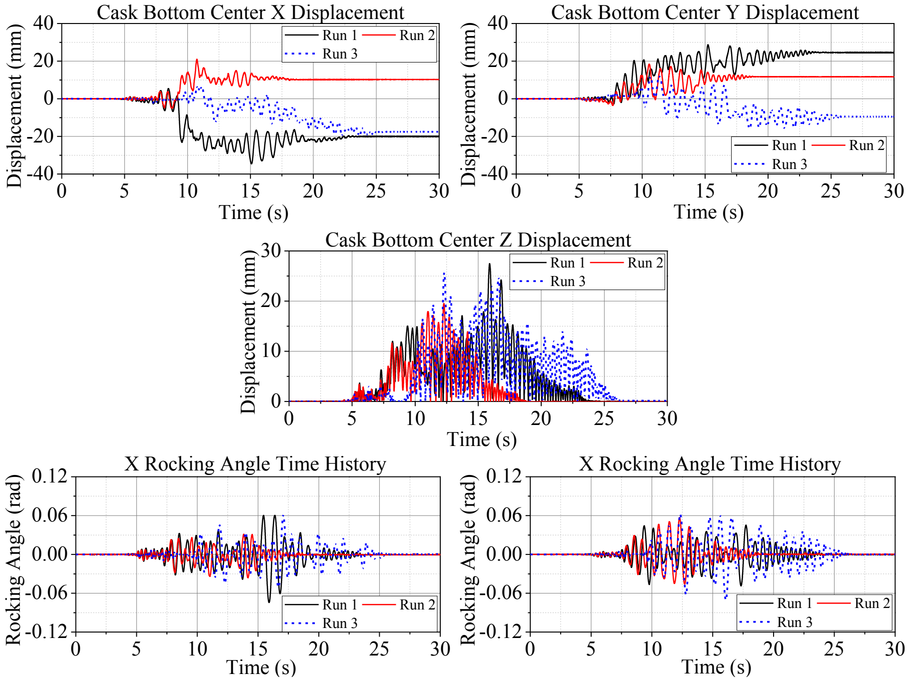

Figure 5.6. Response of FS.39 under repeated 75% of 10,000-year Chi-Chi (X and Y only)

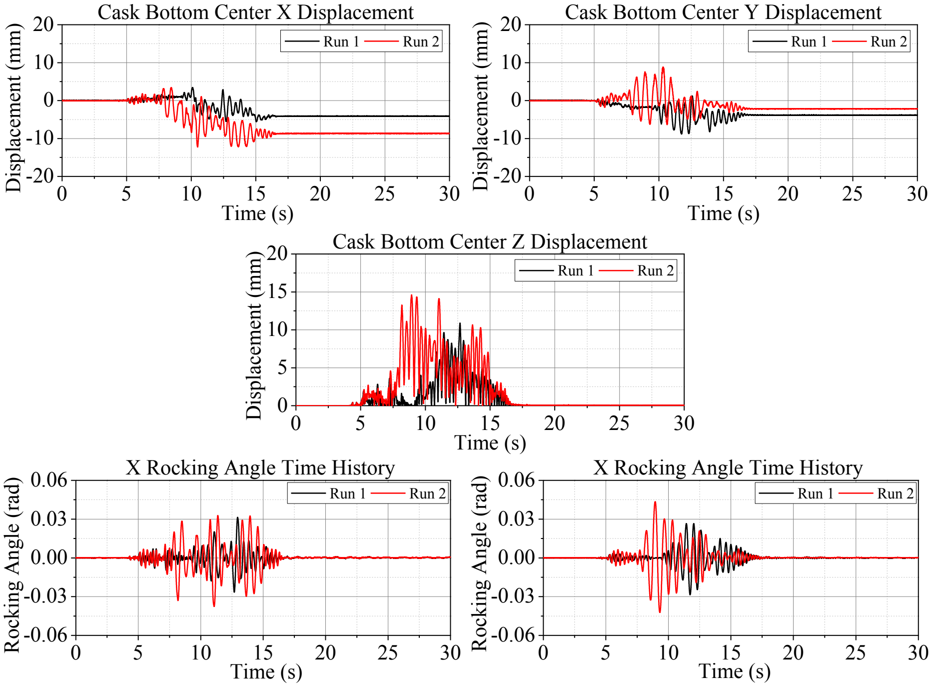

Figure 5.7. Response of FS.39 under repeated 75% of 10,000-year Chi-Chi (X and Z only)

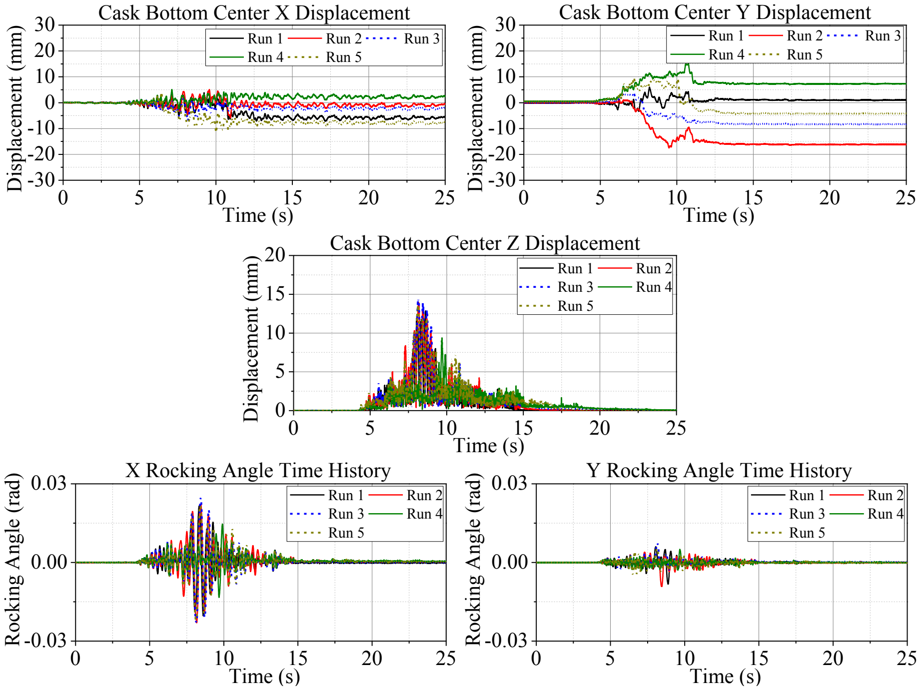
Cask Bottom Center X Displacement
Cask Bottom Center Y Displacement
Cask Bottom Center Z Displacement
X Rocking Angle Time History
Y Rocking Angle Time History

Figure 5.8. Response of FS.62 under repeated 100% of 10,000-year Chi-Chi (X only)

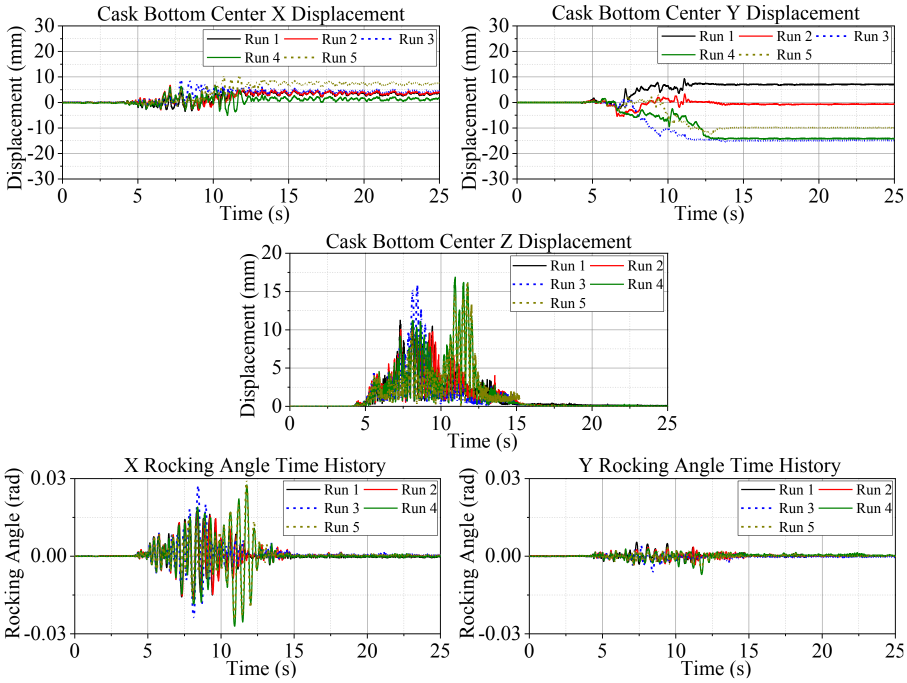
Cask Bottom Center X Displacement
Cask Bottom Center Y Displacement
Cask Bottom Center Z Displacement
X Rocking Angle Time History
Y Rocking Angle Time History

Figure 5.9. Response of FS.62 under repeated 100% of 10,000-year Chi-Chi (X and only)

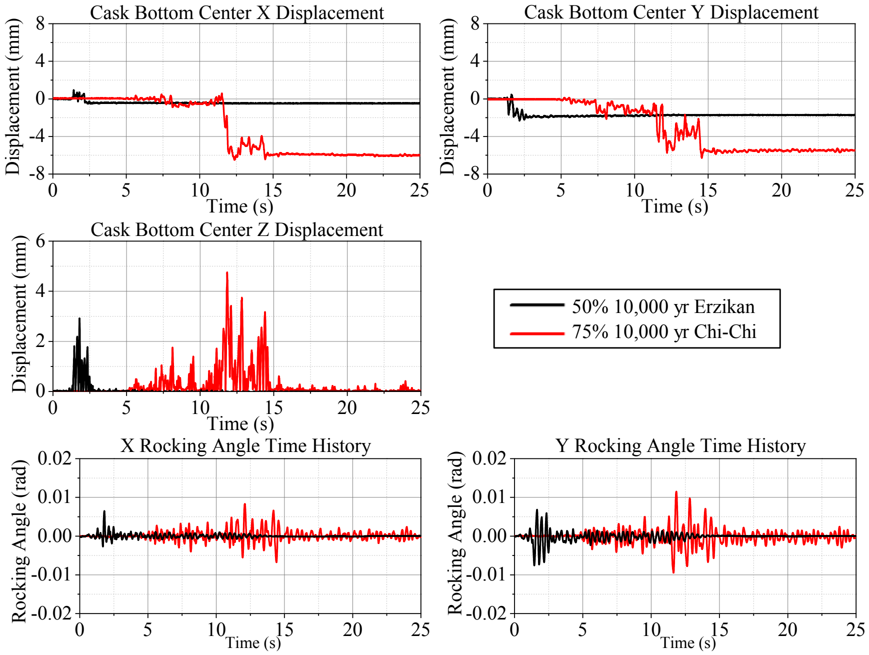

Figure 5.10. Response of FS.43 under 50% of 10,000-year Erzican and 75% of 10,000-year Chi-Chi

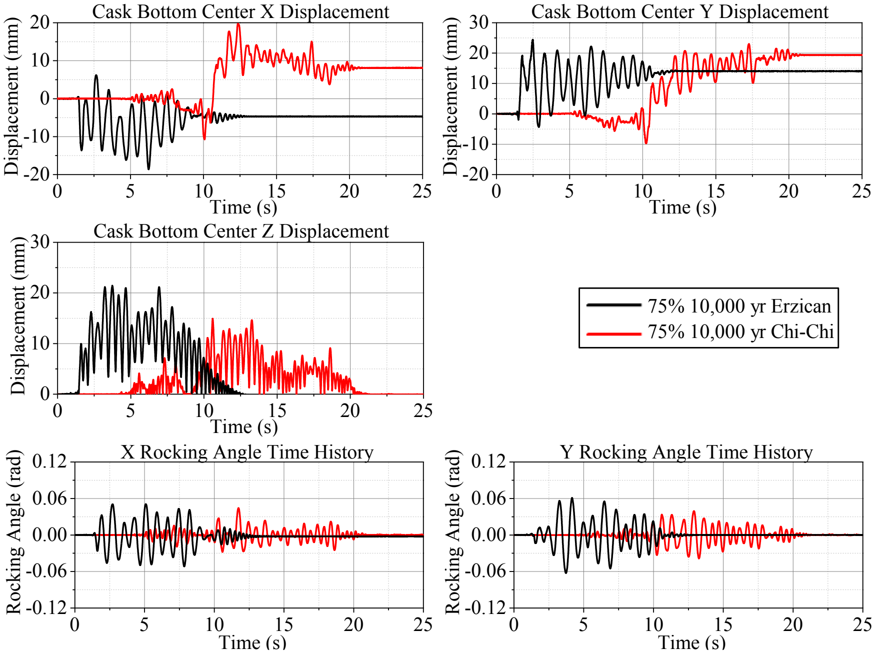

Figure 5.11. Response of FS.39 under 75% of 10,000-year Erzican and 75% of 10,000-year Chi-Chi

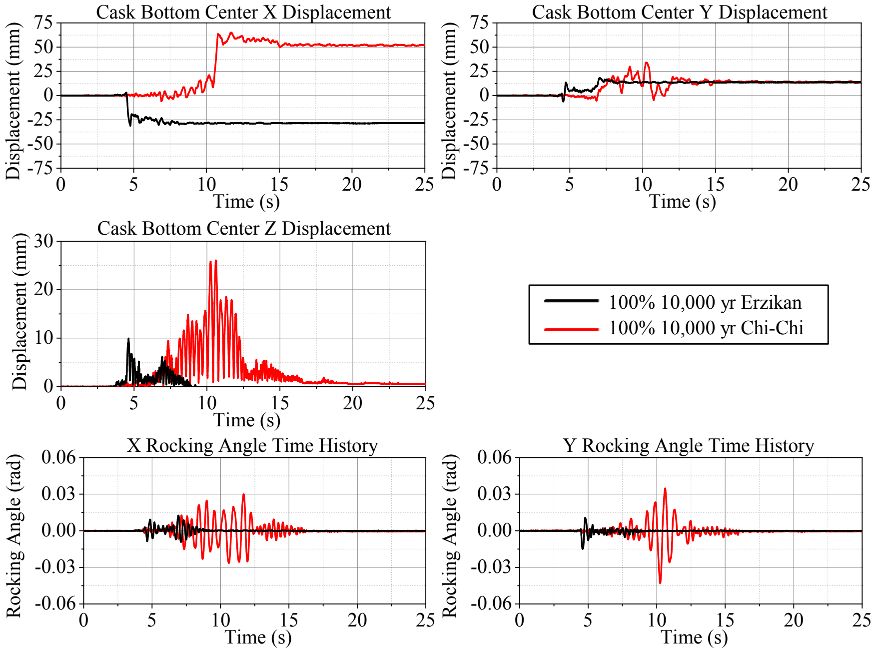

Figure 5.12. Response of FS.62 under 100% of 10,000-year Erzican and 100% of 10,000-year Chi-Chi

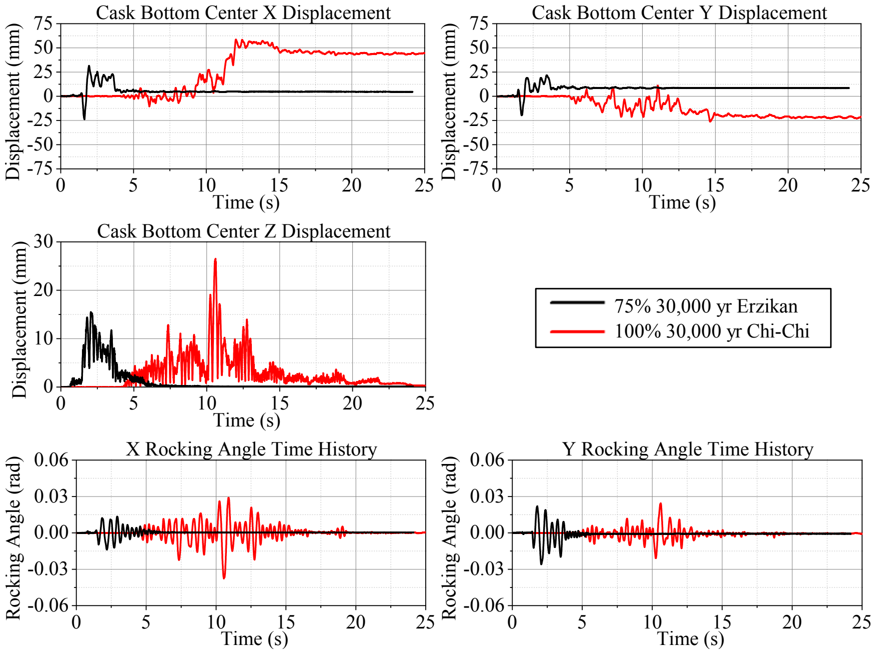

Figure 5.13. Response of FS.62 under 75% of 30,000-year Erzican and 100% of 30,000-year Chi-Chi

CHAPTER 6

RESULTS OF FINITE ELEMENT SIMULATION:
CASK-PAD MODEL

6.1 Validation of FE Models

This chapter presents the validation of FE models created in LS-DYNA [3]. Results from the experimental tests performed on the 6-DOF shaking table, presented in Chapter 5, were used to validate the FE models. Ground motions and their respective intensity shown in Table 5.1 were used as input at the bottom of concrete pad of the FE models presented in Section 4.2. The experimental results indicated that the cask response is not repeatable under the same seismic loading (Figures 5.1-5.9). Because of this variation in the repeated experiments, an FE model was considered to be validated if it was able to reproduce one of the responses from one of the repeat runs. Therefore, validation of FE models should considered as conditional validation.

Figures 6.1-6.3 compare experimental test results from FS.43, FS.39, and FS.62 FE models, respectively. As observed, the FE model satisfactorily reproduces the experimental test. Figure 6.1 shows that during experimental tests, the FS.43 underwent early displacements (less than 10 s.) and later movements (later than 15 s.) that were not captured by FE model. This movement was caused by the gap between the base of free-standing body and concrete pad.

6.2 Harmonic Excitation

6.2.1 Overturning Spectra under Single Pulse Excitation

Numerous FE simulations were performed for free-standing cylinder of aspect ratio 0.43 (FS.43), under single full-cycle sinusoidal loads, which were applied as horizontal excitation at the pad base, while the vertical and the other horizontal degree of freedom were restrained. Based on the applied horizontal acceleration presented in Equation (6.1), a series of simulations were performed sweeping through a range of input excitation frequencies and PGAs.

$$\ddot{u}_g(t) = \begin{cases} a_p \sin(\omega_p t), & 0 \le t \le (2\pi)/\omega_p \\ 0 & > (2\pi)/\omega_p \end{cases} \tag{6.1}$$

where, a_p is the peak ground acceleration, and ω_p is the circular frequency of the sinusoidal wave. The results were normalized to represent acceleration and frequency as nondimensional amplitude (A) and nondimensional frequency (Ω):

$$A = \frac{a_p}{\alpha \cdot g}; \qquad \Omega = \frac{\omega_p}{p} \tag{6.2}$$

The overturning and safe areas resulting from these simulations are shown in Figure 6.4 for a free-standing body of aspect ratio 0.43. Figure 6.4 is qualitatively similar to the overturning spectrum obtained for 2D rigid body, as shown in previous study (α = 0.25) [10]. The "Overturning Loop Mode 1" tag indicates the region where the cask overturns during a rotation reversal (i.e., after one or more impacts). The region marked as

“Overturning Area Mode 2” is where the cask overturns during the first rotational excursion (without impact).

Figure 6.5 shows input acceleration and normalized rocking angle time histories for rocking (no overturn), overturning with impact, and overturning without impact for a specific frequency of sinusoidal excitation ($\Omega = \omega_p / p = 6.28 / 2.37 = 2.65$, corresponding to an excitation period $T_p = 2\pi /(p\Omega) = 1$ s.), applied only in one direction. As observed, the DSC overturns at a_p = 1.36g with one impact, while it survives at slightly higher peak acceleration (a_p = 1.37g). The DSC does not overturn and exhibits rocking response until the peak acceleration reaches 1.65g, when it overturns without a previous impact or rotation reversal. This shows the existence of a safe zone in between the two overturning modes for 3D free-standing bodies, similar to the behavior reported by Zhang and Makris [10] for 2D rigid blocks. The overturning loop caused by cask tip-over during reversals is only present at small frequencies. In this case, the overturning loops end at normalized frequencies ω_p / p of about 4, indicating that T_p has to be larger than about 0.67. The threshold is relevant because the amplitudes in the safe zone can be significantly higher if the overturning loop is not present. Figure 6.5 also shows that although the excitation was only in horizontal direction X, the cask also displaced along the transverse horizontal direction. It is easier for 3D cylindrical bodies to have out of plane motion, as compared to rectangular base bodies, because they can roll along its circular edge during the motion (tumbling or nutation).

Simulations were also performed for the FE model for FS.55 cask (r/h_{cg} = 0.55, see Table 3.2 and Figure 4.4). The model was subjected to a similar series of time histories using the single pulsed sinusoidal excitation. The obtained overturning spectra for FS.55 is also plotted in Figure 6.4. As expected, the squat DSC (with higher r/h_{cg}) requires larger accelerations compared to slender DSC to overturn.

Figure 6.6 shows the spectra obtained from rocking only equation of motion, Equation (4.1), for FS.43 and FS.55, using geometric properties given in Table 4.2. The spectra from FE models (Figure 6.4) are plotted in the same figure for comparison. The FE and analytical models show a good agreement for the low frequency region ($\Omega < 2$), although the analytical solution only considers pure rocking, whereas the FE model accounts for rocking and sliding. As observed, the solutions divert from each other for higher normalized frequencies ($\Omega > 2$), particularly for the squat cask (FS.55, α = 0.50). The analytical overturning loop for the squat cask is much smaller than that from the FE model. Also, the FE solutions for squat and slender casks require larger accelerations to reach the overturning region, compared to the analytical solutions. This difference is partly caused by the use of a 3D FE model, as opposed to the 2D analytical solutions. Figure 6.5 shows that although the excitation is only in one horizontal direction (X axis), there is considerable movement along transverse direction (Y axis), particularly after impact or large rotations. This out-of-plane motion makes significant impact on the overturning spectra.

The difference may also be attributed to consideration of sliding motion in the FEM, which likely dissipates energy. However, it is difficult to produce a pure rocking condition for FE 3D bodies for this comparison, because of the existence of free-flight (i.e., complete separation of cask from the pad). Figure 6.7 presents the FE overturning spectra for a squat cask (FS.55) for friction coefficients μ_s = 1.0. Increasing coefficient of friction to such extreme values resulted in a free-flight condition, particularly for larger accelerations, reducing the likelihood of cask overturning for high frequencies, in agreement with Hao and Zhou's results [12]. For smaller accelerations, however, the overturning loop is smaller and closer to that obtained from the analytical solution. The reduction of overturning loop area is consistent with the findings of Chatzis and Smyth [60]. Their study showed that reducing the coefficient of friction increased the size of the overturning loop where a 2D body overturns with one impact. Figure 6.7 also shows the increase in the acceleration required for overturning without impact, which is caused by the complete cask-pad separation (free-flight response) at larger accelerations.

6.2.2 Response Sensitivity under Multicycled Harmonic Excitations

The experimental tests displacements presented in Chapter 5 for DSCs subjected to seismic events show lack of repeatability of the response. However, results for the response to single-cycle horizontal sinusoidal excitation (Figure 6.5) generate stable and predictive overturning regions, such as the spectra presented in Figure 6.4, 6.6 and 6.7. This section investigates the effect of multicycled sinusoidal excitations and the effect of dynamic input in several orthogonal directions on the sensitivity of free-standing bodies' response Equation (4.1), and FE simulations are used to evaluate the sensitivity of cask response to a multipulsed sinusoidal excitation of 20 cycles. The dynamic input is applied first only in the horizontal direction, and then on horizontal and vertical directions. For both cases, the excitation in one direction was changed by 1%. For the analytical equation's solution the time step at which the response was computed was changed by factor of 0.1. To reduce variables, both horizontal and vertical excitation have the same frequency and no phase difference between them. The applied excitation(s) are given by Equations (6.3) and (6.4).

$$\ddot{u}_g(t) = \begin{cases} A_h \alpha g \sin(\Omega p t), & 0 \le t \le 20 \cdot (2\pi)/\omega_p \\ 0 & > 20 \cdot (2\pi)/\omega_p \end{cases} \tag{6.3}$$

$$\ddot{v}_g(t) = \begin{cases} A_v \alpha g \sin(\Omega p t), & 0 \le t \le 20 \cdot (2\pi)/\omega_p \\ 0 & > 20 \cdot (2\pi)/\omega_p \end{cases} \tag{6.4}$$

Figure 6.8 shows the analytical rocking response of FS.43, based on Equation (4.1), when subjected to horizontal and vertical excitations. The normalized amplitudes are A_h = 3.00 and A_v = 2.00, normalized frequency is Ω = 5, and the time step (*dt*) at which Equation (4.1) was integrated was set to 0.001 s. The figure also shows the rocking response time history for three realizations with slightly different input parameters:

i) horizontal excitation is increased 1%, while the rest of input parameters remain the same (i.e., A_h = 3.03, A_v = 2.00, *dt* = 0.001s.),

ii) time step is reduced 10 times (i.e., A_h = 3.00, A_v = 2.00, *dt* = 0.0001s.), and

iii) horizontal excitation is increased 1% and time step is reduced 10 times (i.e., A_h = 3.03, A_v = 2.00, *dt* = 0.0001 s.).

As observed in Figure 6.8, the resulting rocking responses are identical for the first 2.4 s., and thereafter the curves evolve into very different time histories. The unpredictability on the response is reflected on the fact that the main differences in response with respect to the original curve do not arise just from 1% increase in acceleration but also the solution time step chosen. The solution time step is consequential because the excitation acceleration and body's angular velocity (particularly during impact) changes ever so slightly using a different time step. These changes are enough to cause almost three times the maximum rocking angle of the original curve towards the end of rocking angle time history.

The same set of analytical analyses was repeated for a cask subjected only to horizontal accelerations (i.e. $A_v = 0$). As shown in Figure 6.9, the rocking angle time histories under horizontal excitation only is more stable and minor differences do not cause significant response deviation as the time history progresses, unlike the response under bi-directional excitation. The results are in agreement with the experimental response from Peña et al. [27,28], who detected repeatability on the response of rectangular concrete blocks under unidirectional harmonic loading, but not when the blocks were subjected to seismic records. Ground motions, unlike sinusoidal excitations, have a combination of different frequencies, amplitude and any minute changes in boundary conditions lead to different response.

To evaluate the precision of FE simulations, the analytical simulations presented above were repeated in the LS-DYNA model described in Section 3. Figures 6.10-6.11 show the FE model response of a FS.43 (Table 3.2) for both horizontal and vertical excitations, and horizontal excitation only, respectively. The normalized amplitudes (A_h and A_v) and the normalized frequency of the sinusoidal excitation were the same as for the 2D analyses (Figures 6.8 and 6.9). For FE simulation, however, instead of using as a variable the solution time step (*dt*), the input acceleration time step (*Accdt*) was modified by a factor of 10. The parameter *Accdt* is, the time step at which Equations (6.3) and (6.4) were computed for input acceleration load curve in the FE model. To assess the effect of small variations on the acceleration, Figure 6.10 compares two realizations: $A_h = 3.00$, $A_v = 2.00$, *Accdt* = 10^{-3}; and $A_h = 3.03$, $A_v = 2.00$, *Accdt* = 10^{-3}.

As observed, an input acceleration variation of 1% results in a drastic change in rocking and sliding displacements. The realizations with A_h = 3.00 case enters into nutation motion and does not come back to rest state at the end of 15 seconds, while the case with A_h = 3.03 comes back to rest. A more drastic change is detected by comparing the realizations with input parameters A_h = 3.00, A_v = 2.00, *Accdt* = 10^{-3} and A_h = 3.00, A_v = 2.00, *Accdt* = 10^{-4}. Both models are identical except the *Accdt* of acceleration time histories. As can be seen, the displacement of the model with smaller *Accdt* was significantly larger and the cask fell off the pad's edge at 9 seconds into the simulation. Figure 6.11 presents similar cases, but without including the vertical excitation. As in the analytical realizations, the rocking angle time histories are nearly identical for all three cases, although differences in lateral displacement are still present. These figures show that when horizontal excitation is accompanied by vertical excitation, the response of free-standing bodies becomes extremely sensitive, and can even depend on the input acceleration time step.

Figure 6.12 shows the FE analysis response for the same model under smaller accelerations in which A_h = 2.00 and 2.02, A_v = 2.00, and Ω = 5 with *Accdt* = 10^{-3} and 10^{-4}. In this case, the cask overturned for two runs with A_h = 2.00 and 2.02; *Accdt* = 10^{-3}, but the cask did not overturn when *Accdt* was changed to 10^{-4}. This is an extreme example of sensitivity in the response of free-standing bodies. As DSCs are cylindrical bodies; the effect of minor changes, even in the resolution of load curve definition, is more significant and leads to more deviation in the response because cylindrical bodies can easily displace perpendicular to direction of excitation due to rolling motion along the circular edge. Off the plane motion is present even if the forcing excitation is in-plane. This motion of cask rolling on its edge while rocking (i.e., nutation or tumbling motion) is difficult to characterize.

6.3 Application of Maximum Intensity 10,000- and 30,000-year Ground Motions

During experimental testing, only a fraction of the ground motion intensity could be successfully applied, because the high impact accelerations exceeded the vertical actuator allowable load capacity. Hence, validated FE models were used for application of 100% of 10,000- and 30,000-year motions on all the specimens. Figures 6.13-16 show the response of the two main scaled DSCs: FS.55 and FS.43 under those excitations. The responses of two additional DSCs (FS.39 and FS.62) are presented in Appendix A. Table 6.1 summarizes the absolute maximum and residual response of FS.55 and FS.43 casks, where it is observed that none of the simulations showed the cask overturning. Since these specimens are scaled models, lateral displacements (X, Y and Z displacement) should be multiplied by N (scale factor, Table 3.1) to obtain the expected displacements in the full scale specimens. However, the rocking angle should remain the same for full scale and scale specimens. These equivalent full scale values are presented in Table 6.2. The figures show that, as the r/h_{cg} decreases, the rocking response increases. None of the simulations showed any overturning of scaled model. With the exception of FS.55 response for 10,000-year Chi-Chi and Erzican, all the simulations consistently show that Chi-Chi, a far field motion with multiple pulses, is more critical to cask response compared to its near field counterpart.

Cylindrical free-standing bodies like DSCs can exhibit “nutation” motion, when they tumble or roll around their circular base, Figure A.1 and A.2 (for Erzican motion). This motion is very difficult to characterize, but it can lead to a larger response in rocking as well as lateral displacements, if successive pulses within the applied ground motion are applied during such motion. This one of the major reasons Chi-Chi results in larger rocking angles. Both figures (Figures A.1 and A.2) are for Erzican motions, which only have a couple of large pulses, resulting in the continuation of nutation motion through the rest of the time history. As can be seen, casks lose considerably less energy during nutation motion, and motion persists for a long time.

6.4 Effect of Frequency Content of Ground Motions

The simulation results presented in Section 6.3 are for the ground motions of Figures 3.7 and 3.8 with the time step modified with the factor $1/\sqrt{2.5}$. The modification or the reduction in time step of the ground motions was done to satisfy the similitude requirements (Table 3.1). The effect of modifying the time step of ground motion on its response spectra will be presented in this section. When time step is reduced, time period of each pulse of the motion is reduced, increasing the frequency content. Although following the similitude requirement is crucial when scaled models are considered, this section investigates parametric variation of the time step modification factor, i.e., variation in frequency content of ground motion or in other words the duration of pulse(s) and its effect on the response of free-standing cylindrical DSCs.

6.4.1 Description of Parametric Study

Based on the similitude law presented in Table 3.1, the ATH time step is modified according to Equation (6.5), where, dt_s and dt_p denotes time step of ground motion for scaled specimen and full-scale prototype. Note that dt_p is equal to the original time step of a given ATH. The parameter *N* is the scale factor for the scaled model (2.5 for the FS.55 and FS.43 specimens). However, in this parametric study, *N* is varied to values 1.0, 1.5, 2.0 and 2.5. The FE analyses presented previously correspond to $N = 2.5$.

$$dt_s = dt_p / \sqrt{N} \tag{6.5}$$

In this section, only ground motions of a 30,000-year return period were considered (Figure 3.8). The original time step (dt_p) of both motions in Figure 3.8 was 0.005. When this time step is modified according to Equation (6.5), the effect on the response spectra (frequency content) of the ground motions can be seen in Figure 6.17. As observed, the spectral acceleration in the longer period region is reduced as N increases from 1.0 to 2.5. Notice that the PGA of each ground motion remains unchanged.

6.4.2 Results of the Parametric Study

The same FE models presented in Section 4.2.1 for FS.55 and FS.43 casks were subjected to the time step modified Erzican and Chi-Chi motions (30,000-year return period) with their respective response spectra given in Figure 6.17. Results from these simulations are presented in Figures 6.18 and 6.19, which compare the absolute maximum displacements of DSCs' bottom center in three directions (horizontal X and Y, and vertical

Z) and absolute maximum rocking angles in X and Y directions. The nomenclature used in Figures 6.18 and 6.19 as 'E-Nx.x or C-Nx.x' refers to E: Erzican; C: Chi-Chi and Nx.x: *N* = x.x. The data along with absolute residual displacements are summarized in Table 6.3.

As *N* decreases, the period of the ground motion pulses elongates, i.e., frequency decreases. The comparison presented in Figures 6.18 and 6.19 shows that when *N* decreases, the displacements and rocking angle tend to increase accordingly. For Erzican NFGM the trend is clearer compared to that for Chi-Chi FFGM. In both figures the maximum rocking angle in one of the directions seems to be lower for C-N1.0 than C-N1.5. However, the rocking in the other horizontal direction and Z displacement show that the trend is still followed. Figures 6.18 and 6.19 compare near field and far field (Erzican and Chi-Chi, respectively) cases for FS.55 and FS.43. For each respective case, Chi-Chi consistently produces larger rocking than Erzican, although it has lower PGA.

These results show that the frequency content of a ground motion in an important parameter to consider while studying the response of free-standing bodies. Ground motions that have spectra with higher acceleration in longer period regions are more critical for a free-standing body's response. This finding has significance when soil effects and soil structure interaction are taken into account. Motions with dominant long period spectra are common in soil sites or when soil effect is considered. This finding underlines the importance of considering soil-structure-interaction (SSI), and soil effect on ground motion characteristics. Soil considerations usually dampen the high frequency peak, and elongate the dominant period.

6.5 Discussion of Results: Scaled Cask-Pad Model

6.5.1 Harmonic Excitation Study

The potential for tip-over of two free-standing casks of different aspect ratio was evaluated under sinusoidal excitations using finite element (FE) models and analytical solutions. FE models of these cylindrical free-standing bodies were created to reproduce simultaneous sliding and rocking response. The generated FE overturning spectrum under single pulse sinusoidal excitation was compared to the spectrum resulting from the 2D equation of motion. Finding similar results, the response of casks under multipulsed excitation was also examined. The main results are summarized below:

i. FE models were used for first time to generate overturning response spectra of cylindrical casks subjected to horizontal single pulse harmonic excitations. Under these conditions, the FE model showed a periodic and stable rocking response, relatively insensitive to minor changes in input parameters.

ii. These 3D cask models can exhibit sliding and rocking, leading to larger accelerations for overturning than those obtained from previous 2D rigid block analytical equations, which do not include sliding in the formulation.

iii. While the overturning spectra obtained from FE models were qualitatively similar to those obtained from analytical equation (rocking only), the presence of sliding and 3D motion decreases the potential for DSC overturning. In other words, a larger acceleration is required for DSCs to overturn. Increasing the friction coefficient to artificial values in the FE models to reduce sliding, led to a free-flight mode that reduced the overturning potential of the system.

iv. The cask displacement and rocking time history become very sensitive to small variation in input parameters, if several horizontal and vertical harmonic cycles are applied. The response for the first couple of cycles still is very similar, but thereafter the displacements start to divert. This is the reason for having stable overturning spectra when only one or two cycles are applied to the cask.

v. The cask response is not very sensitive to multicycle harmonic loading applied only in the horizontal direction.

vi. Cylindrical free-standing bodies become sensitive to minute input parameter variations if multicycle harmonic loads are applied simultaneously in horizontal and vertical direction. This phenomenon is related to the intrinsic behavior of the cask movement, and not to the technique used for obtaining the response.

vii. The response sensitivity of cylindrical casks is more pronounced than that of rectangular bodies, because cylindrical casks can easily displace perpendicular to the direction of excitation due to rolling motion along the circular edge. This complex motion increases the acceleration required to overturn the cask.

6.5.2 Seismic Excitation and Effect of Frequency Content

This section evaluates the response of free-standing casks under long-term seismic events. Two main aspect ratios (r/hcg = 0.43 and 0.55; FS.43 and FS.55, respectively) were considered, and generic casks with overpack and MPC were fabricated with 1:2.5 scaling ratio. Ground motion spectra were developed for 10,000-year and 30,000-year return period based on NUREG 6728; FE simulations were performed using experimental tests as a tool for validation, and the effect of frequency of ground motion was also studied using the same FE models. The following findings were made from the study:

i. The results obtained for scaled DSCs' response for ground motions of long return period (10,000- and 30,000-year) did not show overturning, despite having large PGA. However, the ground motion containing multiple large pulses produces larger rocking compared to the motions that have only one or two large pulses.

ii. DSCs having cylindrical geometry are highly prone to nutation or tumbling motion. If the applied ground motion contains multiple pulses, the initial pulses may result in rocking of DSCs, which is usually followed by nutation motion. Subsequent pulses acting on such DSCs undergoing nutation motion can induce larger rocking and displacements. This is one of the major reasons for FFGMs resulting in larger rocking, despite having smaller peak accelerations.

iii. The parametric study of frequency content variation by changing the time step modification factor shows that motions with larger spectral acceleration in a long period region produce larger response (displacements and rocking).

Table 6.1. Peak (absolute) response of scaled specimen

Ground Motion	Cask	Rocking Angle (rad)		Cask Bottom Displacement (m)		Cask Top Displacement (m)		Residual Displacement Cask Bottom (m)	
		X	Y	X	Y	X	Y	X	Y
10,000-year Chi-Chi	FS.55	0.010	0.015	0.014	0.009	0.028	0.041	0.001	0.003
	FS.43	0.059	0.085	0.065	0.076	0.173	0.216	0.020	0.033
10,000-year Erzican	FS.55	0.021	0.014	0.032	0.043	0.077	0.070	0.023	0.032
	FS.43	0.042	0.042	0.054	0.058	0.147	0.134	0.036	0.035
30,000-year Chi-Chi	FS.55	0.044	0.044	0.040	0.036	0.132	0.124	0.021	0.007
	FS.43	0.107	0.075	0.073	0.062	0.259	0.200	0.040	0.000
30,000-year Erzican	FS.55	0.039	0.028	0.073	0.087	0.147	0.128	0.025	0.020
	FS.43	0.082	0.044	0.056	0.098	0.230	0.174	0.005	0.029

Table 6.2. Equivalent peak (absolute) response of full-scale casks

Ground Motion	Cask	Rocking Angle (rad)		Cask Bottom Displacement (m)		Cask Top Displacement (m)		Residual Displacement Cask Bottom (m)	
		X	Y	X	Y	X	Y	X	Y
10,000-year Chi-Chi	FS.55	0.010	0.015	0.035	0.023	0.070	0.103	0.003	0.008
	FS.43	0.059	0.085	0.163	0.190	0.433	0.540	0.050	0.083
10,000-year Erzican	FS.55	0.021	0.014	0.080	0.108	0.193	0.175	0.058	0.080
	FS.43	0.042	0.042	0.135	0.145	0.368	0.335	0.090	0.088
30,000-year Chi-Chi	FS.55	0.044	0.044	0.100	0.090	0.330	0.310	0.053	0.018
	FS.43	0.107	0.075	0.183	0.155	0.648	0.500	0.100	0.000
30,000-year Erzican	FS.55	0.039	0.028	0.183	0.218	0.368	0.320	0.063	0.050
	FS.43	0.082	0.044	0.140	0.245	0.575	0.435	0.013	0.073

Table 6.3. Peak response of FS.43 under 30,000-year motions: different *N*

Specimen	Motion	Cask bottom center relative displacement (m)					Rocking Angle (rad)	
		X		Y		Z	X	Y
		Max.	Res.	Max.	Res.	Max		
FS.55	E-N1.0	0.132	0.055	0.183	0.027	0.054	0.093	0.080
	E-N1.5	0.138	0.061	0.148	0.035	0.035	0.059	0.052
	E-N2.0	0.088	0.028	0.096	0.007	0.027	0.048	0.031
	E-N2.5	0.073	0.025	0.087	0.020	0.022	0.039	0.028
	C-N1.0	0.283	0.089	0.206	0.090	0.112	0.186	0.123
	C-N1.5	0.294	0.081	0.249	0.172	0.090	0.130	0.142
	C-N2.0	0.065	0.045	0.073	0.066	0.062	0.057	0.104
	C-N2.5	0.040	0.021	0.033	0.007	0.029	0.044	0.044
FS.43	E-N1.0	0.153	0.045	0.321	0.077	0.113	0.216	0.128
	E-N1.5	0.116	0.009	0.199	0.011	0.068	0.130	0.066
	E-N2.0	0.057	0.012	0.117	0.040	0.053	0.099	0.045
	E-N2.5	0.056	0.005	0.098	0.029	0.044	0.082	0.044
	C-N1.0	0.482	0.186	0.409	0.168	0.143	0.139	0.258
	C-N1.5	0.285	0.117	0.343	0.172	0.116	0.219	0.197
	C-N2.0	0.055	0.017	0.113	0.111	0.060	0.109	0.075
	C-N2.5	0.073	0.040	0.062	0.000	0.060	0.107	0.075

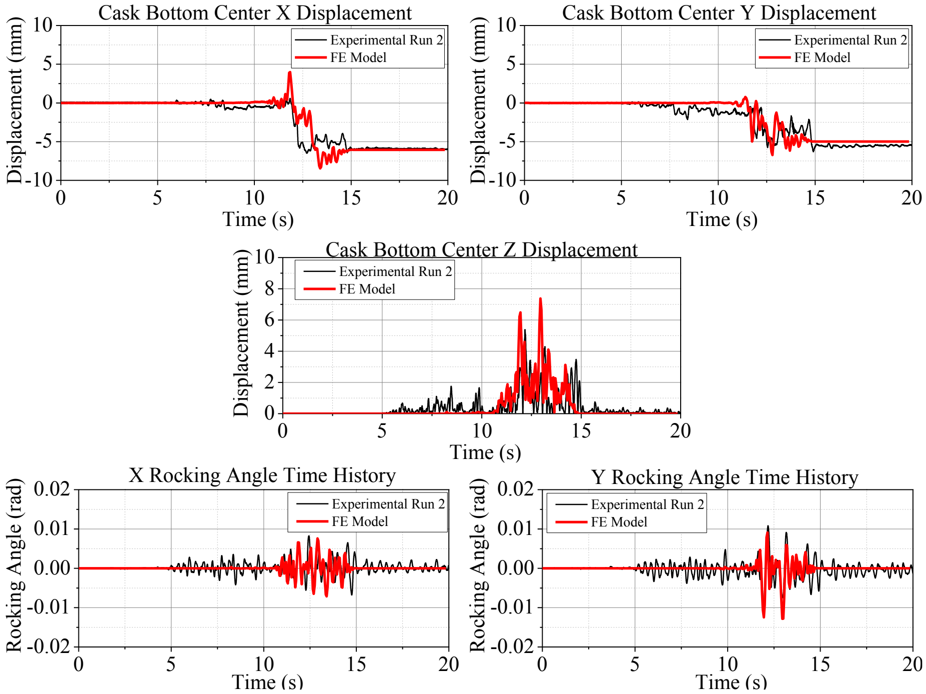
Cask Bottom Center X Displacement

Cask Bottom Center Y Displacement

Cask Bottom Center Z Displacement

X Rocking Angle Time History

Y Rocking Angle Time History

Figure 6.1. FS.43 – Experimental and FE model results (75% of 10,000-year Chi-Chi)

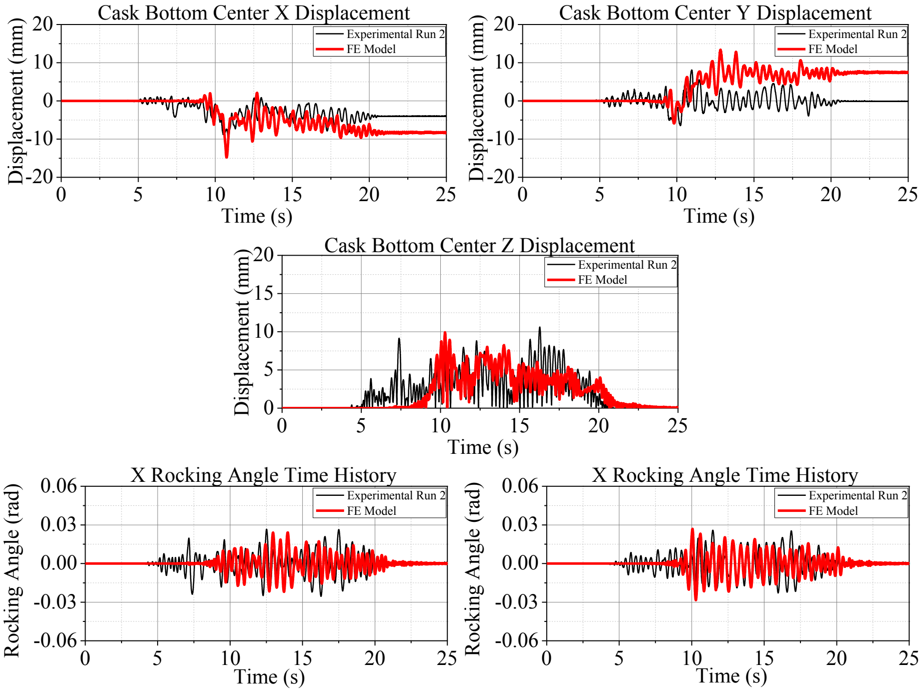
Cask Bottom Center X Displacement

Cask Bottom Center Y Displacement

Cask Bottom Center Z Displacement

X Rocking Angle Time History

X Rocking Angle Time History

Figure 6.2. FS.39 – Experimental and FE model results (75% of 10,000-year Chi-Chi)

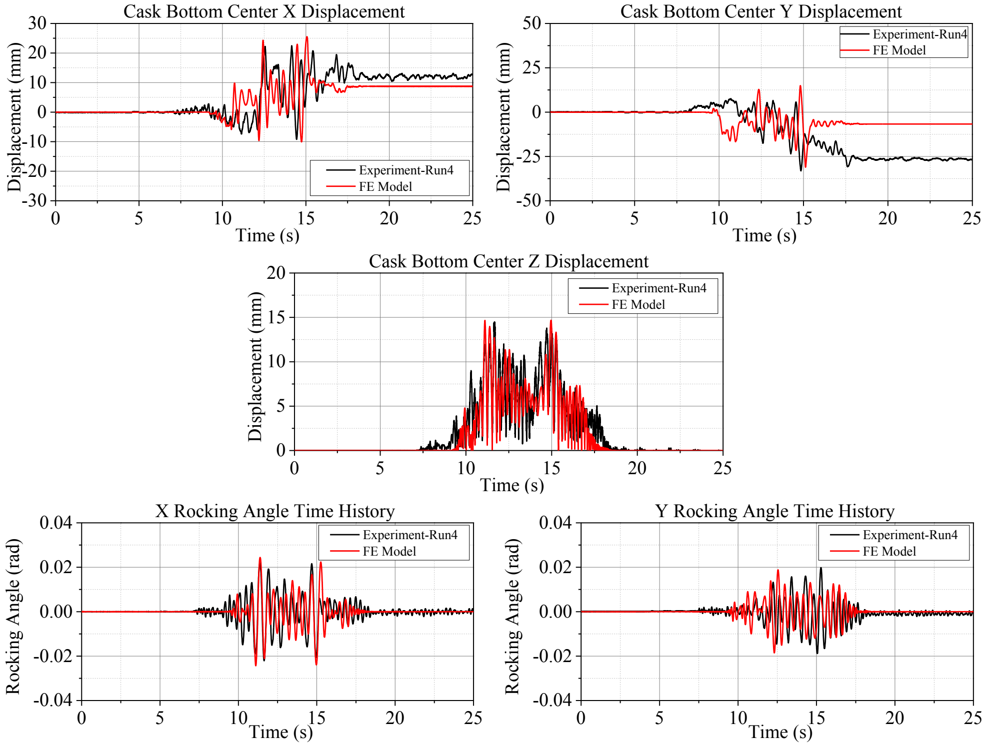

Figure 6.3. FS.62 – Experimental and FE model results (100% of 10,000-year Chi-Chi)

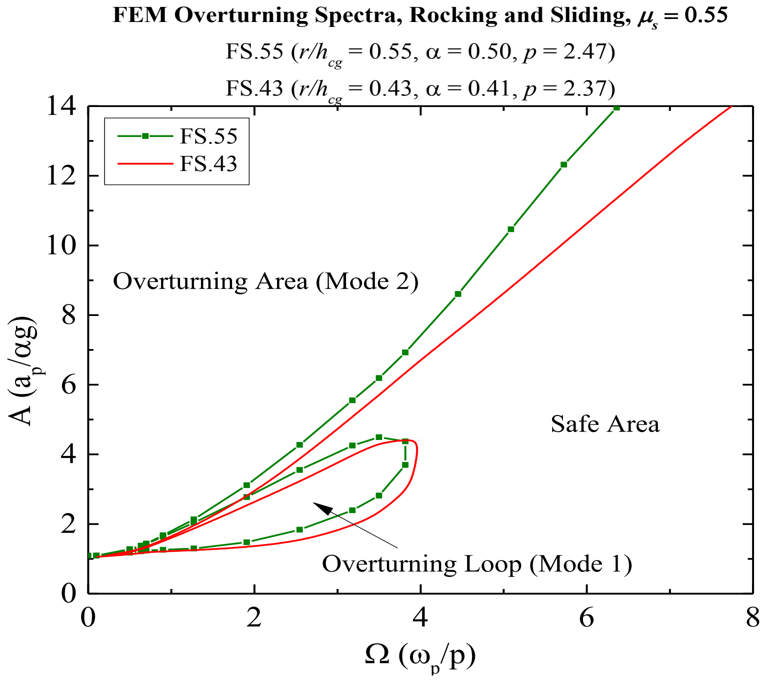

Figure 6.4. FEM overturning regions (spectrum) for FS.43 and FS.55 DSCs

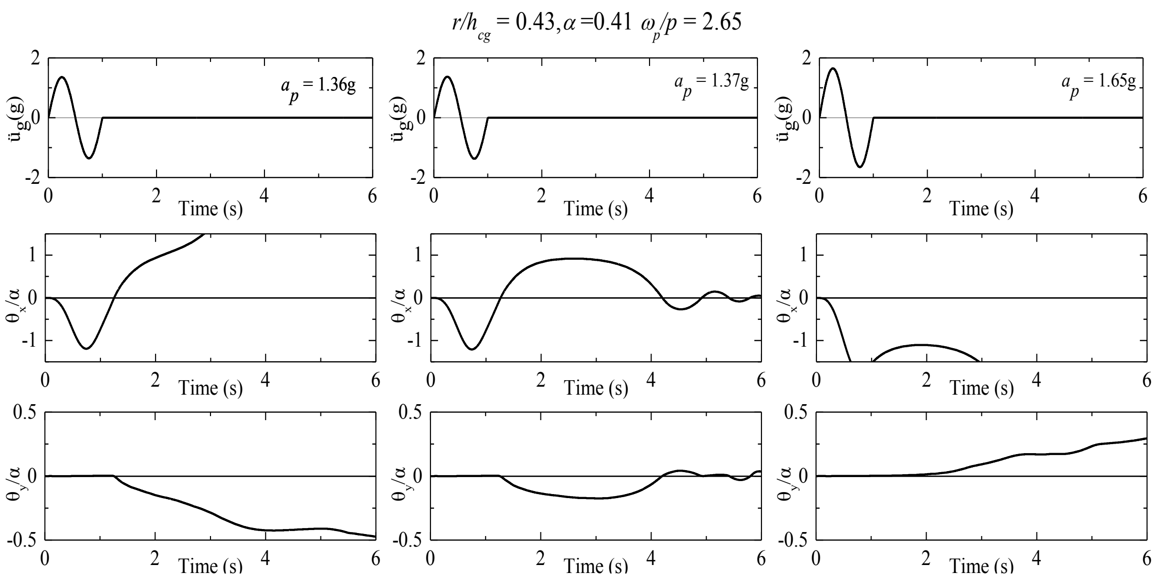

(a) (b) (c)

Figure 6.5. Input harmonic excitation and rocking angle of FS.43: (a) overturning with one impact, (b) rocking response (no overturning), (c) overturning without impact

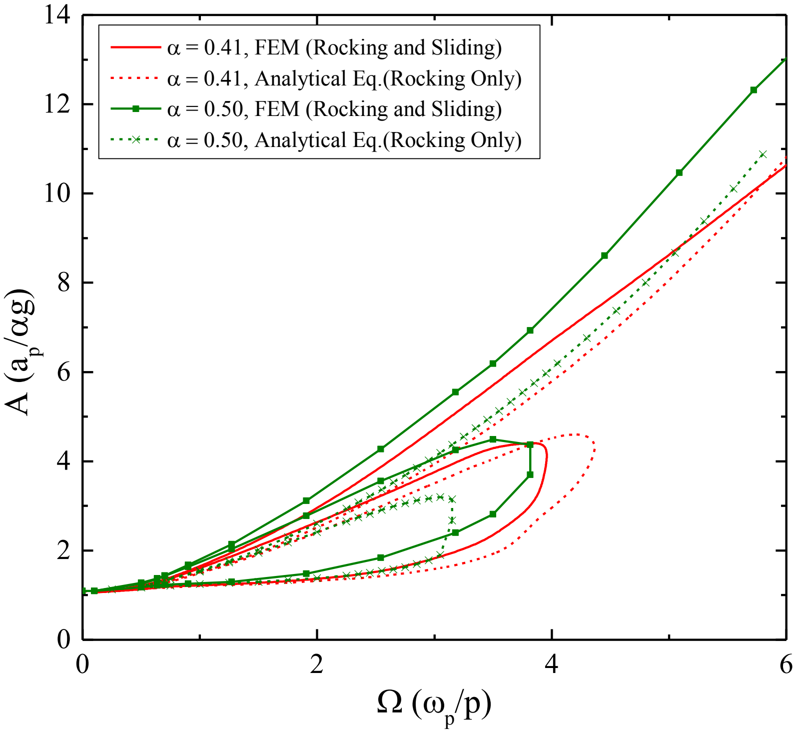

Figure 6.6. Comparison of overturning spectra obtained from FEM and analytical equation [FE Models $\mu_s = 0.55$; Analytical: $e = 0.761$ for $\alpha = 0.41$ and $e = 0.655$ for $\alpha = 0.50$]

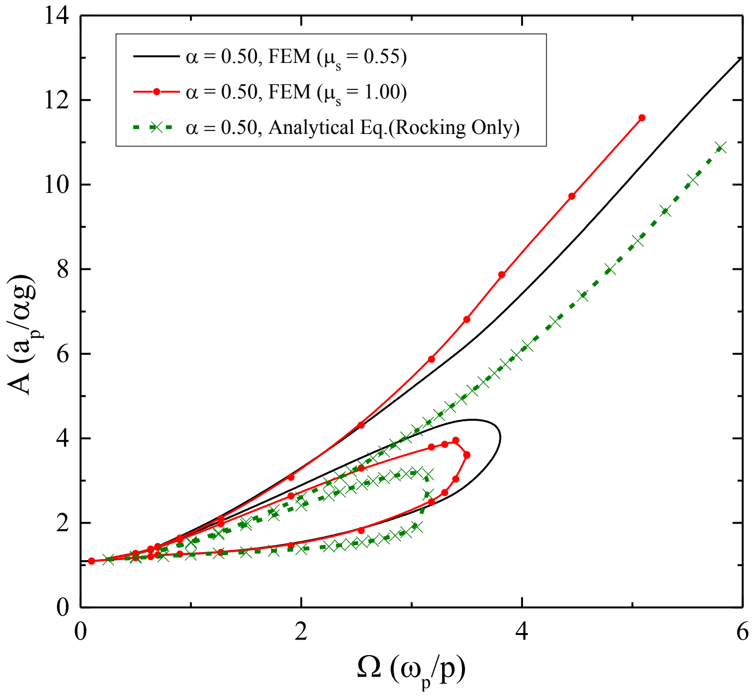

Figure 6.7. Comparison of squat cask's (FS.55) overturning spectra (variation in μ = 0.55 and 1.00)

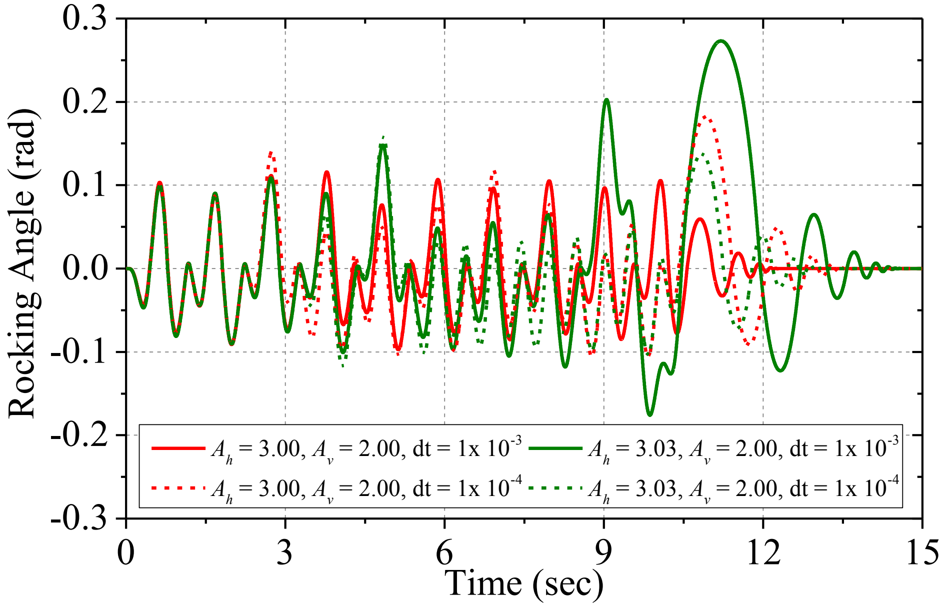

Figure 6.8. Rocking angle time history from Equation (4.1) [r/h_{cg} = 0.43, α = 0.41, p = 2.37; Ω = 5, A_h = 3.00 and 3.03, A_v = 2.00, dt = 10^{-3} and 10^{-4}]

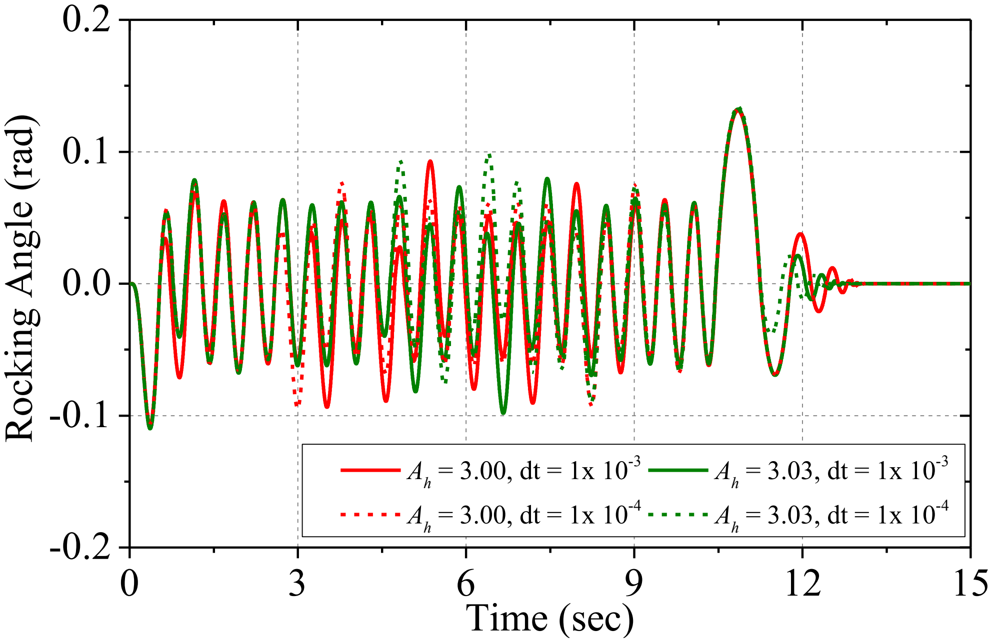

Figure 6.9. Rocking angle time history from Equation (4.1) [r/h_{cg} = 0.43, α = 0.41, p = 2.37; Ω = 5, A_h = 3.00 and 3.03, A_v = 0, dt = 10^{-3} and 10^{-4}]

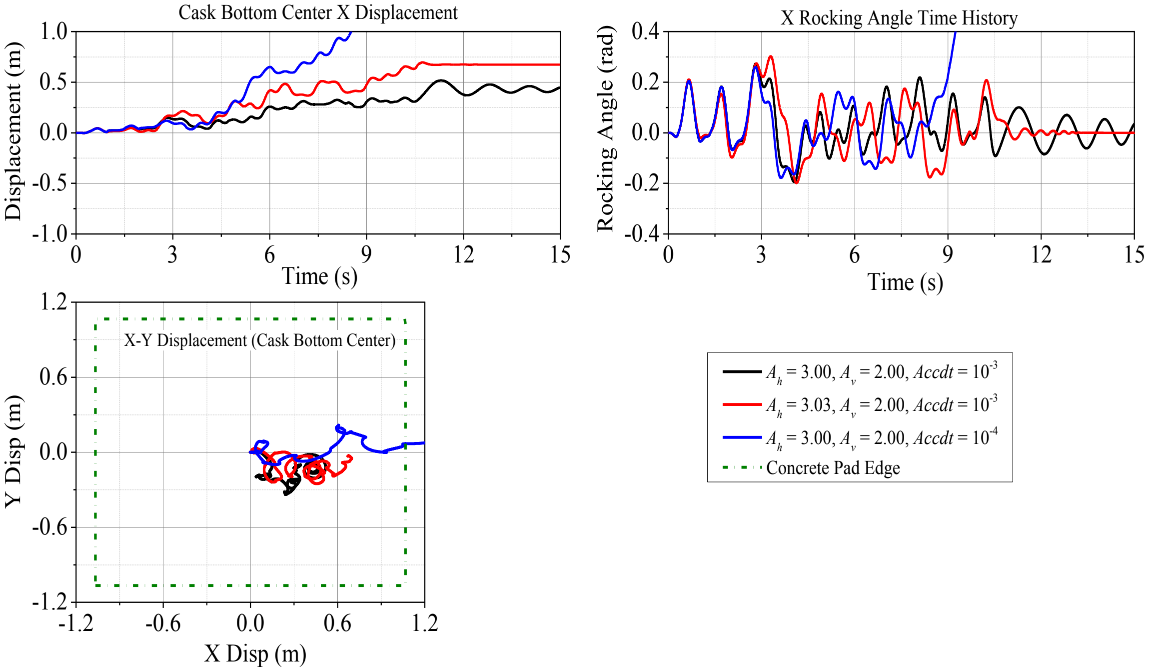

Figure 6.10. FEM response for FS.43 [r/h_{cg} = 0.43, Ω = 5, A_h = 3.00 and 3.03, A_v = 2.00, $Accdt$ = 10^{-3} and 10^{-4}]

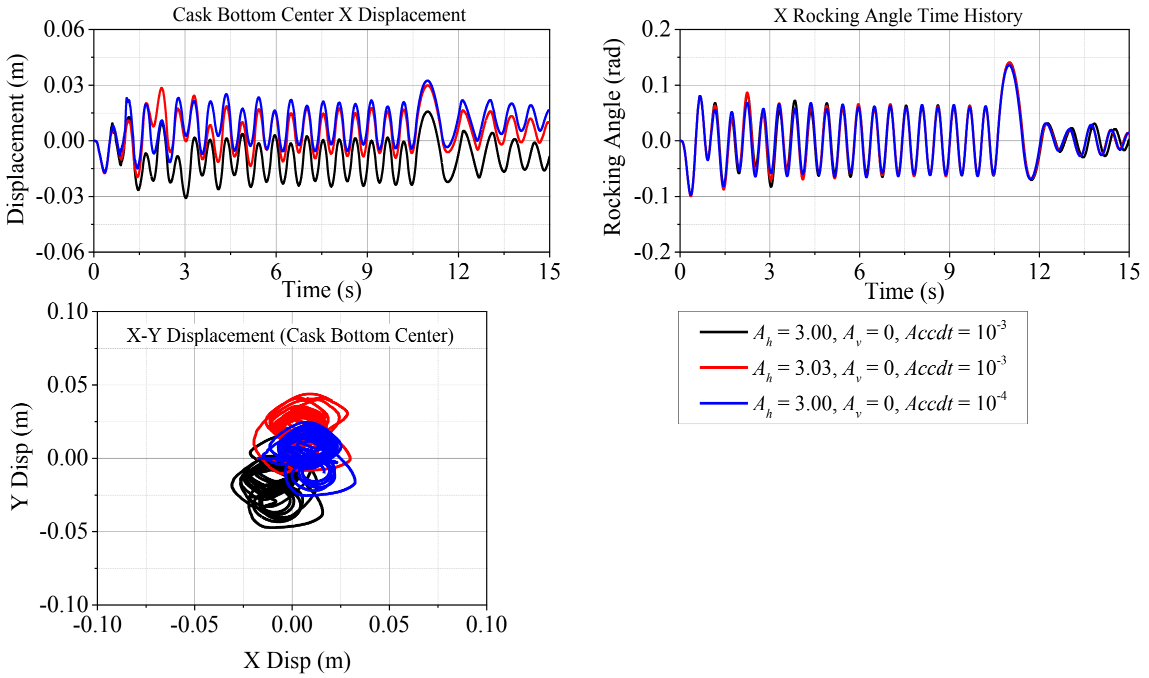

Figure 6.11. FEM response for FS.43 [$r/h_{cg} = 0.43$, $\Omega = 5$, $A_h = 3.00$ and 3.03, $A_v = 0$, $Accdt = 10^{-3}$ and 10^{-4}]

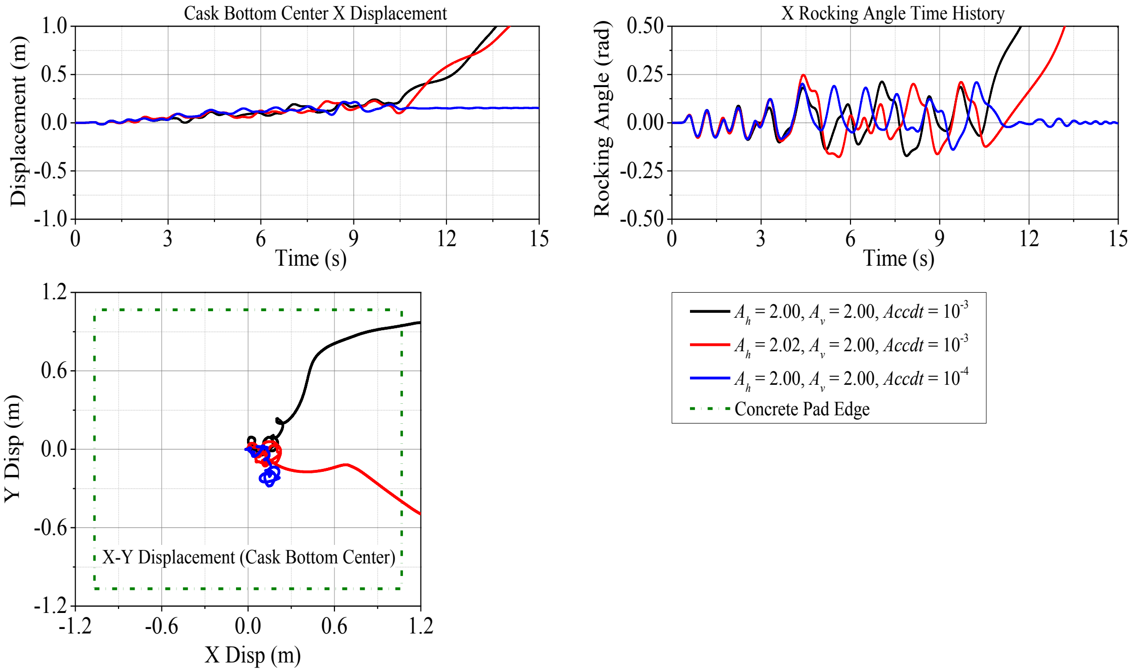

Figure 6.12. FEM response for slender cask [$r/h_{cg} = 0.43$, $\Omega = 5$, $A_h = 2.00$ and 2.02, $A_v = 2.00$, $Accdt = 10^{-3}$ and 10^{-4}; cask overturning for two cases]

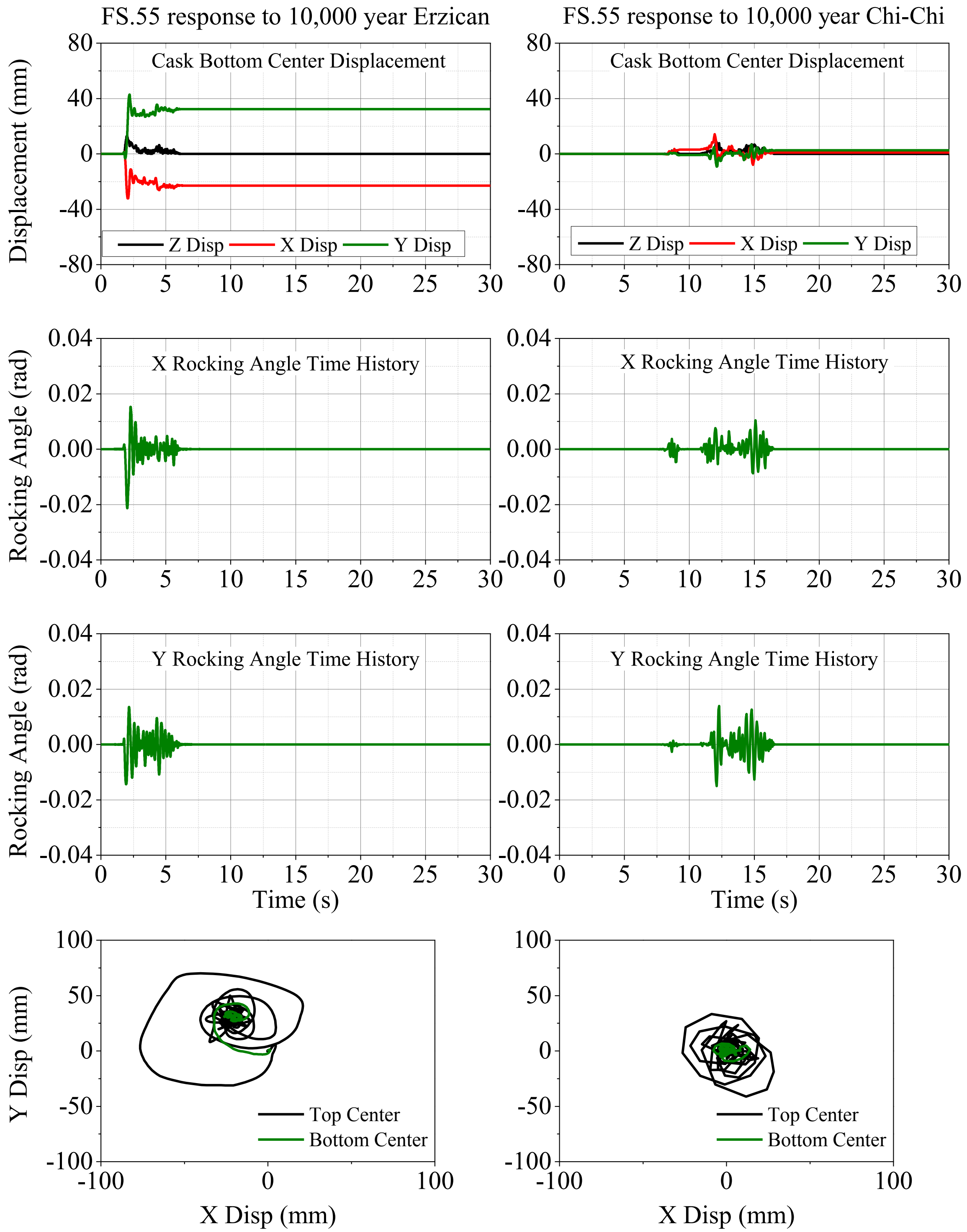

Figure 6.13. FS.55 cask’s response under 10,000-year ground motions

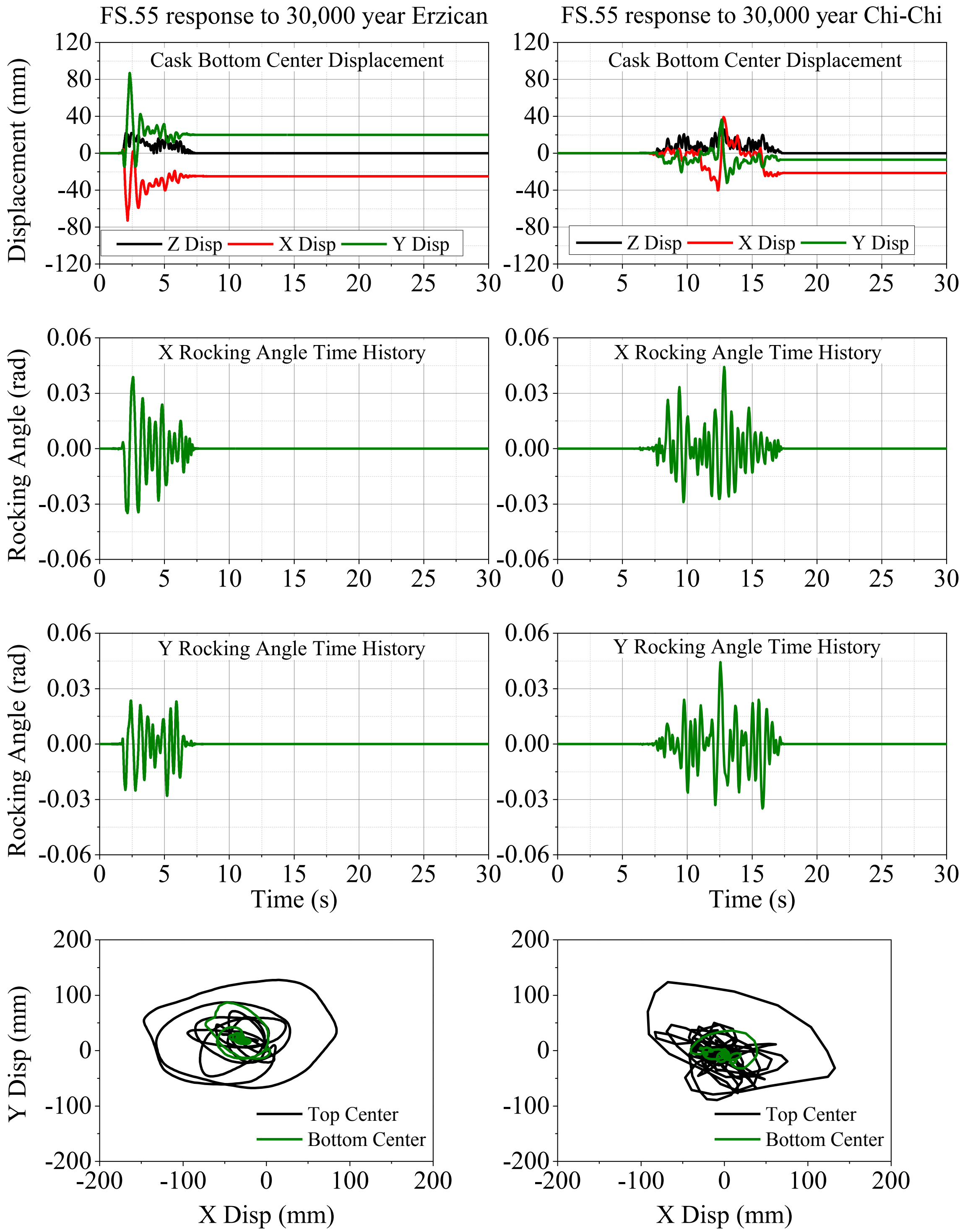

Figure 6.14. FS.55 cask’s response under 30,000-year ground motions

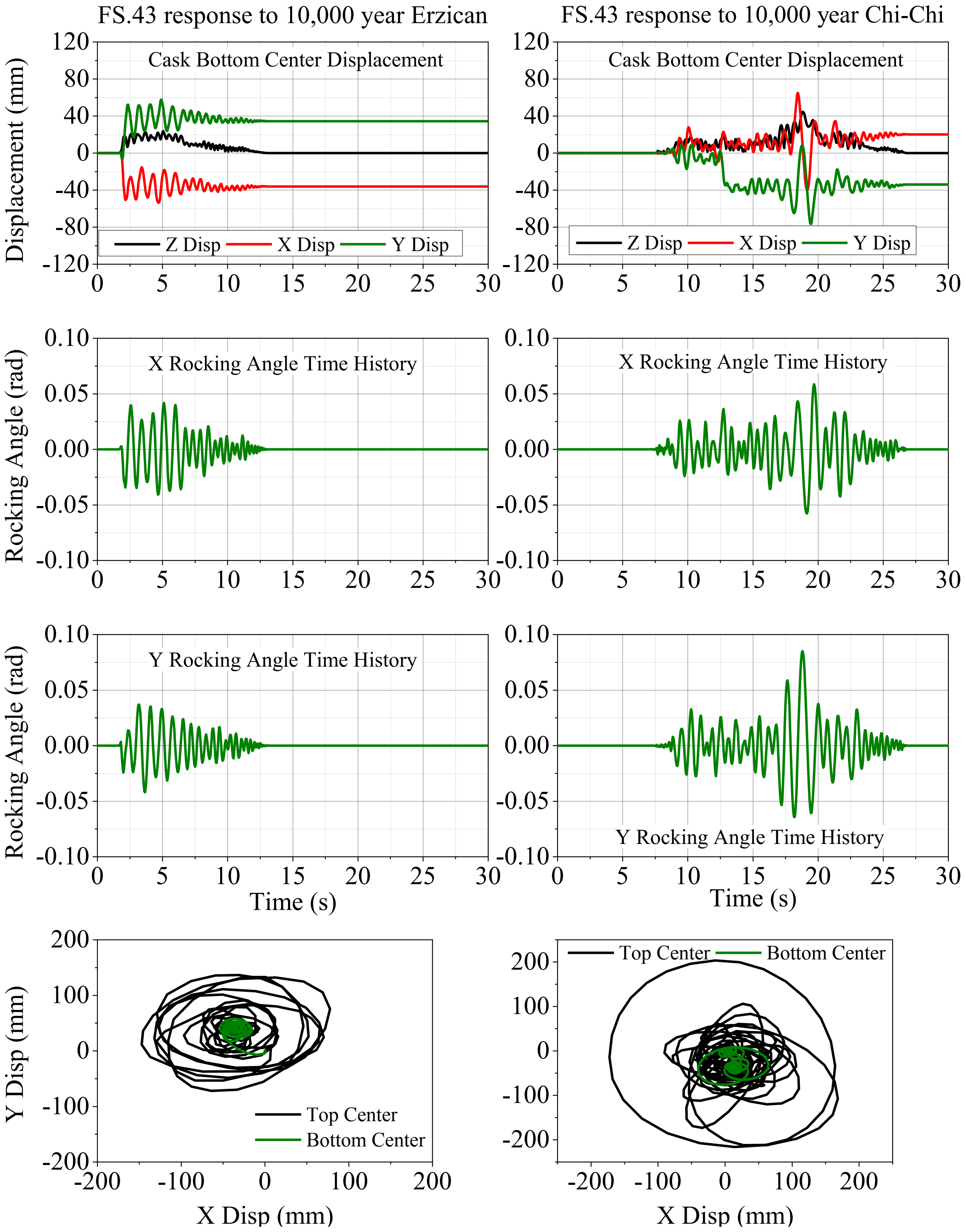

Figure 6.15. FS.43 cask's response under 10,000-year ground motions

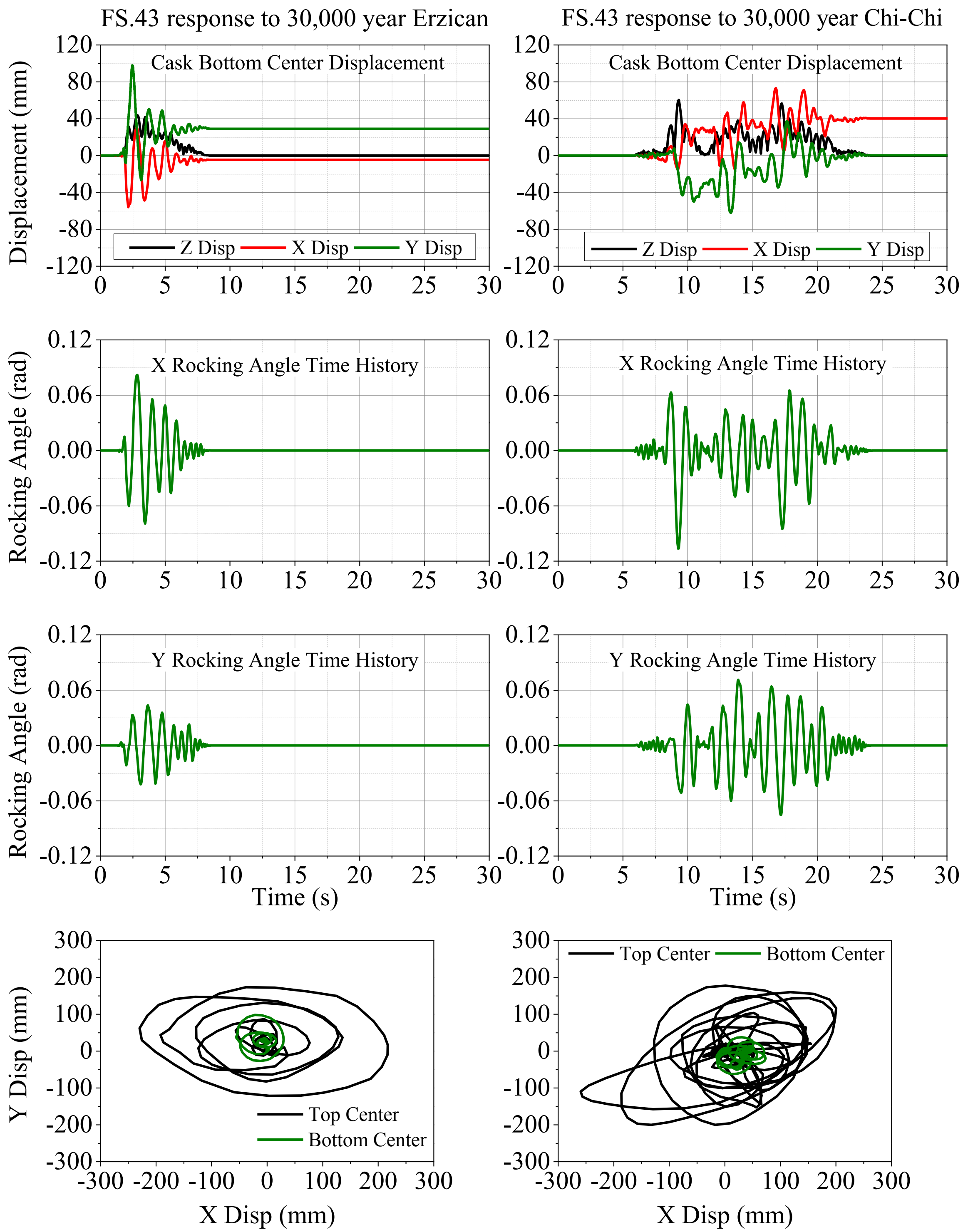

Figure 6.16. FS.43 cask’s response under 30,000-year ground motions

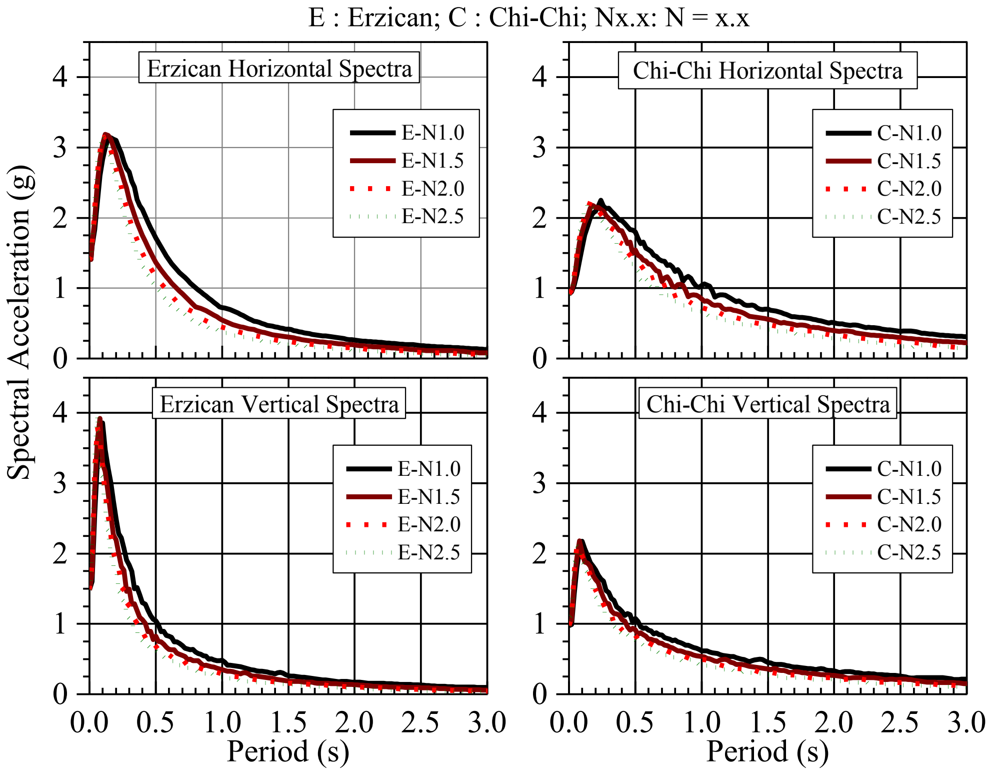

Figure 6.17. Response spectra variation with change in time step modification factor

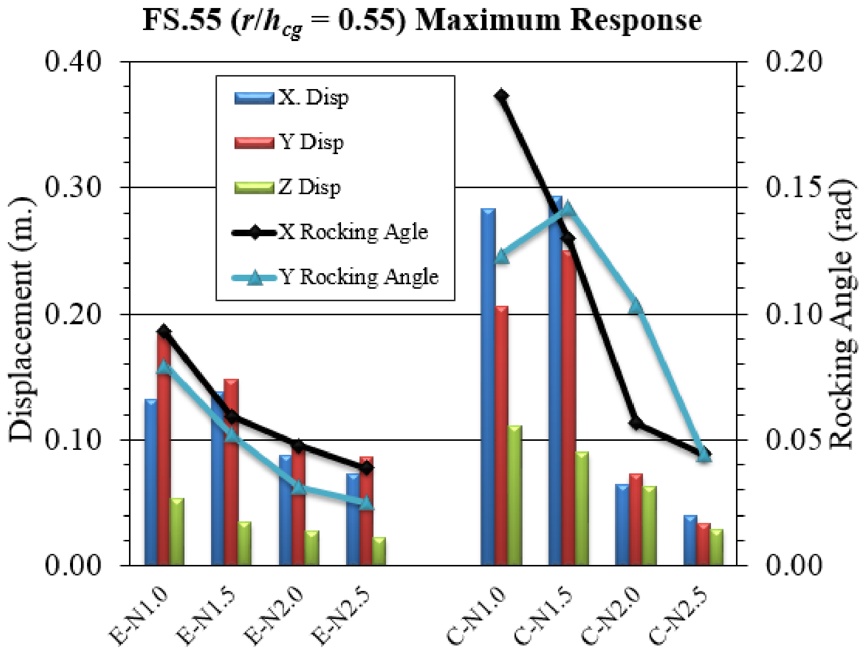

Figure 6.18. FS.55 (r/h_{cg} = 0.55) absolute maximum rocking and sliding comparison

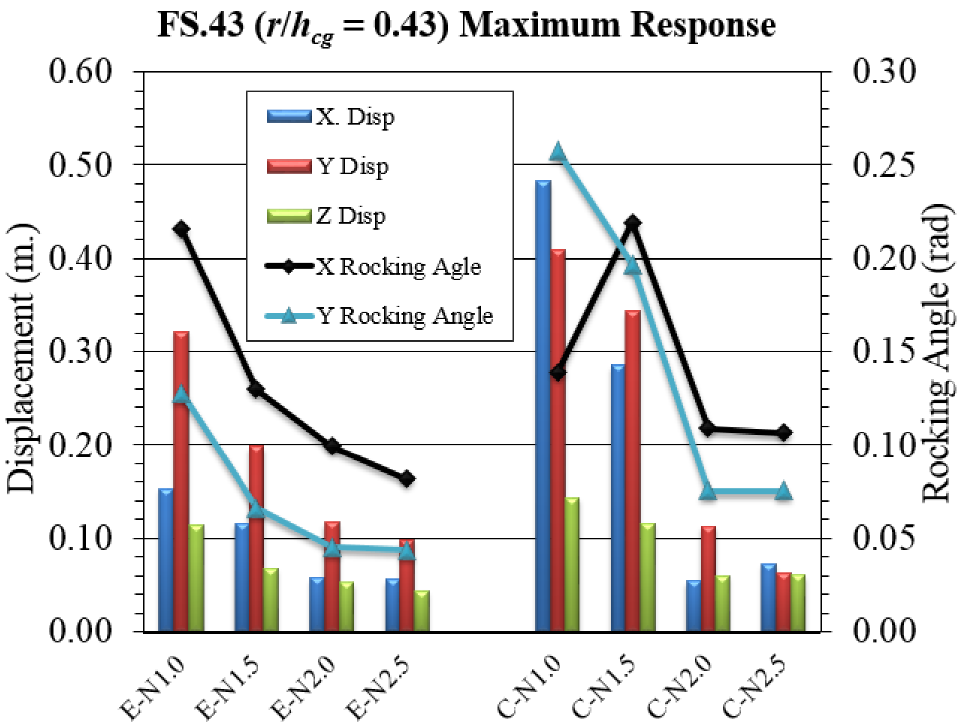

Figure 6.19. FS.43 (r/h_{cg} = 0.43) absolute maximum rocking and sliding comparison

CHAPTER 7

SOIL STRUCTURE INTERACTION

7.1 Deconvolution and Convolution of Surface Rock Motion

The deconvolution and convolution process is used to obtain soil motion at the surface or within a soil layer. In this research, a generalized site specific study for typical WUS rock and soil profile was performed to account for the soil effect on ground motion characteristics. The motions obtained after the deconvolution and convolution process were used as input in FE simulations to find the cask response. In general, soil sites de-amplify PGA and maximum rock accelerations in the high frequency (low period) region. In addition, the spectral shape of rock motion can be significantly modified by soil effects [47].

The spectral shapes for 10,000- and 30,000-year return period, and ultimately the spectrally matched ground motions, are only appropriate for rock sites. These spectral values cannot be used directly for response analyses in soil sites. The soil effect on the ground motion characteristics, particularly for high levels of strong motion, is an area of active research and needs further investigation [47]. The effect of soil for a given ground motion is dependent upon the levels of strains it experiences. The higher the strain, the softer the soil becomes, and the larger the soil damping. As the ground motions considered for this study have high accelerations, even very dense soil and stiff soil (Site Class C and

D, respectively [61]) may undergo considerable softening. Although, amplification factors to convert rock spectra to soil spectra are available in literature, the uncertainty associated with these factors published in current building and bridge codes is high. Because of this fact, Bartlett [47] recommends a site specific response analysis for soft and stiff soils. The softening leads to higher shear strain and damping, resulting in (i) deamplification of high frequency spectral accelerations, and (ii) longer predominant period of the spectral shape.

To perform the site specific response analysis, the computer programs ProShake [62] and DEEPSOIL [56] were used. ProShake was used for the deconvolution process, in which surface rock motion is deconvolved to a certain depth. DEEPSOIL was used for convolving the resulting motion from the deconvolution process to obtain the soil surface motion. The equivalent linear (EQL) method was used for both programs. The spectrally matched free-field WUS rock motions was deconvolved to a depth of 2,000m (6,562 ft.) of the generic WUS rock profile [47,63]. Figure 7.1 shows the considered generic rock profile. The deconvolved motion at the depth of 2,000 m was obtained as "outcrop" motion from the ProShake.

The deconvolved motion was then be applied at the base of same profile, for the convolution process, with the top 152.4 m (500 ft.) of rock replaced with standard soil profile for a typical nuclear power plant site (Figure 7.2). For the convolution process, soil properties were defined as per Darendeli (2001) [64] material model for granular soil (with over-consolidation ratio OCR = 1 and Ko = 0.4) for the top 152.4 m (500 ft.).

Replacing the top 152.4 m of rock profile (Figure 7.1) with standard soil profile (Figure 7.2) results in a sharp change in the shear wave velocity (Vs) profile. Figure 7.3a shows the discontinuity in the shear wave velocity profile. This abrupt change resulted in artificial amplification of the spectral accelerations of the convolved soil spectra. For this reason, the Vs profile was adjusted to have a smoother change in Vs profile (Figure 7.3b). This change was made to soil layers below 152.4 m (500 ft.). The material properties for the modified soil layers (below 152.4 m or 500 ft.) were obtained using the same Darendeli (2001) [64] model. The artificial amplification was not seen in the spectra after the Vs modification. The soil profile in Figure 7.3b was then used to convolve the ground motion to obtain the ground motion at the soil surface. Figures 7.4-7.7 compare spectra developed for WUS rock to the average spectra obtained for soil after deconvolution and convolution process. Figure 7.8 summarizes the soil spectra, while Table B.1 and Tables B.2-B.5 provide the average soil layer properties before and after convolution analysis. Soil properties from Tables B.2-B.5 were used in FE Cask-Pad-Soil model Section 4.2.2 (Chapter 4). These figures show that soil amplified the spectral acceleration in long period region, while PGA and short period spectral accelerations are deamplified.

7.2 Validation of Soil Column Model

Ground motions were applied at the base of the soil column to verify that the soil column can produce the surface soil spectra obtained from deconvolution and convolution. The four casks shown in Figure 4.5 were removed, but their weight was included by applying pressure load on top of the entire pad. Once the simulation was complete the spectra of motion obtained at "Soil Top Far Edge" (Figure 4.5) was compared to that obtained after the convolution process (Section 7.1). The input motion for the FE model was obtained from the convolution process. During the convolution process, ground motion at the base of Layer 28 (i.e., at the depth of 152.4 m) was requested in DEEPSOIL

[56] as a “within layer motion.” This motion was then applied to the base of the soil column. Figure 7.9 compares the original rock spectra (10,000-year), soil spectra obtained from DEEPSOIL convolution, and that obtained from FE model at the edge of soil column. The soil spectra obtained from DEEPSOIL and FE model are in good agreement. This validates that the FE model can reproduce the expected surface soil motion.

7.3 Response of Fully Coupled Cask-Pad-Soil Model

7.3.1 Cask with Aspect Ratio 0.43

The validated model (Figure 4.5) was then subjected to ground motions applied at the model’s soil column base. These motions were obtained from the DEEPSOIL [56] convolution at a depth of 152.4 m. This section presents the fully coupled cask-pad-soil model performance for FS.43 ($r/h_{cg} = 0.43$). The simulations shows that the change in the ground motion dominant frequency due to SSI plays a relevant role in the casks’ response.

Figure 7.10 shows the casks in motion subjected to the convolved 30,000-year Chi-Chi record, representing one of the most extreme seismic excitations that a cask could experience. As observed, the casks undergo large rocking, tumbling, and nutation motions, leading to top two casks colliding with each other. In spite of the large rocking and horizontal cask displacements, no overturning was observed for this extreme excitation. However, the rocking angle came really close to the theoretical critical angle $\alpha = 0.41$. Figures 7.11-7.14 show the plots of rocking and displacements response for the same case. The large difference in the displacements (bottom and top center of casks) presented in Figure 7.11-7.13 is a result of the large rotations experienced by the cask (Figure 7.14). In addition to the large displacement and rocking response of DSCs, the figures show the independent motion of the four casks. While similarities exist between them during the early part of the excitation, each cask responds differently as the time progresses, as observed in the rocking angle time history of Figure 7.14, a finding consistent with those reported in Chapter 6.

As a result of impact between the two casks (Cask1 and Cask 2), large accelerations were observed by the two casks at the instance of impact. Figure 7.15 shows the horizontal (X and Y direction) acceleration time histories at the top center of the two casks. It can be seen that at the time of impact, Cask1 experiences a maximum (absolute) acceleration of 7.06g and 7.18 g, X and Y direction, respectively. Similarly, due to the impact among themselves, Cask2 experiences 10.44g (X direction) and 4.69g (Y direction) absolute maximum acceleration.

Three more simulations for soil motion corresponding to 10,000-year Chi-Chi and Erzican, and 30,000-year Erzican were carried out (Appendix B). Table 7.1 summarizes peak rocking angles and displacements for each cases. A comparison of the corresponding peak rocking angle values from Table 6.2 and 7.1 shows that the SSI effect is crucial in the response of DSCs. Rocking of DSCs under soil motion increases by an average factor of 2.8, suggesting that the elongation of ground motion of the dominant time period can cause excessive movement of free-standing DSCs.

7.3.2 Cask with Aspect Ratio 0.55

Another full scale cask-pad-soil model was created for FS.55 cask (r/h_{cg} of 0.55) (Figure 4.5). The model was subjected to convolved ground motions applied at the model's soil column base. Figure 7.16 shows the model where casks are in motion, with Cask1 impacting with Cask4. This impact or collision among casks was also seen for casks with r/h_{cg} of 0.43 (Figure 7.10). However, unlike slender casks, the impact was mainly caused by excessive lateral displacement (Y-direction, Figure 7.19) rather than large rocking of the casks. Nevertheless, the rocking makes it easier for casks to move as they can have the nutation or precession motion. Figures 7.17-7.19 show the plots of casks' displacement response under 30,000-year Chi-Chi motion. Figure 7.19 shows Cask 4's excessive lateral (Y-direction) movement towards Cask 1, also seen in Figure 7.17, resulting in the impact between them. Figure 7.20 shows the rocking angle time history of the four casks. The figure shows a maximum rocking angle of 0.34 rad (X-direction) and 0.3 rad (Y-direction). These values are smaller than the theoretical critical angle $\alpha = 0.50$ (for $r/h_{cg} = 0.55$) and smaller than the maximum rocking angle observed for casks with r/h_{cg} of 0.43 (Figure 7.14) under the same ground motion excitation. This is expected since casks with larger r/h_{cg} show smaller rocking and larger lateral displacements for a given excitation.

In this simulation, impact between the two casks (Cask1 and Cask 4) occurs multiple times as Cask4 has large Y displacement towards Cask1. Impacts led to large cask accelerations. Figure 7.21 shows the horizontal acceleration time histories at the top center of the two casks. It can be seen that at the time of impact Cask1 experiences a maximum (absolute) acceleration of 3.60g and 6.62g, X and Y direction, respectively. Similarly, Cask4 experiences 2.88g (X direction) and 6.47g (Y direction) absolute maximum acceleration.

Three more simulations for soil motion corresponding to 10,000-year Chi-Chi and Erzican and 30,000-year Erzican (soil motions) were also performed. The response plots are shown in Appendix B. Table 7.2 summarizes peak rocking angles and displacements for each cases. Again, comparison between respective peak rocking angle between Tables 6.2 and 7.2 shows large increase (average factor of 5.3) in the rocking angle of casks of the same aspect ratio under soil effect.

Another interesting observation for r/h_{cg} = 0.55 cask's response under 10,000 and 30,000 Erzican runs (Figures B.17-B.24), is that all four casks have similar rocking and displacement response. The main reason is that even the convolved Erzican motion have one major pulse, i.e., NFGM characteristics. Figure B.25 shows the VTH of convolved 10,000- and 30,000-year Erzican motion recovered at Far Soil Top point (Figure 4.5). This behavior, however, did not occur for the casks with r/h_{cg} 0.43.

7.4 Discussion of Results: Full Scale Cask-Pad-Soil FE Model (SSI)

This chapter presented the effects of SSI on the response of free-standing DSCs. Full scale FE models of fully coupled cask-pad-soil were developed. The strain compatible soil properties used in the model were obtained from deconvolution and convolution analysis, which results in a change in spectral ground motion characteristics caused by the soil effect. While most of the previous studies use deconvolution and convolution to obtain the same starting target motion, this study used surface rock motion and performed a site specific soil effect study that resulted in ground motions with different spectral characteristics. The main conclusions are:

i. Deconvolution of rock motions and convolving them back through soil resulted in changes in the spectral characteristics of the original rock motion. The dominant ground motion period elongates (T > 0.5s), and the high frequency content, including the PGA of ground motions, is deamplified (muted) by soil effects.

ii. This change in frequency content has the most impact on the response of DSCs. The change in frequency resulted in 3 to 5 times the rocking, and produced a similar increase in displacements compared to those resulting from application of rock motions. This finding agrees with the parametric studies performed by changing the scale factor for time (Section 6.4).

iii. Simulations for both squat (r/h_{cg} = 0.55) and slender (r/h_{cg} = 0.43) casks, for the 30,000-year Chi-Chi motion showed excessive movement of casks, led to impact between them, and the casks experiencing impact accelerations of up to 10.44g.

iv. This study also showed that the response of casks, within the same model, follows a similar trend during the early part of ground motion excitation. But as time history progresses, differences in the response occur.

Table 7.1. Peak (absolute maximum) responses of FS.43 ($r/h_{cg} = 0.43$, full scale cask-pad-soil model) under convolved soil motions

Ground Motion	Cask	Rocking Angle (rad)		Cask Bottom Displacement (m)		Cask Top Displacement (m)		Residual Displacement Cask Bottom (m)	
		X	Y	X	Y	X	Y	X	Y
10,000-year Chi-Chi (Soil)	1	0.123	0.187	0.508	0.282	0.742	1.074	0.041	0.195
	2	0.165	0.179	0.414	0.485	1.287	1.503	*	*
	3	0.184	0.203	0.624	0.498	1.390	1.691	*	*
	4	0.174	0.172	0.667	0.376	1.457	1.363	0.527	0.277
10,000-year Erzican (Soil)	1	0.114	0.126	0.229	0.151	0.594	0.862	0.098	0.076
	2	0.113	0.126	0.245	0.215	0.931	0.865	*	*
	3	0.116	0.131	0.228	0.153	0.607	0.888	*	*
	4	0.121	0.116	0.219	0.153	0.657	0.808	0.062	0.059
30,000-year Chi-Chi (Soil)	1	0.375	0.326	1.277	0.697	2.136	2.281	*	*
	2	0.236	0.262	0.713	0.907	1.459	1.497	*	*
	3	0.349	0.230	0.707	1.548	2.047	2.515	0.381	1.427
	4	0.336	0.194	0.686	1.227	1.855	1.981	0.227	0.355
30,000-year Erzican (Soil)	1	0.107	0.163	0.515	0.458	0.903	1.311	0.067	0.059
	2	0.105	0.158	0.522	0.473	0.918	1.311	0.003	0.208
	3	0.145	0.161	0.581	0.493	1.182	1.332	*	*
	4	0.121	0.159	0.471	0.516	0.898	1.366	*	*
Note: * - Tumbling or nutation motion continues (not back to complete rest)									

Table 7.2. Peak (absolute maximum) responses of FS.55 ($r/h_{cg} = 0.55$, full scale cask-pad-soil model) under convolved soil motions

Ground Motion	Cask	Rocking Angle (rad)		Cask Bottom Displacement (m)		Cask Top Displacement (m)		Residual Displacement Cask Bottom (m)	
		X	Y	X	Y	X	Y	X	Y
10,000-year Chi-Chi (Soil)	1	0.036	0.030	0.084	0.058	0.287	0.200	0.044	0.024
	2	0.149	0.173	0.622	0.540	1.344	1.482	0.262	0.179
	3	0.044	0.056	0.044	0.043	0.235	0.325	0.011	0.021
	4	0.057	0.045	0.122	0.087	0.328	0.303	0.066	0.042
10,000-year Erzican (Soil)	1	0.063	0.092	0.388	0.221	0.738	0.726	0.257*	0.049*
	2	0.071	0.092	0.340	0.176	0.731	0.680	0.233*	0.006*
	3	0.071	0.088	0.335	0.154	0.723	0.628	0.221	0.004
	4	0.063	0.099	0.344	0.198	0.631	0.746	0.216	0.074
30,000-year Chi-Chi (Soil)	1	0.323	0.296	0.745	1.205	1.864	2.469	0.319	0.532
	2	0.320	0.297	0.695	0.894	2.097	1.800	0.222	0.024
	3	0.247	0.252	1.143	0.623	1.889	1.605	0.856	0.273
	4	0.339	0.178	0.997	2.858	2.222	3.187	0.941	2.569
30,000-year Erzican (Soil)	1	0.149	0.130	0.829	0.694	1.440	1.322	*	*
	2	0.130	0.110	0.580	0.510	1.182	0.966	*	*
	3	0.130	0.115	0.544	0.357	1.035	0.815	*	*
	4	0.135	0.120	0.656	0.412	1.085	0.914	*	*
Note: * - Tumbling or nutation motion continues (not back to complete rest)									

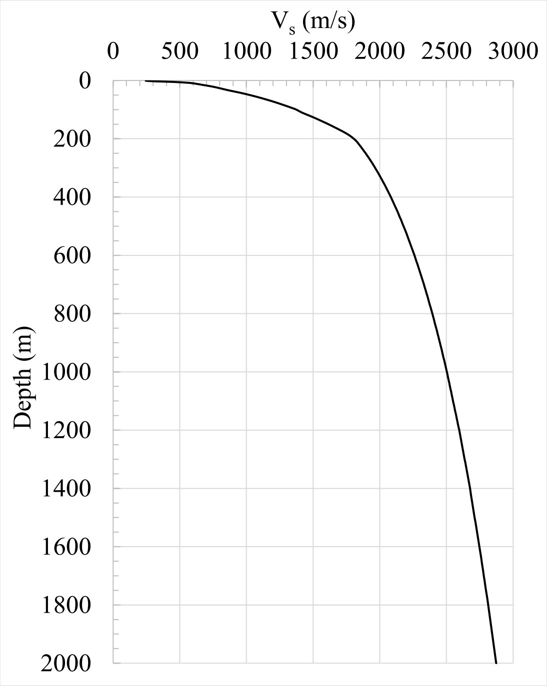

Figure 7.1. Generic Western U.S. rock Vs profile [63] adapted from Bartlett [47]

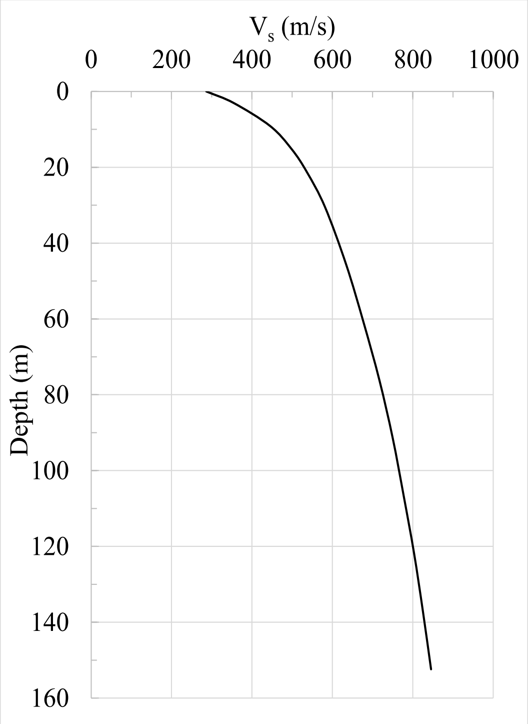

Figure 7.2. Typical shear wave velocity (Vs) – Standard Profile for nuclear power plant sites, adapted from [19]

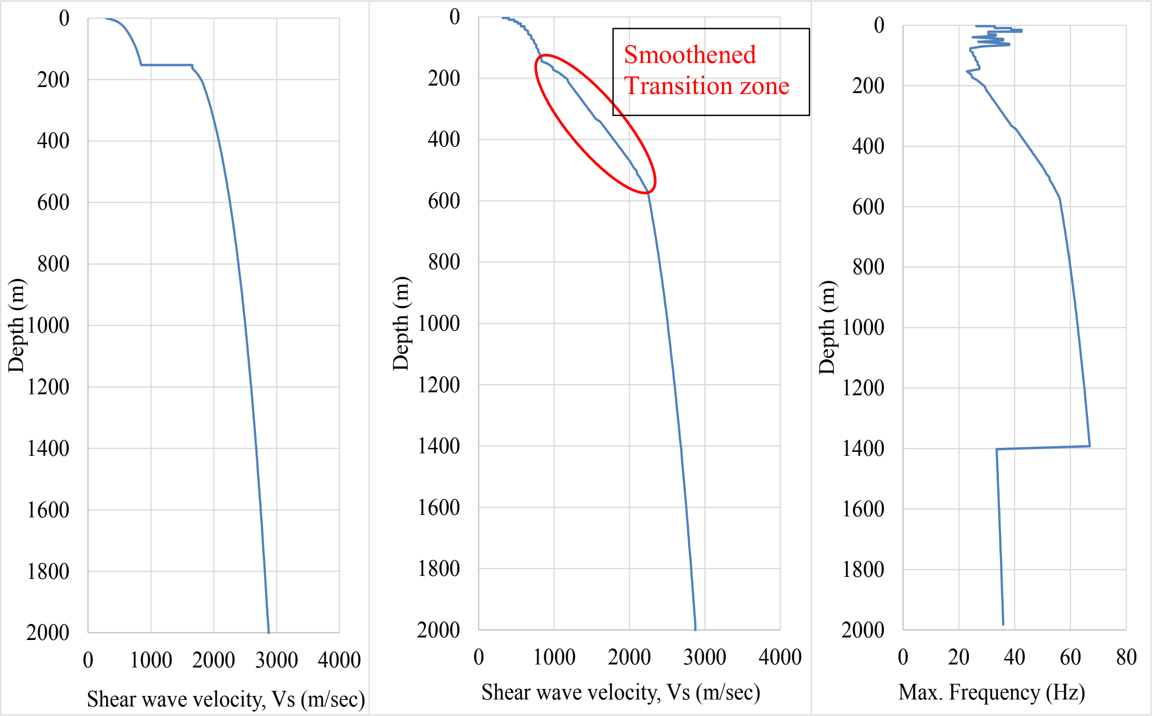

(a) (b) (c)

Figure 7.3. Shear velocity (Vs) profile for convolution analyses: (a) Discontinuity in Vs profile; (b) Soil profile for convolution analysis [with modified Vs below 500ft (152.4 m), smooth transition]; (c) Maximum frequency supported by modified soil profile

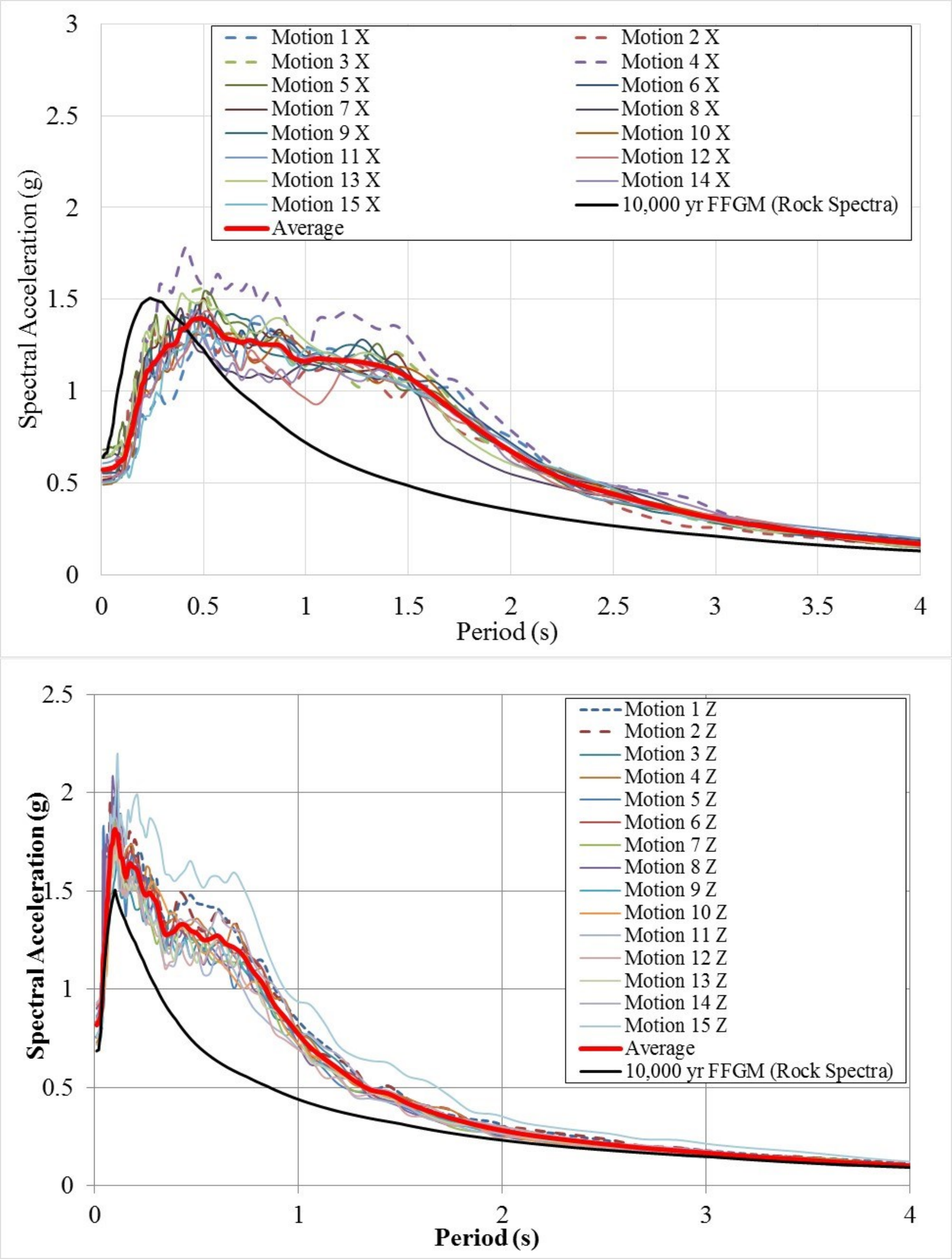

Figure 7.4. Comparison of 10,000-year far field WUS rock spectra (solid black line) and average soil spectra (solid red line): Horzontal (Top); Vertical (Bottom)

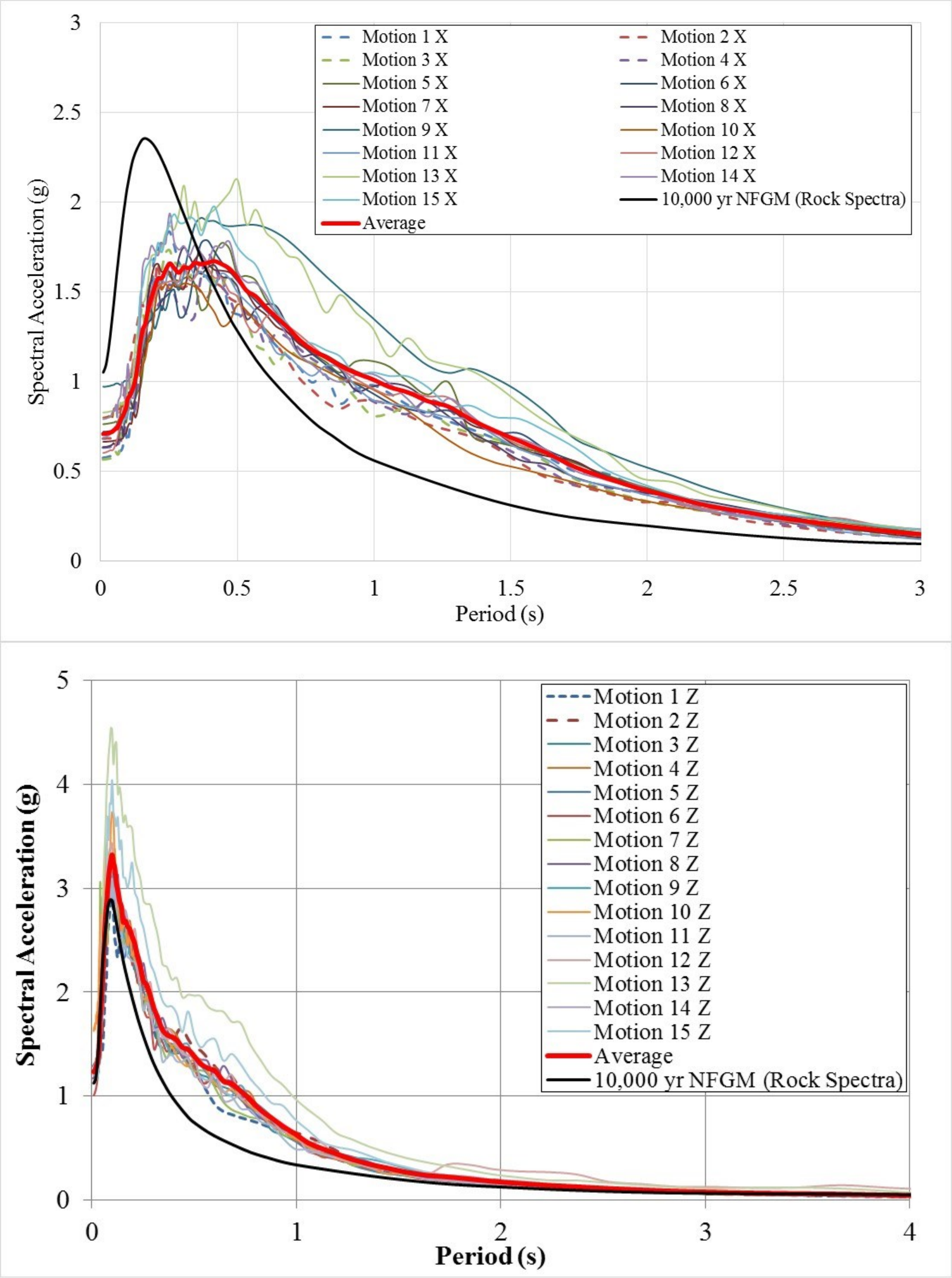

Figure 7.5. Comparison of 10,000-year near field WUS rock spectra (solid black line) and average soil spectra (solid red line): Horzontal (Top); Vertical (Bottom)

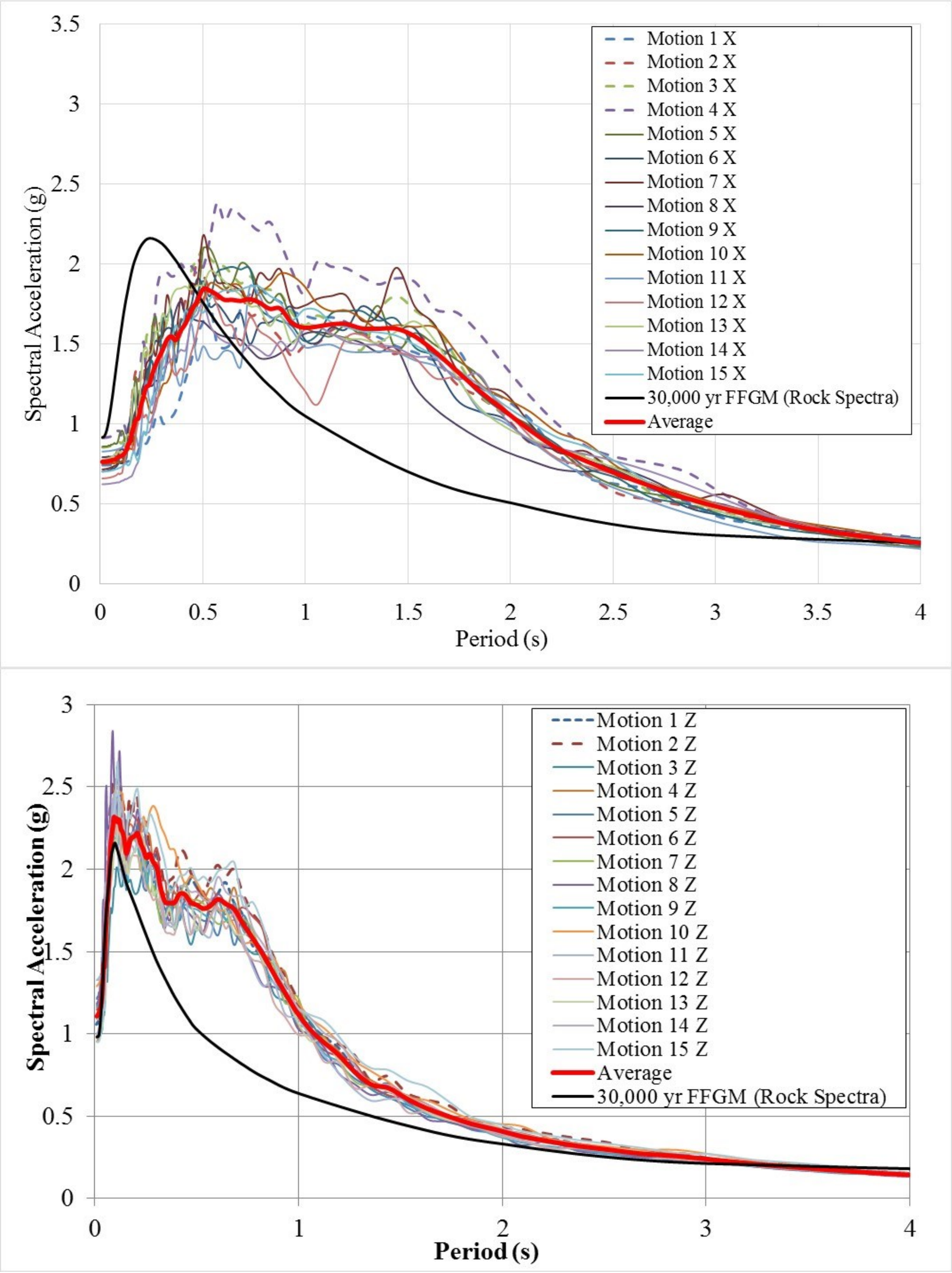

Figure 7.6. Comparison of 30,000-year far field WUS rock spectra (solid black line) and average soil spectra (solid red line): Horzontal (Top); Vertical (Bottom)

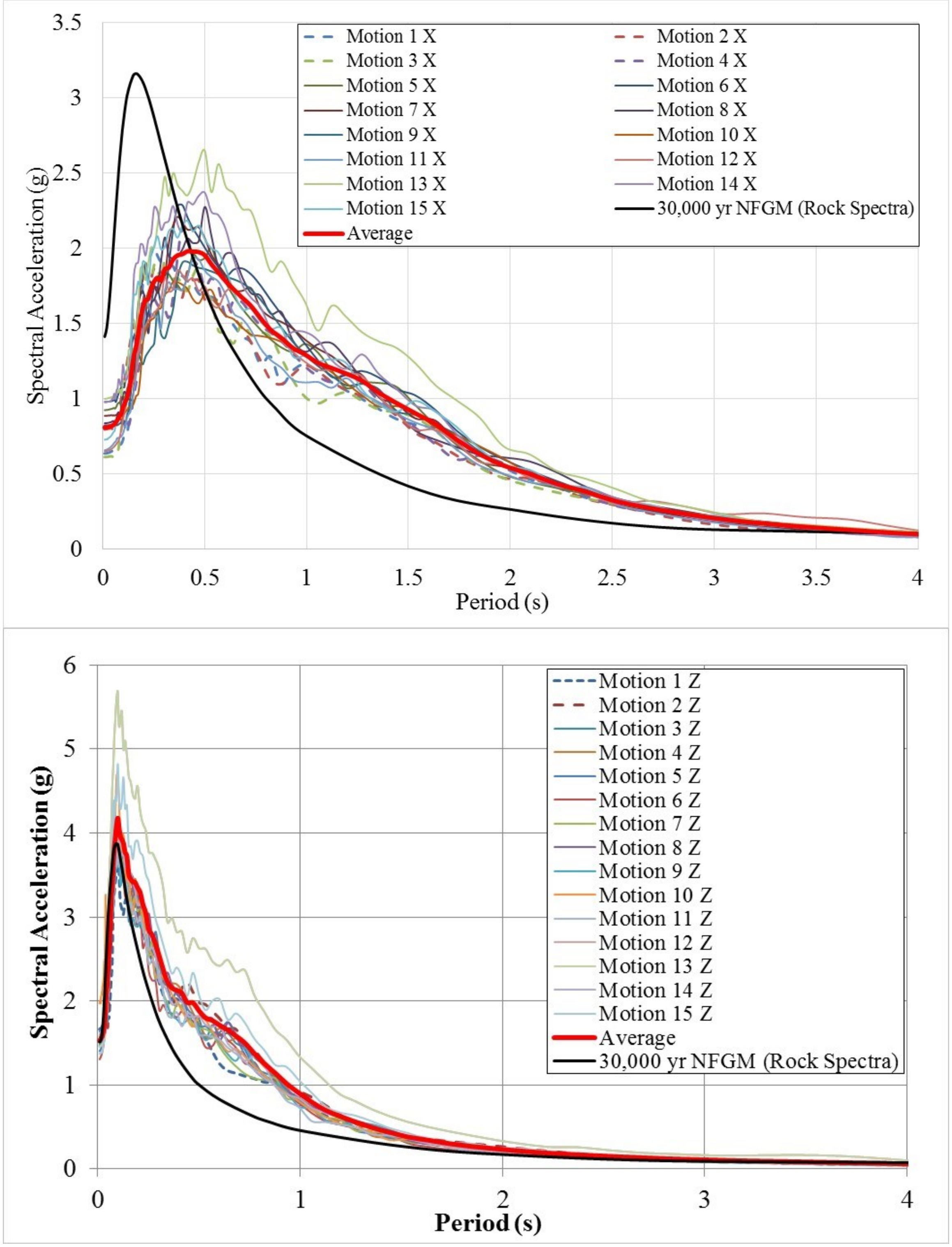

Figure 7.7. Comparison of 30,000-year near field WUS rock spectra (solid black line) and average soil spectra (solid red line): Horzontal (Top); Vertical (Bottom)

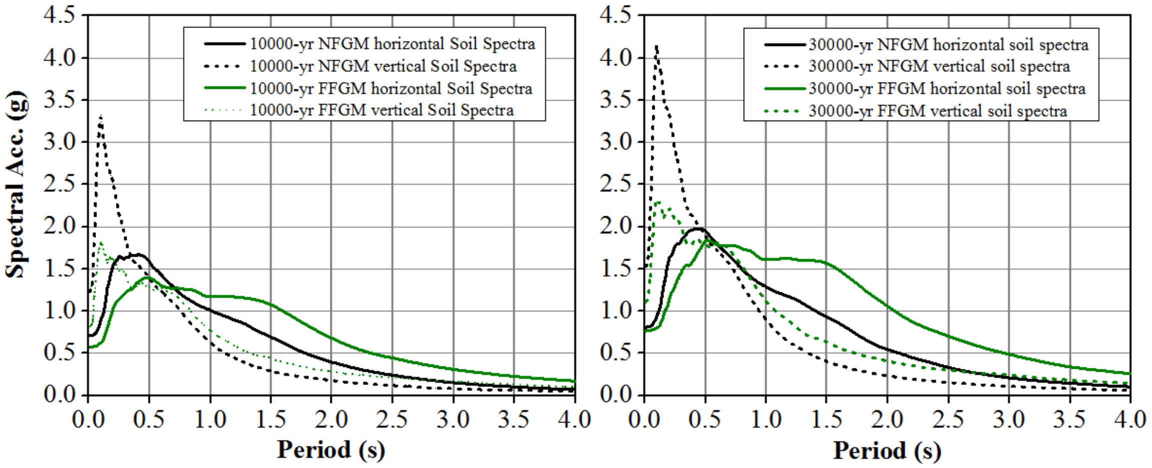

Figure 7.8. Summary of average soil spectra after deconvolution and convolution

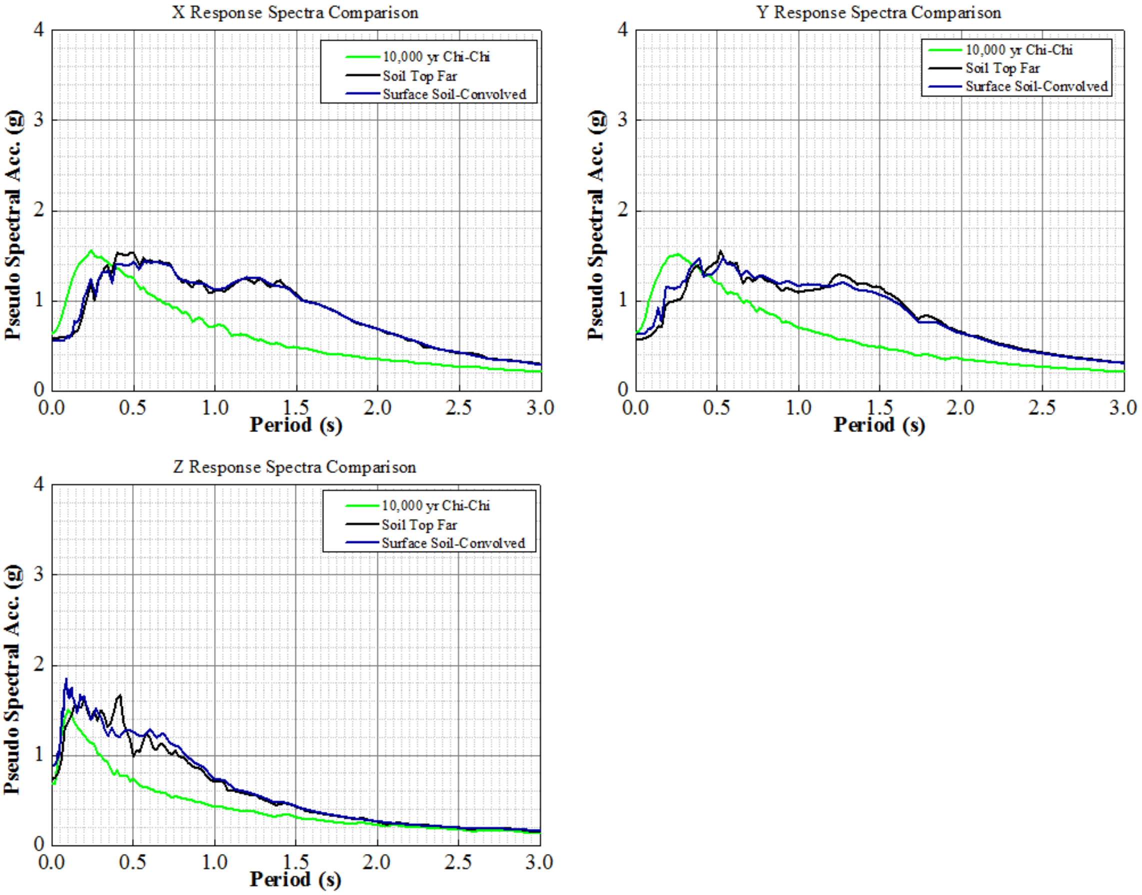

Figure 7.9. Spectra comparison for DEEPSOIL and FE model

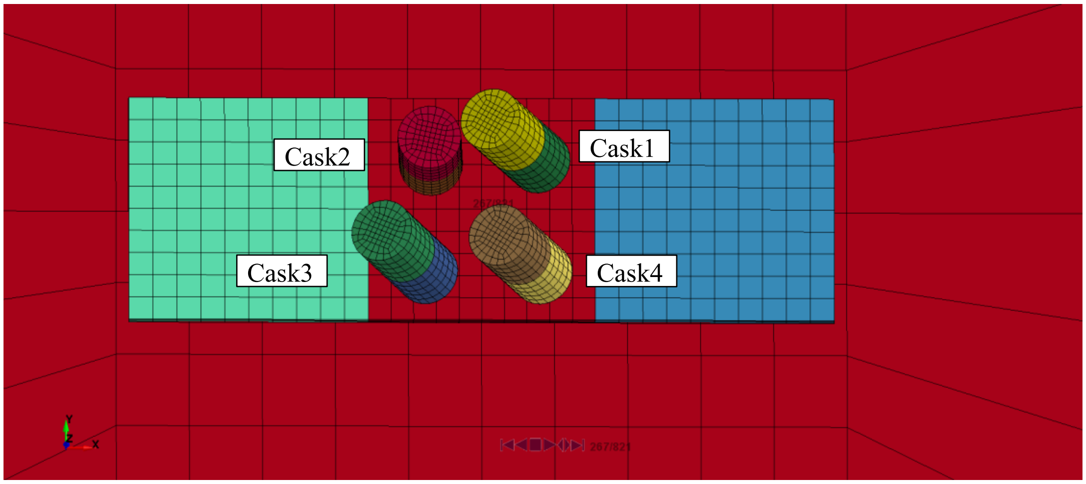

Figure 7.10. FE cask-pad-soil model showing casks (r/h_{cg} = 0.43) in motion under an extreme seismic excitation (convolved 30,000-year Chi-Chi soil ground motion)

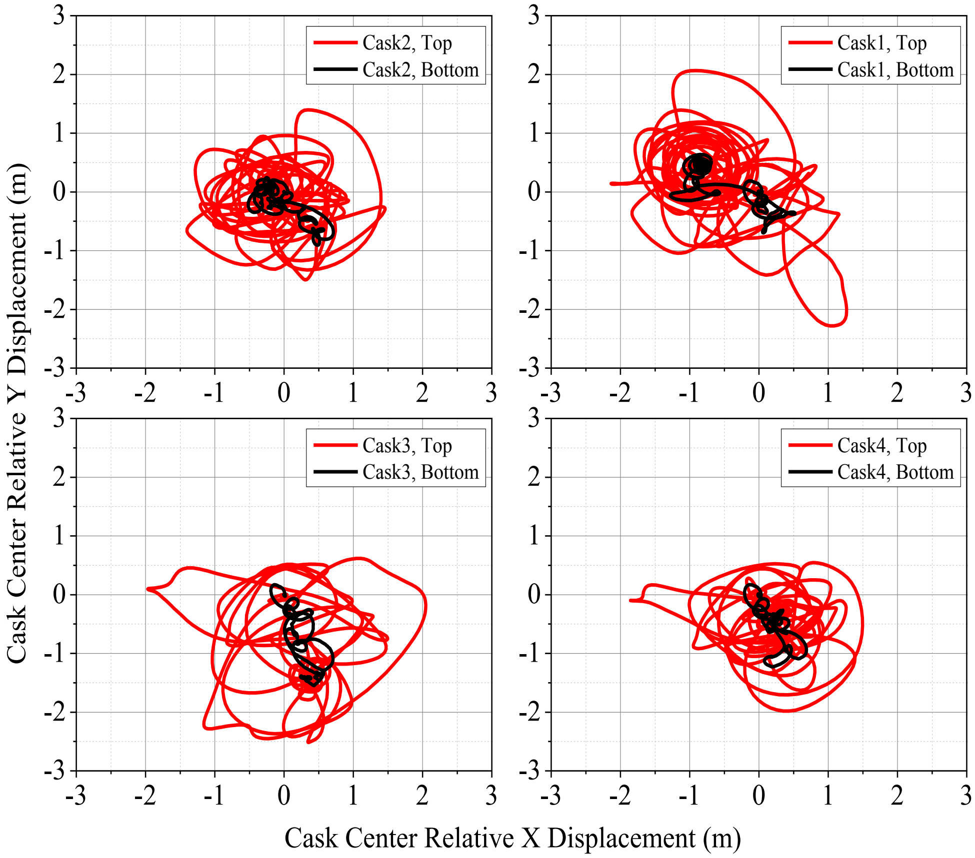

Figure 7.11. Cask centers' XY lateral displacement relative to pad, cask-pad-soil model (full scale), r/hcg = 0.43, μ_s = 0.55, convolved 30,000-year Chi-Chi

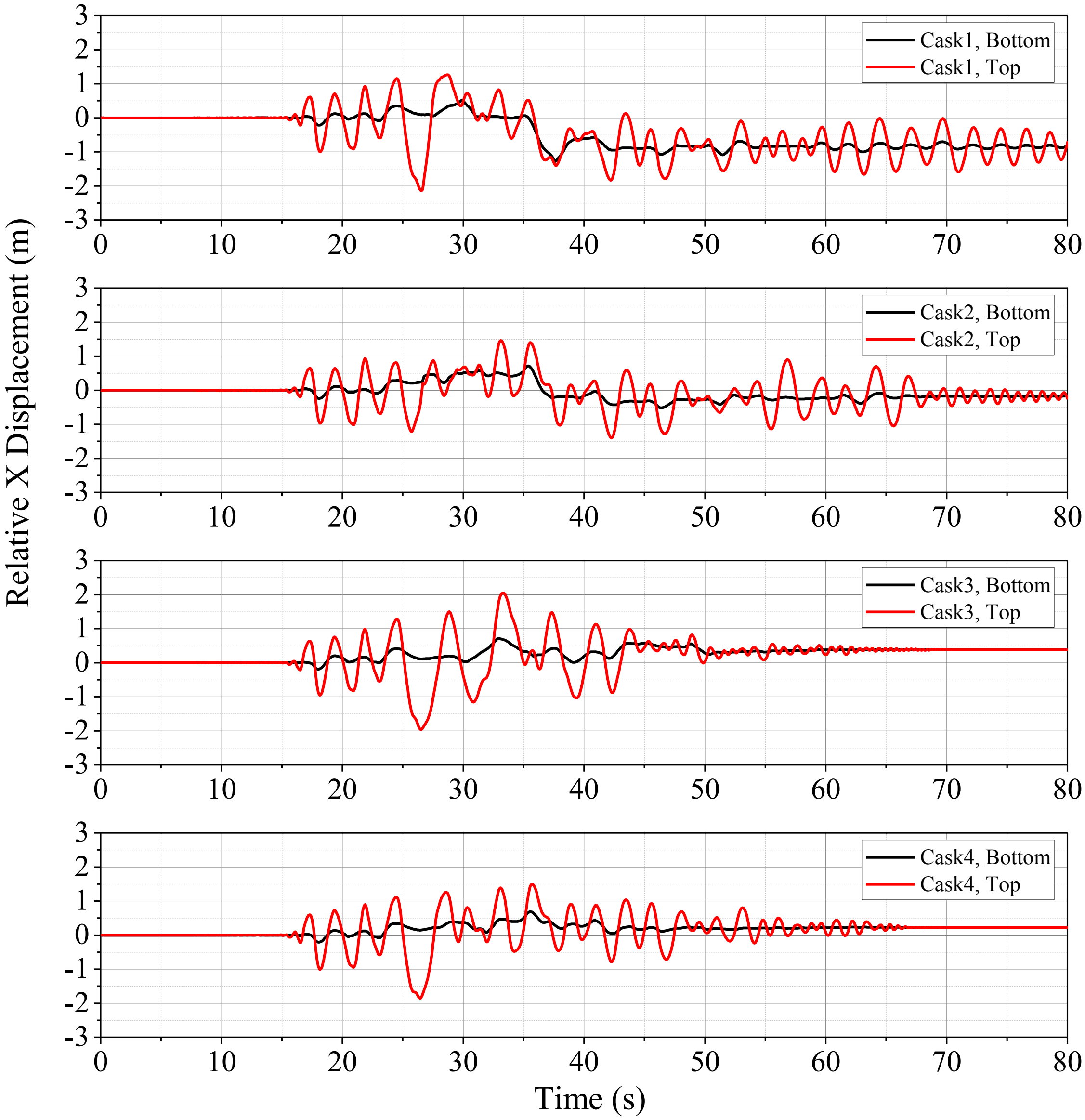

Figure 7.12. Time histories of casks X displacement relative to pad, cask-pad-soil model (full scale), r/hcg = 0.43, $\mu_s = 0.55$, convolved 30,000-year Chi-Chi

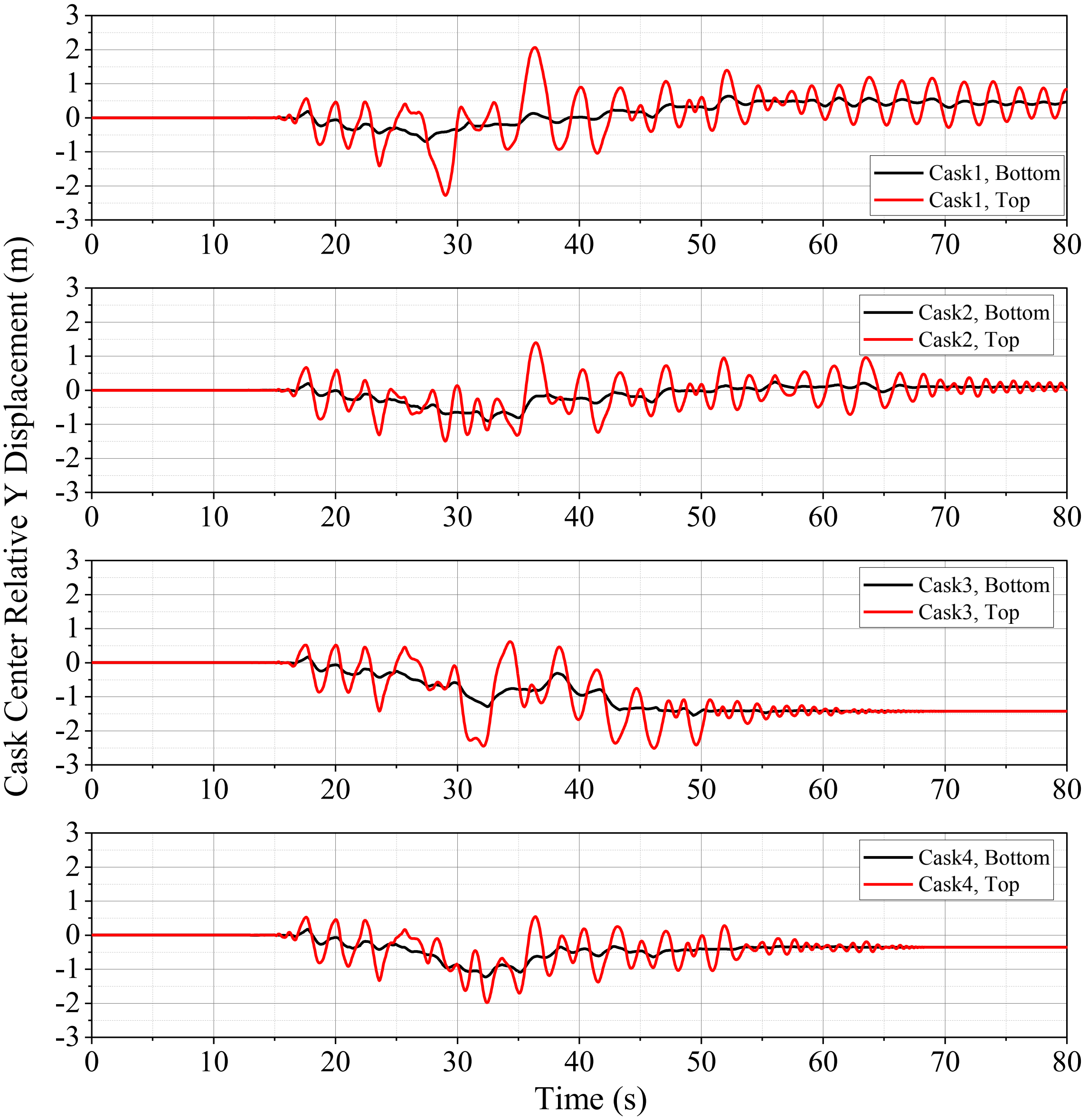

Figure 7.13. Time histories of casks Y displacement relative to pad, cask-pad-soil model (full scale), r/hcg = 0.43, μ_s = 0.55, convolved 30,000-year Chi-Chi

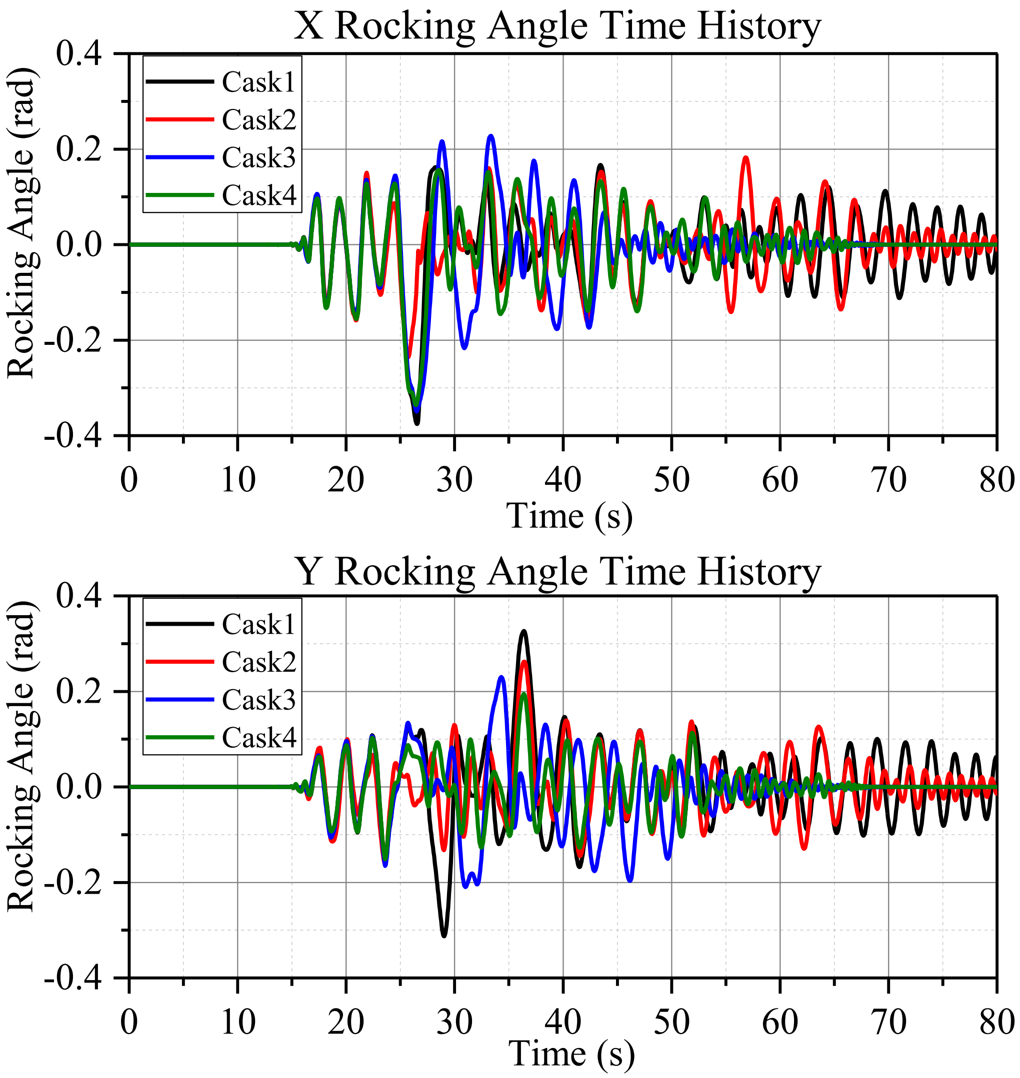

Figure 7.14. Rocking angle time histories, cask-pad-soil model (full scale), r/hcg = 0.43, $\mu_s = 0.55$, convolved 30,000-year Chi-Chi

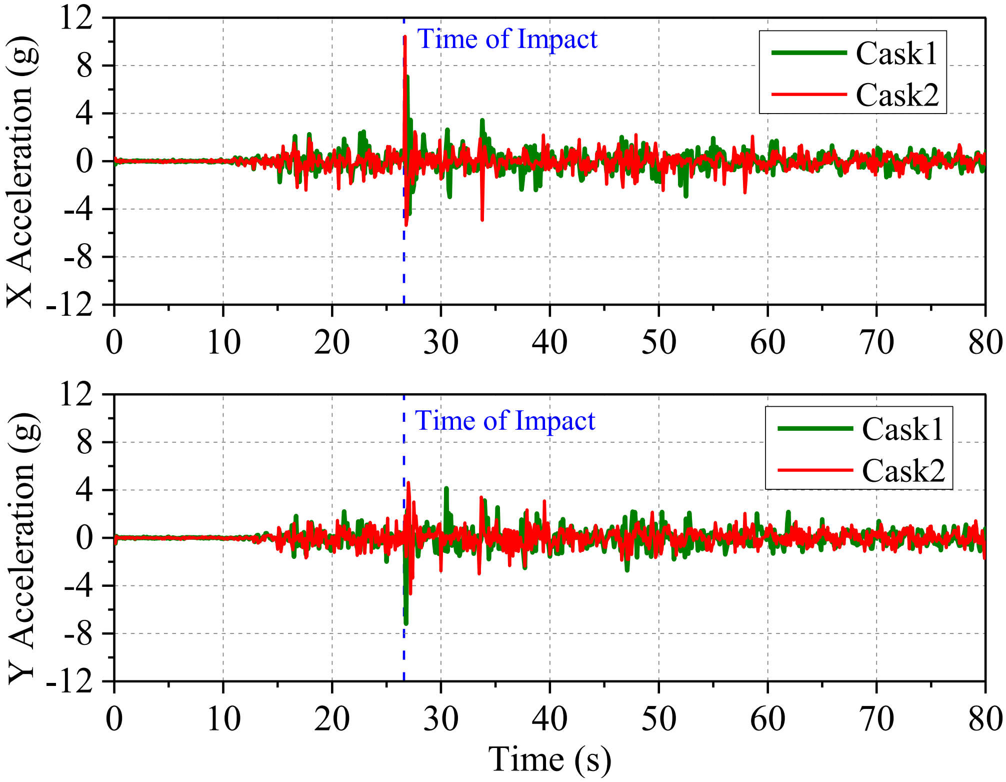

Figure 7.15. Horizontal acceleration experienced by Cask1 and Cask2 ($r/h_{cg} = 0.43$) top center (30,000-year Chi-Chi, SSI)

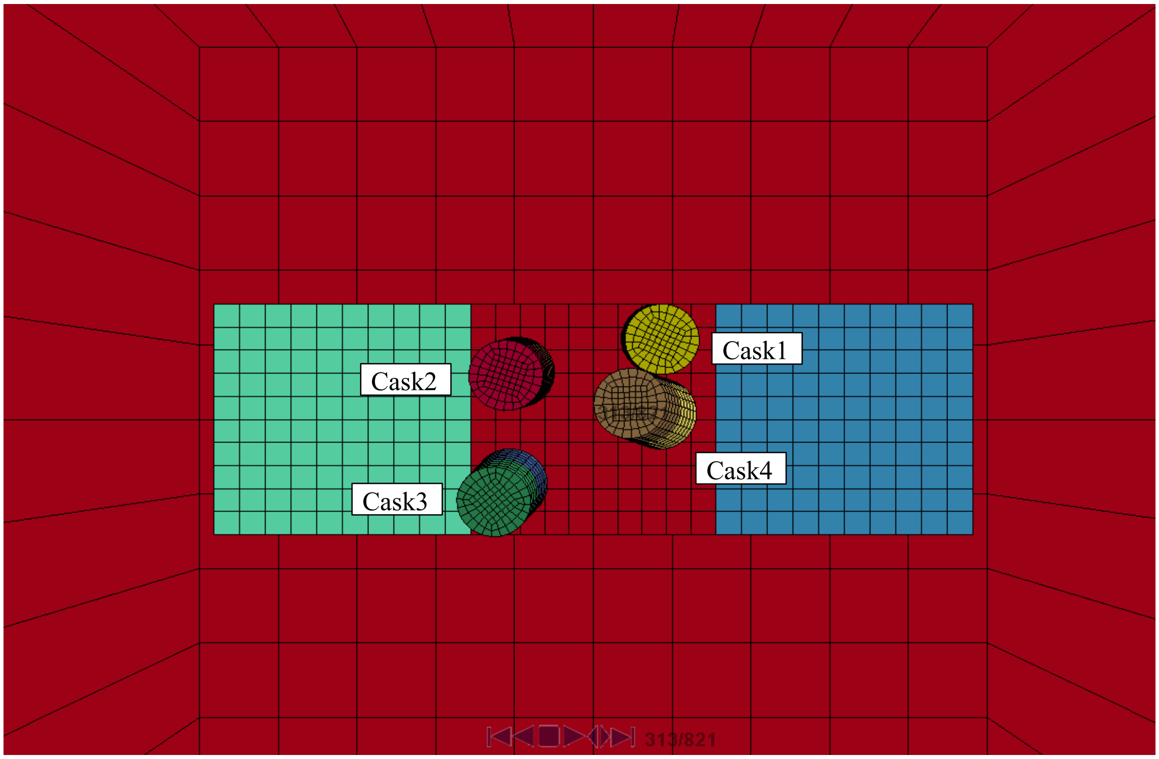

Figure 7.16. FE cask-pad-soil model showing casks ($r/h_{cg} = 0.55$) in motion (Cask1, Cask4 impact) under an extreme seismic excitation (convolved 30,000-year Chi-Chi soil ground motion)

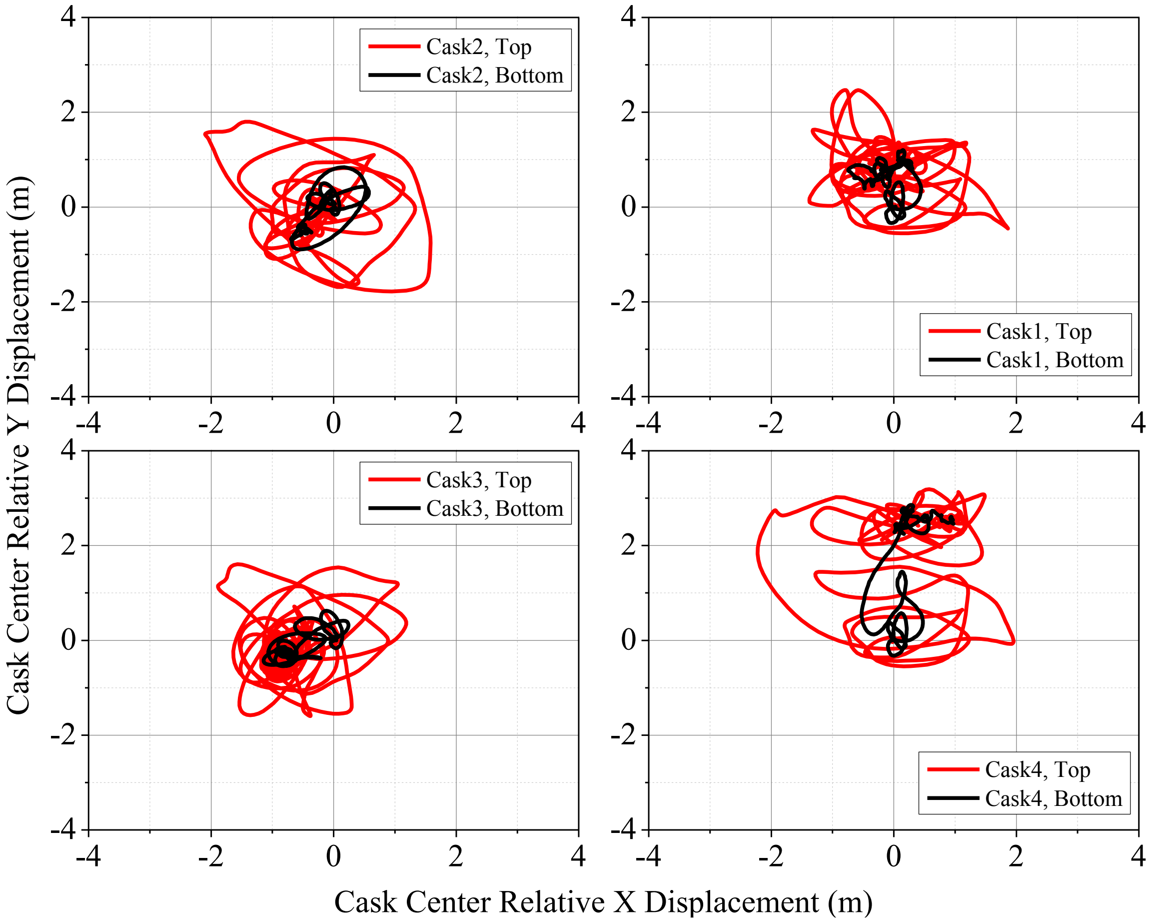

Figure 7.17. Cask centers' XY lateral displacement relative to pad, cask-pad-soil model (full scale), r/hcg = 0.55, μ = 0.55, convolved 30,000-year Chi-Chi

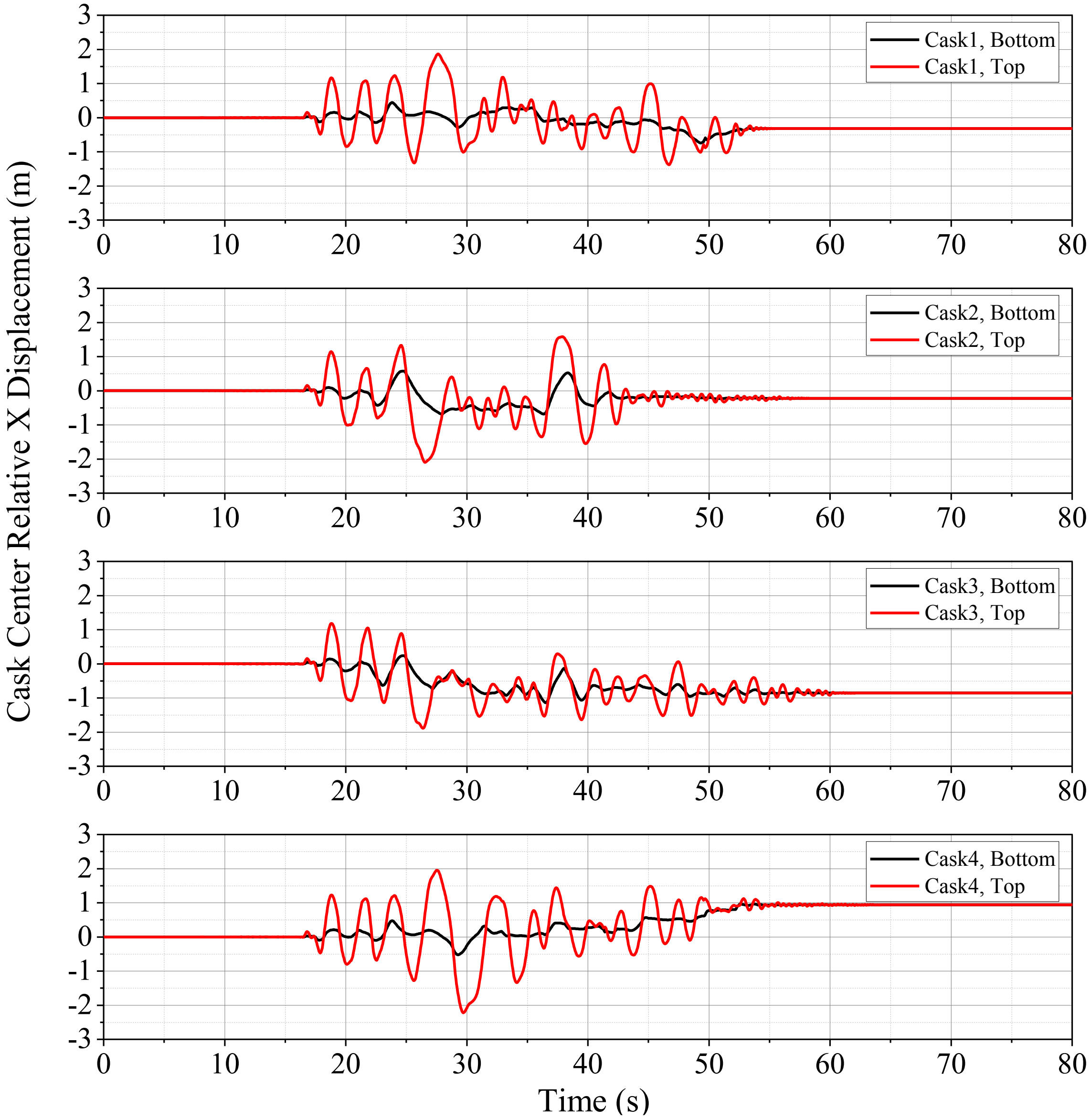

Figure 7.18. Cask centers' X lateral displacement relative to pad, cask-pad-soil model (full scale), r/hcg = 0.55, μ = 0.55, convolved 30,000-year Chi-Chi

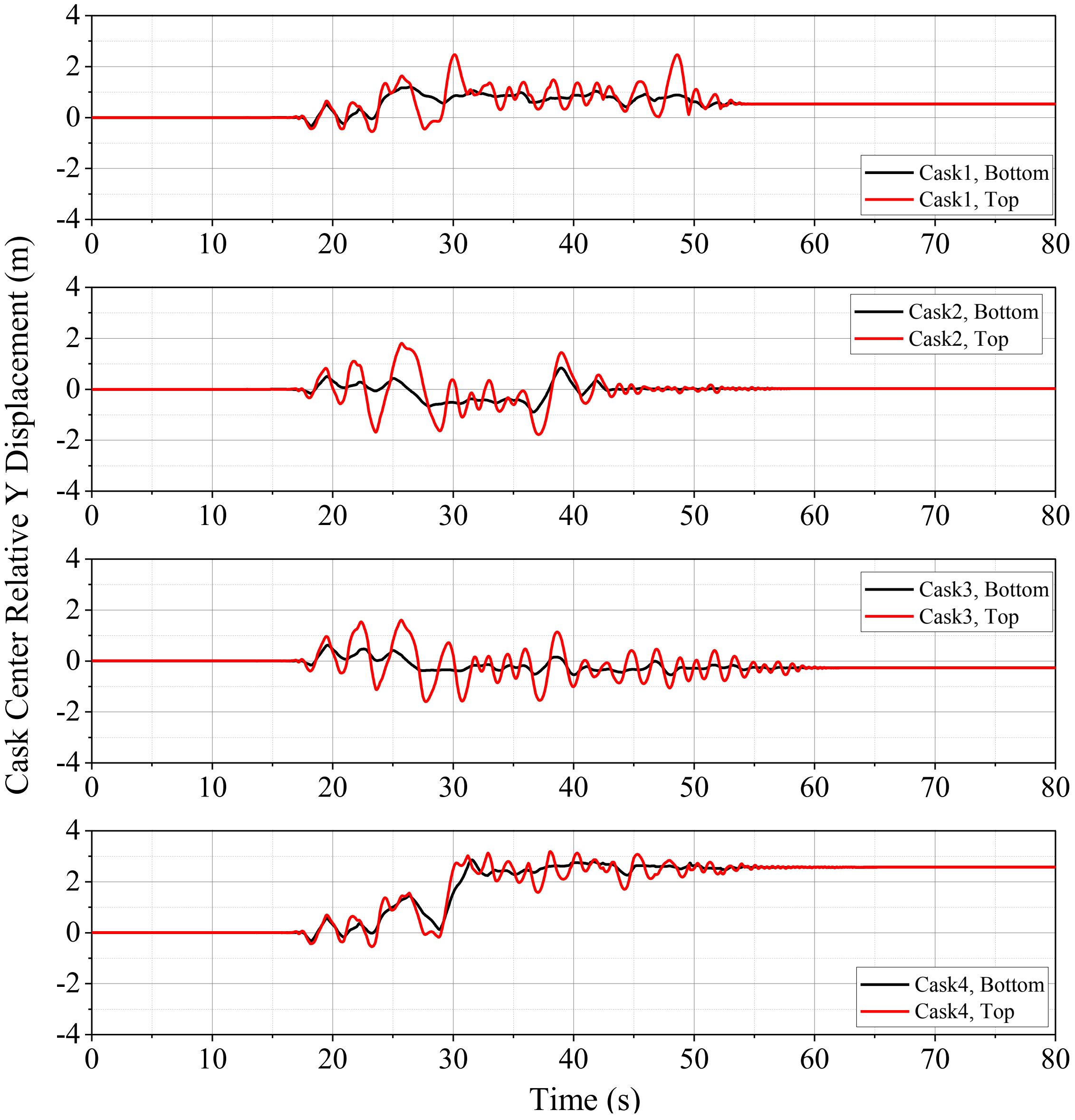

Figure 7.19. Cask centers’ Y lateral displacement relative to pad, cask-pad-soil model (full scale), r/hcg = 0.55, μ = 0.55, convolved 30,000-year Chi-Chi

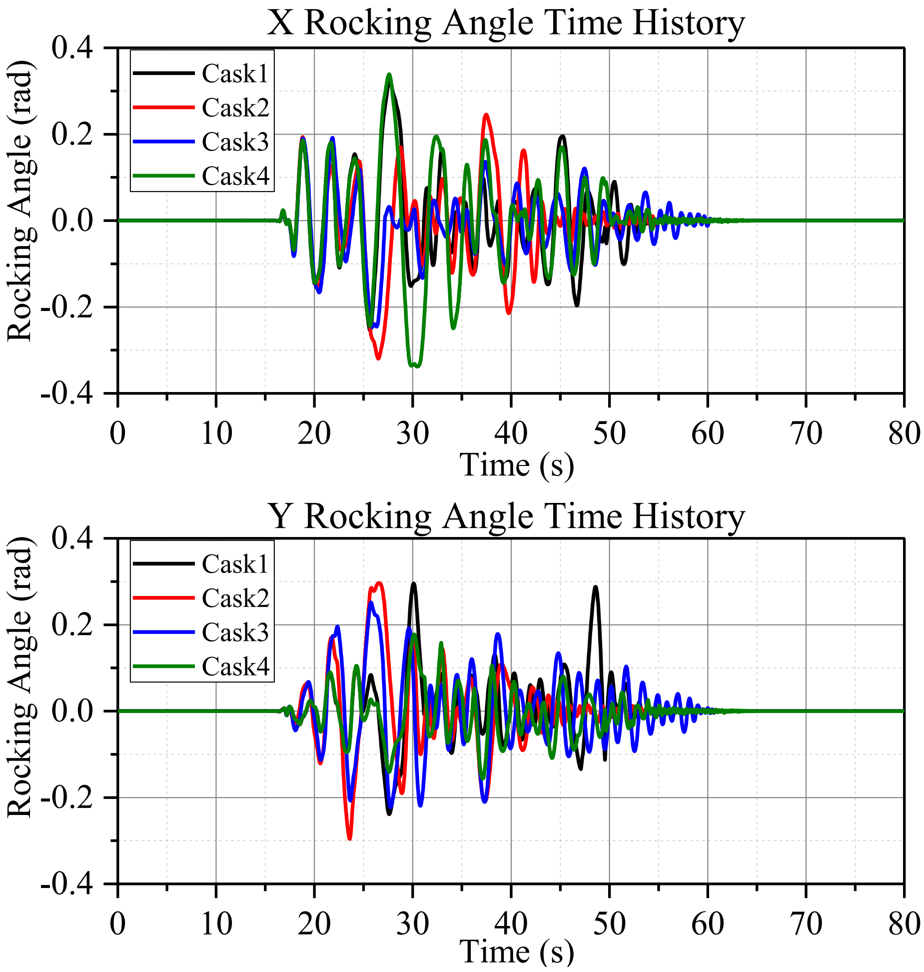

Figure 7.20. Rocking angle time histories, cask-pad-soil model (full scale), r/hcg = 0.55, μ = 0.55, convolved 30,000-year Chi-Chi

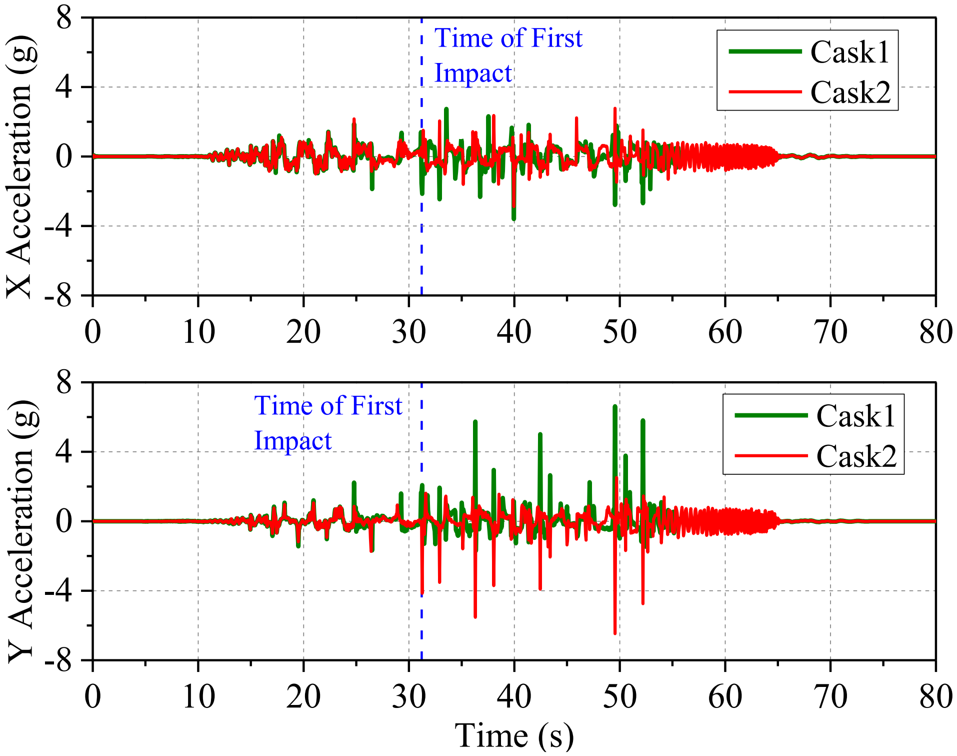

Figure 7.21. Horizontal acceleration experienced by Cask1 and Cask2 (r/h_{cg} = 0.55) top center (30,000-year Chi-Chi, SSI)

CHAPTER 8

RESPONSE SENSITIVITY: LACK OF REPEATABILITY AND CHAOS

The dynamic response of free-standing bodies for a simplified 2D rocking system, and especially for 3D bodies, is highly complex, resulting in a nonlinear and sensitive phenomenon. Yim et al. [29] showed that the rocking-only response of an idealized body is highly sensitive to system parameters and dynamic input characteristics, a finding confirmed experimentally by Aslam et al.[30]. This unpredictability and nonrepeatability in the response has been observed in other studies. For instance, Hogan [31] carried out analytical studies of harmonically excited 2D rigid body (horizontal excitation only), concluding that unpredictability in the response is only observed for long duration excitations.

This repeatability and stability in response of rocking blocks, under relatively short duration unidirectional harmonic excitation only, was also found experimentally by Peña et al. [28]. In the same study Peña et al. found lack of repeatability in the response under seismic ground motion records, even when only one horizontal direction was considered. Also, Jeong et al. [14] analytically investigated the effect of sliding, in addition to rocking, on the response of free-standing planar bodies. They concluded that rocking-only motion can be chaotic under simultaneous horizontal and vertical excitations, even for sinusoidal excitations. They also show sliding can introduce chaotic behavior when it would not have been otherwise. Recent studies on free-standing cylindrical dry storage casks (DSCs) used to store spent nuclear fuel confirmed that the dynamic response is nonrepeatable [52,54,65]. These studies included experimental tests, as well as finite element and numerical simulations.

While the sensitive or chaotic nature of free-standing bodies' response has been known for a long time, the sensitivity of the response under seismic ground motions has not been evaluated. Yim et al. [29] in 1980 made some attempts towards addressing this issue by changing input and body parameters by a small amount. DeJong [66] also obtained the stochastic response of slender 2D rocking blocks using 1,000 generated ground motions of identical intensity and strong shake duration, differing only in phase, showing large variation in the maximum rocking angle.

8.1 Presence of Chaos in Response of Free-Standing Bodies

The experimental tests performed in this research (Chapter 5) show that the response of free-standing casks under similar motions is not repeatable and has large variations. The results suggest that small differences in the initial condition and/or minute variations in the applied motion (e.g., shake-table's inability to reproduce exact motion) lead to large differences in the cask response. In Section 6.2.2, the response sensitivity under multicycled harmonic excitation was evaluated using FE models, and the equation of motion, also concluding that the response is extremely sensitive when simultaneous horizontal and vertical harmonic excitation is present. However, the sensitivity is not observed when only horizontal harmonic motion is applied. This finding supports the experimental tests performed by Peña et al. [27,28]. In the case of earthquake motion, the presence of vertical motion was not necessary for the extreme sensitivity.

This extreme sensitivity and lack of repeatability indicates a potential chaotic behavior. Chaos can be defined as extreme sensitivity of the response to initial conditions. However, for a system to be chaotic it has to have certain properties. These properties can be checked using methods for chaotic analysis. Three of these methods are used in this study: phase-space plot, Fourier spectra, and Poincaré sections (also called Poincaré maps). These approaches can indicate the presence of chaos in the rocking response, and were implemented for Equation (4.1), the 2D equation of pure rocking motion for idealized DSCs (Section 4.3) under sinusoidal waves.

A phase-space plot displays the continuous displacement versus velocity curve over time. Periodic motions are characterized by closed orbits in phase plane (phase-space) [67]. An indication of possible existence of chaos is an open ended or discontinuous phase-space plot. In other words, chaotic motions will have orbits that never close or repeat. Figure 8.1 shows examples of a periodic and a chaotic trajectory.

The existence of chaos is also indicated by the appearance of a broad spectrum of frequencies in the output, even though the input is a single frequency harmonic motion. This frequency spectrum can be seen in the Fourier Spectrum or Power Spectrum of the output. Another indication of chaos can be obtained from Poincaré sections. For harmonic, subharmonic or period systems, the Poincaré map or section would show a set of finite number of points or closed loop(s). For chaotic systems the map will not show such finite number of points and closed loop(s), but would rather show points distributed in wide space and/or forms strange attractors. Figures 8.2 and 8.3 present examples of periodic and chaotic Fourier spectra and Poincaré sections, respectively.

8.1.1 Application of Chaotic Analysis to Idealized DSCs

The methods described in the previous section to identify chaos were applied to the evaluated DSCs with aspect ratios of 0.43 and 0.55 (Table 4.2). Numerically, chaotic analysis methods can be used to determine if the system's response is nonharmonic and/or nonperiodic when subjected to a harmonic or periodic excitation. For instance, the free-standing specimen's response can be obtained, by numerically solving Equation (4.1), under the harmonic excitation given by Equation (8.1).

$$\begin{aligned} \ddot{u}_g &= A_h \alpha g \sin(\Omega p t + \psi) \\ \ddot{v}_g &= A_v \alpha g \sin(\Omega p t + \psi) \end{aligned} \tag{8.1}$$

where, A_h, A_v = normalized amplitude given by Equation(6.2) and $\psi = \sin^{-1}(1/A_h)$ = phase angle.

From the solution, phase-plane plot, Fourier spectra and Poincaré sections can then be plotted. Figure 8.4 shows plots for DSC of $r/h_{cg} = 0.55$, $e = 0.655$ (theoretical), $A_h = 3$, $A_v = 2.5$ and $\Omega = 10$. Similarly, Figure 8.5 shows the plots for $r/h_{cg} = 0.43$, $e = 0.761$ (theoretical), under $A_h = 2.5$, $A_v = 2.0$ and $\Omega = 10$. Figure 8.6 presents the same chaotic analysis plot as shown in Figure 8.5, but the experimental coefficient of restitution $e = 0.872$ was used. The three figures show chaotic response for these representative systems, indicating a high sensitivity of the response to input parameters. The figures suggest that models cannot predict the exact response of these free-standing bodies because there are always minute differences in starting conditions (e.g., initial rocking angle due to imperfections, differences in geometry, and other parameters like *e* and *p*), or difference in boundary conditions while the cask is in motion (e.g., angular velocity and coefficient of friction). Because these differences can lead to very different responses, it is relevant to investigate if upper and lower bounds can be set for these systems.

Figure 8.7 shows a similar plot for FS.43 under horizontal sinusoidal excitation only (A_h = 2.5, A_v = 0 and Ω = 10, *e* = 0.872). In the absence of vertical excitation, the system under a horizontal excitation does not result in chaotic behavior. Figures 8.4-8.7 show that for idealized analytical systems, vertical excitation is needed to trigger a chaotic response when applying a sinusoidal excitation.

8.2 Sensitivity Study for Ground Motions: Monte Carlo Simulation

The finding of chaotic motion does not address the practical problem of the extent of variation that can be observed when a free-standing body is subjected to an actual ground motion. Repeating experimental tests a large number of times to get any statistically significant parameters is not always possible. Also, numerical solutions under sinusoidal excitation help understand the fundamental behavior of the rocking problem, but real ground motions are not periodic motions. They may contain a varied number of pulse(s) with varied frequency content. Therefore, in this section the effect of small changes in the parameters: input, geometric and initial condition; and the resulting variation in response, is investigated for seismic loading.

Equations (4.1) and (4.2) for 2D pure rocking show that the body response can be influenced by the following parameters:

i. $\ddot{u}_g$ = horizontal acceleration

ii. $\ddot{v}_g$ = vertical acceleration

iii. f = ground motion frequency

iv. e = coefficient of restitution (COR) or damping

v. p = frequency parameter

vi. θ_0 = Initial rocking angle at time = 0

vii. dt = solution time step

The first three parameters are related to the input dynamic excitation or ground motion characteristics. The parameters e and p are only related to the geometric properties of a free-standing bodies. Not only does the e differ experimentally from the theoretical value, but also experimental tests performed by Peña et al. [28,68] show that the frequency parameter (p) also differs. The parameter θ_0 refers to initial condition and/or imperfection that might be present.

To perform the sensitivity analysis of simplified rocking motion, Monte Carlo simulations were performed for the specimen with r/h_{cg} of 0.43, using Equations (4.1) and (4.2). The goal of the simulation was to evaluate the response dispersion caused by small variations in the parameters. For each considered parameter, a set of 10,000 random numbers were generated in MATLAB [69] using a uniform distribution to generate random values for e, p, and PGA parameters with a variation of ±1%. The solution time step (dt) parameter was varied between 10^{-3} and 10^{-4}. Finally, the initial rocking angle (θ_0) parameter was varied in the range of ±0.004 radians (1% of $\alpha = 0.40$). The positive and negative sign for rocking angle denotes clockwise (rocking about O) and counter-clockwise (rocking about O'), respectively, as seen in Figure 4.8. Note that as actual ground motion was used instead to sinusoidal excitation for this investigation, frequency, *f*, was not considered in this case.

The varied parameters were then randomly paired along with 15 ground motions (Tables 3.3 and 3.4) spectrally matched to a given target spectra. Thus a 10,000 realization Monte Carlo set has an average of 667 realizations for each ground motion. This procedure was applied to the four sets of 15 spectrally matched ground motions: 10,000-year NFGM and FFGM; and 30,000-year NFGM and FFGM (Figure 3.6).

Separate simulations varying the applied horizontal component (X or Y) and loading direction (horizontal only and horizontal and vertical) were conducted. Therefore, four loading conditions were considered: X only, X and Z, Y only and X and Z for each of the four sets of ground motions. Table 8.1 summarizes all the cases studied and variation in parameters, which resulted in 16 simulation cases run with 10,000 realizations.

8.2.1 Variation in Response for Individual Motions (Analysis I)

Figures 8.8 and 8.9 present variation in the absolute maximum rocking angles for each of 15 ground motions obtained from simulations carried out for the 4 ground motion sets (10,000- and 30,000-year NFGM and FFGM). Each figure presents the percentile distribution: 97.5th percentile, 50th percentile (median) and 2.5th percentile; and coefficient of variation (cov) for a particular excitation component (Table 8.1) of the 15 ground motions (average of 667 runs per ground motion). Table 8.2 presents the average maximum rocking angle and the cov, averaged from the values for the 15 motion for each simulation case. This analysis is designated as Analysis I.

Figure 8.8 shows the rocking angle dispersion when input parameters are varied according to Table 8.1, and only $\ddot{u}_g$= X is considered, while Figure 8.9 presents similar results under $\ddot{u}_g$ = X and $\ddot{v}_g$ = Z. As observed, small changes in the input parameters result in a large variation in the maximum rocking angle, which is reflected in a large cov. Note that the cov is consistently larger for FFGMs than for NFGMs, which may be caused by two factors: i) NFGMs have shorter durations of high energy content, and ii) NFGMs have one or two large cycles due to forward directivity effects. The former reason does not appear relevant after computing the Arias intensity (Ia) for both sets of records. The NFGM average duration based on this intensity is only 4.5 and 6 % lower than that of FFGMs for 10,000- and 30,000-year motions, see Figure 8.10. The main reason for a lower cov is the presence of forward directivity effects on one or both horizontal directions of NFGM acceleration records. As described in Section 3.2, NFGMs (and FFGMs) were rotated to reduce the correlation among the records, and even after this rotation, forward directivity effects are present in both independent directions, as evidenced by the presence of one or two large pulses in the examples presented in Figure 8.11. In total 10 of the 15 NFGM records show this trend. The spectrally matched records do not clearly show this trend, given that high frequencies are added to match the target spectrum.

In any case, the presence of a couple of dominant pulses in both horizontal directions is the main reason for the lower cov of this set of records, setting an analogy to the behavior of free-standing casks under horizontal sinusoidal pulses. As presented in Section 6.2.2, the cask response under unidirectional harmonic excitations is deterministic for the first 2-3 cycles. Thereafter, small variations in the system parameters lead to large differences in the maximum rocking angle. The main reason for the small cov of NFGMs is the presence of only a couple of strong cycles.

As expected, Figures 8.8 and 8.9, as well as Table 8.2, show that the 30,000-year events result in larger rocking angles for both sets of records. However, the variability expressed in the cov parameter is reduced, particularly for FFGMs. The main reason is that under smaller GMs the free-standing body may only be excited under certain system parameter values, leading to binary situations of moderate rocking in some realizations and practically no rotation in others (see for instance ground motions 11-13 in Figure 8.8a). On the other hand, the stronger motions associated to the 30,000-year events always create rotations that tend to be of the same order, reducing the cov.

8.2.2 Combined Variation in Response (Analysis II)

The previous section presented results for 10,000 realizations per simulation case grouped according to the individual motion. In this section the 10,000 realizations were considered as a single data set. This method of analysis method is designated as Analysis II. Although the 15 ground motions spectrally matched to a target spectra have the same spectral characteristics, including the PGA, they differ in duration and location of major pulses. The goal of Analysis II is to investigate the variation in rocking angle resulting from these different ground motions, even though they have the same spectra.

Figure 8.12 presents representative histogram plots of maximum rocking angle obtained from four Monte Carlo simulations (10,000 realizations each) for different spectrally matched records (X and Z direction of excitation). Figure 8.13 presents the cumulative probabilities (empirical, normal, and log-normal) for the same histogram plots shown in Figure 8.12. As observed, the application of FFGMs lead to larger maximum rocking angles, although FFGMs in this study have a smaller PGA than NFGMs (Table 6.1). Even though the average and median values of $\theta_{\max} / \alpha$ (Table 8.2) are larger for 10,000-year NFGMs compared to FFGMs, the possible maximum rocking angle is always larger for FFGM. This results in very large cov (normal distribution) and β (standard deviation of natural logarithm of values) for the 10,000-year FFGM. Table 8.2 also presents the cov (normal distribution) and β for Analysis II. A cov comparison for Analysis I and Analysis II results (Table 8.2) shows that when differences in ground motion characteristics are considered, the variation in maximum rocking response is twice as large, in general. This indicates that the differences in ground motions (having same spectral characteristics) results in greater distribution of the response.

8.2.3 Variation Comparison under Varied Scale Factor for Time

The results presented in Sections 8.2.1 and 8.2.2 correspond to an idealized 2D free-standing body with the same geometric details of FS.43 cask. The scale factor for ground motion time step was set to $1/\sqrt{N}$ assuming the body was 1:2.5 scale (Equation (6.5)). This section investigates the same variation in possible maximum rocking angle (as in Sections 8.2.1 and 8.2.2), however, the scale factor (N) in Equation (6.5) was set to 1.

The effect of changing this time scale factor on the spectra of ground motions has already been shown in Figure 6.17 (Section 6.4.1). With higher spectral acceleration in the longer period region, larger rocking angles should be expected. The goal is to compare the variation observed in rocking angles when $N = 2.5$ and 1, using the same parameters variation presented in Table 8.1.

Figures 8.14-8.16 present the percentile-cov plot, cumulative probability and histogram of the obtained maximum rocking angles when $N = 1$. Table 8.3 compares Analysis I and Analysis II average rocking angle, cov, and β ($\sigma_{\ln}$) when using different N values.

As expected, the average rocking angle increases when N decreases from 2.5 to 1. However, the cov and β do not change significantly, as shown in Table 8.3. One apparent exception, 30,000 FFGMs, shows increase in the variation, which is caused by a large number of overturning cases (10.7%). The overturning cases are the cases falling above the theoretical tip-over line in Figure 8.14 and the cases $\theta_{\max}/\alpha > 1$ in Figure 8.16. In any case, the dispersion parameters remain more or less stable, especially average cov calculated using the Analysis I method. Figure 8.14 shows that FFGMs consistently result in a large deviation around median values, while NFGMs result in comparatively limited variation with respect to median values. Only a single case (Motion 4) for 30,000-year NFGM has large variation with cov greater than 0.4.

8.2.4 Variation Comparison for Varied Parameter Change

To assess the sensitivity of the response to a different variation range in input parameters, Monte Carlo simulations were carried out for the 15 FFGMs (30,000-years), varying the parameters only ±0.1%, instead of ±1%, under a constant dt of 10^{-4}. Table 8.4 summarizes four cases used for comparison. In Table 8.4, the designation or the nomenclature used for cases studied in this subsection is explained in the following:

i. Case N2.5-1: In this case, the scale factor N is set to 1, while parameters are varied by ± 1% and dt is varied from 10^{-3} to 10^{-4} s (baseline case).

ii. Case N2.5-0.1: In this case, the scale factor N is set to 2.5, while parameters are varied by ± 0.1% and dt is varied from 10^{-3} to 10^{-4} s.

iii. Case N2.5-1C: In this case, the scale factor *N* is set to 2.5, while parameters are varied by ± 0.1% and *dt* remains unchanged as 10^{-4} s.

iv. Case N1-1: In this case, the scale factor *N* is set to 1, while parameters are varied by ± 1% and *dt* is varied from 10^{-3} to 10^{-4} s.

Figures 8.17-8.19 compare the distribution of maximum rocking angle obtained for different cases of 30,000-year FFGM Monte Carlo runs. Figure 8.17 shows very similar rocking angle distributions for cases N2.5-1, N.25-0.1 and N.25-1C (Table 8.4). The cov curve for these cases is also almost identical. Similar observations can be made for the cumulative probability distributions and the histogram plots of these three cases (Figure 8.18 and Figure 8.19, respectively). The fourth case, N1-1 has different probability distribution and histogram, because this is the run where the ground motion time step is different after modifying the scale factor to $N = 1$. However, the cov plot for N1-1 is not very different from those of the other three cases (Figure 8.17). The average cov for all cases (determined as per Analysis I) is similar too. It appears that the average cov remains stable for ground motions spectrally matched to a particular target spectrum.

Table 8.5 presents the average cov (Analysis I) and cov and β (Analysis II) obtained for these cases. The figures and table show that changing the parameters by ±0.1% and not including the variation in the solution time step results in the similar cov and β. These results suggest that for the given spectrally matched ground motions the variability in the possible response of free-standing body can be bounded using the obtained cov and β (assuming normal and log-normal distribution, respectively). For any given ground motion, spectrally matched to the target spectra (30,000-year FFGM, Figure 3.6b), a cov of 0.24 can be used to determine upper and lower bound maximum response of a free-standing body. More research is needed for system parameters and ground motions (consistent with spectral characteristics other than that developed for WUS rock) not considered in this research.

8.3 Probabilistic Variation of Parameters

The COR (*e*) and PGA parameters can have a large uncertainty. Although the ground motions used in this study (a set of 15 motions) were spectrally matched to a target spectra for a particular return period and a specific characteristic, in previous sections results show that smallest change in the PGA and also ground motion itself resulted in large variation in the maximum rocking angle. In this section the two parameter COR (*e*) and PGA are varied log-normally to study the variation obtained from these changes. One additional parameter whose distribution can be estimated using normal distribution is coefficient of friction (μ_s) [19]. However, the analytical model used in this study is for idealized rocking-only motion. Therefore variation in the coefficient of friction is not considered.

8.3.1 Log-Normal Variation of COR only

Experiments show that even for free-rocking, *e* has different value at each impact. For this study *e* was assumed to have a log-normal distribution. To cover a range of possible values of *e*, it is assumed to have a log-normal variation around a median value. The median *e* was assumed to be the experimentally determined *e*. The following steps were taken to generate log-normally distributed random values of *e*, and at the same time prevent very large values (greater than or equal to 1):

i. The mean COR ($\bar{e}$) for FS.43 was experimentally determined as 0.872, and the coefficient of variation (cov) for this specific case was approximated as 0.1. For more general conditions, a cov = 0.2 was adopted to account for additional uncertainties due to variations on system specifications. Based on the data, the standard deviation and variance are obtained as:

$$\begin{aligned} \sigma &= \bar{e} * \mathrm{cov} = 0.1744 \\ Var &= \sigma^2 = 0.030 \end{aligned} \tag{8.2}$$

ii. The log-normally distributed random values for the parameter $e' = (1-e)$ are obtained, where e' can be considered as complementary e value and is assumed to be a median value.

$$\begin{aligned} & median(e') = 1 - \bar{e} \\ & \overline{\ln e'} = \ln(median(e')) \qquad \text{[= Mean of logarithm of} e'] \\ & \sigma_{\ln} = \sqrt{\ln\left(\frac{1+Var}{\bar{e}}\right)} = 0.198 \end{aligned} \tag{8.3}$$

iii. Random e' normally distributed values are generated with mean and standard deviation ($\overline{\ln e'}$ and $\sigma_{\ln}$, respectively) within ±3 $\sigma_{\ln}$.

iv. Finally, the required coefficient of restitution values are obtained as,

$$e = 1 - \exp(e') \tag{8.4}$$

Figure 8.20 shows the generated log-normally distributed e with median value of 0.872, while Monte Carlo simulation (10,000 realizations) were generated by randomly paring the probabilistically varied PGA and e with the ground motions. Other parameters, such as p

(2.37 rad/s), dt (10^{-4} s) and θ_0 (set to 0) were not varied.

Figures 8.21-8.23 compare the maximum rocking angle and its distribution for individual motions and ground motion sets, similar to Section 8.2. The figures show similar distributions of maximum rocking angle, as those observed in Figures 8.9, 8.12 and 8.13 (for ±1% variation of all parameters, designated as Baseline Case). Table 8.6 summarizes the dispersion measures obtained for this study. Comparing results shown in Table 8.6 to the corresponding results (results for same ground motion set and excitation condition) of Table 8.2 (also summarized in Table 8.3 as $N = 2.5$-baseline case), it can be observed that average maximum rocking angles are similar. For ease of comparison the results for baseline case are again presented in Table 8.6. It can be seen that the dispersion parameters cov (Analysis I and Analysis II) and β, are slightly larger (2%-25%) than those of the baseline case.

The comparison also shows that the response dispersion can be easily captured using the later approach of changing the parameters by a small amount. This finding is unusual and suggests the chaotic nature of the problem, given that minute changes in input parameters result in similar response dispersion than large input parameter variation, and it is comparable to the results of the first two cases of Table 8.5 where variation of input parameters was changed from ±1% to ±0.1%.

Finding similar dispersion of rocking angle obtained for log-normal distribution of e and baseline case performed in Section 8.2, analyses were also performed for ±1% change in e only, while keeping the other parameters constant. These parameters were set to $\alpha = 0.41$, $p = 2.37$, $dt = 10^{-4}$, $\theta_0 = 0$. The objective of this simulation was to study the influence of coefficient of restitution, alone and the resulting dispersion of rocking angle from it. The results from this analysis is also presented in Table 8.6. Comparison of results for ±1% change in *e* (only) to the base line case, where all the parameters were varied by the same ±1% show that all ground motion sets have similar dispersion parameter obtained both from Analysis I and Analysis II, with the exception of 10,000-year FFGM. For the 10,000-year FFGM motion set, the average cov (Analysis I) is almost half of that obtained from log-normal distribution of *e* for every motion set. However, the cov and β (Analysis II), are again very similar. This suggests that different ground motions, although spectrally matched, have a larger influence on the response variation compared to *e*.

8.3.2 Log-Normal Variation of PGA only

The results from Section 8.2 show that even minor changes in PGA and variation in ground motion (even though they were spectrally matched to same target spectra) resulted in large range of possible maximum rocking angle of the system. It should also be noted that the target spectra developed for this study is for WUS Rock sites. However, characteristics and PGA of the next earthquake are not known in advance. In this section effect of PGA of spectrally matched ground motion set is varied log-normally to represent such uncertainty. PGA for each spectra given in Table 3.5, was taken as median value and was varied assuming $\sigma_{\ln} = 0.2$. The generated distribution was truncated at $\pm 2\sigma_{\ln}$.

Figure 8.24 presents the histogram of generated PGA distribution for each target spectra (10,000- and 30,000-year NFGM and FFGM). The histogram presents 10,000 values of log-normally distributed PGA for each return period and spectra. Similar log-normally distributed PGA for vertical component were also generated. Monte Carlo simulation were also performed for this case by randomly pairing the individual ground motion from the set of spectrally matched motions (set of 15 motions for each spectra) with the generated horizontal and vertical PGA values. The motions were then linearly scaled to the PGA values.

The obtained distribution of maximum rocking for Analysis I and Analysis II are presented in Figures 8.25-8.27. Figure 8.25 presents the percentile plot for individual ground motions. Compared to Figures 8.9, 8.17 and 8.21 the range of maximum rocking angle is lager in Figure 8.25. Figures 8.26 and 8.27 also the increase in the range of maximum rocking angle obtained from the log-normal variation of PGA. The average cov (Analysis I), also presented in Table 8.7, is also increased by almost two times compared to Figures 8.9, 8.17 and 8.21 (Tables 8.2, 8.3 and 8.6). This increase in average cov is consistent with increase in cov in Analysis II where variation in ground motion is considered. The reason for such a large increase in average cov is that varying PGA log-normally introduces record-to-record variability which is similar to the effect of considering the different ground motions in Analysis II.

Varying the 15 ground motions in this case (shown in Analysis II, Table 8.7) does not show large in the cov compared to average cov (Analysis I). Although there is increase (21%-33%) in cov (Analysis II) compared to average cov (Analysis I), the increase is not as large as other cases (Tables 8.2, 8.3 and 8.6). However, it should be noted that cov and β (Analysis II) shown in Table 8.7 is on average 47% larger than those reported in Tables 8.2, 8.3 and 8.6.

Figure 8.28 compares average cov (Analysis I) and cov, β (Analysis II) for all Monte Carlo runs. The nomenclature in Figure 8.28 for different Monte Carlo runs is described in the following:

i. MC 1: Monte Carlo simulation with parameters: $\ddot{u}_g = X, \ddot{v}_g = Z$, $e = 0.872 \pm 1\%$, $p = 2.37 \pm 1\%$, $dt = 10^{-3}$ to 10^{-4}, $\theta_0 = 10^{-3}$ to 10^{-4}, PGA ± 1%, N = 2.5

ii. MC 2: Monte Carlo simulation with parameters: $\ddot{u}_g = X, \ddot{v}_g = Z$, $e = 0.872 \pm 1\%$, $p = 2.37 \pm 1\%$, $dt = 10^{-3}$ to 10^{-4}, $\theta_0 = 10^{-3}$ to 10^{-4}, PGA ± 1%, N = 1.0

iii. MC 3: Monte Carlo simulation with parameters: $\ddot{u}_g = X, \ddot{v}_g = Z$, log-normal variation of (Median $e = 0.872$, cov = 0.2), $p = 2.37$, $dt = 10^{-4}$, $\theta_0 = 0$, N = 2.5

iv. MC 4: Monte Carlo simulation with parameters: $\ddot{u}_g = X, \ddot{v}_g = Z$, $e = 0.872 \pm 1\%$, $p = 2.37$, $dt = 10^{-4}$, $\theta_0 = 0$, N = 2.5

v. MC 5: Monte Carlo simulation with parameters: $\ddot{u}_g = X, \ddot{v}_g = Z$, $e = 0.872$, $p = 2.37$, $dt = 10^{-4}$, $\theta_0 = 0$, N = 2.5, log-normal variation of PGA ($\sigma_{\ln} = 0.2$, $\pm 2\sigma_{\ln}$)

Figure 8.28 shows that all three variation measures remain almost constant for all simulation cases, except MC 5, i.e., for log-normal variation of PGA. For the MC 5 case, the average cov (Analysis I) show a large increase compared to the other four Monte Carlo runs. It can also be seen that the average cov (Analysis I) for MC 5 is similar in values to the cov (Analysis II) of MC 1-MC4. This shows that log-normal variation of PGA has the same effect of changing the ground motions within the spectrally matched set. The figure also shows that the effect of ground motion variation is dominant over the variation of other parameters. However for a given ground motion the response variation due to small changes in parameters cannot be ignored.

Results from analytical models (like SRM used in this chapter) or FEM (Chapter 6 and 7) are usually considered deterministic. Although almost all previous studies agree on the high sensitivity of the models' response to initial conditions, most studies usually ignore the fact that the parameters used in the models themselves have uncertainty in them. Parameter like coefficient of restitution is not always a constant value but differs for every impact and like coefficient of friction that can differ from one location to other even for same contacting surfaces. These variations in in-situ conditions make the exact reproduction of experimental results and deterministic prediction of response time history nearly impossible. Therefore statistical or probabilistic approach to the response of free-standing bodies like DSCs is a much better approach.

8.4 Supplementary Monte Carlo Simulations (Erzican and Chi-Chi Motions)

Supplementary Monte Carlo realizations for the two main ground motions selected for experimental tests, and FE simulations Erzican and Chi-Chi (10,000- and 30,000-year return period), were also performed. These runs included ±1% variation of parameters, probabilistic variation of COR (*e*), and PGA (assuming log-normal distribution for both parameters). The final supplementary case utilized convolved Erzican and Chi-Chi soil motions at the surface instead of rock motions for both ± 1% variation and probabilistic variation of *e* and PGA. These runs were subdivided into three cases: Supplementary Run I (SR-I), Supplementary Run II (SR-II) and Supplementary Run III (SR-III). Detailed discussion of the parameter variation considered and results obtained from these runs are presented in Appendix C.

8.5 Discussion of Results

This chapter investigated the response of a simple rocking system under seismic loading, specifically the sensitivity and the variation in the response caused by minute changes in input parameters. Monte Carlo simulations with 10,000 realizations for each case were performed to study the variation in response. Four target response spectra for WUS rock sites were generated and two sets of ground motions were spectrally matched to the respective response spectra. The rocking body was subjected to minute variation (±1%) in input parameters to obtain the variation in absolute maximum rocking angle. The main findings study can be summarized as follows:

i. The coefficient of restitution (*e*) used in this study was experimentally determined and was 14.5% larger than that estimated by equation conventionally used for simple rocking motion. This finding is consistent with previous studies.

ii. Monte Carlo simulation results indicate that differences as small as ±0.1% in system parameters, such as coefficient of restitution (*e*), frequency parameter (*p*), and peak ground acceleration (PGA) could result in large variation in the response.

iii. The response of two-dimensional blocks was tested to detect chaotic behavior, using phase-plane plots, Fourier spectra, and Poincaré sections. The results show that 2D blocks subjected to simple rocking under horizontal sinusoidal motions have a repeatable response. However, 2D blocks subjected to rocking under horizontal and vertical accelerations exhibit lack of repeatability and chaotic response.

iv. The results show that when an actual ground motion is applied, the presence of vertical accelerations is not necessary to produce lack of repeatability in the response.

v. The maximum rocking angle distribution for individual ground motions within a particular target spectra showed that the average cov had a range of 0.44-0.52 and 0.14-0.23 for FFGMs (10,000- and 30,000-year return period, respectively); 0.13-0.17 and 0.13-0.2 for NFGMs (10,000- and 30,000-year return period, respectively). These large variations are not expected in conventional anchored systems subjected to dynamic loading.

vi. When the variation in the ground motion (differences in actual time history, number of pulses and location, etc.) within a spectrally matched set (having same spectral characteristics) was considered, the cov doubled for almost every case.

vii. Analyses were conducted for varied change in parameters (N2.5-1, N2.5-0.1, N2.4-1C and N1-1) varied time scale factor (Section 8.2.3) set as $N = 2.5$ and 1. They indicate that the dispersion parameters: cov (Analysis I) and cov and β (Analysis II) to be relatively stable for ground motions with a given spectra. For instance, a ground motion spectrally matched to the 30,000-year spectra has an average cov of 0.24. This cov could be used to determine the bounds to possible rocking angles.

viii. Varying the coefficient of restitution log-normally resulted in similar dispersion parameters to those obtained from varying all the parameter by ±1%. While, log-normal variation of PGA resulted in similar dispersion as obtained from Analysis II (considering variation in ground motions) for other Monte Carlo simulations that include small variation of parameters and log-normal variation of *e*.

ix. Supplementary Monte Carlo simulations performed for Erzican and Chi-Chi motions show similar variability for individual ground motions and a 6.3%

probability of overturning of FS.43 casks under 30,000-year Chi-Chi (soil motion) even for ±1% parameter variation.

Table 8.1. Parameters considered and variation range for Monte Carlo runs (r/h_{cg} = 0.43)

Ground Motion Set	Excitation Component		COR (e)	p	PGA *	dt (s)	θ_0 (rad)
	$\ddot{u}_g$	$\ddot{v}_g$					
10,000-year FFGM	X	-	0.872 ± 1%	2.37 ± 1%	±1%	10^{-3} to 10^{-4}	±0.004
10,000-year NFGM	X	Z	0.872 ± 1%	2.37 ± 1%	±1%	10^{-3} to 10^{-4}	±0.004
30,000-year FFGM	Y	-	0.872 ± 1%	2.37 ± 1%	±1%	10^{-3} to 10^{-4}	±0.004
30,000-year NFGM	Y	Z	0.872 ± 1%	2.37 ± 1%	±1%	10^{-3} to 10^{-4}	±0.004

* Note: PGA was varied by linearly scaling the ground motion by scale factor = 1 + (% change)

Table 8.2. Variation in maximum rocking angle (θ_{max}/α) and coefficient of variation

Spectra	Excitation Component	Analysis I		Analysis II			
		Avg. ($\theta_{\max}/\alpha$)	Avg. cov	Normal Distribution		Log-normal Distribution	
				μ	cov	Median = $\exp(\mu_{\ln})$	$\beta = \sigma_{\ln}$
10,000-year FFGM	X	0.027	0.461	0.027	1.212	0.014	1.127
	XZ	0.040	0.451	0.040	0.853	0.027	1.006
	Y	0.020	0.436	0.020	0.853	0.013	1.046
	YZ	0.035	0.401	0.035	0.677	0.026	0.868
10,000-year NFGM	X	0.042	0.138	0.042	0.331	0.040	0.353
	XZ	0.051	0.174	0.051	0.380	0.047	0.408
	Y	0.044	0.126	0.044	0.315	0.041	0.337
	YZ	0.047	0.125	0.047	0.245	0.046	0.257
30,000-year FFGM	X	0.134	0.202	0.134	0.382	0.124	0.399
	XZ	0.163	0.233	0.163	0.487	0.146	0.477
	Y	0.113	0.135	0.113	0.530	0.099	0.500
	YZ	0.126	0.207	0.126	0.494	0.113	0.481
30,000-year NFGM	X	0.073	0.129	0.073	0.316	0.069	0.331
	XZ	0.088	0.169	0.088	0.354	0.083	0.372
	Y	0.071	0.168	0.071	0.307	0.067	0.352
	YZ	0.087	0.196	0.087	0.375	0.081	0.380

Table 8.3. Comparison of variation in maximum rocking angle ($\theta_{\max}/\alpha$): *N*=1 and 2.5

Spectra	Excitation	Analysis I		Analysis II			
		Avg. ($\theta_{\max}/\alpha$)	Avg. cov	Normal Distribution		Log-normal Distribution	
				μ	cov	Median = exp($\mu_{\ln}$)	β = $\sigma_{\ln}$
***N* = 2.5 (Baseline)**							
10,000 FFGM	XZ	0.040	0.451	0.040	0.853	0.027	1.006
10,000 NFGM	XZ	0.051	0.174	0.051	0.380	0.047	0.408
30,000 FFGM	XZ	0.163	0.233	0.163	0.487	0.146	0.477
30,000 NFGM	XZ	0.088	0.169	0.088	0.354	0.083	0.372
***N* = 1.0**							
10,000 FFGM	XZ	0.110	0.432	0.111	0.910	0.064	1.203
10,000 NFGM	XZ	0.130	0.163	0.129	0.400	0.119	0.423
30,000 FFGM	XZ	0.565	0.289	0.565	0.666	0.467	0.606
30,000 NFGM	XZ	0.233	0.156	0.233	0.404	0.215	0.408

Table 8.4. Parameters variation for different cases of Monte Carlo runs: 30,000-year FFGM

Ground Motion Set	Case	*N*	*e*	*p*	PGA*	*dt* (s)	θ_0 (rad)
30,000-year FFGM (X and Z)	N2.5-1	2.5	0.872 ± 1%	2.37 ± 1%	±1%	10^{-3} to 10^{-4}	±0.004
	N2.5-0.1	2.5	0.872 ± 0.1%	2.37 ± 0.1%	±0.1%	10^{-3} to 10^{-4}	±0.0004
	N2.5-1C	2.5	0.872 ± 1%	2.37 ± 1%	±1%	10^{-4} (Const.)	±0.004
	N1-1	1	0.872 ± 1%	2.37 ± 1%	±1%	10^{-3} to 10^{-4}	±0.004
* Note: PGA was varied by linearly scaling the ground motion by scale factor = 1 + (% change)							

Table 8.5. Results for different cases of Monte Carlo runs: 30,000-year FFGM

30k FFGM XZ Analysis Case	Analysis I		Analysis II			
			Normal Distribution		Log-normal Distribution	
	Avg. $(\theta_{\max}/\alpha)$	Avg. cov	μ	cov	Median = $\exp(\mu_{\ln})$	$\beta = \sigma_{\ln}$
N2.5-1 (baseline)	0.163	0.233	0.163	0.487	0.146	0.477
N2.5-0.1	0.163	0.218	0.163	0.478	0.147	0.473
N2.5-1C	0.161	0.237	0.161	0.503	0.143	0.494
N1-1	0.565	0.289	0.563	0.666	0.467	0.606

Table 8.6. Maximum rocking angle dispersion: Log-normally distributed *e* (cov =0.2) and, $p = 2.37$, $dt = 10^{-4}$, $\theta_0 = 0$; $\ddot{u}_g =$ X, $\ddot{v}_g =$ Z

Spectra	Excitation	Analysis I		Analysis II			
				Normal Distribution		Log-normal Distribution	
		Avg. (θ_{max}/α)	Avg. cov	μ	cov	Median = $\exp(\mu_{\ln})$	$\beta = \sigma_{\ln}$
Log-normal distribution of *e* (cov = 0.2)							
10,000 FFGM	XZ	0.042	0.546	0.042	0.911	0.023	1.265
10,000 NFGM	XZ	0.051	0.208	0.051	0.390	0.047	0.421
30,000 FFGM	XZ	0.164	0.313	0.164	0.530	0.144	0.526
30,000 NFGM	XZ	0.088	0.197	0.088	0.370	0.082	0.380
***N* = 2.5 (Baseline)**							
10k FFGM	XZ	0.040	0.500	0.040	0.853	0.027	1.006
10k NFGM	XZ	0.051	0.174	0.051	0.380	0.047	0.408
30k FFGM	XZ	0.163	0.233	0.163	0.487	0.146	0.477
30k NFGM	XZ	0.088	0.169	0.088	0.354	0.083	0.372
±1% variation of *e* (only)							
10k FFGM	XZ	0.039	0.287	0.039	0.907	0.023	1.180
10k NFGM	XZ	0.051	0.124	0.051	0.393	0.047	0.425
30k FFGM	XZ	0.164	0.221	0.164	0.497	0.145	0.491
30k NFGM	XZ	0.088	0.118	0.088	0.347	0.083	0.355

Table 8.7. Maximum rocking angle dispersion: log-normally distributed PGA ($\sigma_{\ln}$ = 0.2, ± 2$\sigma_{\ln}$), p = 2.37, $dt = 10^{-4}$, θ_0 =0; $\ddot{u}_g$ = X, $\ddot{v}_g$ = Z

Spectra	Excitation	Analysis I		Analysis II			
		Avg. (θ_{max}/α)	Avg. cov	Normal Distribution		Log-normal Distribution	
				μ	cov	Median = exp($\mu_{\ln}$)	$\beta = \sigma_{\ln}$
Log-normal distribution of PGA ($\sigma_{\ln}$ = 0.2, ± 2$\sigma_{\ln}$)							
10,000 FFGM	XZ	0.048	0.775	0.048	1.023	0.018	1.963
10,000 NFGM	XZ	0.048	0.444	0.048	0.537	0.042	0.595
30,000 FFGM	XZ	0.173	0.556	0.173	0.742	0.134	0.758
30,000 NFGM	XZ	0.092	0.377	0.092	0.462	0.082	0.486

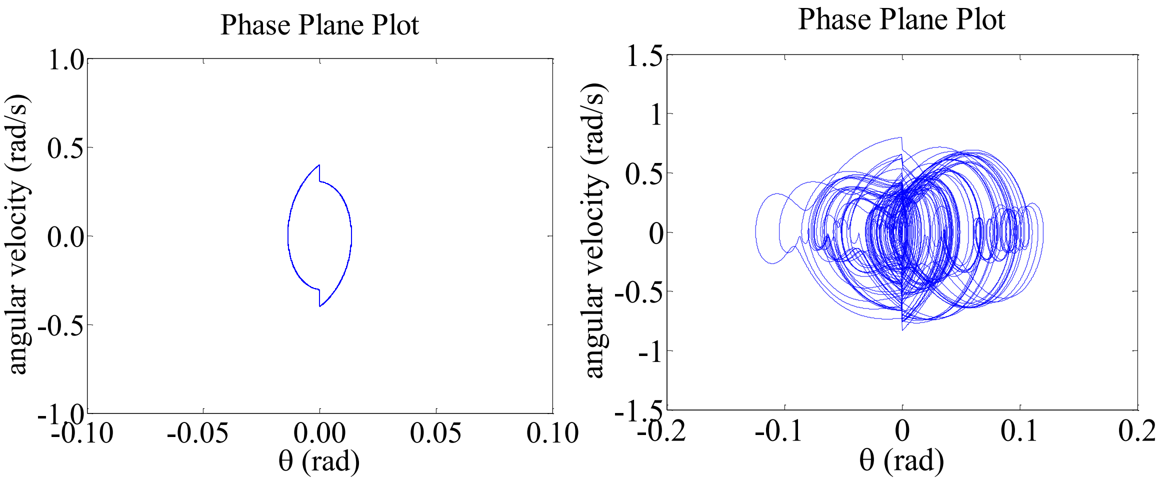

Figure 8.1. Example of phase plane plots: period motion (left), chaotic trajectory (right)

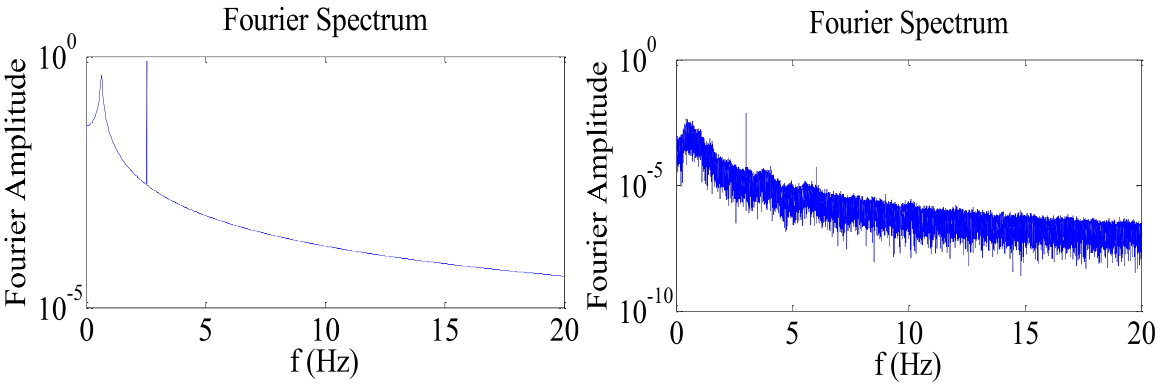

Figure 8.2. Example of Fourier spectra plots: period motion (left), chaotic trajectory (right)

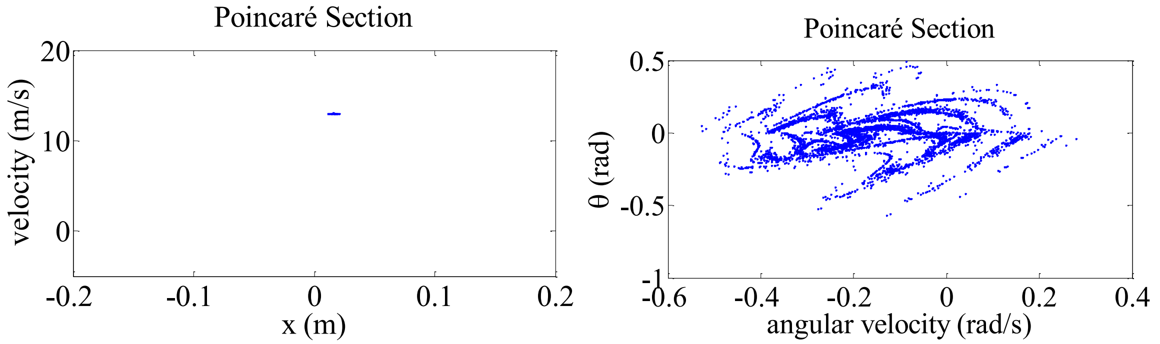

Figure 8.3. Example of Poincaré sections: period motion (left), chaotic trajectory (right)

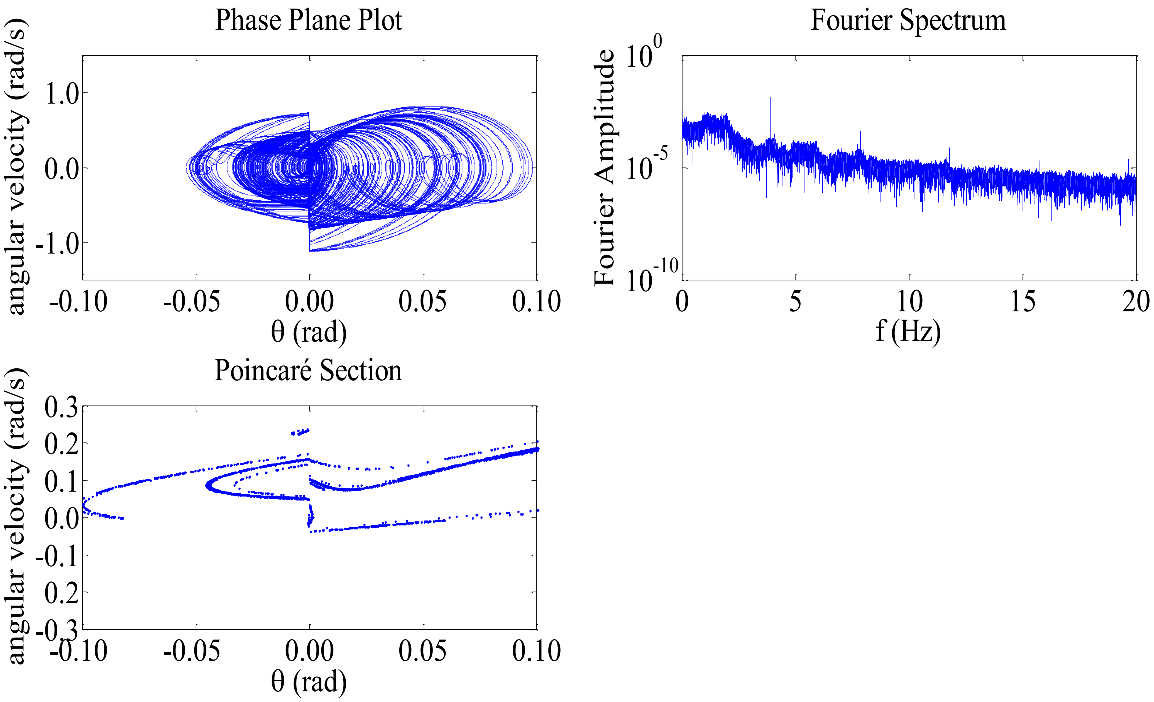

Figure 8.4. Chaos analysis plots FS.55: $A_h = 3$, $A_v = 2.5$, $\Omega = 10$, $e = 0.655$, $p = 2.47$

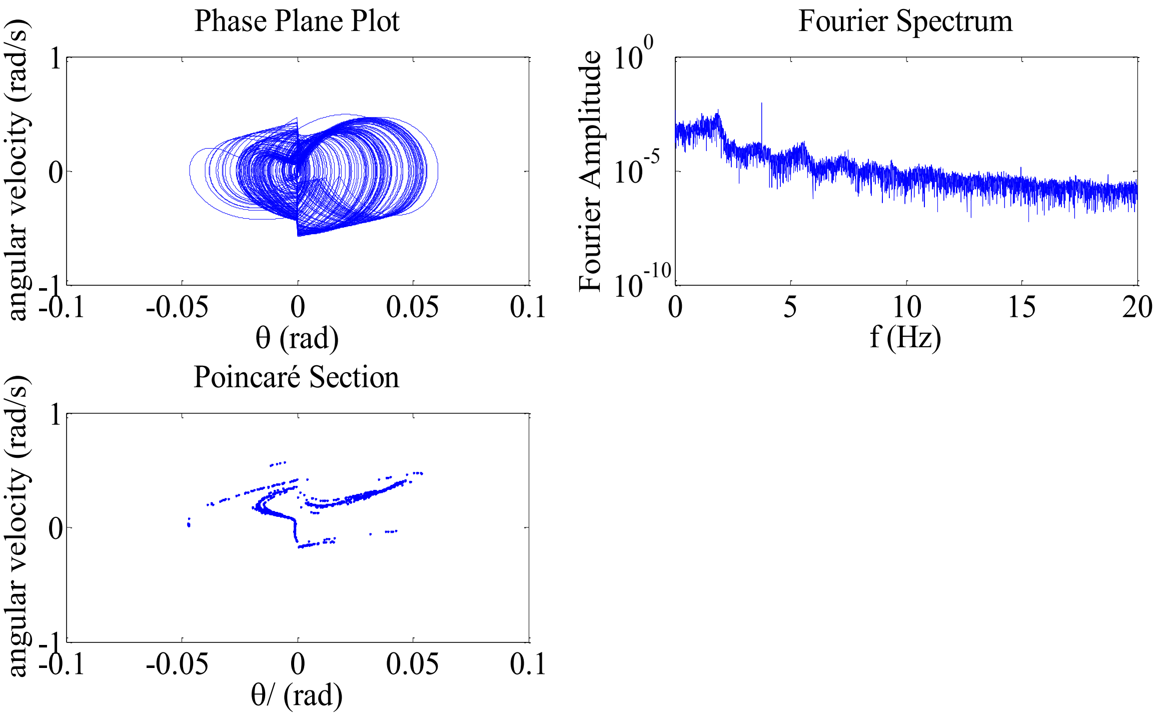

Figure 8.5. Chaos analysis plots FS.43: $A_h = 2.5$, $A_v = 2.0$, $\Omega = 10$, $e = 0.761$, $p = 2.37$

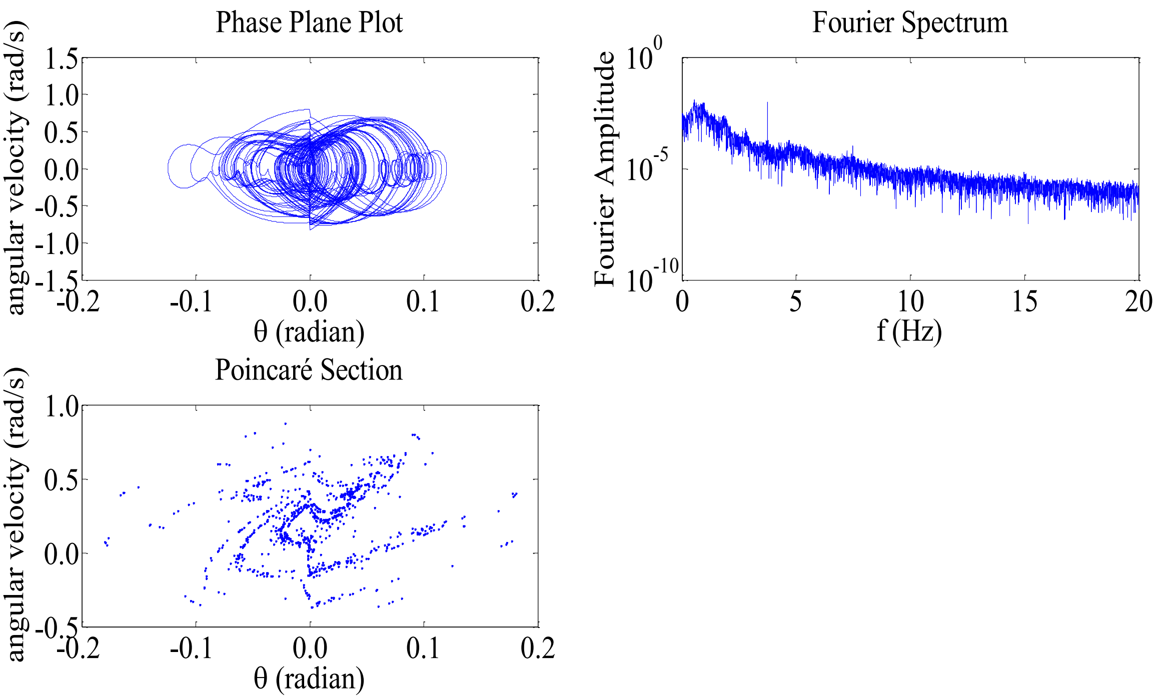

Figure 8.6. Chaos analysis plots FS.43: $A_h = 2.5$, $A_v = 2.0$, $\Omega = 10$, $e = 0.872$, $p = 2.37$

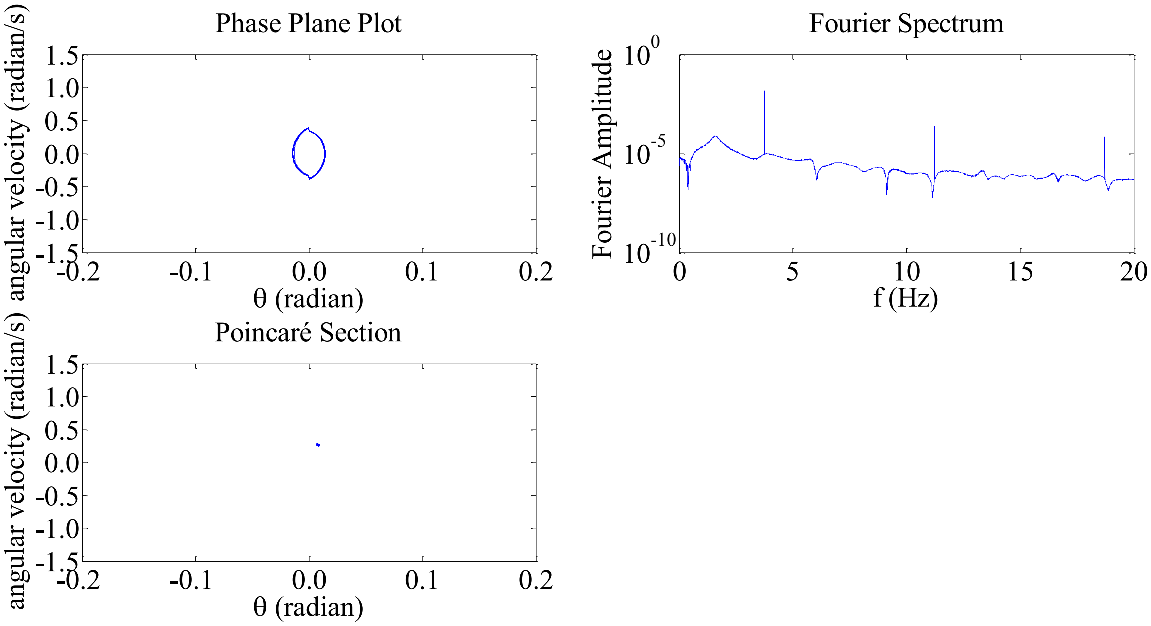

Figure 8.7. Chaos analysis plots FS.55: $A_h = 2.5$, $A_v = 0$, $\Omega = 10$, $e = 0.655$, $p = 2.47$

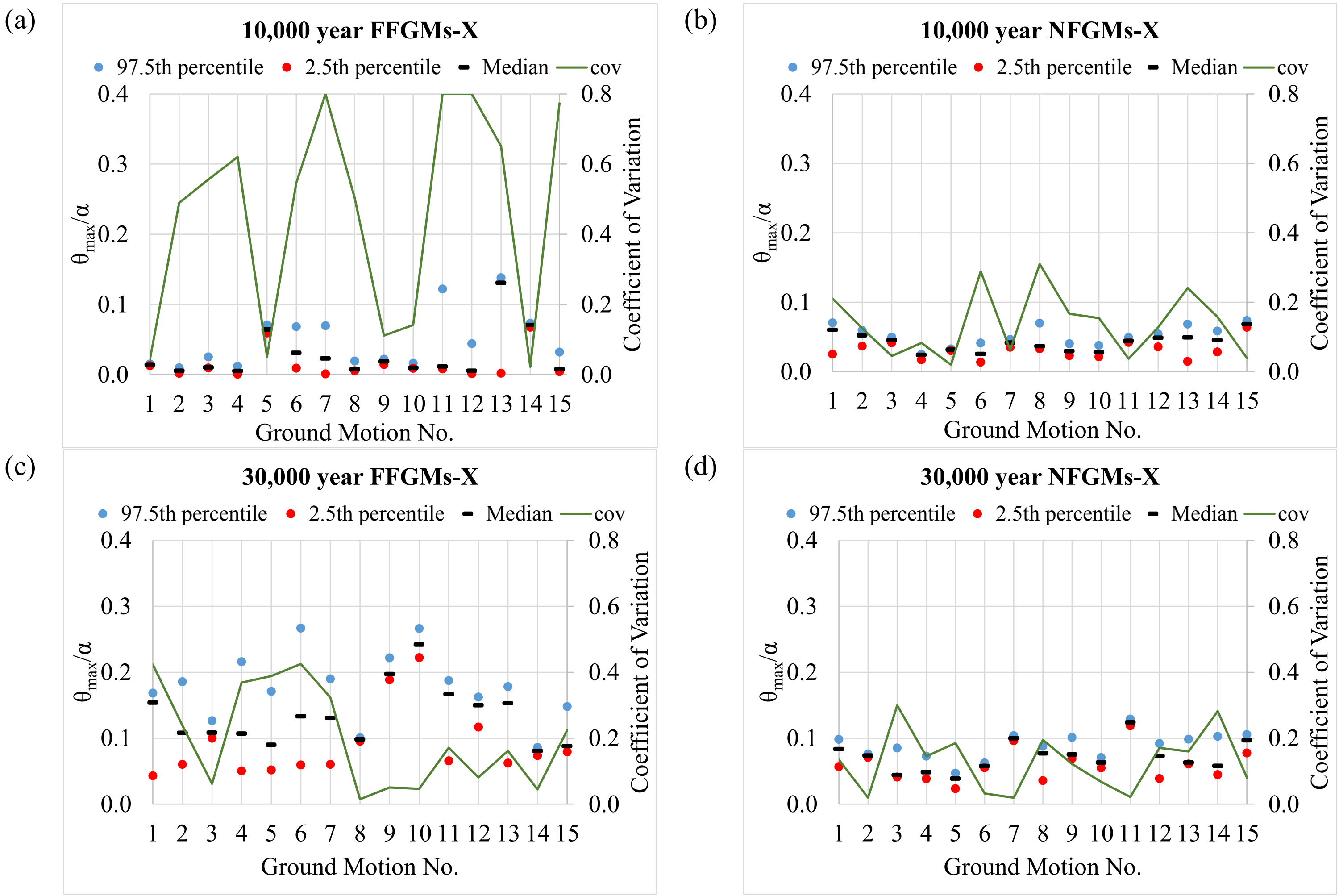

Figure 8.8. Percentile distribution and COV: $\ddot{u}_g = X$, $\ddot{v}_g = 0$ [$e = 0.872 \pm 1\%$, $p = 2.37 \pm 1\%$, $dt = 10^{-3}$ to 10^{-4}, $\theta_0 = 10^{-3}$ to 10^{-4}, PGA ± 1%]

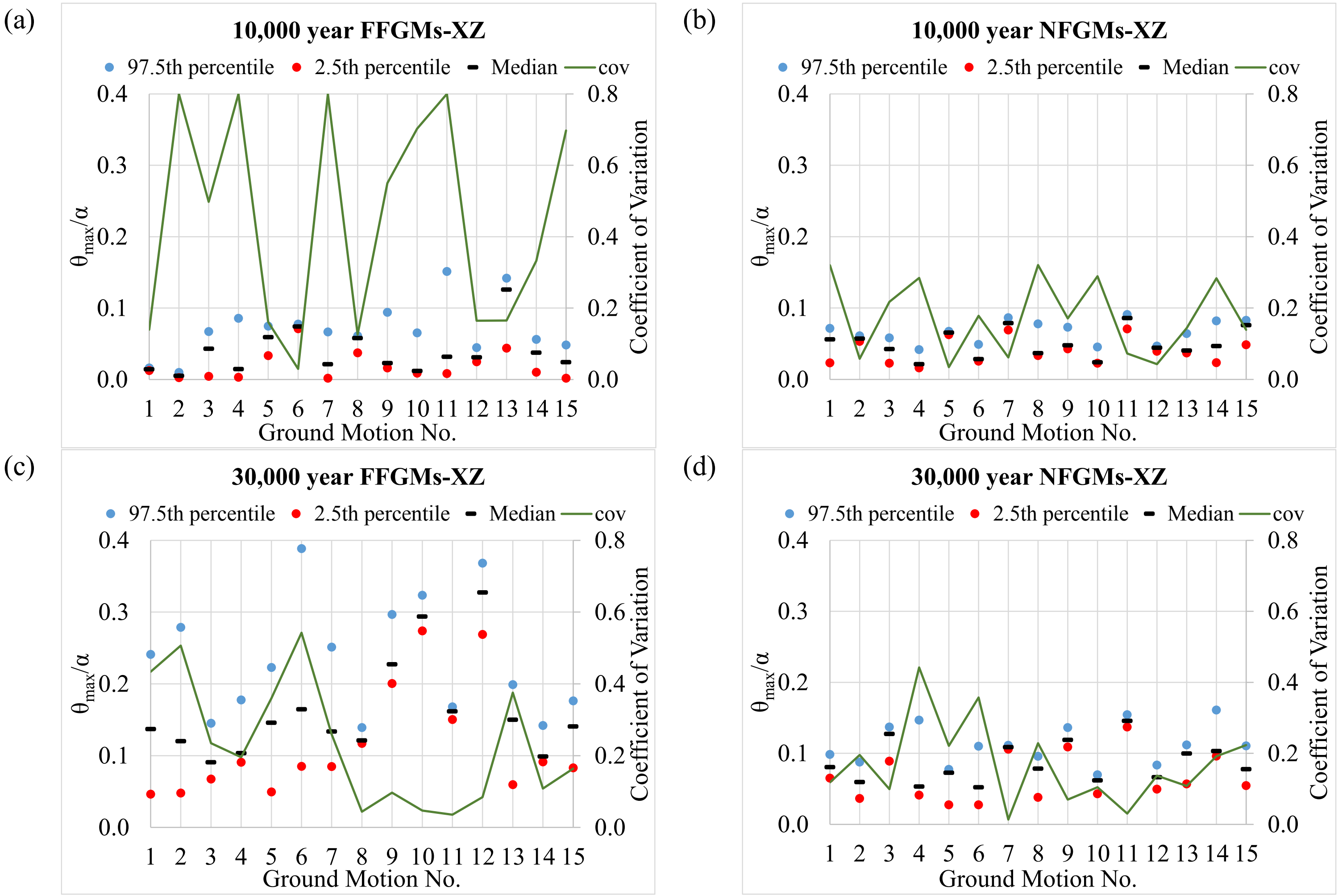

Figure 8.9. Percentile distribution and COV: $\ddot{u}_g$ = X, $\ddot{v}_g$ = Z [$e = 0.872 \pm 1\%$, $p = 2.37 \pm 1\%$, $dt = 10^{-3}$ to 10^{-4}, $\theta_0 = 10^{-3}$ to 10^{-4}, PGA ± 1%]

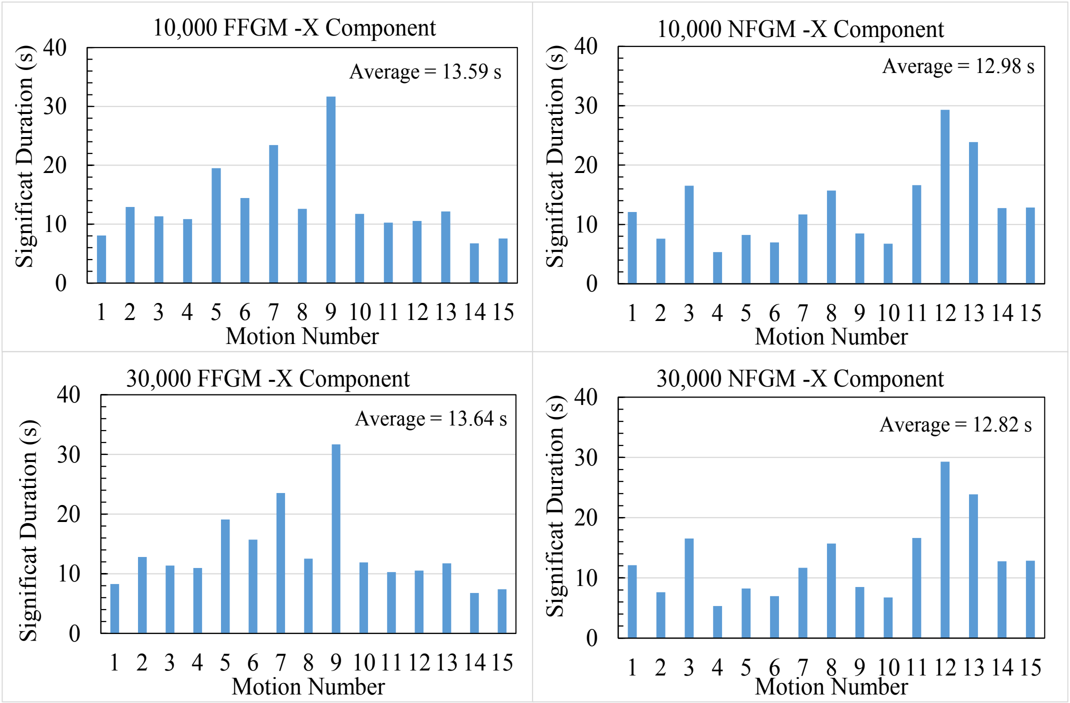

Figure 8.10. Significant duration (5%-95% arias intensity, Ia) of spectrally matched ground motions

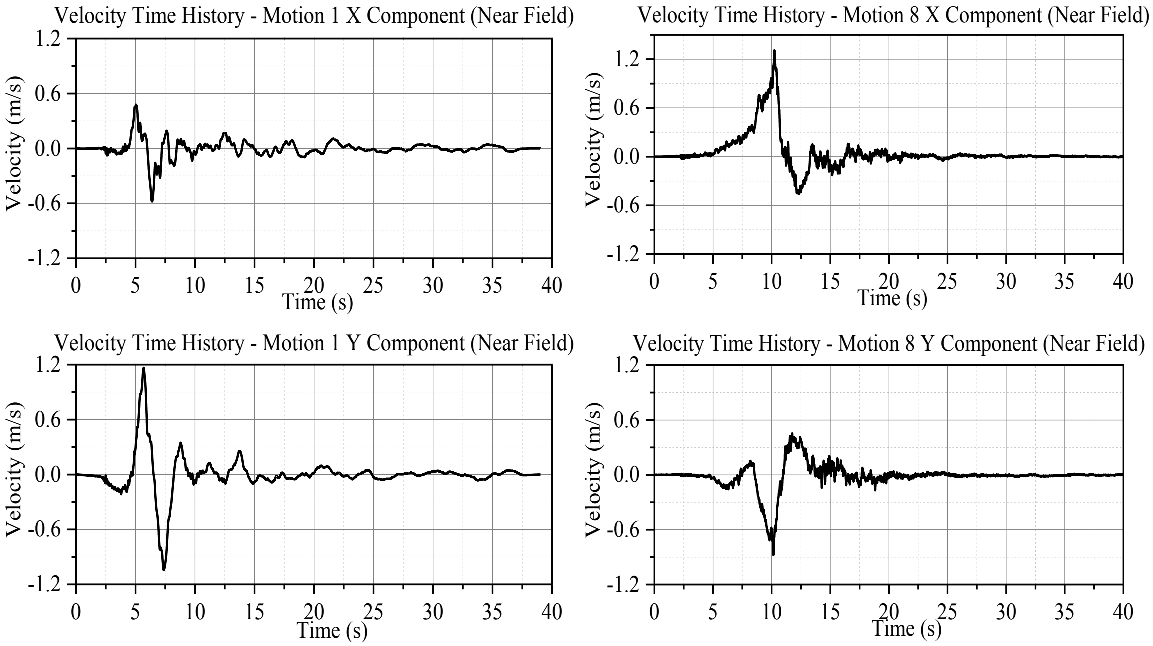

(a) (b)

Figure 8.11. Velocity time history of rotated near field record set: (a) Motion 1, (b) Motion 8

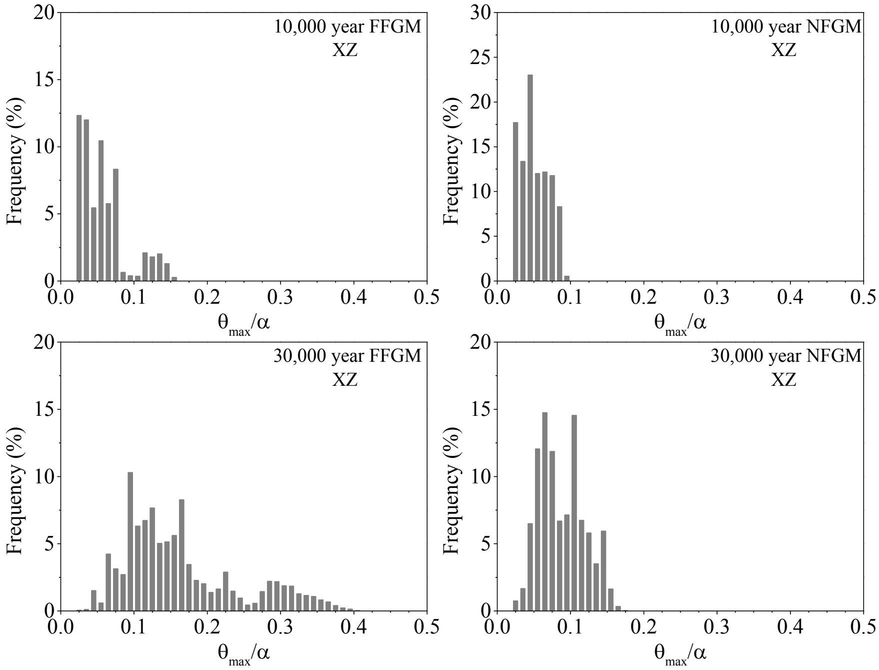

Figure 8.12. Maximum rocking angle distribution for a rocking block: (α = 0.41, XZ excitation); [e = 0.872 ± 1%, p = 2.37 ± 1%, dt = 10^{-3} to 10^{-4}, θ_0 =10^{-3} to 10^{-4}, PGA ± 1%]

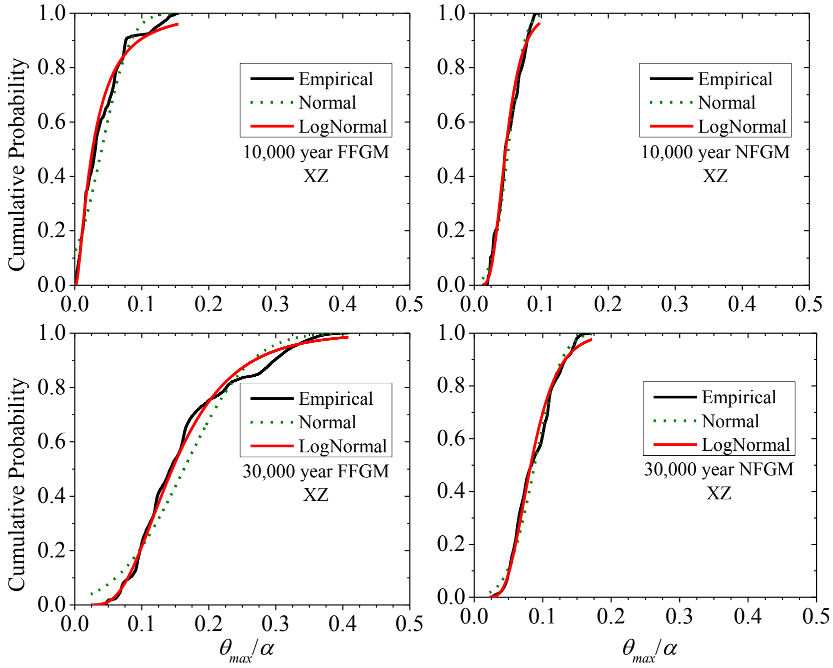

Figure 8.13. Cumulative probability distribution of maximum rocking angle (α = 0.41, XZ excitation) [e = 0.872 ± 1%, p = 2.37 ± 1%, dt = 10^{-3} to 10^{-4}, θ_0 =10^{-3} to 10^{-4}, PGA ± 1%]

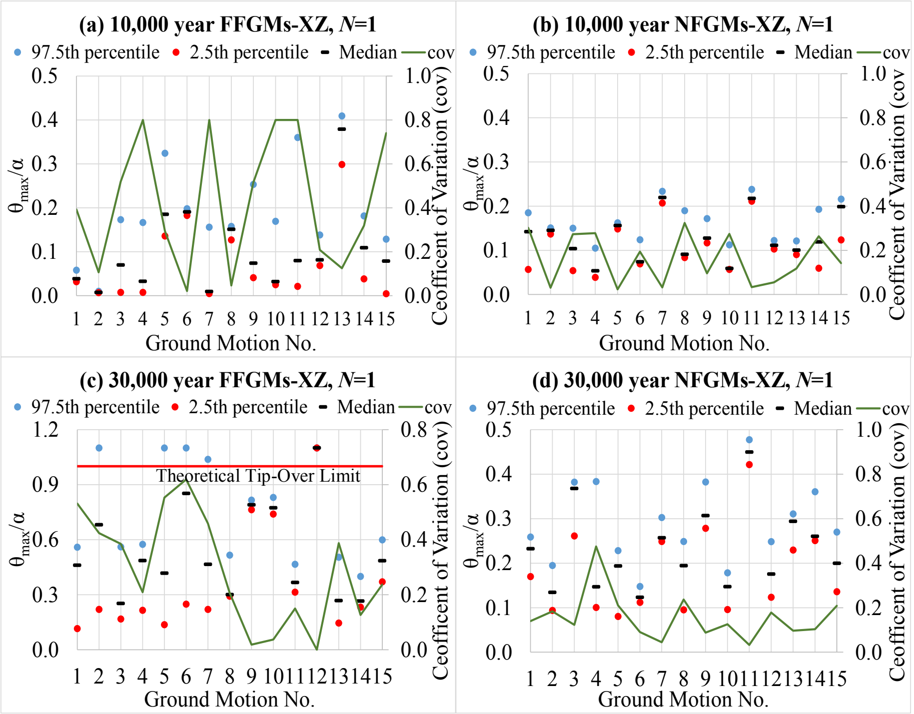

Figure 8.14. Percentile distribution and cov plot for rocking block: $\ddot{u}_g = X$, $\ddot{v}_g = Z$; [N = 1.0, $\alpha = 0.41$, $e = 0.872 \pm 1\%$, $p = 2.37 \pm 1\%$, $dt = 10^{-3}$ to 10^{-4}, $\theta_0 = 10^{-3}$ to 10^{-4}, PGA ± 1%]

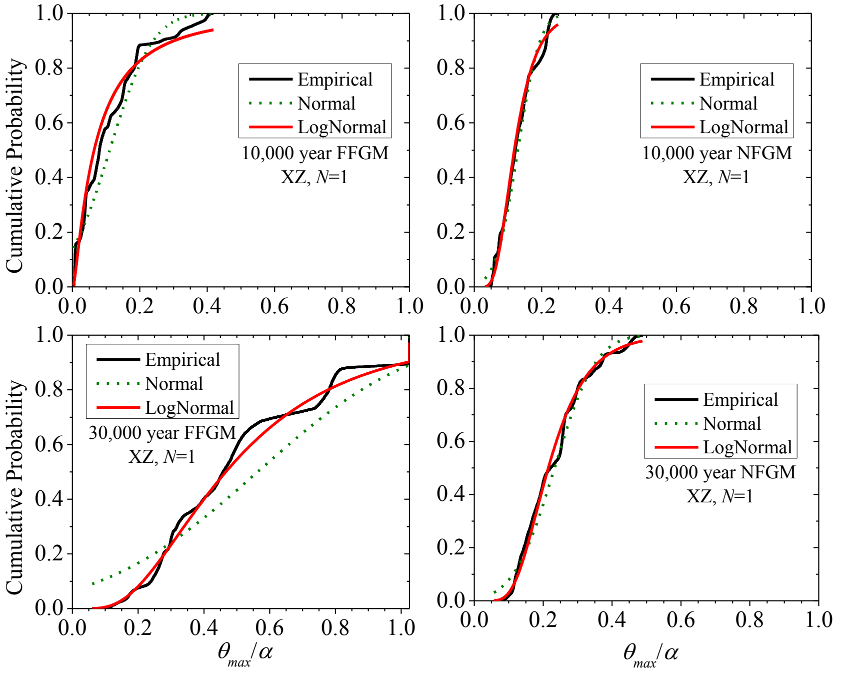

Figure 8.15. Cumulative probability distribution of maximum rocking angle: [N = 1.0, α = 0.41, $e = 0.872 \pm 1\%$, $p = 2.37 \pm 1\%$, $dt = 10^{-3}$ to 10^{-4}, $\theta_0 = 10^{-3}$ to 10^{-4}, PGA ± 1%]

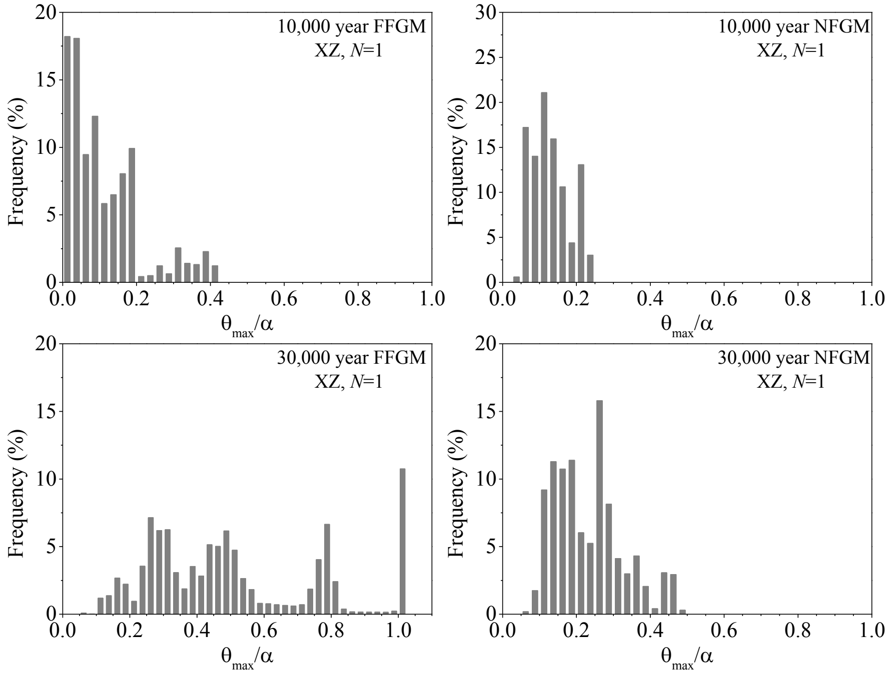

Figure 8.16. Maximum rocking angle distribution: [$N = 1.0$, $\alpha = 0.41$, $e = 0.872 \pm 1\%$, $p = 2.37 \pm 1\%$, $dt = 10^{-3}$ to 10^{-4}, $\theta_0 = 10^{-3}$ to 10^{-4}, PGA ± 1%]

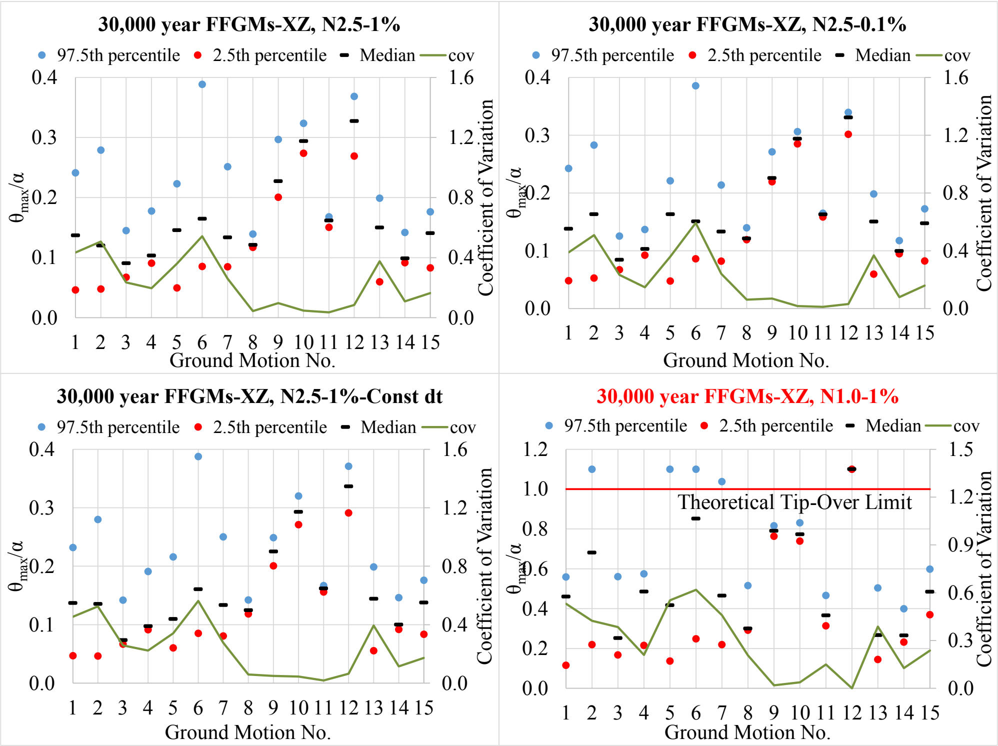

Figure 8.17. Percentile distribution and cov plot for 30,000 FFGMs ($\ddot{u}_g = X$, $\ddot{v}_g = Z$)

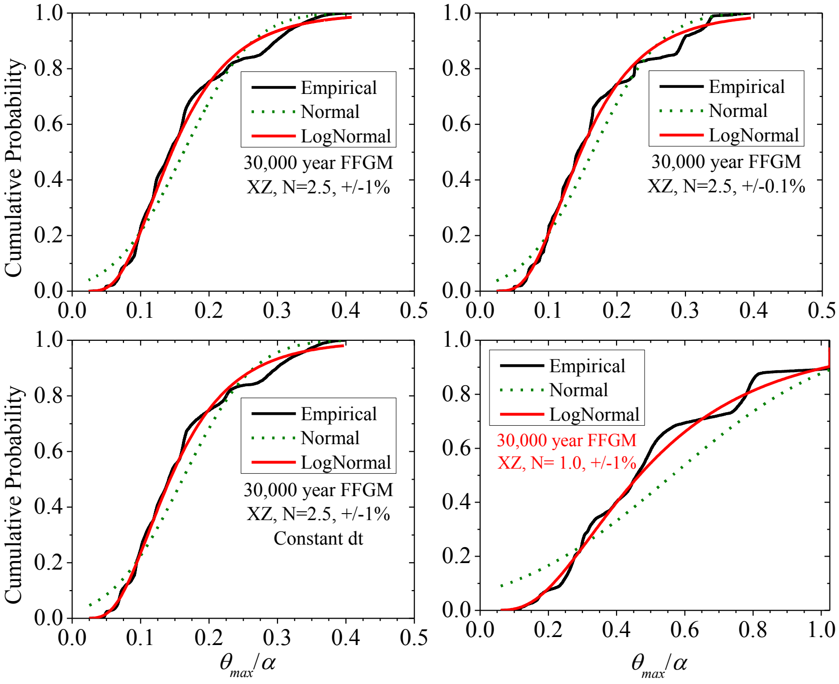

Figure 8.18. Cumulative probability distribution comparison for different cases: 30,000-year FFGMs (X and Z)

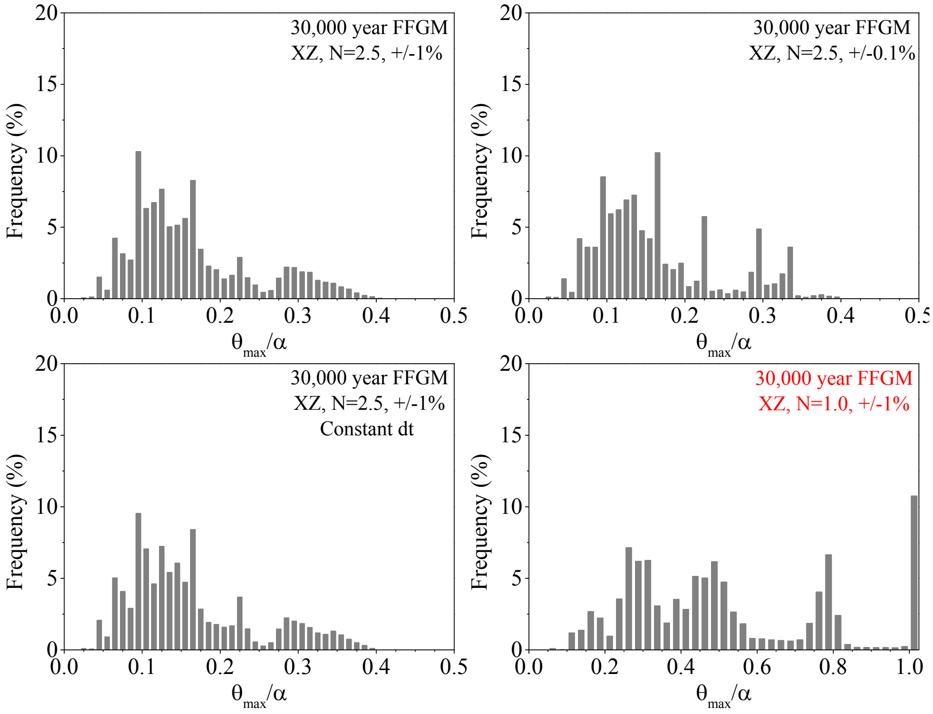

Figure 8.19. Maximum rocking angle distribution comparison for different cases: 30,000 FFGMs (X and Z)

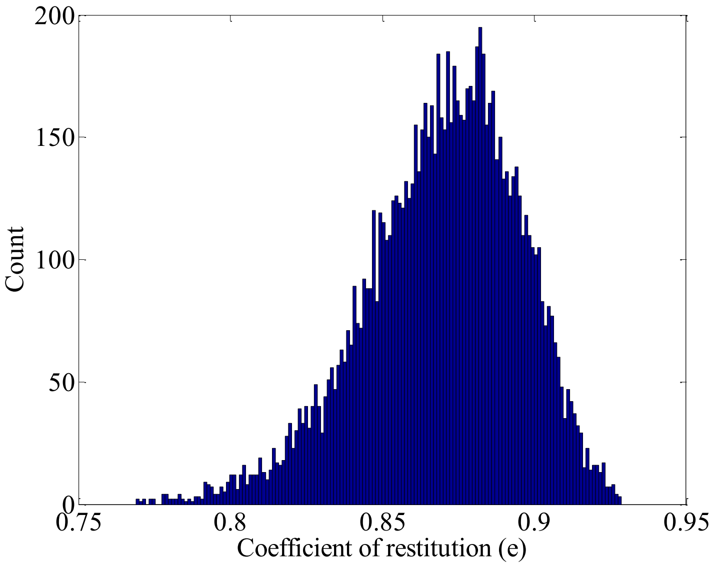

Figure 8.20. Log-normally distributed *e* values used in Monte Carlo simulations

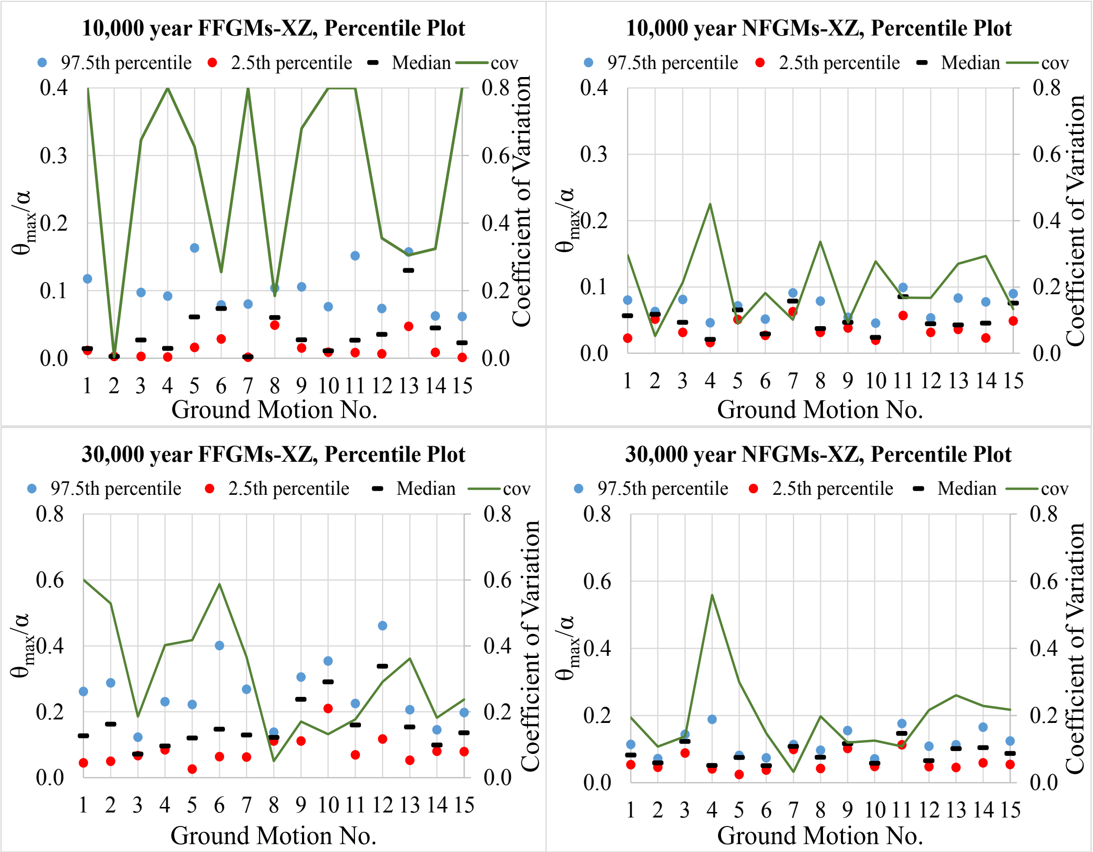

Figure 8.21. Percentile distribution and cov plot for probabilistic variation of *e* (cov = 0.2), $p = 2.37$, $dt = 10^{-4}$, $\theta_0 = 0$; $\ddot{u}_g = \text{X}$, $\ddot{v}_g = \text{Z}$

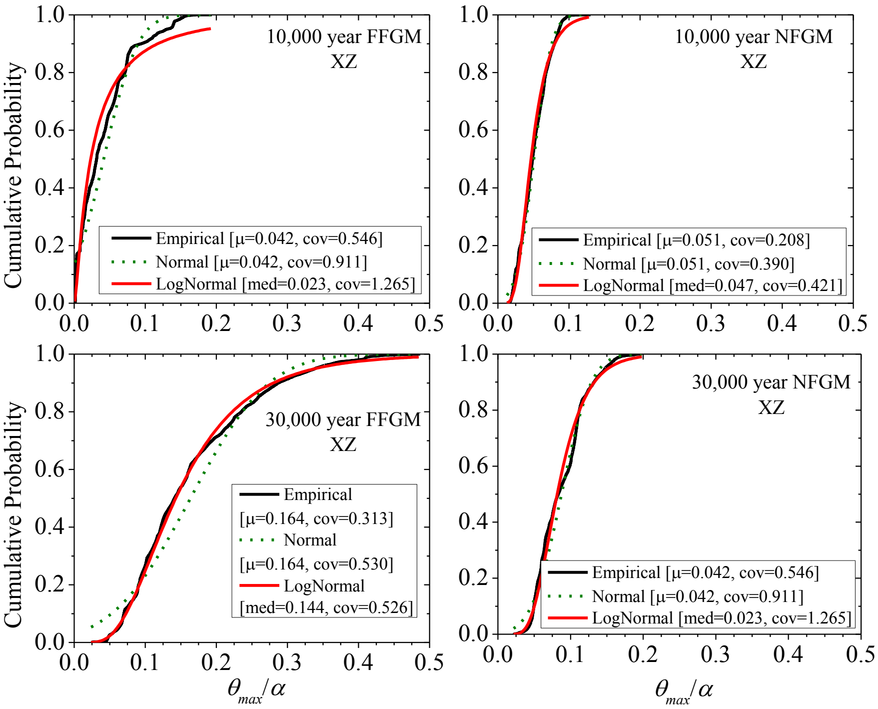

Figure 8.22. Cumulative probability distribution for probabilistic variation of *e* (cov = 0.2), $p = 2.37$, $dt = 10^{-4}$, $\theta_0 = 0$; $\ddot{u}_g = \mathrm{X}$, $\ddot{v}_g = \mathrm{Z}$

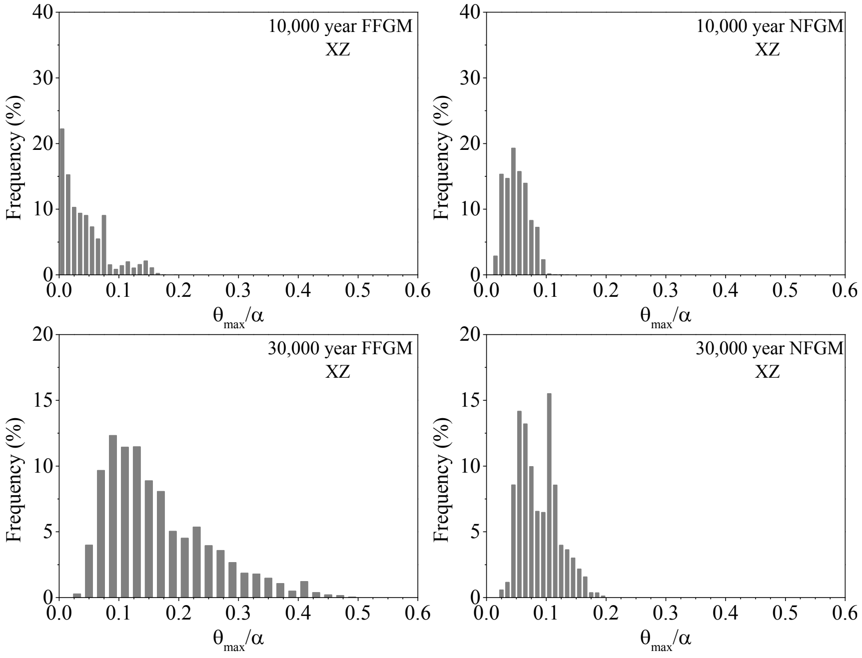

Figure 8.23. Maximum rocking angle distribution comparison for probabilistic variation of *e* (cov = 0.2), $p = 2.37$, $dt = 10^{-4}$, $\theta_0 = 0$; $\ddot{u}_g = \mathrm{X}$, $\ddot{v}_g = \mathrm{Z}$

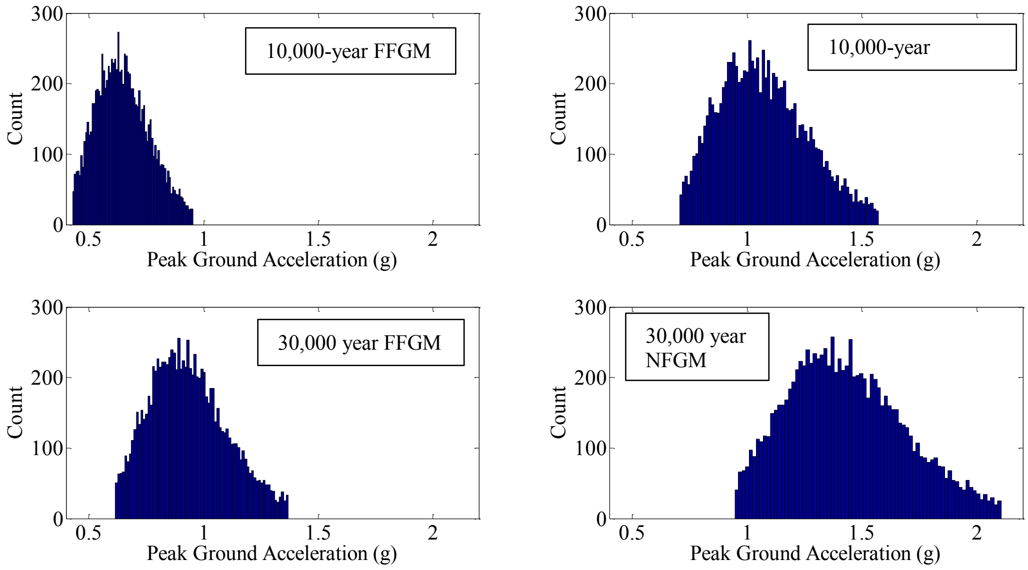

Figure 8.24. Log-normally ($\sigma_{\ln} = 0.2$, ± $2\sigma_{\ln}$) varied peak ground acceleration for horizontal component of WUS rock spectra.

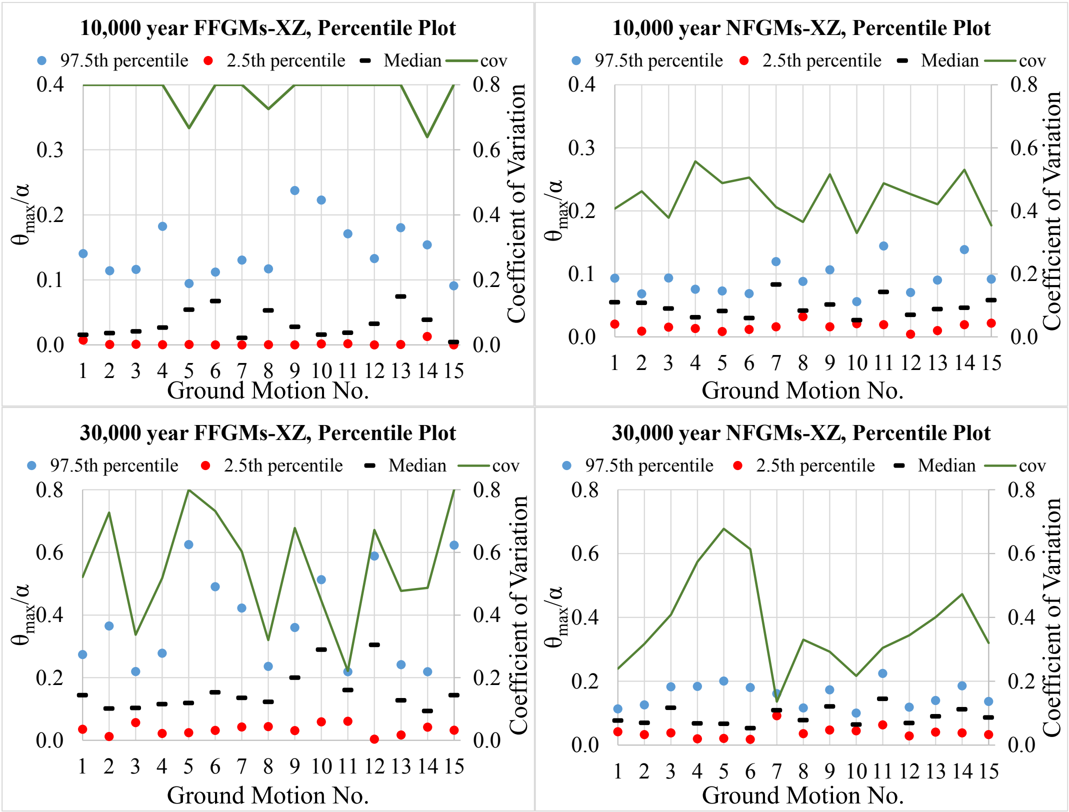

Figure 8.25. Percentile distribution and cov plot for log-normal variation of PGA ($\sigma_{\ln}$ = 0.2, ± $2\sigma_{\ln}$), $p = 2.37$, $dt = 10^{-4}$, $\theta_0 = 0$; $\ddot{u}_g = \mathrm{X}$, $\ddot{v}_g = \mathrm{Z}$

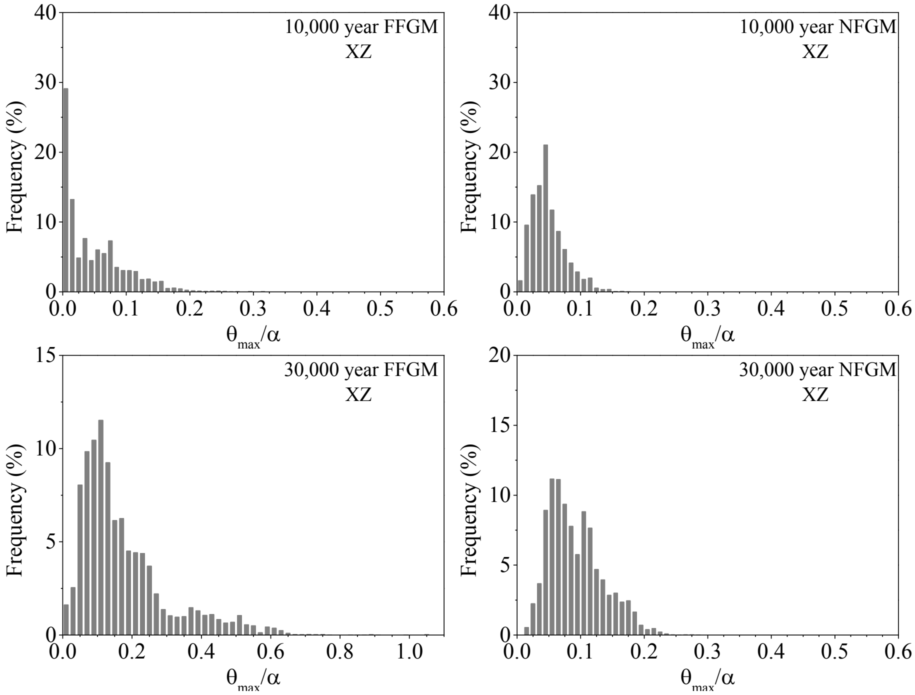

Figure 8.26. Maximum rocking angle distribution comparison for log-normal variation of PGA ($\sigma_{\ln}$ = 0.2, ± 2$\sigma_{\ln}$), $p = 2.37$, $dt = 10^{-4}$, $\theta_0 = 0$; $\ddot{u}_g$ = X, $\ddot{v}_g$ = Z

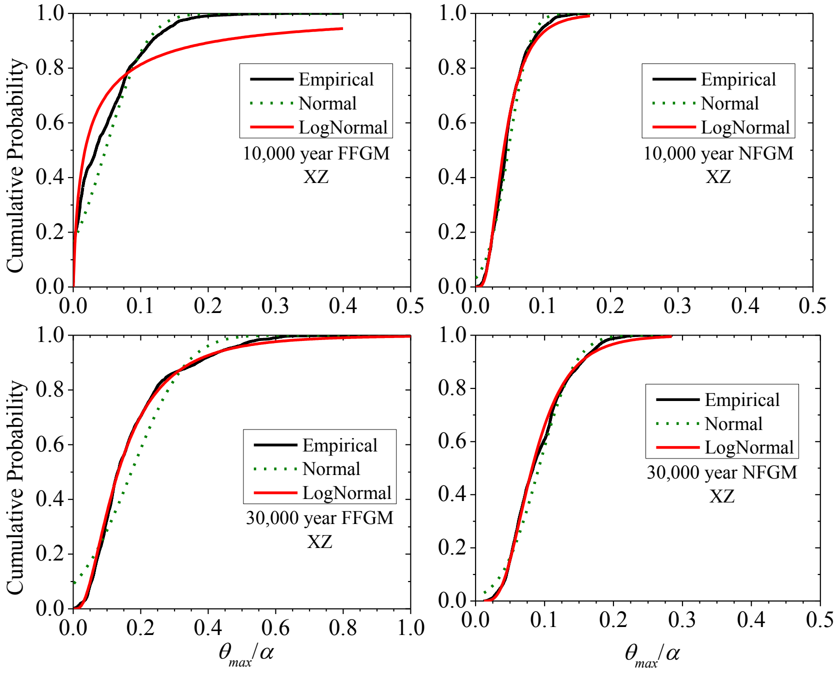

Figure 8.27. Cumulative probability distribution for log-normal variation of PGA ($\sigma_{\ln}$ = 0.2, ± 2$\sigma_{\ln}$), $p = 2.37$, $dt = 10^{-4}$, $\theta_0 = 0$; $\ddot{u}_g$ = X, $\ddot{v}_g$ = Z

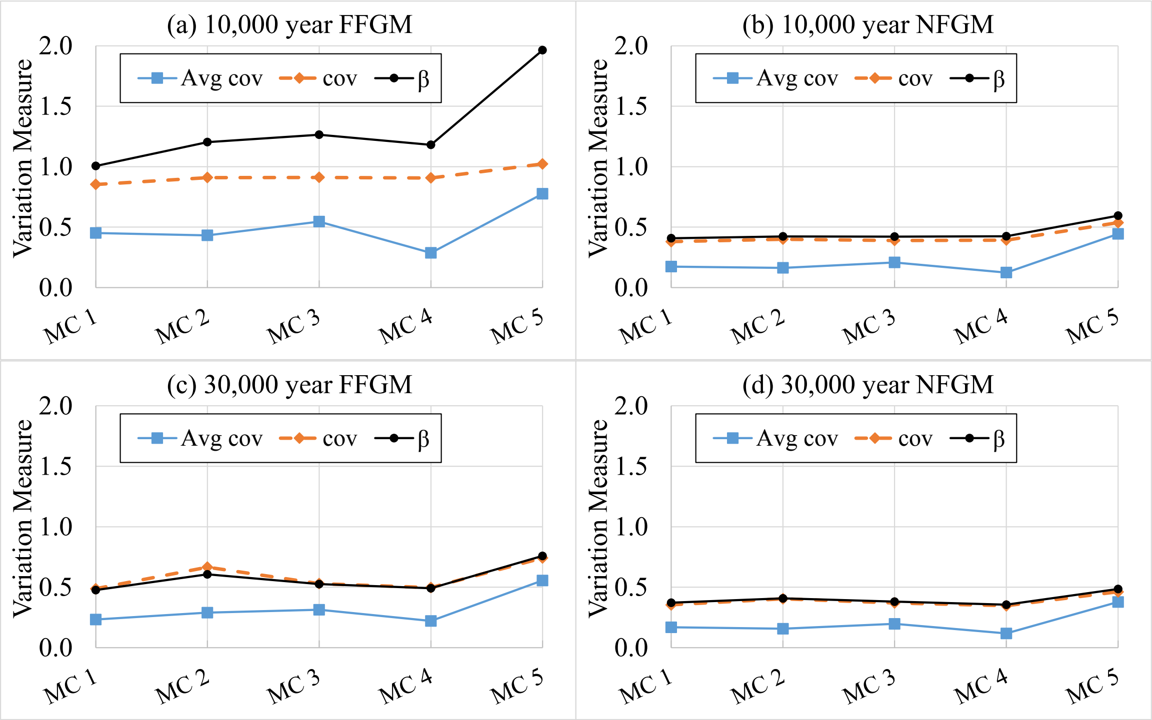

Figure 8.28. Comparison of variation measure (average cov, cov and β) for different Monte Carlo runs

CHAPTER 9

CONCLUSIONS

This research evaluates the response of free-standing casks under long-term seismic events. Two main aspect ratios ($r/h_{cg} = 0.43$ and 0.55; FS.43 and FS.55, respectively) were considered and generic casks with overpack and MPC were fabricated using a 1:2.5 scaling ratio. Two additional specimens (FS.39 and FS.55) were tested to apply larger motion intensities, providing better data for calibrating FE models. FE simulations were performed to evaluate the response of DSCs under seismic motions with 10,000- and 30,000-year return periods. The FE models were conditionally validated using experimental test results. Since, the experimental tests resulted in varied response under repeated tests, FE models were considered to be validated when their responses were within the bounds of the experimental response. Effect of soil in the ground motion spectra was also studied and full scale cask-pad-soil (fully coupled) FE models were created to study the soil structure interaction.

Investigations were also carried out to study repeatability of free-standing DSCs' response under similar seismic excitations, and to assess the presence of chaotic response. The response sensitivity and the presence of chaotic motion were studied using rocking only equation of motion for 2D rocking rigid block with geometric properties similar to those of the DSCs' geometry. Detailed discussion of findings from this study are presented in the following sections.

9.1 Experimental Tests

Scaled free-standing casks were subjected to similar ground motions to investigate the variation on the dynamic response of free-standing casks. The casks had aspect ratios of 0.62, 0.55, 0.43 and 0.39; and were subjected to multidirectional earthquake motions. The results also compared the response under motions with multiple pulses (FFGMs), and a couple of major pulses (NFGMs). The main findings are summarized below:

i. Repeated experimental tests under identical (repeated) ground motions showed lack of repeatability in the response. Large variation in the dynamic response of free-standing DSCs were observed for all specimens.

ii. A small change in initial conditions and excitation time history, leading to change in boundary conditions of a specimen, causes large variations in the response.

iii. The variation in response not only exists when accelerations are applied in three orthogonal directions, but also under bidirectional and unidirectional excitations.

iv. While most of the previous analytical or numerical studies focus on block type structures (2D or 3D), this study investigated response of 3D cylindrical free-standing DSCs. The fact that DSCs have a circular base increases the likelihood of motions along the cask edge, resulting in tumbling or nutation motion. Any minute differences at an instance of DSCs' response (initial condition at that instance), while on its edge, can lead to different results in the rest of the time history.

v. A series of pulses contained in FFGMs increases the potential for rocking and tumbling motion of the free-standing bodies, as the input motion unfolds. Early pulses cause the free-standing casks to rock or tumble, making it easier for the casks to move (lateral or rocking motion) when subsequent pulses occur.

vi. Free-standing bodies subjected to FFGMs consistently show that the multiple pulses contained in these records lead to larger displacements than those expected from NFGMs.

9.2 FE Cask-Pad Only Model

This research investigated the potential for tip-over of two cylindrical free-standing casks of different aspect ratios under sinusoidal excitations, using FE models that are capable of accounting for all possible modes of response like sliding, 3D movement and free-flight response. The tip-over spectra were then compared to that obtained from analytical solutions for 2D rocking only equation (which most studies use for free-standing body). FE models of these cylindrical free-standing bodies were created to reproduce simultaneous sliding and rocking response. The response of casks under multipulsed excitation was also examined. The main findings are:

i. FE models for cylindrical free-standing DSCs were used for the first time to generate overturning response spectra of cylindrical casks subjected to horizontal single pulse harmonic excitations. Under these conditions, the FE model showed a periodic and stable rocking response, relatively insensitive to minor changes in input parameters.

ii. As the FE model included sliding along with rocking, larger accelerations for overturning were required compared to those obtained from previous 2D rigid block analytical equations, which do not include sliding in the formulation. The presence of sliding reduces the overturning potential of a free-standing body.

iii. Increasing the friction coefficient to artificial values in the FE models to reduce sliding led to a free-flight mode that also reduced the overturning potential of the system.

iv. The cask response is not very sensitive to multicycle harmonic loading applied only in the horizontal direction. However, the response under both horizontal and vertical sinusoidal excitation becomes very sensitive and even minute arbitrary differences result in different response of the cask.

v. The response for the first couple of cycles still is very similar, but thereafter the displacements start to diverge. For this reason, overturning spectra of free-standing bodies subjected to one pulse sinusoidal motion are repeatable, even for systems that are considered chaotic under multicycle sinusoidal input motions.

vi. Cylindrical free-standing bodies become sensitive to minute input parameter variations if multicycle harmonic loads are applied simultaneously in a horizontal and vertical direction. This phenomenon is related to the intrinsic behavior of the cask movement, and not to the technique used for obtaining the response.

FE simulations were also used to obtain the response of scaled DSCs under full intensity of 10,000- and 30,000-year ground motions used in the experimental tests. The effect of frequency of ground motion was studied by changing the scale factor of ground time step. The following conclusions were obtained:

vii. Scaled cask-pad only FE simulation under full intensity of 10,000- and 30,000-year motion showed that the ground motion containing multiple smaller pulses produces larger rocking compared to the motions that have only one or two large pulses, similar to the experimental finding.

viii. Cylindrical geometry of DSCs makes them highly prone to nutation or tumbling motion. If the applied ground motion contains multiple pulses, initial pulse(s) may result in rocking of DSCs which is usually followed by nutation motion. The subsequent pulses contained in the ground motion can then induce larger rocking and in some instances larger displacements.

ix. A parametric study of frequency content variation was performed by changing the time step modification factor. The study shows that motions with larger spectral acceleration in long period region produce a larger response in terms of displacements and rocking.

9.3 Soil Structure Interaction (SSI: Cask-Pad-Soil Model)

Soil structure interaction's effect on the response of free-standing DSCs was studied for full scale FE models of coupled cask-pad-soil along with the strain compatible soil properties (obtained from deconvolution and convolution analysis). Application of this soil effect into the ground motion leads to following conclusions:

i. The deconvolution and convolution process resulted in changes in the spectral characteristics of the original rock motion. The process showed that the predominant ground motion period elongates, shifting to the longer period range.

ii. This change in spectral characteristics of ground motions has a large effect on the DSC response. The change in frequency resulted in 3-5 times the amount of rocking and produced similar increase in displacements compared to those resulting from application of rock motions.

iii. Simulations for squat (r/h_{cg} = 0.55) and slender (r/h_{cg} = 0.43) casks, under the

30,000-year Chi-Chi motion, showed an excessive movement of casks, and impacts among them. Impact cask accelerations of up to 10.44g were obtained.

iv. The response of four casks in the same model followed a similar trend during the early part of ground motion excitation. But as the time history progresses, differences in the response occur.

9.4 Analytical Model and Monte Carlo Simulation

The experimental tests showed extreme sensitivity in the response of free-standing bodies. This extreme sensitivity is indicative of chaotic nature. Investigations were also carried out to determine the presence of chaos on the modelled response of free-standing 2D rigid blocks subjected to harmonic excitation. Monte Carlo simulations were then performed to study the response sensitivity under seismic ground motions. The main findings are:

i. The coefficient of restitution (*e*), 0.872, used in this study was experimentally determined, and it was 14.5% larger than the theoretical value (0.761). This finding is consistent with other studies.

ii. Three methods of identifying chaos were used: phase-plane plots, Fourier spectra, and Poincaré sections. The results show that 2D blocks subjected to simple rocking under horizontal motions have a repeatable response. However, 2D blocks under horizontal and vertical accelerations exhibit a lack of repeatability, chaotic response.

iii. The results show that when an actual ground motion is applied, the presence of vertical acceleration is not necessary for response variation, unlike free-standing bodies under sinusoidal motion, where horizontal acceleration only does not result in such variations.

iv. Monte Carlo simulation show that differences as small as ±0.1% in system parameters, such as coefficient of restitution (*e*), frequency parameter (*p*), and peak ground acceleration (PGA), could result in large variation (cov of 0.2 for individual ground motion and 0.48 for a set of ground motions) in the response.

v. When the ground motion variation within a spectrally matched set (having the same spectral characteristics) was considered, the cov doubled for almost every case. This suggested that even for ground motions having the same spectral characteristics, the differences among individual ground motions (differences in actual time history, number and location of pulses, etc.) could result in very large variance in response.

vi. Analyses under varied ground motion time step and also under varied change in parameters (N2.5-1, N2.5-0.1, N2.4-1C and N1-1) showed the dispersion parameters: cov (Analysis I) and cov and β (Analysis II) were relatively stable for a particular spectrum. For a ground motion spectrally matched to the 30,000-year spectra, a cov of 0.24 can be used to determine the confidence interval of possible rocking angles. However, it should be noted that any bound determined using cov or β is only applicable to a 2D analytical solution.

vii. Varying the coefficient of restitution log-normally resulted in a similar dispersion parameter to that obtained from varying all the parameter by ±1%.

viii. Log-normal variation of PGA shows that the record-to-record variation of ground motions result in the largest dispersion of maximum rocking angle. This suggests that the effect ground motion variation overshadowing effect of any other parameters. However, dispersion resulting from minute changes in parameters to single ground motion cannot be ignored. If the response is considered as deterministic and chaotic response is ignored, minute variation and changes to parameters makes any model unreliable to accurately predict or reproduce response of free-standing body to a given ground motion or experimental tests.

9.5 Fundamental Conclusion on DSC Response

The primary objective of this research's was to evaluate the response of free-standing DSC under a seismic event of long return period. It was found from the experiments, numerical (FE) and analytical simulations that the response DSCs and free-standing structure in general are not repeatable and are highly sensitive to initial and boundary conditions. Although no overturning was observed in all analysis techniques for WUS rock spectra with 10,000- and 30,000-year return periods, the ability of numerical and analytical technique to deterministically predict the response of free-standing bodies may not always be reliable.

Experiments performed for this study show nonrepeatability of DSC response. This not only reinforces the high sensitivity of response, but also makes validation of FE models or analytical simulations very difficult. This in turn, along with variability in the parameters (coefficient of restitution, coefficient of friction, etc.), makes the deterministic prediction of response almost impossible. The results from FE and analytical simulations show that with the exception of single-pulsed harmonic excitation and multipulsed harmonic excitation without vertical excitation, the response is not repeatable and is extremely sensitive to small arbitrary changes to input parameters and modelling parameters. The response of free-standing bodies like DSCs under actual ground motion does not require presence of vertical component for response variation. Hence a probabilistic or statistical approach appears to be more rational approach and provides certain confidence interval bounds to the possible maximum response.

This finding, however, should not be inferred as FE and analytical tools to be in error. The nature of the response of free-standing bodies itself is extremely complex and sensitive to many factors including ground motions, coefficient of restitution, friction coefficients and also three-dimensional motion (which 2D approximation is not able to consider). A single simulation from FE or analytical model should be taken as an approximation, one of the possible responses, and apply a confidence interval bound using dispersion parameters like cov and β.

CHAPTER 10

RECOMMENDATIONS FOR FUTURE RESEARCH

One of the major findings of the study was the lack of repeatability in results, and the existence of chaotic response. More research should be conducted on the current understanding of motions of cylindrical free-standing bodies. This includes three-dimensional (3D) analytical formulations, further experimental tests, and numerical simulations to capture possible variation in the response. As a large number of experimental tests may not always be possible, numerical simulations will have to supplement those tests.

FE simulations performed in this study uses a constant value of coefficient of friction (μ_s and μ_k). However, in field condition, coefficient of friction may vary at different location of the same concrete pad surface. This is due the nonhomogenous nature of concrete and surface finish quality. As free-standing bodies like DSCs move around, the difference in coefficient of friction also leads to differences in response. This variation of coefficient of friction, even during evolution of the same response time history requires further study.

The coefficient of restitution (e) during impact of 2D planar body has been studied in the past. However, experimental tests show that theoretical equations consistently under-estimate e. In other words the theoretical equation gives larger damping (smaller e).

Previous studies show that, even for block type (prismatic) free-standing structures, damping seems to decrease with three-dimensional (3D) motion of a free-standing body. Cylindrical free-standing bodies can easily have such 3D motion (orthogonal to excitation plane), particularly during nutation motion. Better understanding of coefficient of restitution or damping associated with motion of cylindrical bodies needs further research.

Methods for better seismic performance of DSCs should be investigated. Anchoring DSCs to the concrete pad could be one of the solutions and can prevent DSCs from experiencing a nonrepeatable response, and also from extreme movement and rocking (as observed in Chapter 7 for SSI). This anchorage is currently being studied by Parks et al. [70]. The findings from this study show that once rocking is present, the response of DSC becomes extremely sensitive to minor variations in system and input parameters. Making sliding-only the primary response mechanism by increasing the aspect ratio (r/h_{cg}), i.e., making DSCs squatter, reducing the coefficient of friction should also be studied. However, it should be noted that reducing the coefficient of friction may result in excessive sliding. Other methods that improve the seismic performance of DSCs could be tying multiple DSCs structurally so that a group of linked DSCs responds as one unit.

Further studies should also include spectra developed for sites other than WUS. This research focused mainly on the spectra obtained from NUREG 6728 [42] for WUS rock sites. More studies are also necessary to consider the nonlinear response of the soil and its effect on ground motions, and ultimately its effect on free-standing bodies.

As mentioned earlier experiments showed nonrepeatability, while analytical and FE models showed extreme sensitivity of modeling assumptions and parameters. This sensitivity renders a single simulation of numerical and FE models unreliable in terms of accurate prediction of response. A statistical or probabilistic approach to provide a bound of confidence interval is a better approach.

The variation parameters (cov and β) presented in this study were determined for the spectra developed for WUS. More research is necessary to determine the variation in free-standing bodies' response for ground motions with different spectral characteristics. In addition, it should be noted that the variation parameters presented in this dissertation are applicable only for 2D rocking-only approximation. Inclusion of sliding and 3D response should be should be studied to obtain similar variation parameters for a more realistic behavior.

APPENDIX A

CASK PAD FE SIMULATION (SEISMIC EXCITATION) OUTPUT

This section presents the results for scaled cask-pad only FE models for additional DSC specimens (FS.39 and FS.62). While these specimens were not the primary specimens targeted in the study and their scaling (N = 3.5) do not correspond to any real casks available, they help in understanding of the role r/h_{cg} in the response of DSCs. The analysis performed for these specimens also revealed the existence of nutation or tumbling motion (more clearly than the two main DSC specimens: FS.43 and FS.55). Nutation motion is where a cask precesses along its bottom circular edge and loses less energy compared to that of clear impact between free-standing body and foundation.

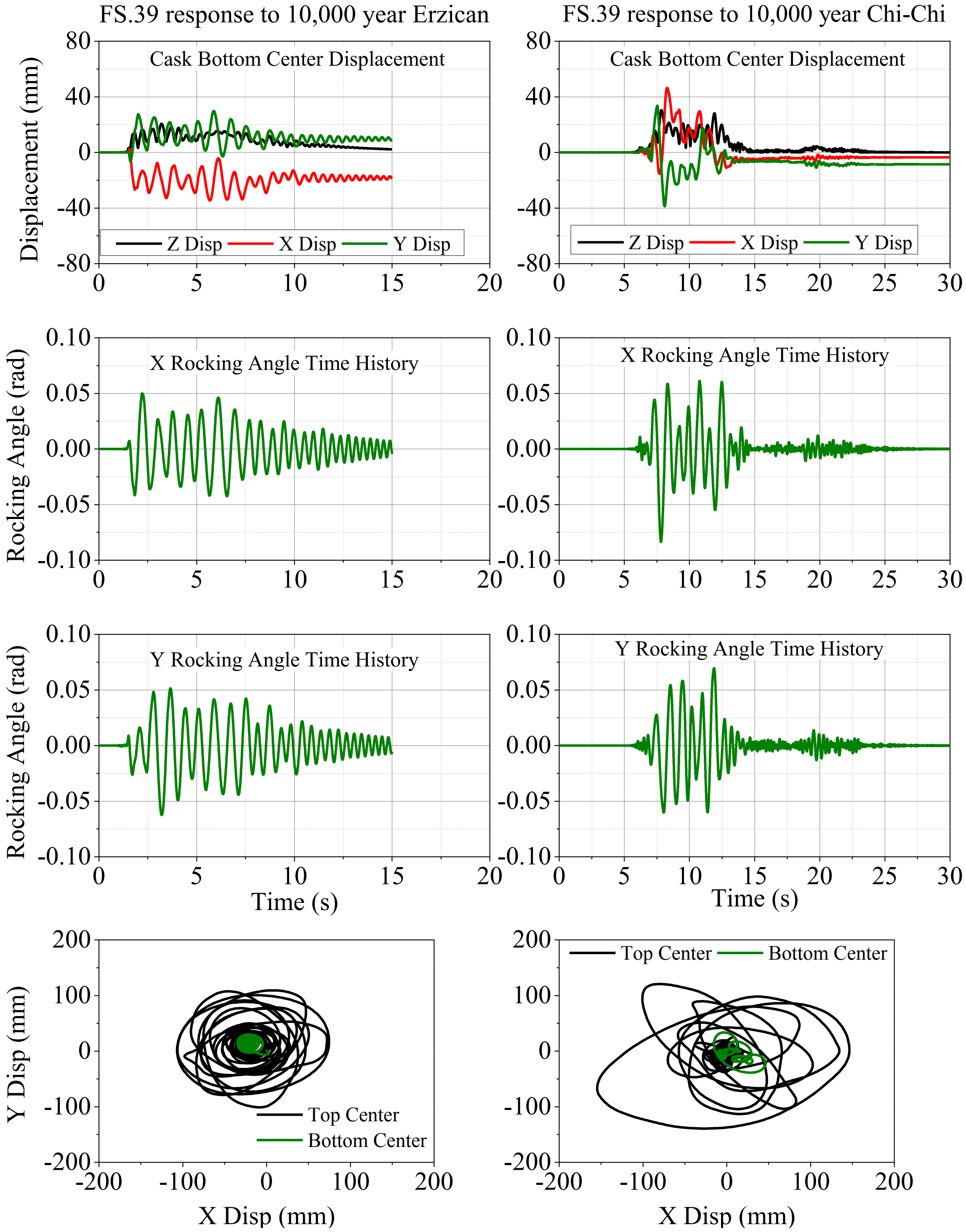

Figure A.1. FS.39 ($r/h_{cg} = 0.39$) response 10,000-year motions

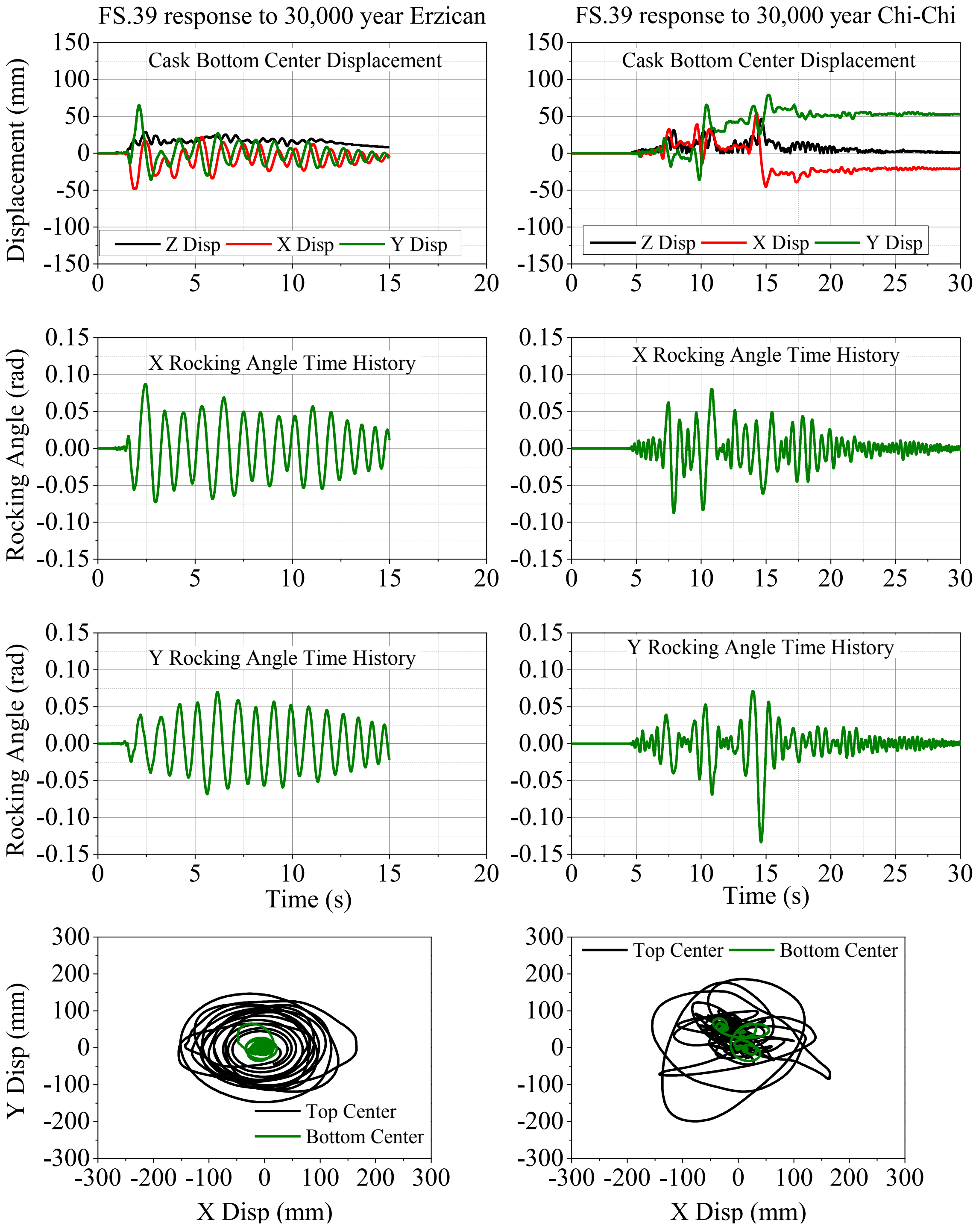

Figure A.2. FS.39 ($r/h_{cg} = 0.39$) response 30,000-year motions

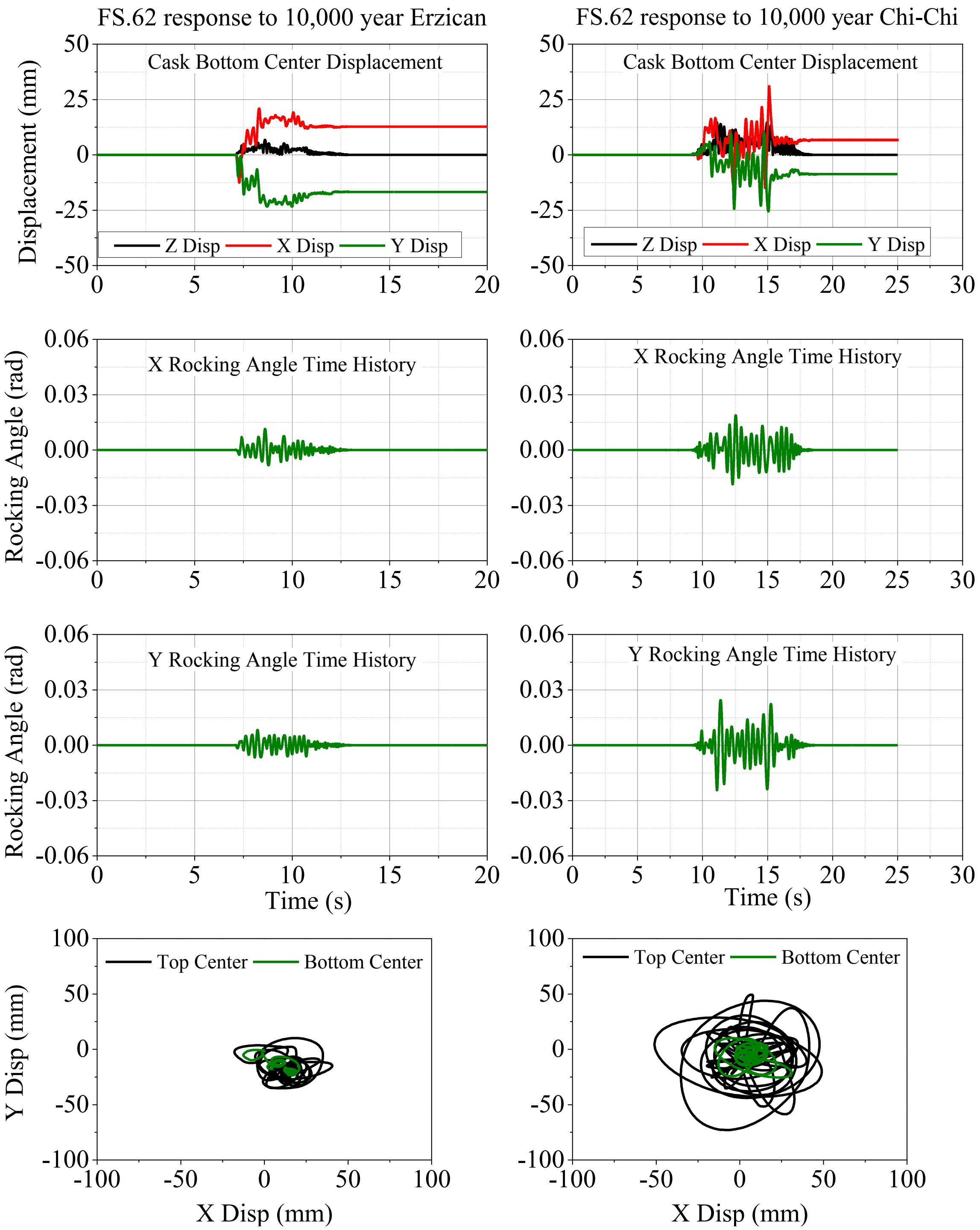

Figure A.3. FS.62 ($r/h_{cg} = 0.62$) response 10,000-year motions

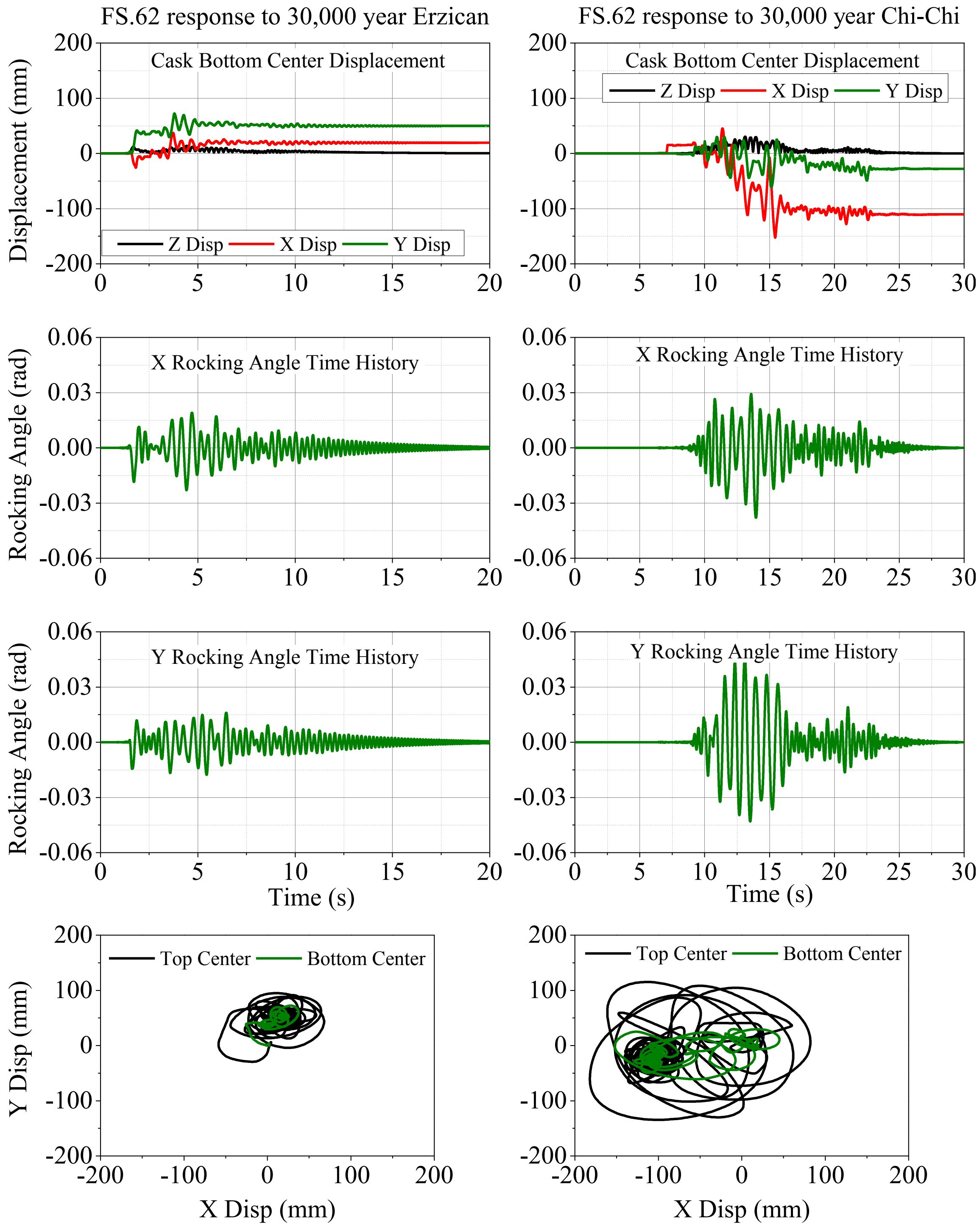

Figure A.4. FS.62 ($r/h_{cg} = 0.62$) response 30,000-year motions

APPENDIX B

SOIL STRUCTURE INTERACTION DATA AND OUTPUT

The first section (B.1) presents the data for soil layer properties used in FE models for SSI study. Outputs or results from the cask-pad-soil model are also presented here in last two sections (B.2 and B.3)

B.1 Soil Layer Properties Data

Table B.1. Soil layer properties before convolution analysis (Poisson’s ratio, ν = 0.4)

Layer #	**Depth (m)**	**h_i (m)**	**Vs (m/s)**	**Vp (m/s)**	**E (MPa)**	**γ (kg/m^3)**
1	3.05	3.05	320.48	785.02	575.83	2002
2	6.10	3.05	400.01	979.82	897.09	2002
3	9.14	3.05	400.01	979.82	897.09	2002
4	12.19	3.05	472.18	1156.61	1250.00	2002
5	15.24	3.05	472.18	1156.61	1250.00	2002
6	18.29	3.05	517.92	1268.63	1503.87	2002
7	21.34	3.05	517.92	1268.63	1503.87	2002
8	25.91	4.57	559.28	1369.95	1753.67	2002
9	30.48	4.57	559.28	1369.95	1753.67	2002
10	35.05	4.57	608.04	1489.38	2072.77	2002
11	39.62	4.57	608.04	1489.38	2072.77	2002
12	45.72	6.10	608.04	1489.38	2072.77	2002
13	50.29	4.57	656.06	1607.01	2413.10	2002
14	54.86	4.57	656.06	1607.01	2413.10	2002
15	60.96	6.10	656.06	1607.01	2413.10	2002
16	65.53	4.57	697.33	1708.11	2726.29	2002
17	70.10	4.57	697.33	1708.11	2726.29	2002
18	76.20	6.10	697.33	1708.11	2726.29	2002
19	83.82	7.62	733.54	1796.79	3016.72	2002
20	91.44	7.62	733.54	1796.79	3016.72	2002
21	99.06	7.62	763.71	1870.69	3269.96	2002
22	106.68	7.62	763.71	1870.69	3269.96	2002
23	114.30	7.62	790.32	1935.89	3501.87	2002
24	121.92	7.62	790.32	1935.89	3501.87	2002
25	129.54	7.62	814.24	1994.46	3716.98	2002
26	137.16	7.62	814.24	1994.46	3716.98	2002
27	144.78	7.62	835.29	2046.04	3911.71	2002
28	152.40	7.62	835.29	2046.04	3911.71	2002

Table B.2. Strain compatible soil properties (10,000-year FFGM)

Layer #	**h_i (m)**	**β =G/G_{max}**	**$Vs_1 = \sqrt{\beta} * Vs$ (m/s)**	**Vp_1 (m/s)**	**E (MPa)**	**Damping (ξ_i) %**	**Rayleigh Damping**	
							α_m	**β_k**
1	3.05	0.620	252.35	618.13	357.02	7.19	0.66	0.003
2	3.05	0.528	290.58	711.76	473.38	8.60	0.79	0.004
3	3.05	0.409	255.96	626.97	367.31	10.95	1.00	0.005
4	3.05	0.464	321.58	787.71	579.80	9.61	0.88	0.005
5	3.05	0.409	301.85	739.37	510.82	10.86	0.99	0.005
6	3.05	0.441	344.13	842.94	663.94	10.07	0.92	0.005
7	3.05	0.404	329.09	806.11	607.20	10.89	1.00	0.005
8	4.57	0.448	374.55	917.45	786.52	9.84	0.90	0.005
9	4.57	0.395	351.66	861.40	693.34	10.98	1.00	0.005
10	4.57	0.443	404.58	991.01	917.69	9.92	0.91	0.005
11	4.57	0.418	393.20	963.15	866.81	10.41	0.95	0.005
12	6.10	0.394	381.65	934.86	816.64	10.89	1.00	0.005
13	4.57	0.445	437.89	1072.61	1075.03	9.77	0.89	0.005
14	4.57	0.431	430.69	1054.96	1039.95	10.05	0.92	0.005
15	6.10	0.414	422.15	1034.06	999.14	10.38	0.95	0.005
16	4.57	0.453	469.50	1150.03	1235.83	9.54	0.87	0.005
17	4.57	0.442	463.49	1135.31	1204.38	9.76	0.89	0.005
18	6.10	0.430	457.40	1120.40	1172.96	9.97	0.91	0.005
19	7.62	0.462	498.78	1221.75	1394.76	9.30	0.85	0.005
20	7.62	0.452	492.89	1207.34	1362.06	9.49	0.87	0.005
21	7.62	0.477	527.63	1292.42	1560.80	8.96	0.82	0.004
22	7.62	0.470	523.35	1281.93	1535.56	9.09	0.83	0.004
23	7.62	0.491	553.84	1356.62	1719.71	8.65	0.79	0.004
24	7.62	0.486	550.84	1349.27	1701.13	8.74	0.80	0.004
25	7.62	0.506	579.20	1418.76	1880.85	8.33	0.76	0.004
26	7.62	0.502	576.99	1413.32	1866.48	8.39	0.77	0.004
27	7.62	0.520	602.17	1475.01	2032.96	8.04	0.73	0.004
28	7.62	0.518	601.47	1473.28	2028.21	8.05	0.74	0.004

Table B.3. Strain compatible soil properties (10,000-year NFGM)

Layer #	**h_i (m)**	**β $=G/G_{max}$**	**$Vs_1 = \sqrt{\beta} * Vs$ (m/s)**	**Vp_1 (m/s)**	**E (MPa)**	**Damping (ξ_i) %**	**Rayleigh Damping**	
							α_m	**β_k**
1	3.05	0.549	237.52	581.79	316.28	8.57	0.79	0.004
2	3.05	0.443	266.21	652.07	397.31	10.25	0.95	0.005
3	3.05	0.312	223.34	547.07	279.66	13.31	1.23	0.006
4	3.05	0.386	293.18	718.13	481.89	11.45	1.06	0.006
5	3.05	0.321	267.54	655.34	401.31	12.88	1.19	0.006
6	3.05	0.371	315.35	772.45	557.55	11.68	1.08	0.006
7	3.05	0.332	298.23	730.52	498.65	12.51	1.15	0.006
8	4.57	0.397	352.28	862.90	695.77	10.97	1.01	0.005
9	4.57	0.350	330.64	809.90	612.92	11.98	1.10	0.006
10	4.57	0.415	391.82	959.77	860.74	10.51	0.97	0.005
11	4.57	0.403	386.09	945.72	835.73	10.73	0.99	0.005
12	6.10	0.394	381.88	935.40	817.59	10.88	1.00	0.005
13	4.57	0.459	444.31	1088.34	1106.79	9.50	0.88	0.005
14	4.57	0.456	443.06	1085.27	1100.56	9.53	0.88	0.005
15	6.10	0.454	441.91	1082.45	1094.85	9.56	0.88	0.005
16	4.57	0.503	494.51	1211.30	1371.02	8.53	0.79	0.004
17	4.57	0.501	493.58	1209.02	1365.87	8.55	0.79	0.004
18	6.10	0.496	490.95	1202.59	1351.36	8.65	0.80	0.004
19	7.62	0.530	534.01	1308.06	1598.80	7.94	0.73	0.004
20	7.62	0.524	530.84	1300.29	1579.87	8.05	0.74	0.004
21	7.62	0.548	565.32	1384.74	1791.73	7.56	0.70	0.004
22	7.62	0.543	562.79	1378.54	1775.73	7.64	0.70	0.004
23	7.62	0.564	593.36	1453.43	1973.92	7.22	0.67	0.003
24	7.62	0.560	591.41	1448.64	1960.92	7.29	0.67	0.004
25	7.62	0.579	619.36	1517.11	2150.68	6.92	0.64	0.003
26	7.62	0.578	618.79	1515.72	2146.74	6.93	0.64	0.003
27	7.62	0.595	644.57	1578.86	2329.31	6.58	0.61	0.003
28	7.62	0.596	644.62	1578.99	2329.69	6.57	0.61	0.003

Table B.4. Strain compatible soil properties (30,000-year FFGM)

Layer #	**h_i (m)**	**β $=G/G_{max}$**	**$Vs_1 = \sqrt{\beta} * Vs$ (m/s)**	**Vp_1 (m/s)**	**E (MPa)**	**Damping (ξ_i) %**	**Rayleigh Damping**	
							α_m	**β_k**
1	3.05	0.525	232.17	568.69	302.20	9.09	0.71	0.005
2	3.05	0.414	257.47	630.67	371.66	10.91	0.85	0.006
3	3.05	0.262	204.77	501.59	235.09	14.51	1.14	0.008
4	3.05	0.336	273.71	670.44	420.01	12.62	0.99	0.007
5	3.05	0.259	240.12	588.16	323.25	14.35	1.12	0.008
6	3.05	0.297	282.45	691.85	447.27	13.34	1.05	0.008
7	3.05	0.266	266.94	653.88	399.51	14.11	1.11	0.008
8	4.57	0.310	311.44	762.87	543.81	12.87	1.01	0.007
9	4.57	0.268	289.28	708.58	469.15	14.03	1.10	0.008
10	4.57	0.309	338.21	828.45	641.32	12.86	1.01	0.007
11	4.57	0.291	328.12	803.72	603.60	13.36	1.05	0.008
12	6.10	0.268	314.87	771.26	555.83	13.98	1.10	0.008
13	4.57	0.317	369.19	904.32	764.16	12.66	0.99	0.007
14	4.57	0.303	361.38	885.21	732.20	13.01	1.02	0.007
15	6.10	0.288	352.36	863.09	696.07	13.40	1.05	0.008
16	4.57	0.330	400.45	980.90	899.07	12.30	0.96	0.007
17	4.57	0.322	395.87	969.68	878.61	12.50	0.98	0.007
18	6.10	0.314	390.49	956.50	854.89	12.72	1.00	0.007
19	7.62	0.347	432.32	1058.95	1047.83	11.84	0.93	0.007
20	7.62	0.341	428.06	1048.52	1027.29	12.01	0.94	0.007
21	7.62	0.368	463.17	1134.52	1202.72	11.31	0.89	0.006
22	7.62	0.363	460.41	1127.77	1188.44	11.43	0.90	0.006
23	7.62	0.387	491.44	1203.78	1354.05	10.84	0.85	0.006
24	7.62	0.384	489.51	1199.05	1343.43	10.92	0.86	0.006
25	7.62	0.406	518.67	1270.48	1508.25	10.36	0.81	0.006
26	7.62	0.406	518.65	1270.44	1508.15	10.37	0.81	0.006
27	7.62	0.426	545.28	1335.67	1667.00	9.86	0.77	0.006
28	7.62	0.427	545.64	1336.55	1669.20	9.85	0.77	0.006

Table B.5. Strain compatible soil properties (30,000-year NFGM)

Layer #	**h_i (m)**	**β =G/G_{max}**	**$Vs_1 = \sqrt{\beta} * Vs$ (m/s)**	**Vp_1 (m/s)**	**E (MPa)**	**Damping (ξ_i)**	**Rayleigh Damping**	
							α_m	**β_k**
1	3.05	0.500	226.62	555.11	287.94	9.61	0.81	0.005
2	3.05	0.393	250.86	614.48	352.82	11.43	0.96	0.006
3	3.05	0.234	193.61	474.23	210.15	15.18	1.28	0.008
4	3.05	0.305	260.86	638.97	381.51	13.34	1.12	0.007
5	3.05	0.247	234.88	575.34	309.30	14.67	1.23	0.008
6	3.05	0.286	276.75	677.91	429.42	13.61	1.14	0.007
7	3.05	0.261	264.34	647.51	391.77	14.26	1.20	0.008
8	4.57	0.312	312.47	765.39	547.40	12.83	1.08	0.007
9	4.57	0.279	295.41	723.61	489.27	13.71	1.15	0.007
10	4.57	0.336	352.60	863.68	697.02	12.21	1.03	0.006
11	4.57	0.326	347.35	850.83	676.43	12.39	1.04	0.007
12	6.10	0.322	344.92	844.89	667.01	12.52	1.05	0.007
13	4.57	0.385	406.90	996.70	928.26	11.05	0.93	0.006
14	4.57	0.381	404.70	991.31	918.24	11.10	0.93	0.006
15	6.10	0.374	401.34	983.08	903.07	11.20	0.94	0.006
16	4.57	0.424	454.28	1112.74	1156.99	10.14	0.85	0.005
17	4.57	0.417	450.48	1103.45	1137.74	10.26	0.86	0.005
18	6.10	0.410	446.52	1093.74	1117.81	10.38	0.87	0.005
19	7.62	0.446	490.14	1200.60	1346.91	9.62	0.81	0.005
20	7.62	0.439	485.94	1190.31	1323.91	9.75	0.82	0.005
21	7.62	0.467	521.63	1277.73	1525.52	9.17	0.77	0.005
22	7.62	0.461	518.60	1270.31	1507.84	9.26	0.78	0.005
23	7.62	0.486	550.93	1349.50	1701.69	8.75	0.74	0.005
24	7.62	0.483	549.48	1345.94	1692.75	8.79	0.74	0.005
25	7.62	0.506	578.95	1418.12	1879.17	8.34	0.70	0.004
26	7.62	0.504	578.11	1416.07	1873.74	8.35	0.70	0.004
27	7.62	0.523	604.27	1480.14	2047.14	7.97	0.67	0.004
28	7.62	0.524	604.67	1481.14	2049.88	7.95	0.67	0.004

B.2 FE Model (Cask-Pad-Soil) Simulation Output: *r*/h_{cg} = 0.43

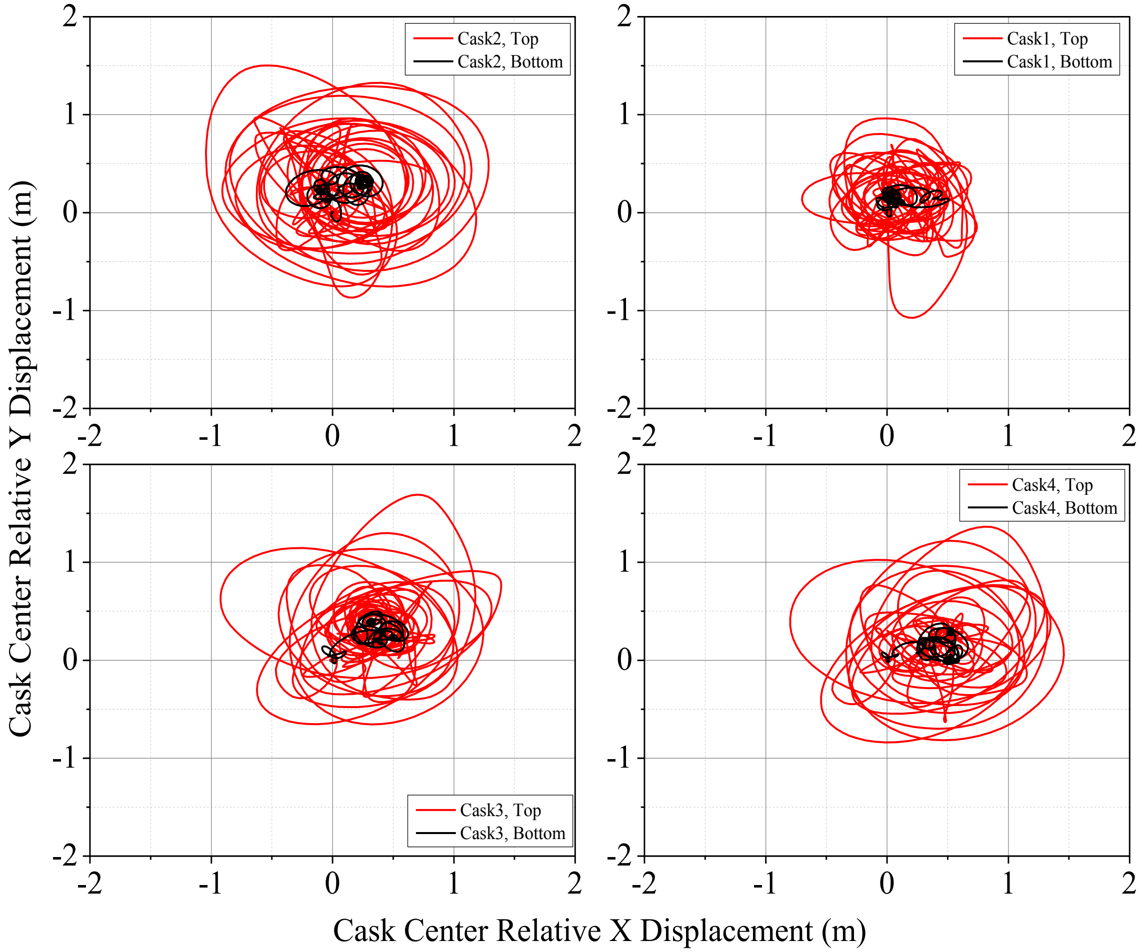

Figure B.1. Cask centers' XY lateral displacement relative to pad, cask-pad-soil model (full scale), $r/h_{cg} = 0.43$, $\mu = 0.55$, convolved 10,000-year Chi-Chi

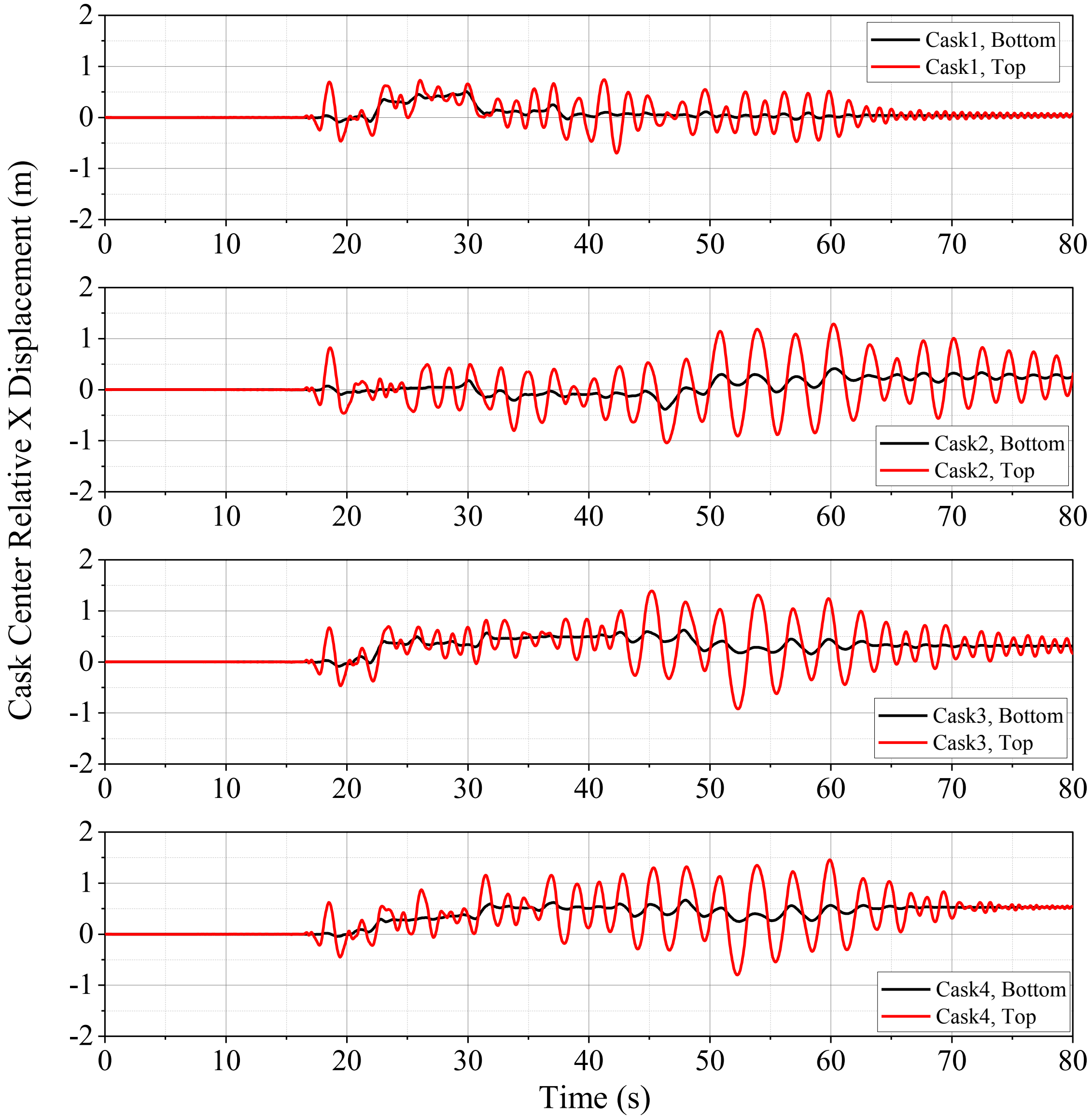

Figure B.2. Time histories of casks X displacement relative to pad, cask-pad-soil model (full scale), $r/h_{cg} = 0.43$, $\mu = 0.55$, convolved 10,000-year Chi-Chi

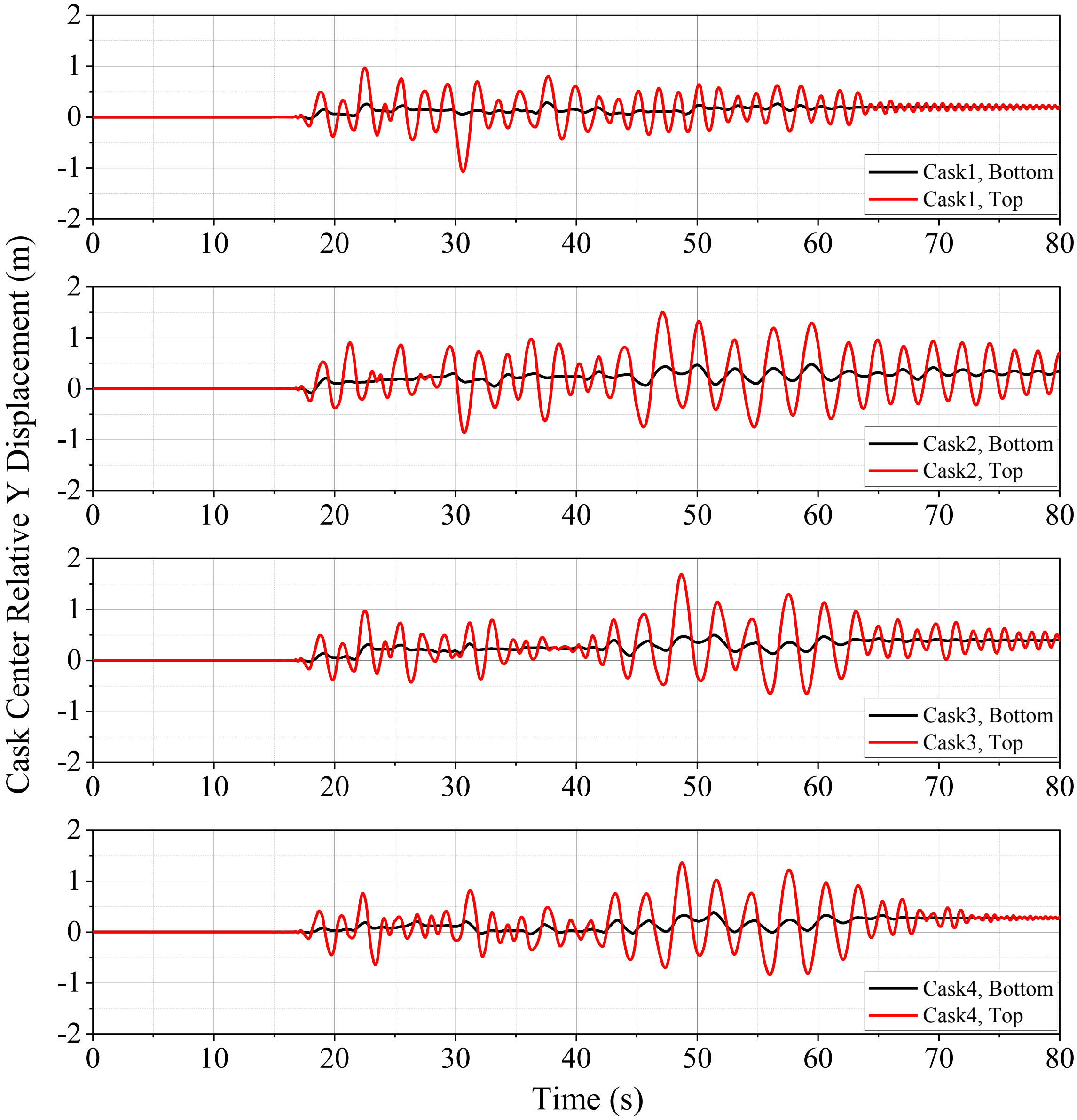

Figure B.3. Time histories of casks Y displacement relative to pad, cask-pad-soil model (full scale), $r/h_{cg} = 0.43$, $\mu = 0.55$, convolved 10,000-year Chi-Chi

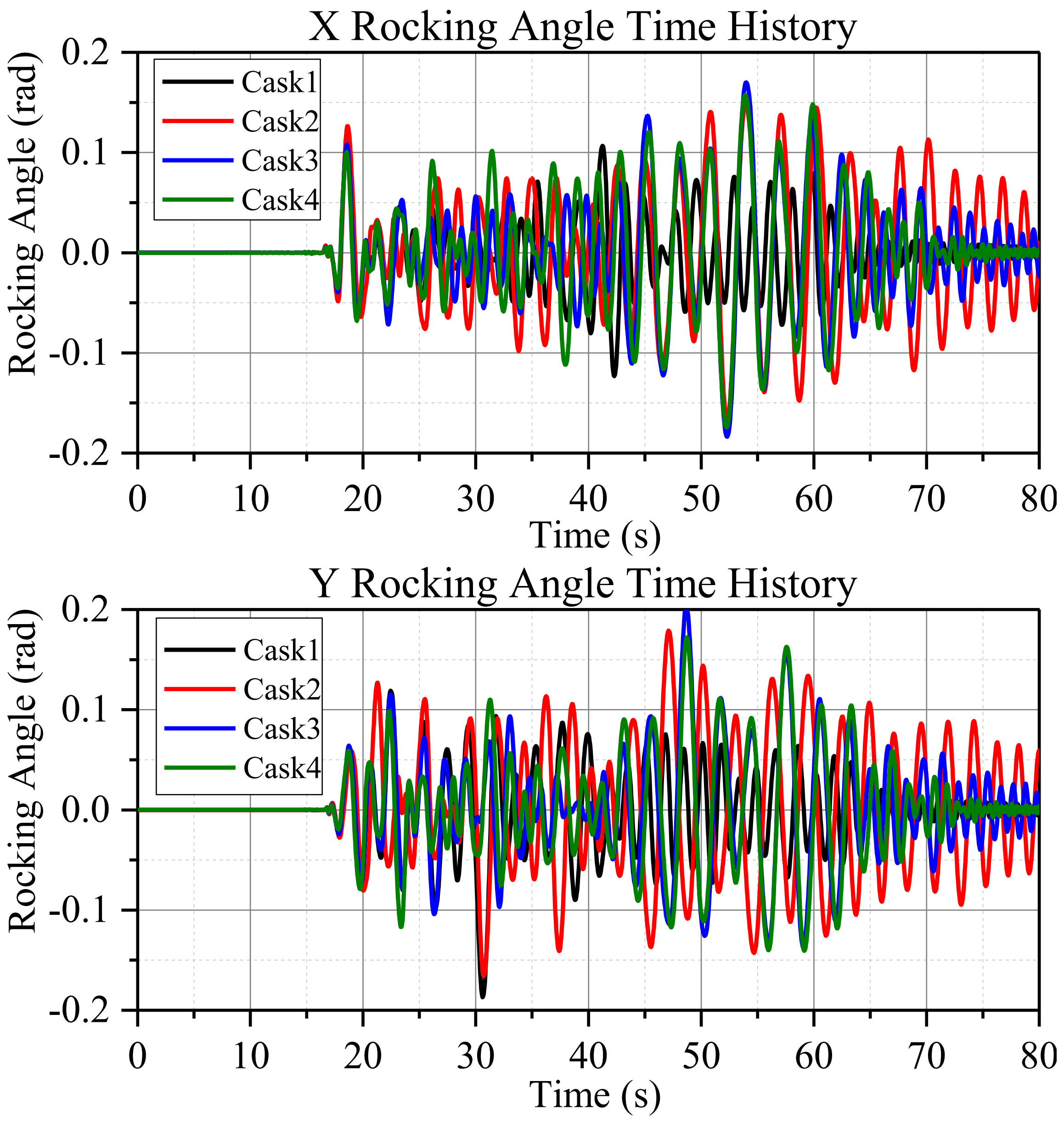

Figure B.4. Rocking angle time histories, cask-pad-soil model (full scale), $r/h_{cg} = 0.43$, $\mu = 0.55$, convolved 10,000-year Chi-Chi

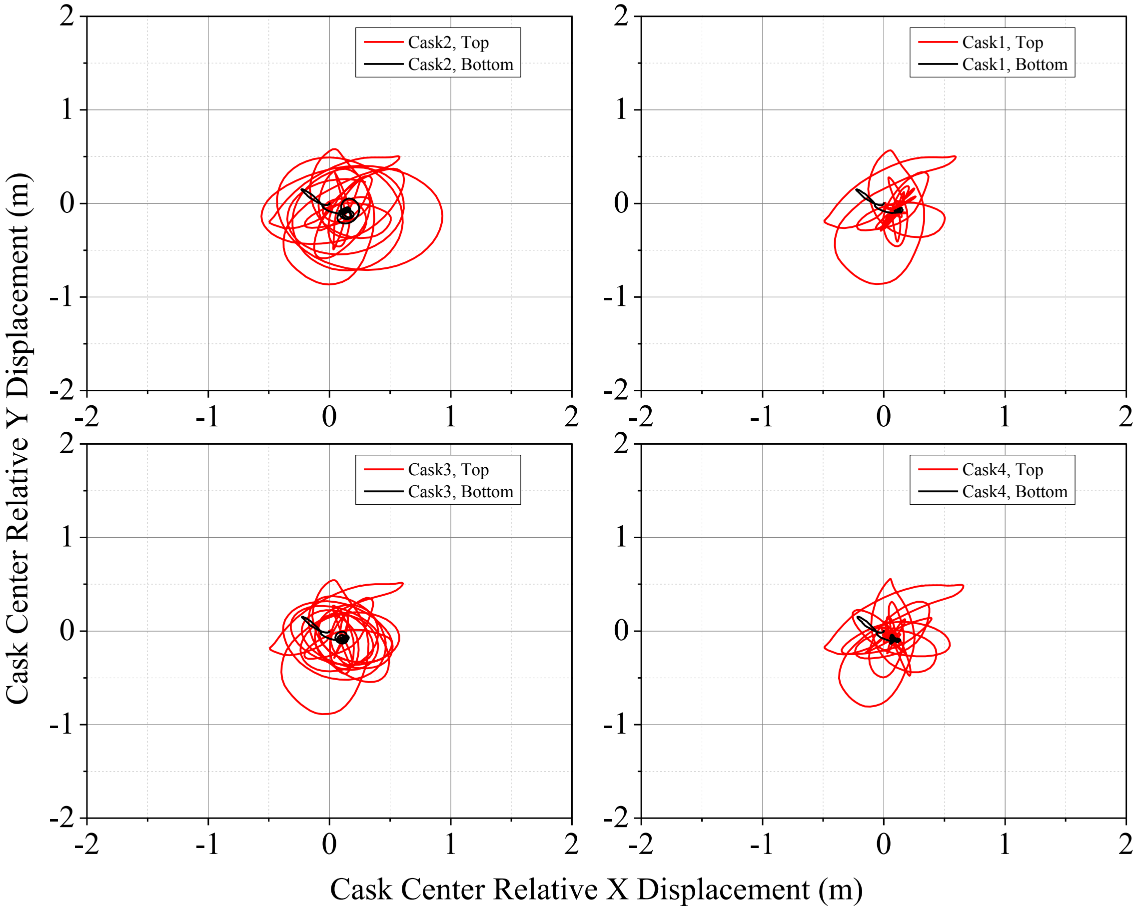

Figure B.5. Cask centers' XY lateral displacement relative to pad, cask-pad-soil model (full scale), $r/h_{cg} = 0.43$, $\mu = 0.55$, convolved 10,000-year Erzican

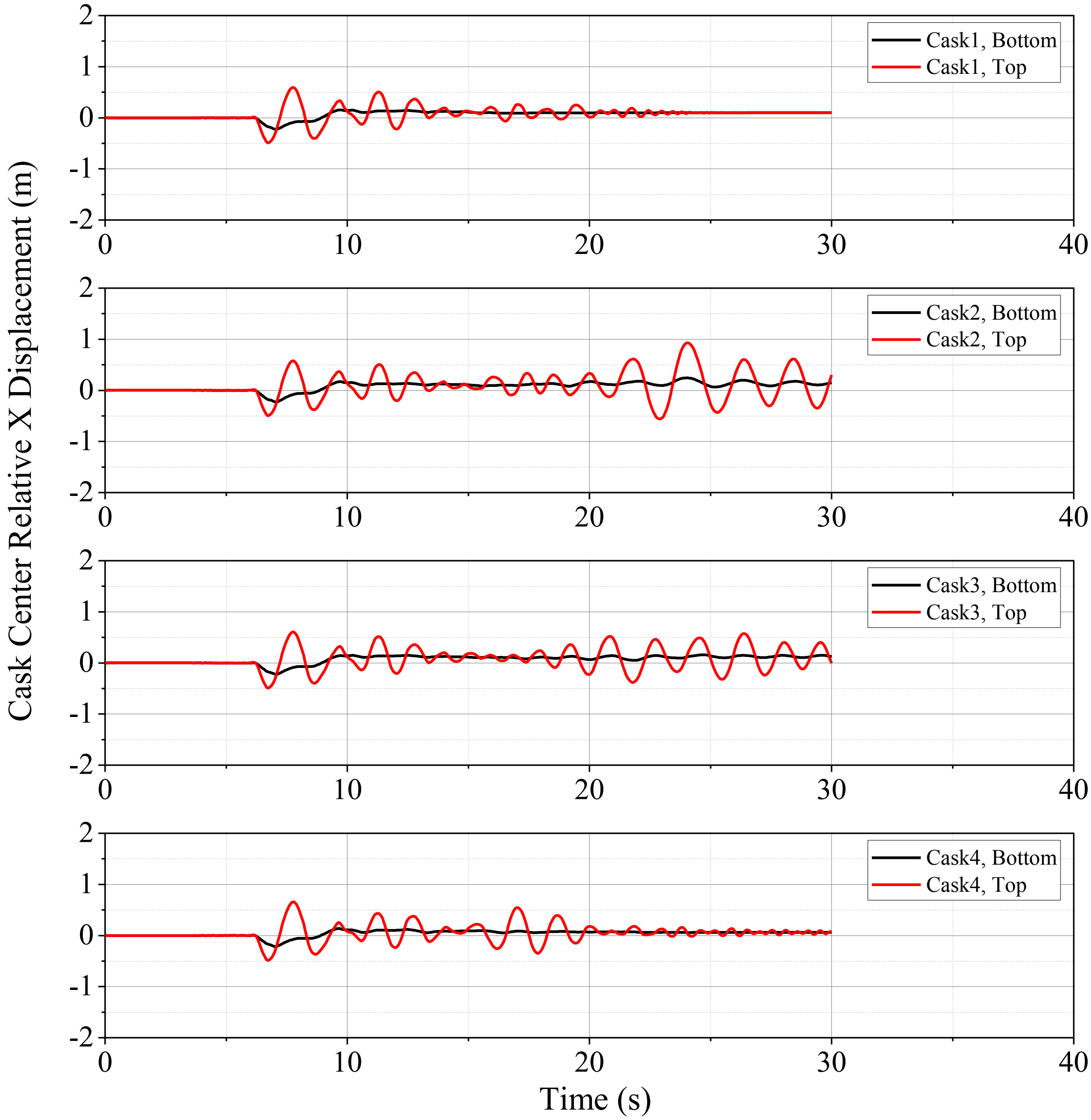

Figure B.6. Time histories of casks X displacement relative to pad, cask-pad-soil model (full scale), $r/h_{cg} = 0.43$, $\mu = 0.55$, convolved 10,000-year Erzican

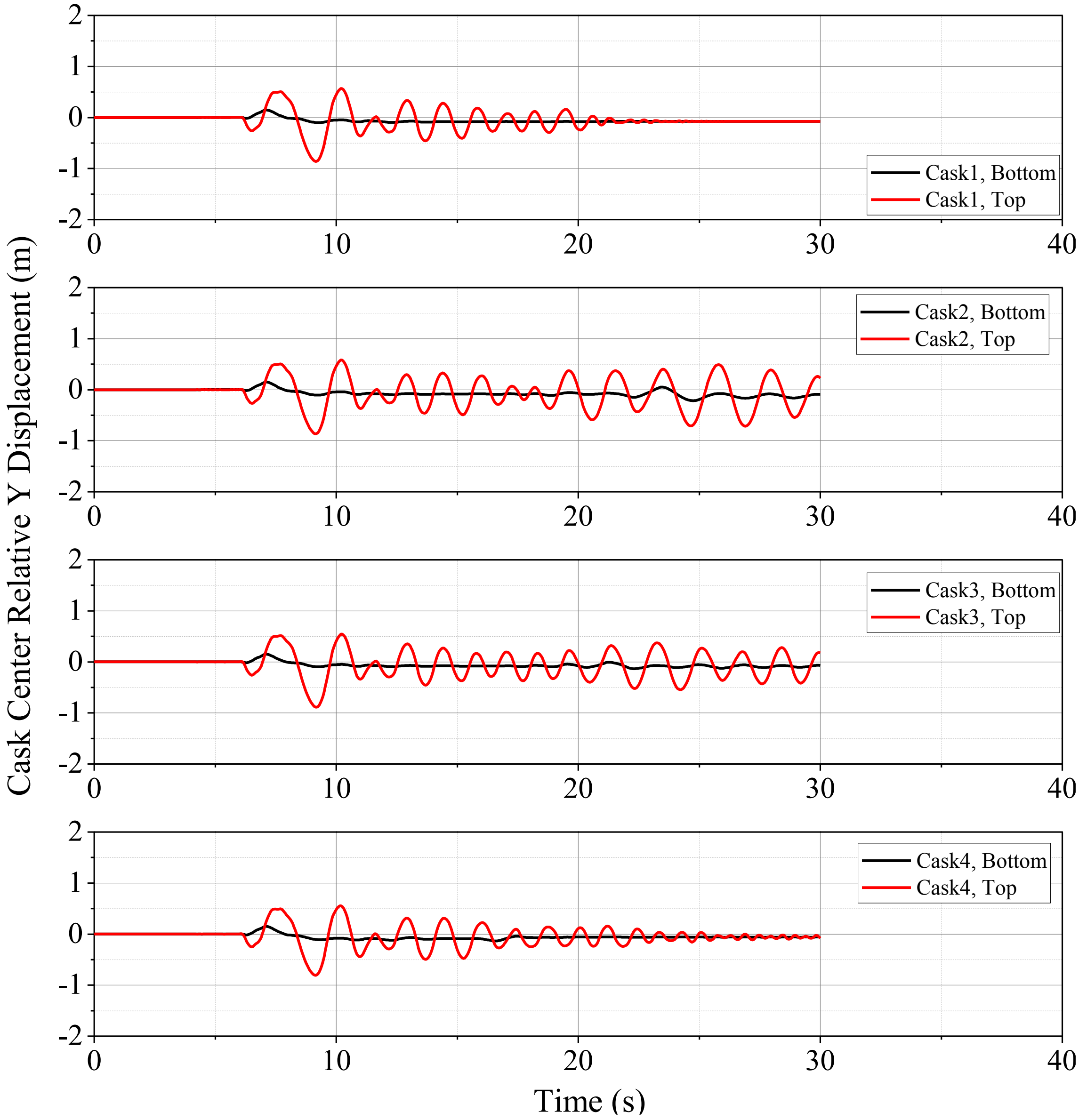

Figure B.7. Time histories of casks Y displacement relative to pad, cask-pad-soil model (full scale), $r/h_{cg} = 0.43$, $\mu = 0.55$, convolved 10,000-year Erzican

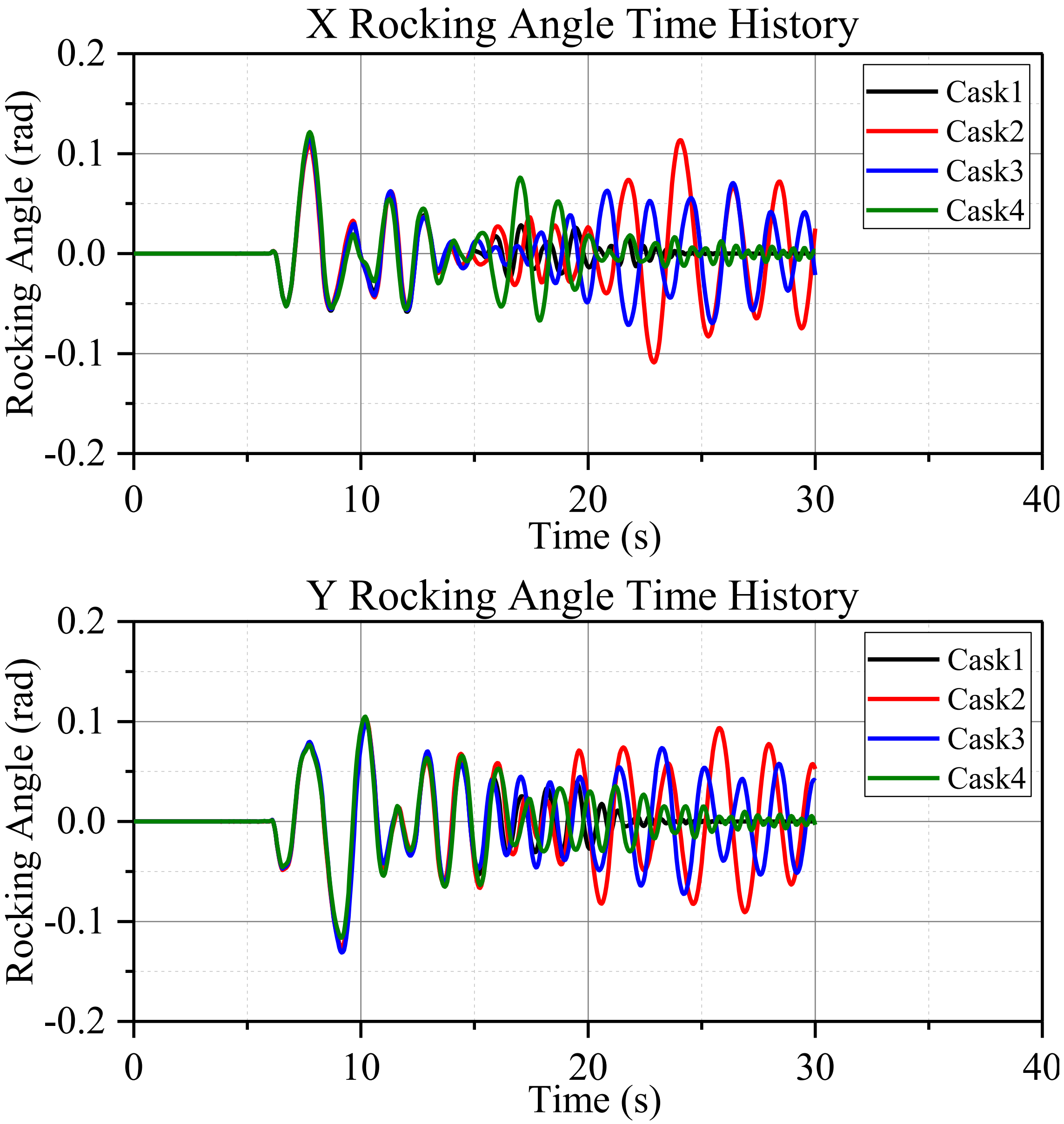

Figure B.8. Rocking angle time histories, cask-pad-soil model (full scale), $r/h_{cg} = 0.43$, $\mu = 0.55$, convolved 10,000-year Erzican

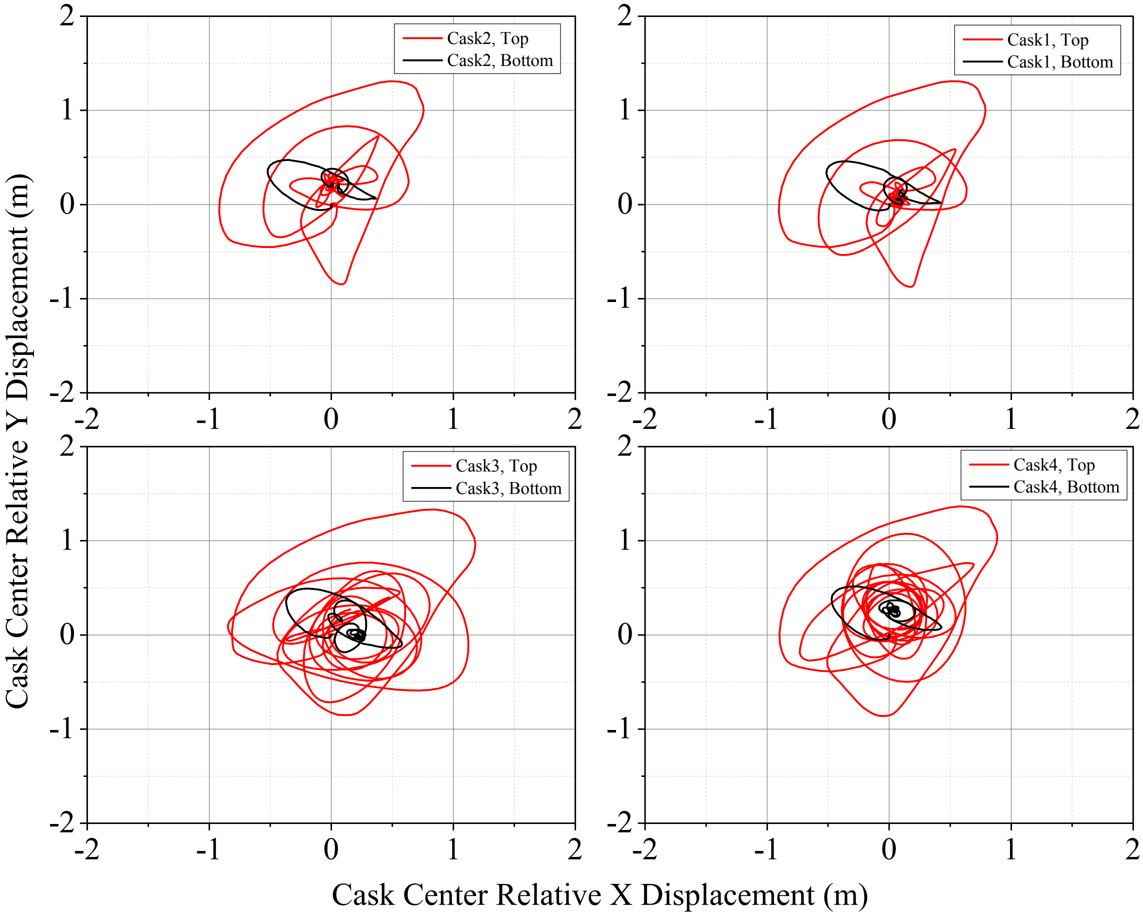

Figure B.9. Cask centers' XY lateral displacement relative to pad, cask-pad-soil model (full scale), $r/h_{cg} = 0.43$, $\mu = 0.55$, convolved 30,000-year Erzican

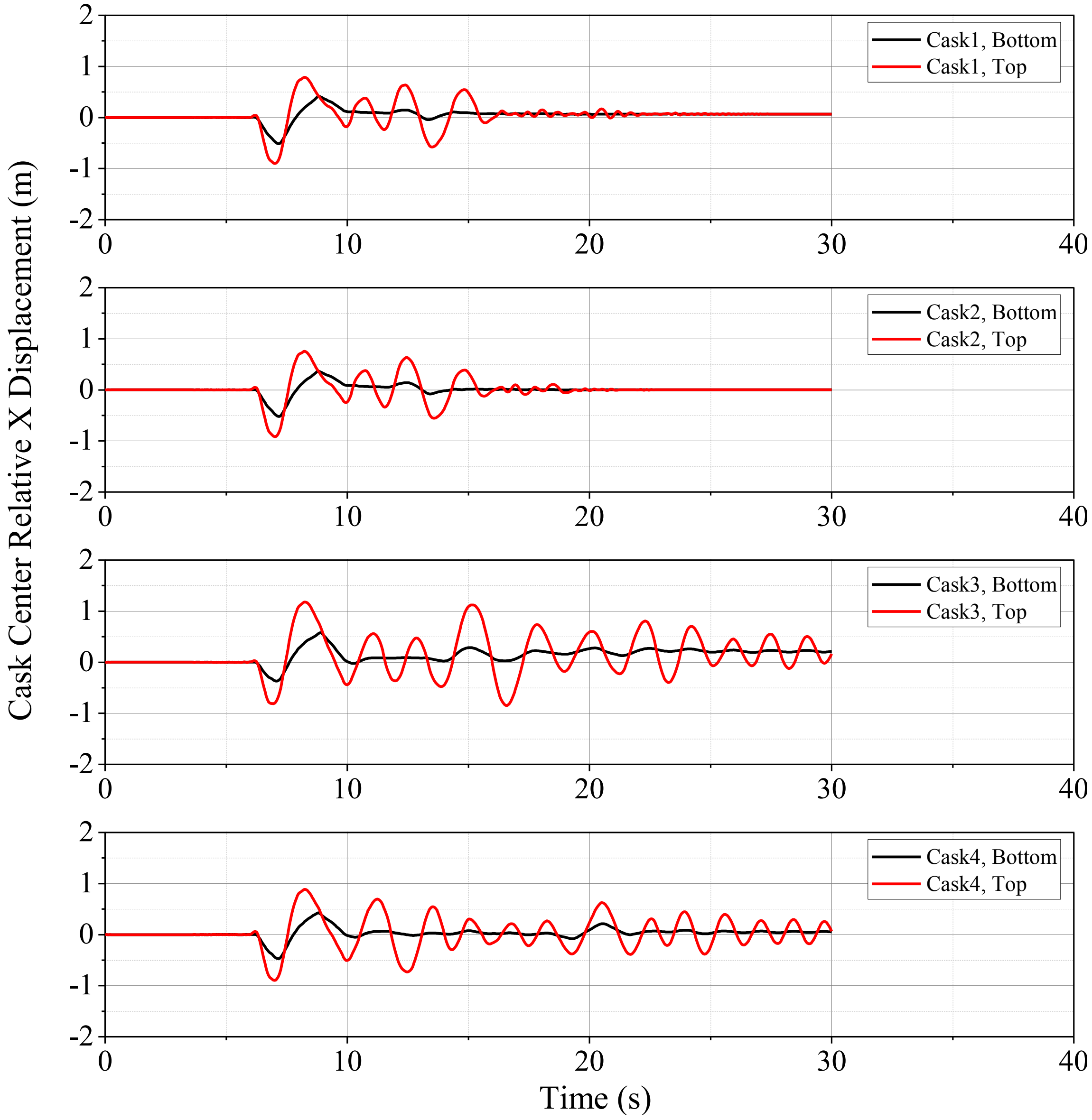

Figure B.10. Time histories of casks X displacement relative to pad, cask-pad-soil model (full scale), $r/h_{cg} = 0.43$, $\mu = 0.55$, convolved 30,000-year Erzican

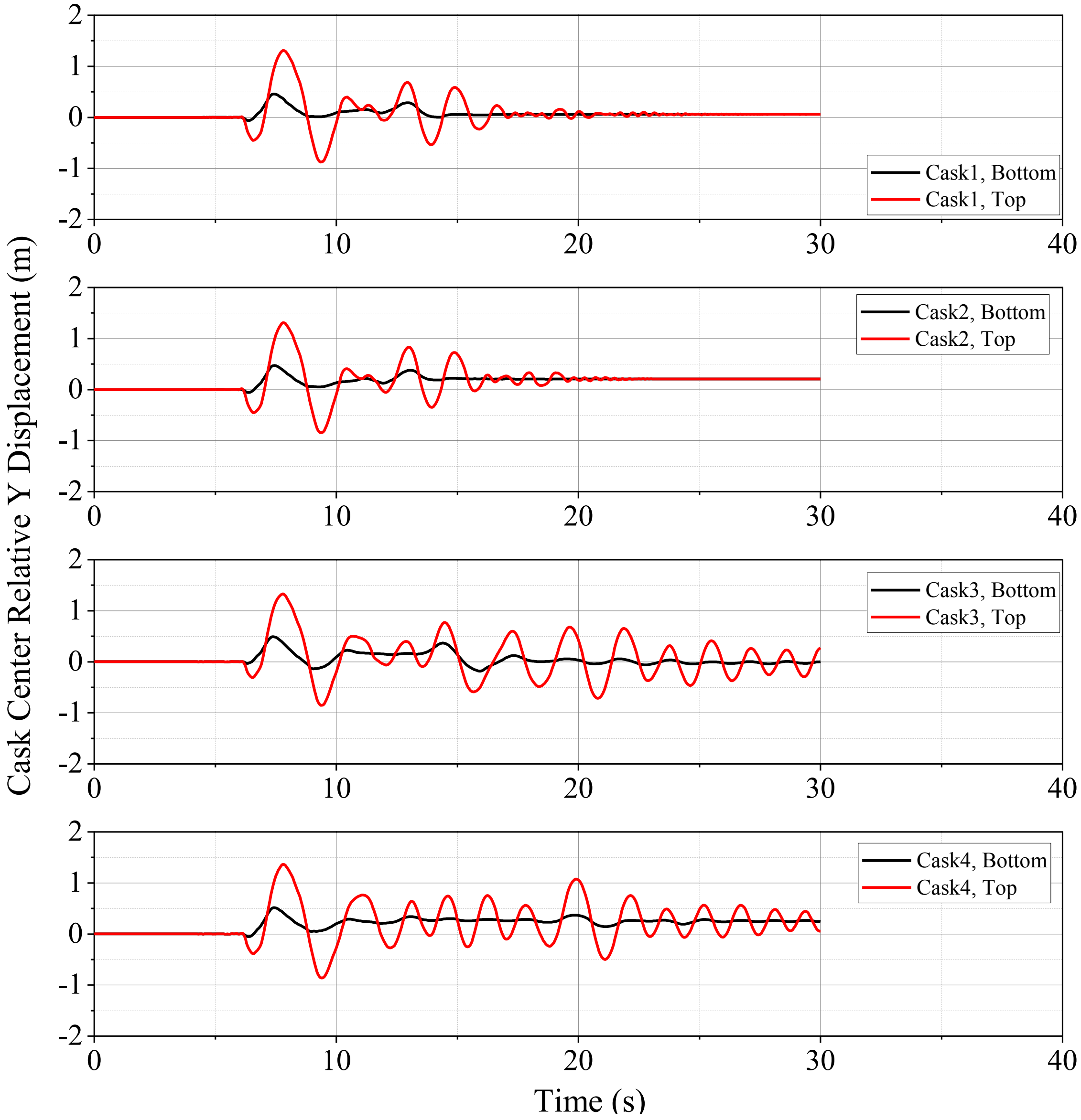

Figure B.11. Time histories of casks Y displacement relative to pad, cask-pad-soil model (full scale), $r/h_{cg} = 0.43$, $\mu = 0.55$, convolved 30,000-year Erzican

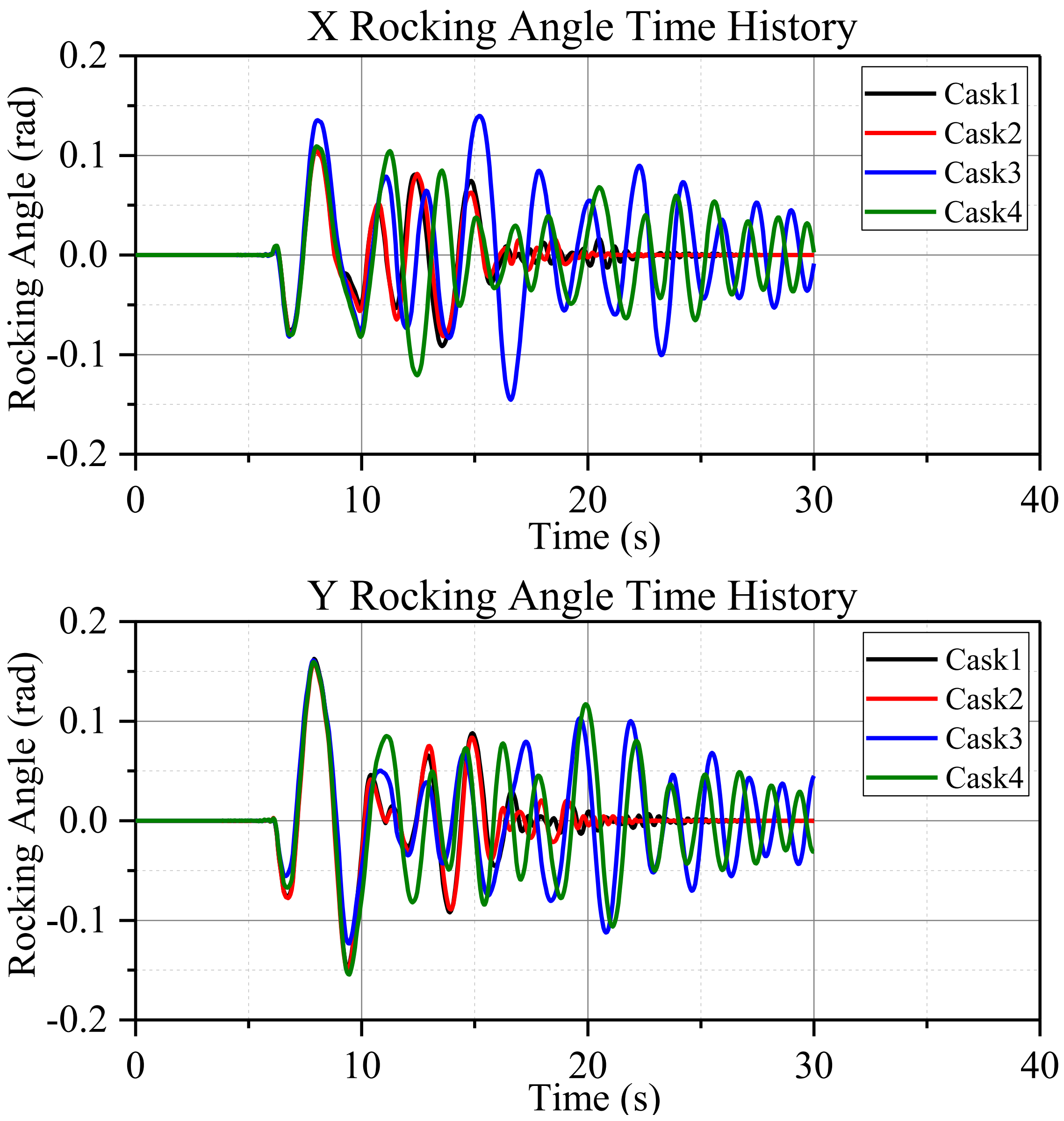

Figure B.12. Rocking angle time histories, cask-pad-soil model (full scale), $r/h_{cg} = 0.43$, $\mu = 0.55$, convolved 30,000-year Erzican

B.3 FE Model (Cask-Pad-Soil) Simulation Output: $r/h_{cg} = 0.55$

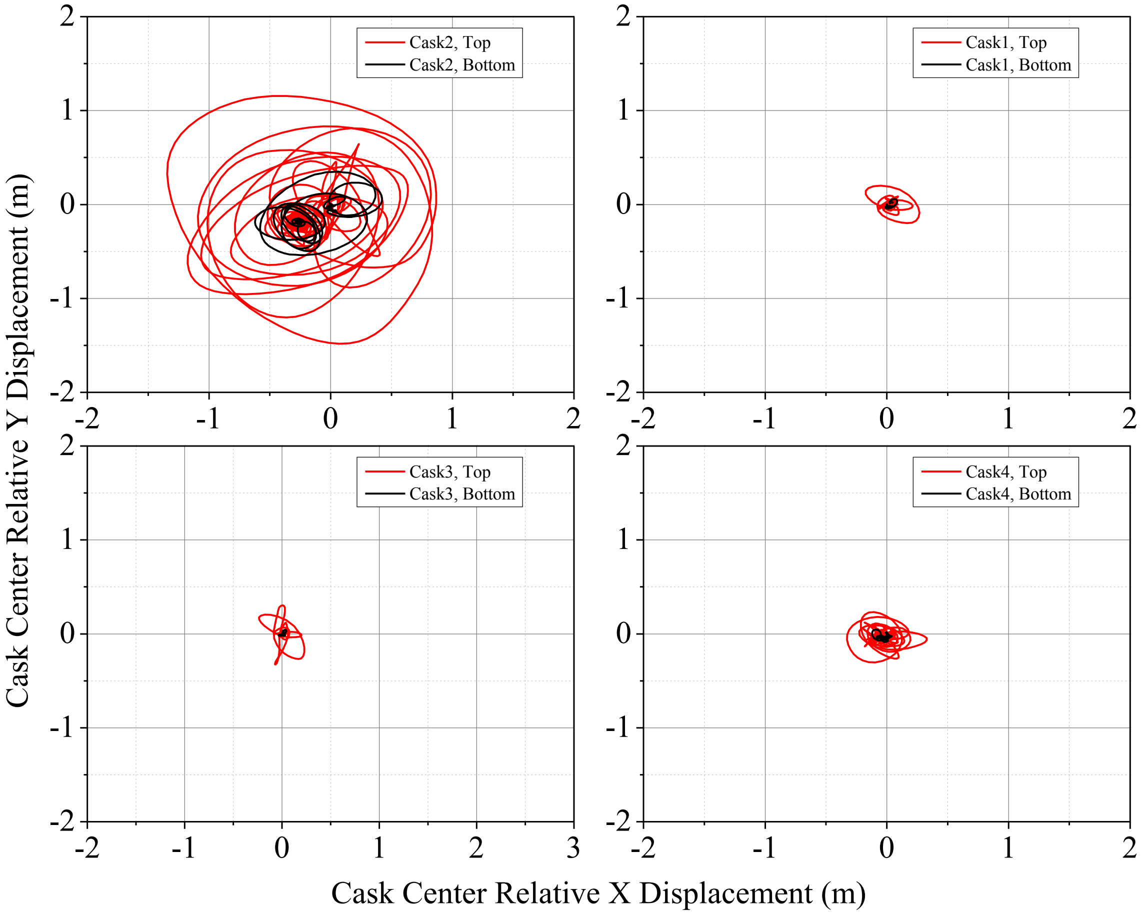

Figure B.13. Cask centers' XY lateral displacement relative to pad, cask-pad-soil model (full scale), $r/h_{cg} = 0.55$, $\mu = 0.55$, convolved 10,000-year Chi-Chi

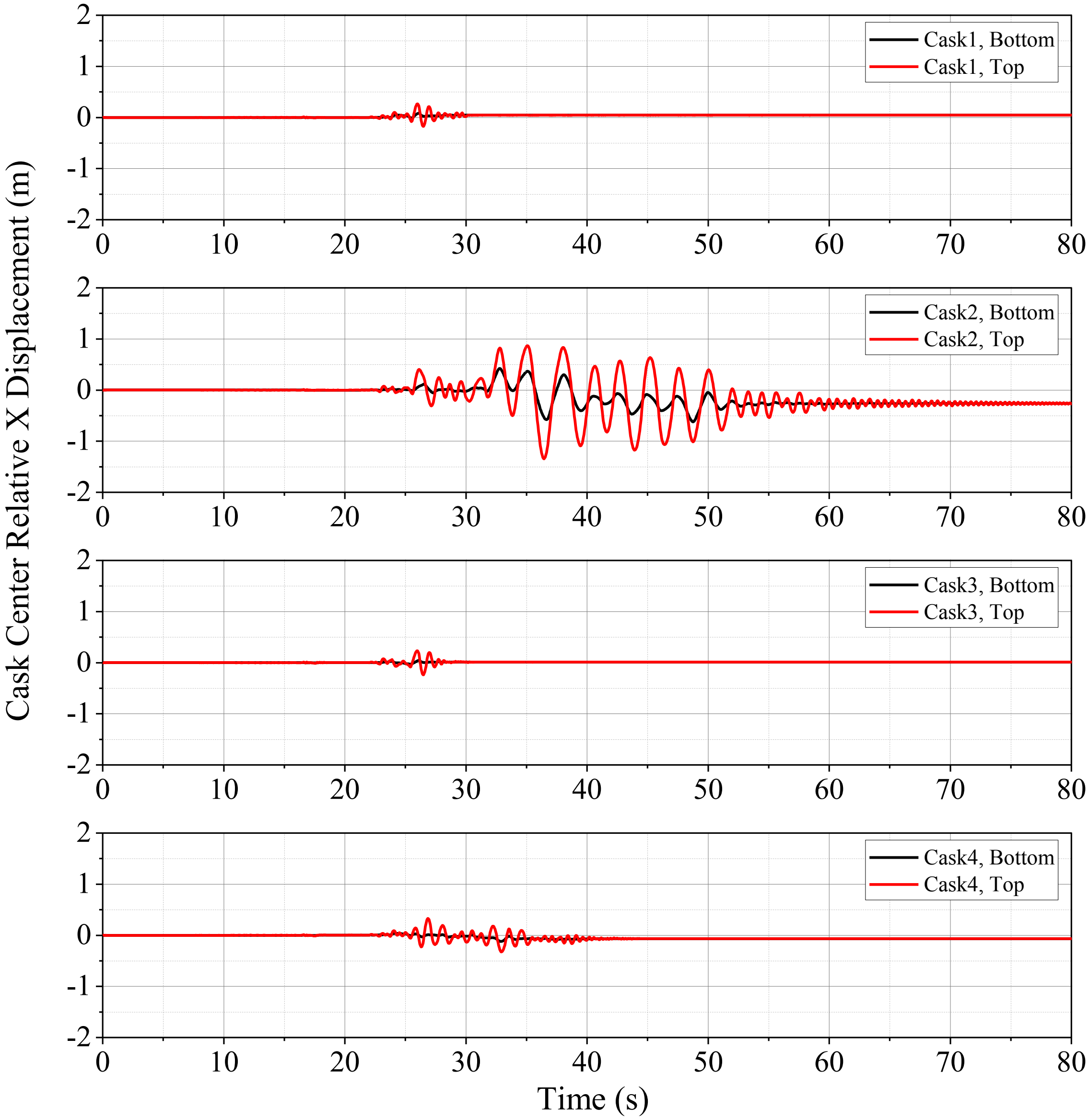

Figure B.14. Time histories of casks X displacement relative to pad, cask-pad-soil model (full scale), $r/h_{cg} = 0.55$, $\mu = 0.55$, convolved 10,000-year Chi-Chi

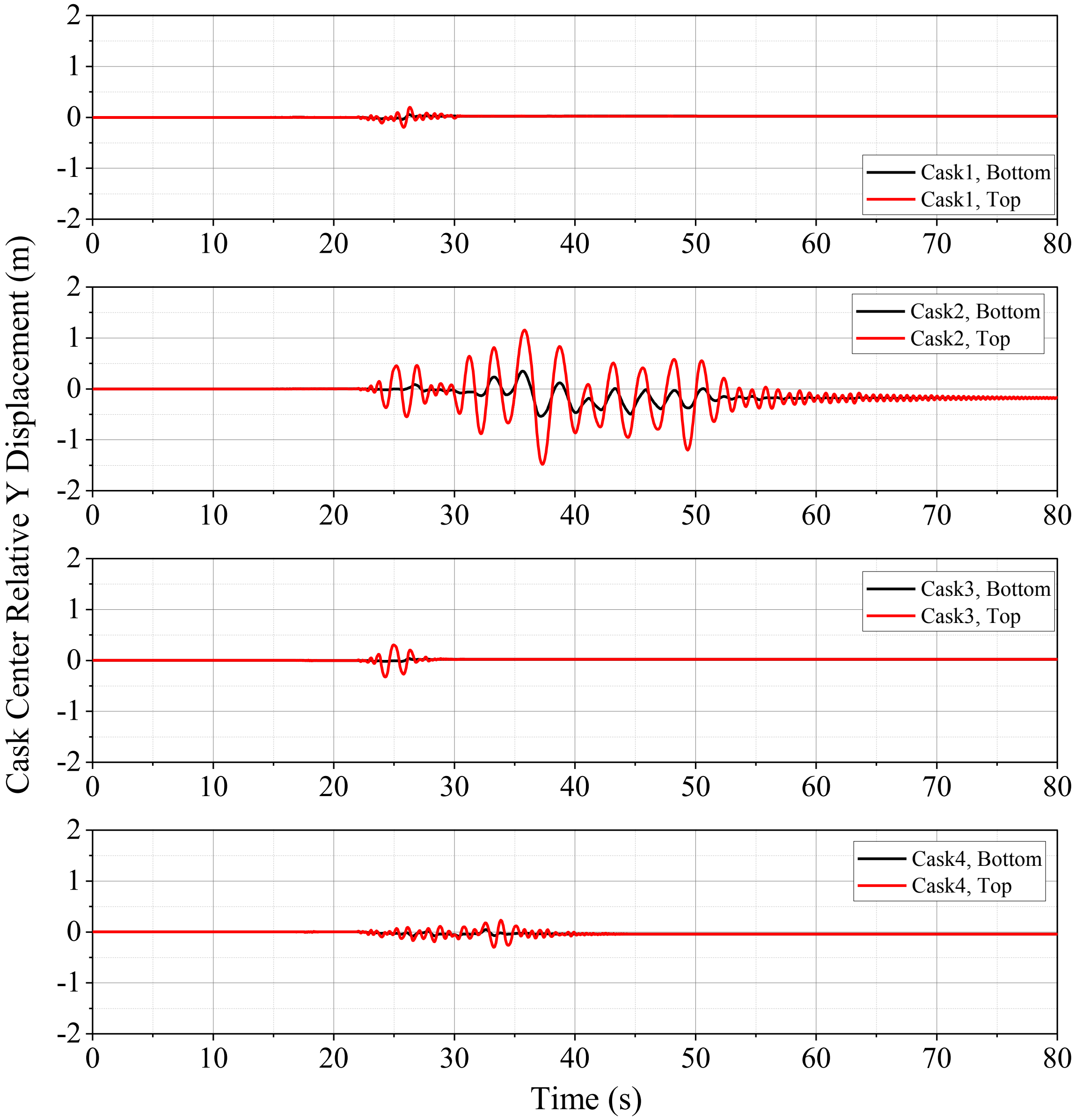

Figure B.15. Time histories of casks Y displacement relative to pad, cask-pad-soil model (full scale), $r/h_{cg} = 0.55$, $\mu = 0.55$, convolved 10,000-year Chi-Chi

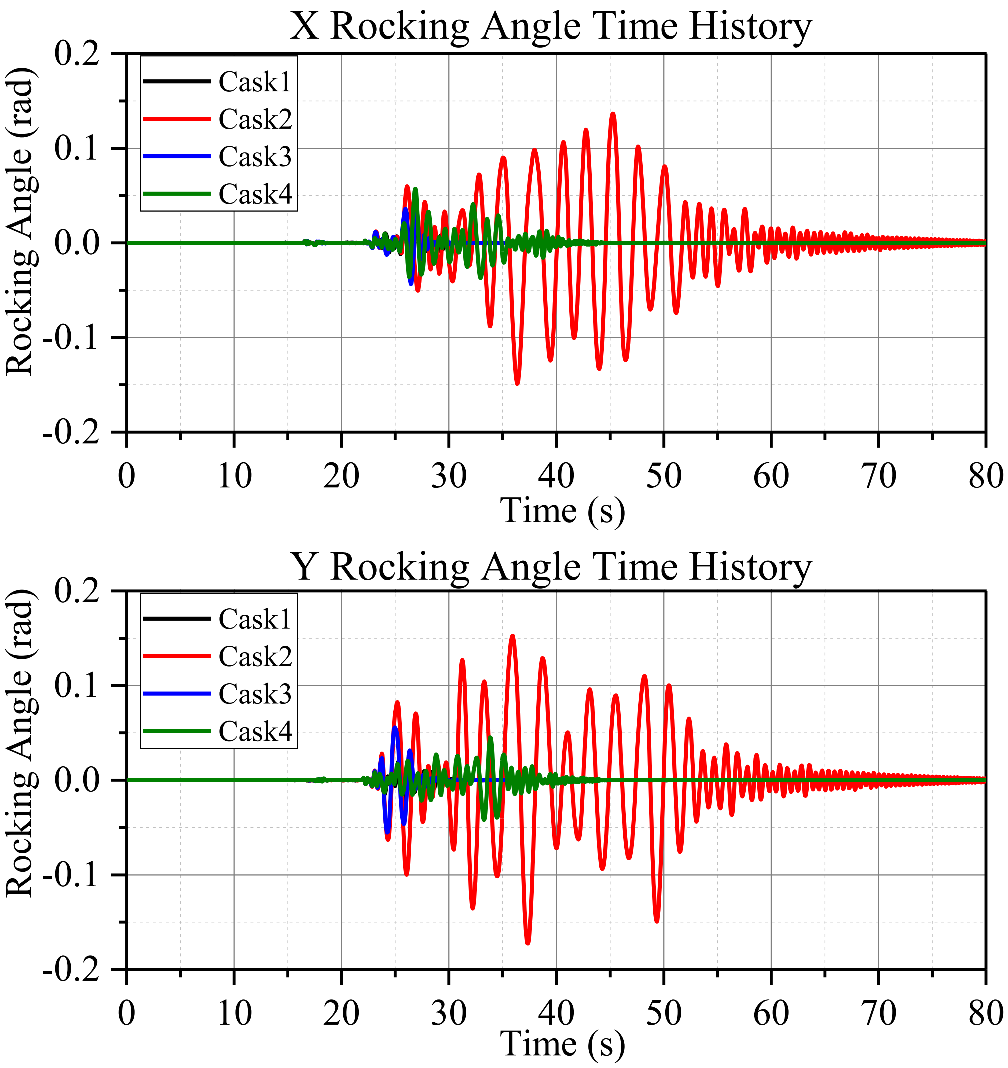

Figure B.16. Rocking angle time histories, cask-pad-soil model (full scale), $r/h_{cg} = 0.55$, $\mu = 0.55$, convolved 10,000-year Chi-Chi

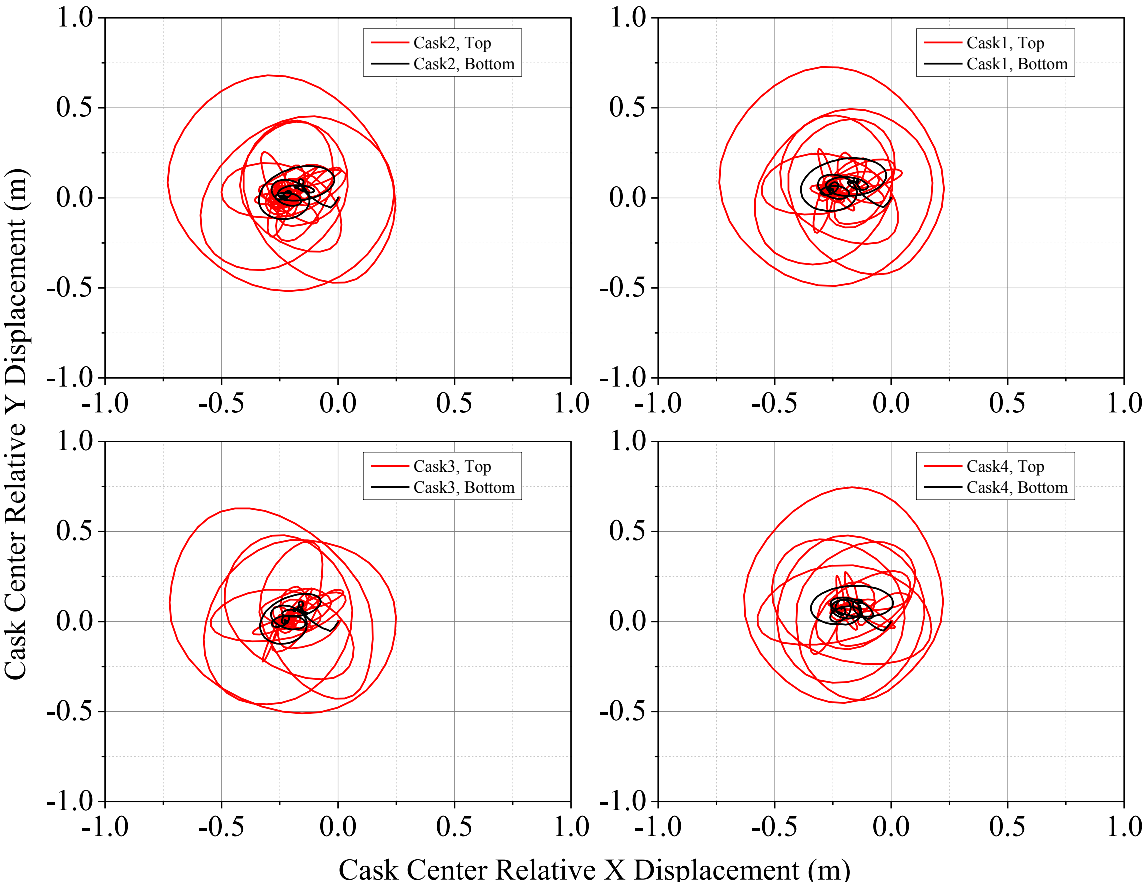

Figure B.17. Cask centers' XY lateral displacement relative to pad, cask-pad-soil model (full scale), $r/h_{cg} = 0.55$, $\mu = 0.55$, convolved 10,000-year Erzican

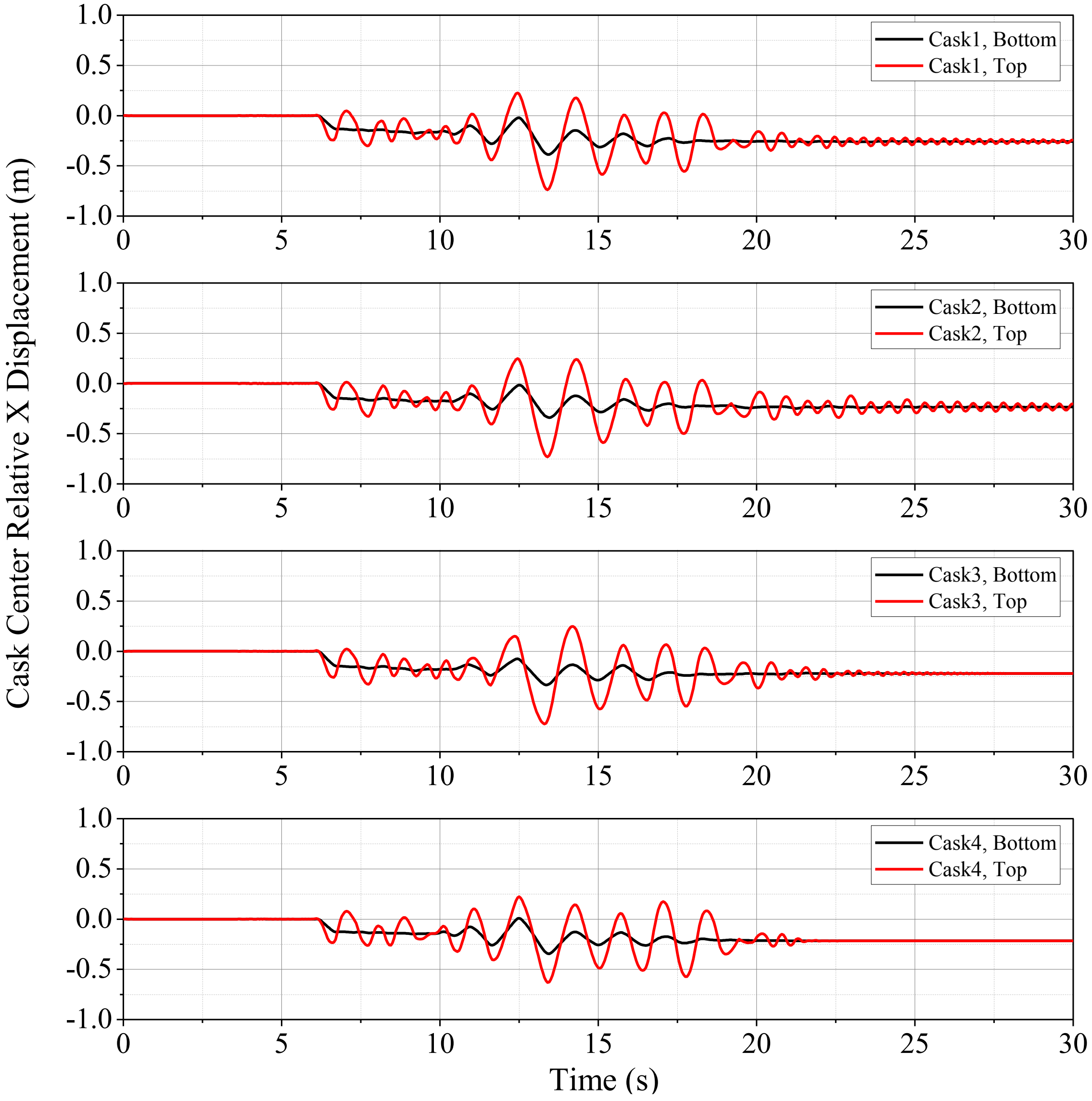

Figure B.18. Cask centers' X lateral displacement relative to pad, cask-pad-soil model (full scale), $r/h_{cg} = 0.55$, $\mu = 0.55$, convolved 10,000-year Erzican

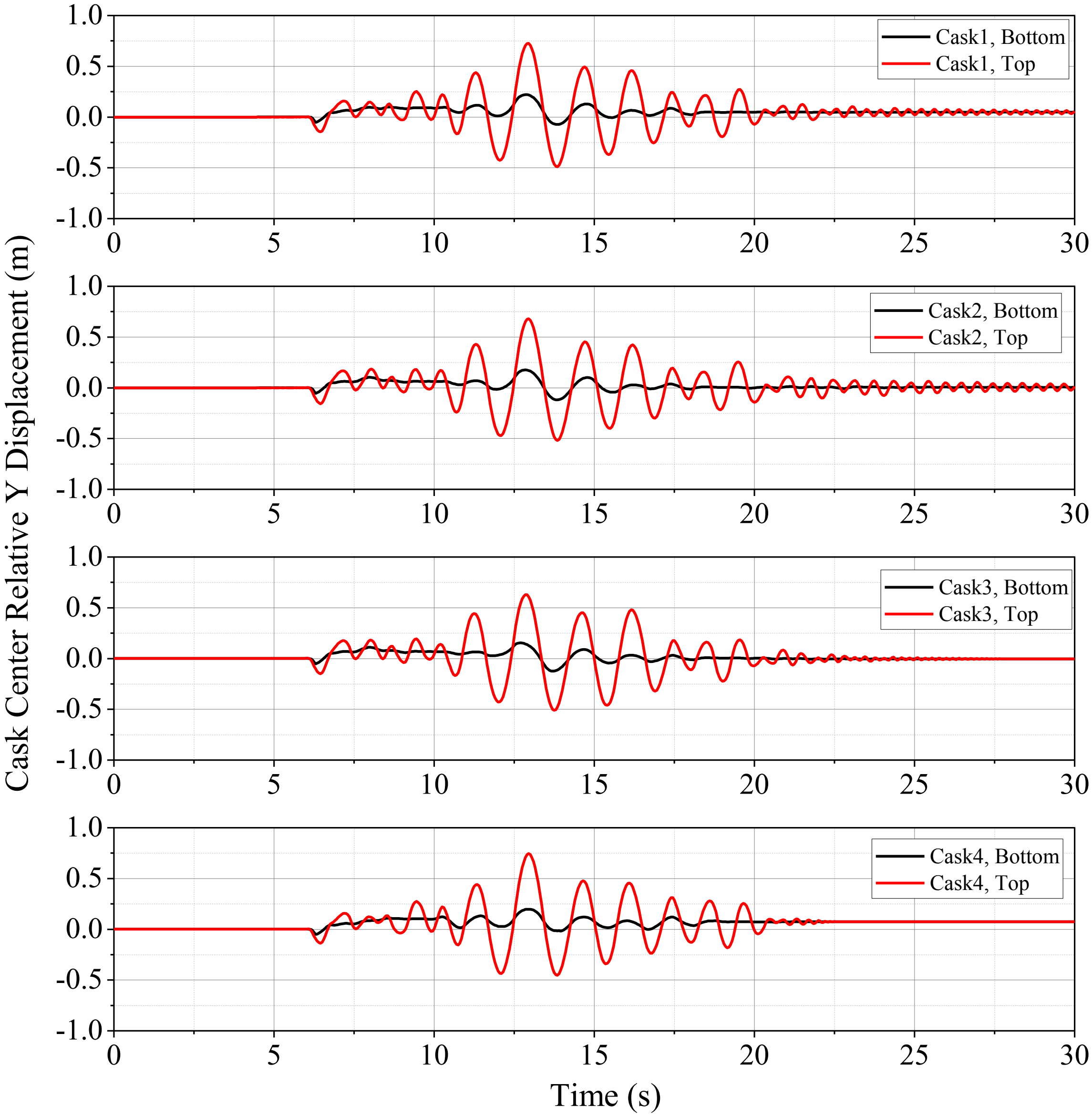

Figure B.19. Cask centers’ Y lateral displacement relative to pad, cask-pad-soil model (full scale), $r/h_{cg} = 0.55$, $\mu = 0.55$, convolved 10,000-year Erzican

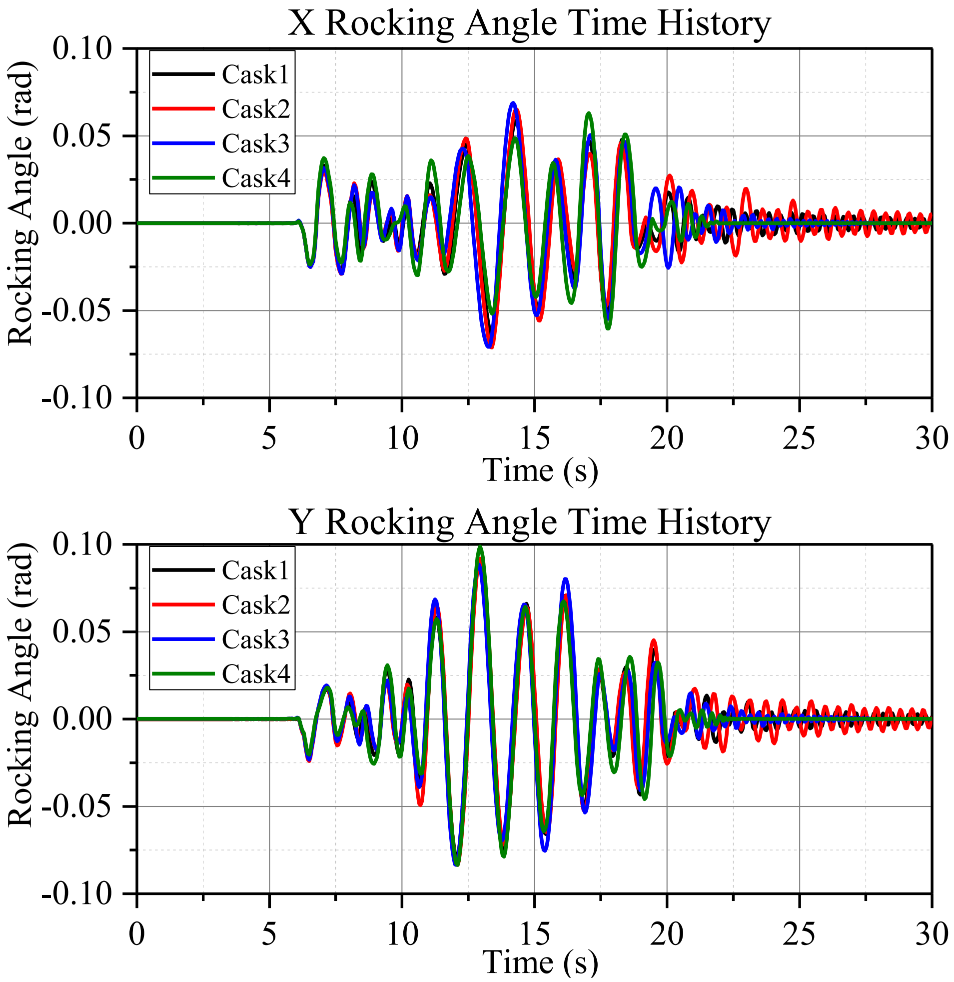

Figure B.20. Rocking angle time histories, cask-pad-soil model (full scale), $r/h_{cg} = 0.55$, μ = 0.55, convolved 10,000-year Erzican

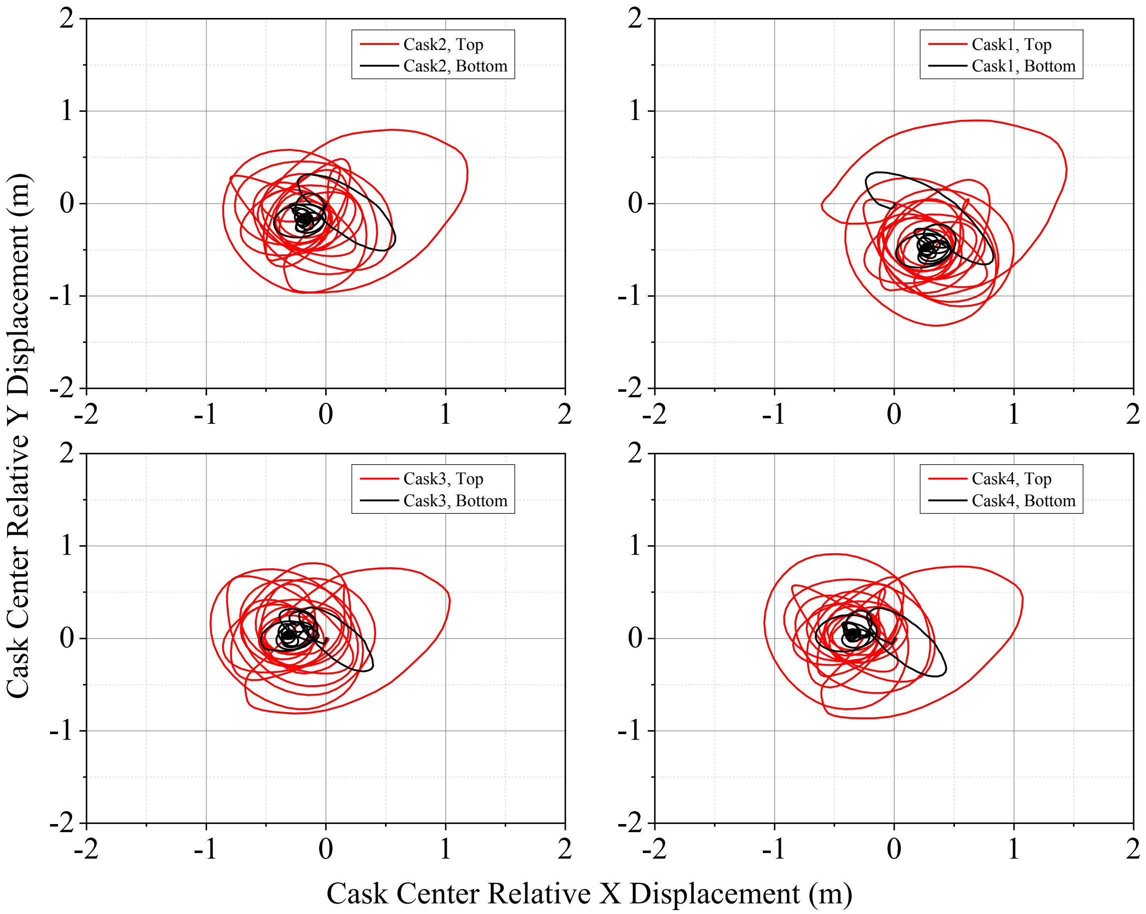

Figure B.21. Cask centers' XY lateral displacement relative to pad, cask-pad-soil model (full scale), $r/h_{cg} = 0.55$, $\mu = 0.55$, convolved 30,000-year Erzican

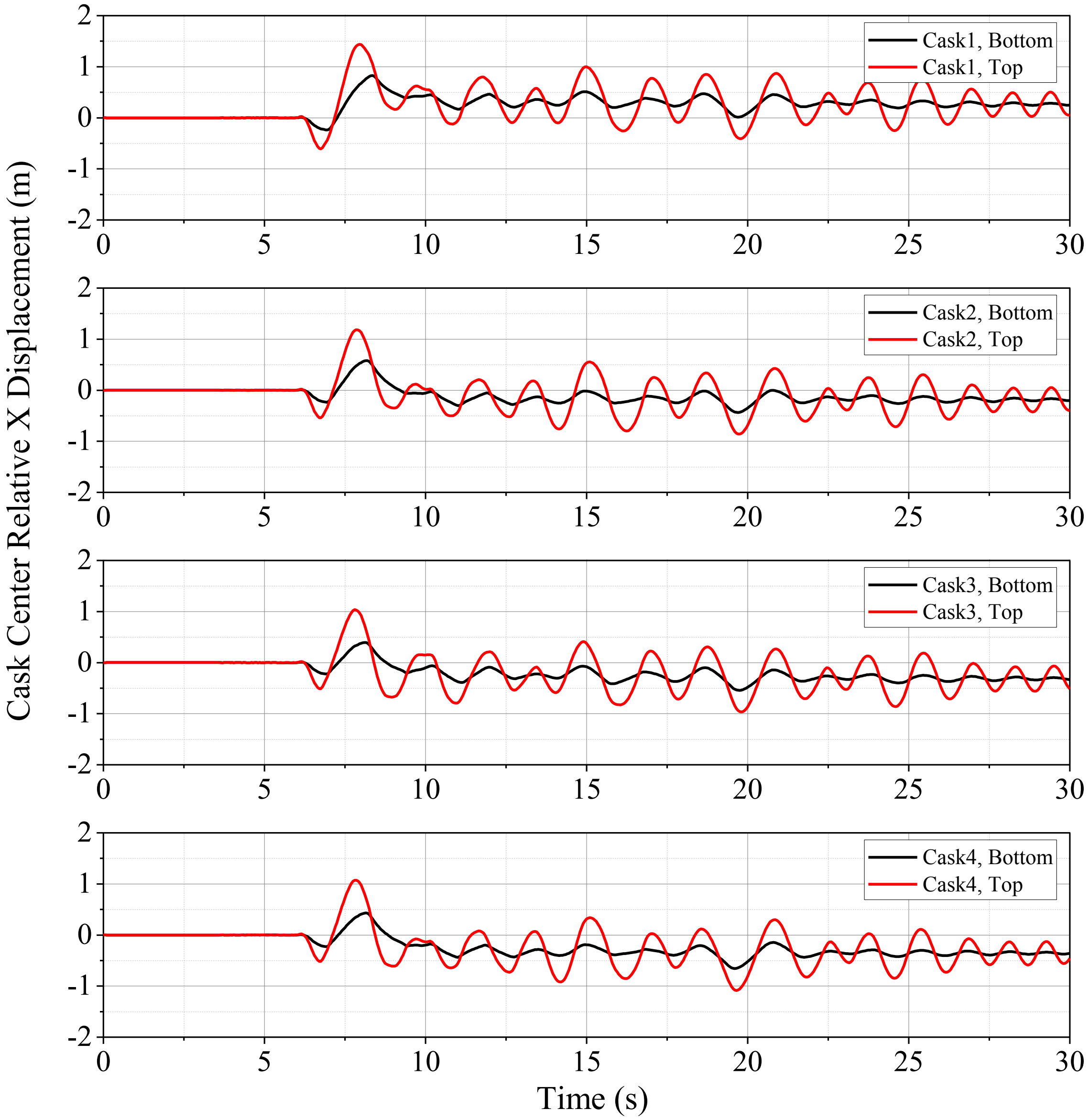

Figure B.22. Cask centers' X lateral displacement relative to pad, cask-pad-soil model (full scale), $r/h_{cg} = 0.55$, $\mu = 0.55$, convolved 30,000-year Erzican

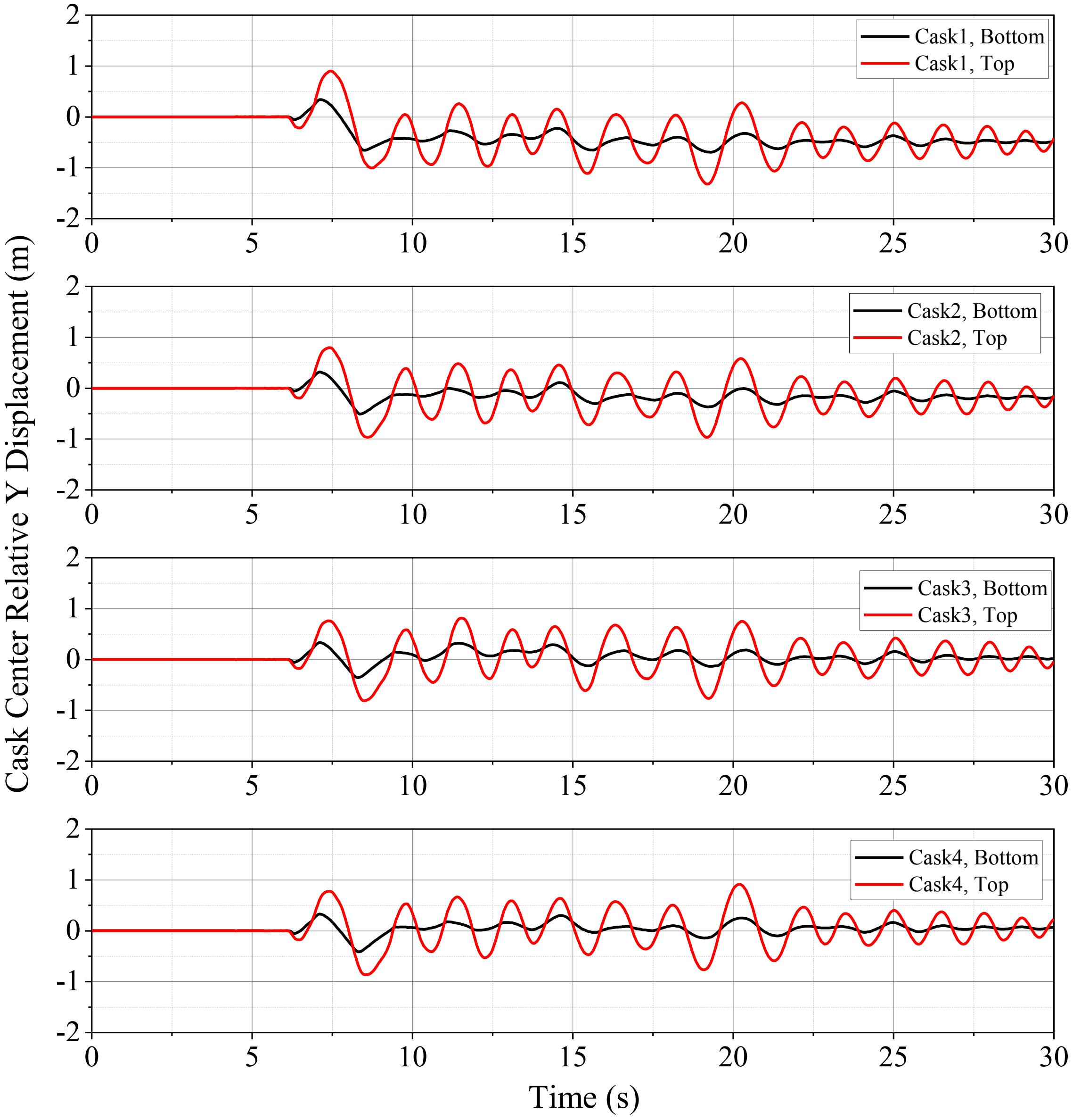

Figure B.23. Cask centers' Y lateral displacement relative to pad, cask-pad-soil model (full scale), $r/h_{cg} = 0.55$, $\mu = 0.55$, convolved 30,000-year Erzican

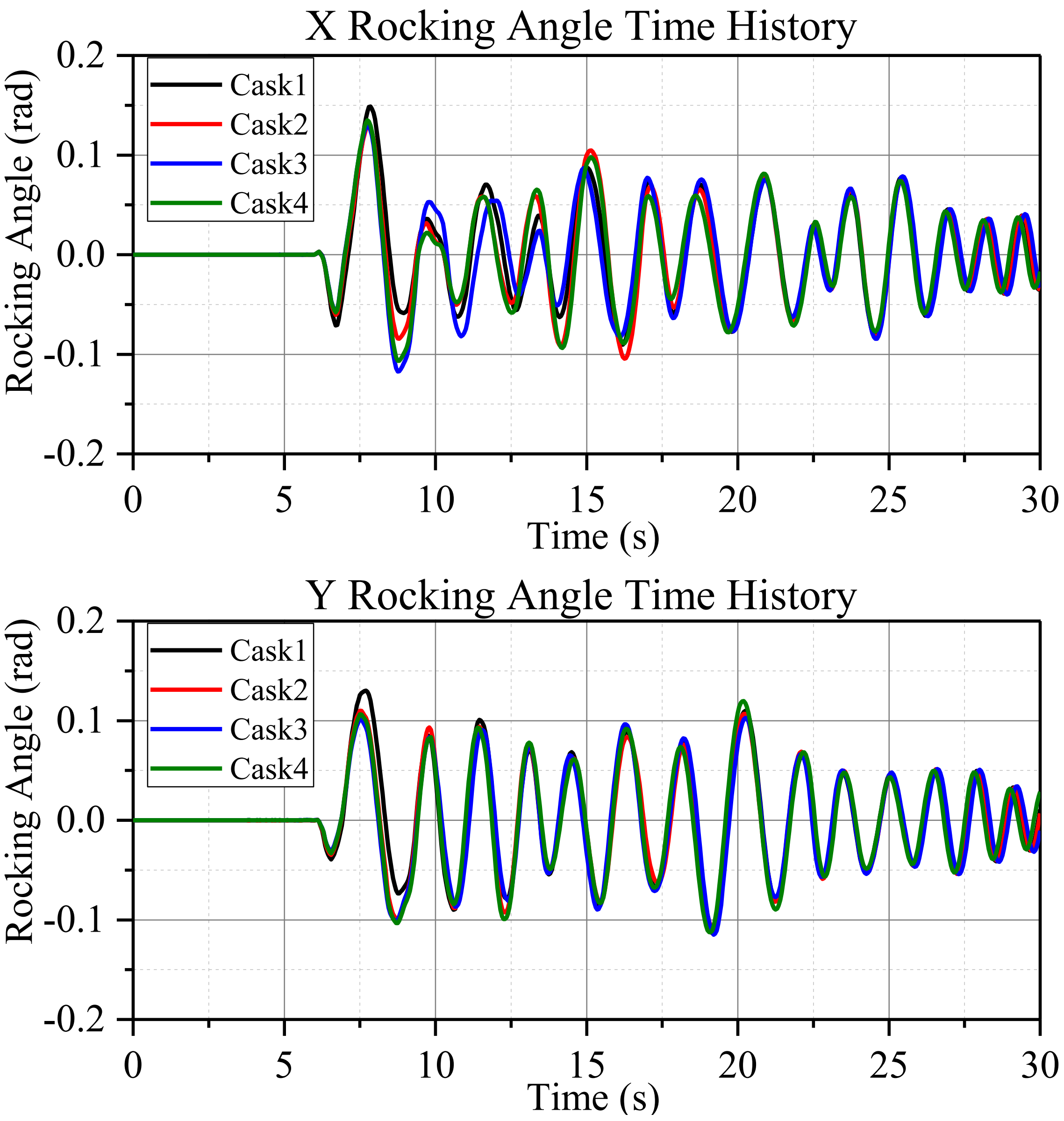

Figure B.24. Rocking angle time histories, cask-pad-soil model (full scale), $r/h_{cg} = 0.55$, $\mu = 0.55$, convolved 30,000-year Erzican

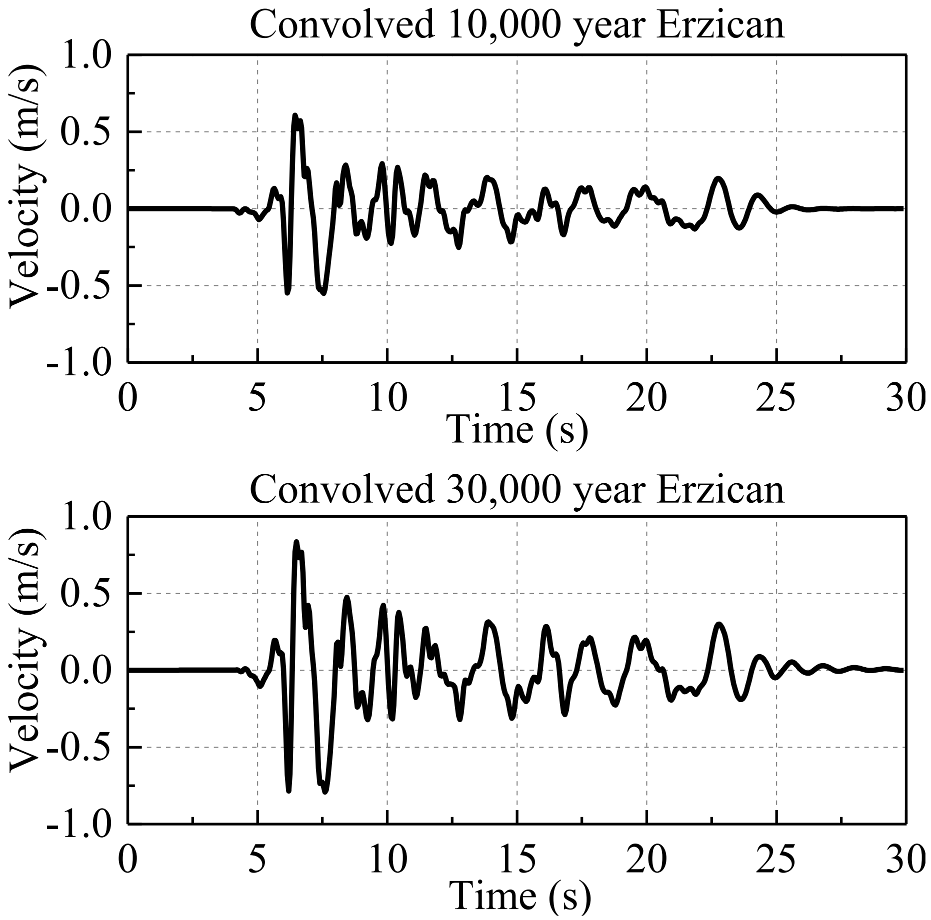

Figure B.25. Velocity time histories, convolved 10,000- and 30,000-year Erzican at surface of soil column

APPENDIX C

SUPPLEMENTARY MONTE CARLO SIMULATIONS

Supplementary Monte Carlo simulations were performed for FS.43 with r/h_{cg} of 0.43, idealized as pure rocking only in a 2D space. For some supplementary runs, the goal of the simulation was to evaluate the potential for chaotic behavior. Therefore, small variations of 1% were considered for the input parameters. In other cases, a more traditional parametric study was carried out using reasonable probabilistic distribution of the input parameters.

C.1 Supplementary Run I (SR-I)

In SR-I, simulations were performed to evaluate the potential for chaotic behavior using spectrally matched ground motions (WUS rock, Figures 3.7 and 3.8), and the original SFPD motion without spectrum matching (Figure 3.9). For each considered parameter, a set of 10,000 random numbers were generated in MATLAB [69] using a uniform distribution to generate random numbers between 0 and 1. To change the range from [0, 1] to a specific range [a, b], the following equation was used.

$$Rn = (b - a) \cdot rand(10000,1) + a \tag{C.1}$$

where, Rn is the final set of random numbers; a and b are the lower and upper bound of the range, respectively, and *rand*(10000,1) is a MATLAB command used to generate a set of 10,000 random numbers between 0 and 1. Parameters COR (e), *p*, and PGA were varied between a range of ±1%. Hence, a = -1 and b = 1 for those parameters. The solution time step (*dt*) parameter was varied between 10^{-3} and 10^{-4}. Finally, the initial angle (θ_0) was varied in the range of ±0.004 radians (1% of α = 0.40). Positive and negative sign for rocking angle denotes clockwise (rocking about O) and counter-clockwise (rocking about O') as seen in Figure 4.8, respectively. Note that the parameter *f* (frequency of the ground motion), was not considered in this case.

Four subcases were studied for SR-I, as can be seen in Table C.1. For each of the 10,000 realizations, the evaluated parameters were randomly paired. The maximum rocking angle was then computed, and a distribution of the maximum rocking angle was obtained.

C.2 Supplementary Run II (SR-II)

Two parameters, COR (*e*) and PGA, were considered for SR-II, which investigates the effect of uncertainty on the input parameters on the rocking angle response. Both parameters were assumed to have a log-normal distribution. Spectrally match ground motions were considered for this case. Like in SR-I, PGA was varied by linearly scaling the ground motion. To generate the distribution, PGA of a given acceleration time history was considered as median and $\sigma_{\ln}$ (standard deviation of natural logarithm of data) was taken as 0.2 and 0.3, and the distribution was truncated at $\pm 2\sigma_{\ln}$.

The procedure adopted for probabilistic variation of *e* has already been presented described in Section 8.3 (Chapter 8). Table C.2 summarizes the parameter variation considered for SR-II.

C.3 Supplementary Run III (SR-III)

SR-III includes "soil motions" for Erzican and Chi-Chi (10,000- and 30,000-year return period) obtained from deconvolution and convolution process (Chapter 7), instead of rock motions. This case was performed to study the effect of change in dominant period of ground motion (i.e., soil effects on the free-standing body's response). Table C.3 summarizes the parameter variations for SR-III.

C.4 Output from the Monte Carlo runs

C.4.1 SR-I

Figure C.1 shows the absolute maximum rocking angle distribution obtained from the MC simulation (10,000 runs) for spectrally matched Erzican and Chi-Chi WUS rock motion at 10,000- and 30,000-year return periods. The rocking angle distribution is also presented for the original SFPD motion without spectral matching. Figure C.2 shows similar distributions for same ground motions, but vertical acceleration is not included. Both figures show realizations that do not include the variation of initial rocking angle (θ_0), whereas Figure C.3 shows data from similar simulations that include the variation in initial rocking angle (θ_0). Figure C.4 presents the results for case where only e is varied, and all other parameters are kept constant.

Table C.4 summarizes the results for four SR-I runs. It can be seen that the coefficient of variation of the maximum rocking angle can be as high as 0.4-0.5, although the input parameters varied by only ±1%. In general, vertical acceleration increased the mean rocking angle, but this effect was not consistent. The results show that when a ground motion is applied to the cask, the vertical acceleration is not necessary for lack of repeatability on the rocking angle variation. However, when a sinusoidal motion is applied, a horizontal acceleration not only does result in response variation, and lack of repeatability in the response is only observed when vertical accelerations are also applied to the cask. This finding is consistent with previous studies [27,28,68] and results from repeated experimental tests performed in this research [53]. The effect of small initial rocking angle variation is also not uniform. A comparison of the four subcases (Figures C.1-C.4 and Table C.4) shows that distribution of maximum rocking angle is larger for far field motions (10,000- and 30,000- year Chi-Chi earthquake) than for near field motions (10,000- and 30,000-year Erzican). This indicates that the lack of repeatability is larger for FFGMs that have more large cycles.

C.4.2 SR-II

In SR-II, the variation in input parameters was expected to represent the intrinsic variability of the *e* and PGA, and not minute changes of ±1% to identify chaotic responses. The results for different combinations of log-normally distributed *e* and PGA are presented in Figures C.5-C.8 and summarized in Table C.5. SR-II results also show a larger variation on the maximum rocking angle for FFGM results, when compared to those obtained for NFGM.

Figure C.5 shows results when only *e* is considered as input random variable. The results of Figure C.6 show the maximum rocking angle variation when the $\sigma_{(\ln PGA)} = 0.2$, showing an increased dispersion on the response, particularly for NFGMs, over that observed for SR-I. The increase for NFGM variation is expected because the maximum response largely depends on the magnitude of the one or two large cycles in the NFGM time history. In this case, the 30,000-year Chi-Chi simulation produced overturning 6 out of 10,000 (0.06%). Figure C.7 present variation on the rocking angle when both the *e* and PGA are varied, and in this case the 30,000-year Chi-Chi simulation resulted in 19 overturning cases out of 10,000 (0.19%) simulations. Figure C.8 presents rocking angle variation when *e* and PGA are varied, although in this case $\sigma_{\ln \text{PGA}}$ increased from 0.2 to 0.3. For this case, simulations for 10,000-year Chi-Chi also produced 1 overturning (0.01%) along with 30,000-year Chi-Chi produced 96 cases of tip-over (0.96%). Note that although Erzican NFGM has a higher median PGA (1.053g vs. 0.64g of FFGM for 10,000-year return period, and 1.412g vs. 0.918g for FFGM 30,000-year return period), no overturning occurred. This shows that having multiple pulses in a ground motion is more detrimental to safety against overturning compared to having one or two large pulses.

C.4.3 SR-III

SR-III also addresses the lack of repeatability and input parameter intrinsic variability on the maximum rocking angle response, but this time the input was convolved soil motions. For the lack of repeatability assessment, Figure C.9 shows results for simulations where *e*, *p*, PGA were varied ±1%, *dt* was varied from 10^{-3} to 10^{-4} and no variation was considered for initial rocking angle ($\theta_0 = 0$). This is similar to simulation case presented by Figure C.1, except for the use of convolved soil motions. Figure C.9 shows that when soil motion is considered the dispersion of peak rocking angle increases even further for FFGM while that for NFGM remains about the same, suggesting that response of free-standing bodies subjected to ground motions containing one or two pulses are more predictable. For FFGMs containing multiple pulses, the results vary dramatically compared to minute changes in the input parameters. This finding further supports the experimental and FE simulations discussed above. Also, the number of overturning cases for convolved 30,000-year Chi-Chi motions were 630 out of 10,000 (6.3%), showing the large influence of soil effects where the dominant period of the motion is elongated.

Figure C.10 shows the distribution of peak rocking angle for case similar to Figure C.8, where only PGA and COR are assumed to exhibit a log-normal distribution. The results for three more simulations using convolved motions are presented in Figures C.11-C.13. The summary for all cases are also tabulated in Table C.6.

Figure C.10 shows that when PGA and COR adopt the specified log-normal distributions, the cask overturns for 0.4% of the realizations for the convolved 10,000-year Chi-Chi, and for 11.24% of the runs for 30,000-year Chi-Chi motions. The rocking angle dispersion increases for NFGM for convolved soil motions, an expected result due to the combination of variation in input parameters and soil effects. However, the cask does not overturn when subjected to Erzican NFGM. An interesting aspect of the cask response under soil motions is that a large number of realizations resulted in almost no rocking of the free-standing body. Apparently, the PGAs of these realizations cross a PGA threshold for rocking response. Many realizations have a PGA smaller than this threshold because of the combination of a PGA distribution on an already reduced PGA due to soil effect. The PGA threshold which results in rocking and no rocking is well defined in literature (e.g., [10,22]) using static force equilibrium. However, the results of this study show that the free-standing planar body will have very small rocking (almost no rocking) for PGAs larger than that predicted by theoretical equations (PGA $\geq r/h_{cg}$*g).

Table C.1. Parameters considered and variation range for Monte Carlo runs (FS.43)

Case		e	Excitation	p	PGA*	dt (s)	θ_0 (rad)
SR-I	1	0.872 ± 1%	X and Z	2.37 ± 1%	±1%	10^{-3} to 10^{-4}	n/a
	2	0.872 ± 1%	X only	2.37 ± 1%	±1%	10^{-3} to 10^{-4}	n/a
	3	0.872 ± 1%	X and Z	2.37 ± 1%	±1%	10^{-3} to 10^{-4}	±0.004
	4	0.872 ± 1%	X and Z	n/a	n/a	10^{-4}	n/a

* Note: PGA was varied by linearly scaling the ground motion by scale factor = 1 + (% change)

Table C.2. Probabilistic variation (log-normal distribution) of *e* and PGA for Monte Carlo runs (FS.43)

Case		e			PGA	
		Median	c_v	Range	$\sigma_{\ln}$	Range
SR-II	1	0.872	0.2	±3σ	n/a	n/a
	2	0.872	n/a	n/a	0.2	±2σ
	3	0.872	0.2	±3σ	0.2	±2σ
	4	0.872	0.2	±3σ	0.3	±2σ

Table C.3. Parameters considered and variation for SR-III (FS.43, convolved soil motion)

Case		**± 1% variation of parameters**					
		e	Excitation	p	PGA	dt (s)	θ_0 (rad)
SR-III	1	0.872 ± 1%	X and Z	2.37 ± 1%	±1%	10^{-3} to 10^{-4}	n/a
	2	0.872 ± 1%	X only	2.37 ± 1%	±1%	10^{-3} to 10^{-4}	n/a
	3	0.872 ± 1%	X and Z	2.37	n/a	10^{-4}	n/a
	Log-normal variation of *e* and PGA only						
		e			PGA		
		Median	c_v	Range	$\sigma_{\ln}$		Range
	4	0.872	0.2	±3σ	0.2		±2σ
	5	0.872	0.2	±3σ	0.3		±2σ

Table C.4. Summary of SR-I (± 1% variations) for spectrally matched rock motion

Earthquake	**Excitation**	**Min.**	**Max**	**Log-normal Parameters**			**Normal Distribution**		
				$\mu_{\ln X}$	$\beta = \sigma_{\ln X}$	**Median =** **exp($\mu_{\ln x}$)**	μ	σ	**cov**
$e = 0.872 \pm 1\%$, p, PGA; dt [10^{-3} to 10^{-4}]									
10,000 yr Chi-Chi	X and Z	0.0034	0.0443	-4.5932	0.3248	0.0101	0.0108	0.0056	0.515
30,000 yr Chi-Chi	X and Z	0.0335	0.1406	-2.3705	0.0846	0.0934	0.0938	0.0085	0.091
10,000 yr Erzican	X and Z	0.0064	0.0219	-4.4326	0.1380	0.0119	0.0120	0.0021	0.173
30,000 yr Erzican	X and Z	0.0097	0.0280	-3.9459	0.2135	0.0193	0.0197	0.0035	0.179
Original SFPD	X and Z	0.0428	0.0561	-3.0172	0.0376	0.0489	0.0490	0.0018	0.038
$e = 0.872 \pm 1\%$, p, PGA; dt [10^{-3} to 10^{-4}]									
10,000 yr Chi-Chi	X Only	0.0008	0.0095	-4.8990	0.1684	0.0075	0.0080	0.0008	0.104
30,000 yr Chi-Chi	X Only	0.0258	0.0949	-2.5080	0.0512	0.0814	0.0815	0.0041	0.050
10,000 yr Erzican	X Only	0.0049	0.0181	-4.6410	0.2899	0.0096	0.0100	0.0030	0.295
30,000 yr Erzican	X Only	0.0186	0.0277	-3.7520	0.0296	0.0235	0.0235	0.0007	0.030
Original SFPD	X Only	0.0215	0.0419	-3.3990	0.0937	0.0334	0.0336	0.0031	0.092
$e = 0.872 \pm 1\%$, p, PGA; dt[10^{-3} to 10^{-4}], θ_0 [-0.004 to +0.004]									
10,000 yr Chi-Chi	X and Z	0.0033	0.0444	-4.5940	0.3478	0.0101	0.0109	0.0060	0.553
30,000 yr Chi-Chi	X and Z	0.0065	0.0266	-4.4350	0.1436	0.0119	0.0120	0.0022	0.179
10,000 yr Erzican	X and Z	0.0219	0.1395	-2.3660	0.0895	0.0939	0.0942	0.0090	0.095
30,000 yr Erzican	X and Z	0.0098	0.0715	-3.8660	0.0211	0.0209	0.0223	0.0090	0.403
Original SFPD	X and Z	0.0420	0.0553	-3.0170	0.0376	0.0489	0.0490	0.0018	0.038
e variation only : 0.872 ± 1%									
10,000 yr Chi-Chi	X and Z	0.0066	0.0145	-4.5031	0.0897	0.0111	0.0111	0.0010	0.088
30,000 yr Chi-Chi	X and Z	0.0837	0.0991	-2.3975	0.0352	0.0909	0.0910	0.0032	0.035
10,000 yr Erzican	X and Z	0.0116	0.0212	-4.4195	0.1060	0.0120	0.0121	0.0016	0.135
30,000 yr Erzican	X and Z	0.0193	0.0266	-3.8993	0.0422	0.0203	0.0203	0.0009	0.046
Original SFPD	X and Z	0.0475	0.0526	-2.9969	0.0260	0.0499	0.0500	0.0013	0.026

Table C.5. Summary of SR-II (spectrally matched rock motion) for assumed log-normal distribution of *e* and PGA

Earthquake	**Excitation**	**Min.**	**Max**	**Log-normal Parameters**			**Normal Distribution**			**Overturn (%)**
				$\mu_{\ln X}$	**$\beta = \sigma_{\ln X}$**	**Median = $\exp(\mu_{\ln x})$**	**μ**	**σ**	**cov**	
e actual distribution (log-normal): Median = 0.872, ±3σ, cov = 0.2 (in normal space)										
10,000 yr Chi-Chi	X and Z	0.0023	0.0817	-4.4117	0.5034	0.0121	0.0141	0.0094	0.671	0
30,000 yr Chi-Chi	X and Z	0.0186	0.1409	-2.3406	0.1874	0.0963	0.0978	0.0154	0.157	0
10,000 yr Erzican	X and Z	0.0100	0.0233	-4.4049	0.1533	0.0122	0.0124	0.0024	0.193	0
30,000 yr Erzican	X and Z	0.0148	0.0419	-3.8700	0.1426	0.0209	0.0211	0.0032	0.152	0
PGA only variation (log-normal): ±2σ (Log Space), σ_{ln} = 0.2; e = 0.872										
10,000 yr Chi-Chi	X and Z	0.0000	0.1262	-5.4943	2.4086	0.0041	0.0163	0.0203	1.247	0
30,000 yr Chi-Chi	X and Z	0.0055	0.6117	-2.7550	0.6899	0.0636	0.0777	0.0474	0.609	0.06
10,000 yr Erzican	X and Z	0.0011	0.0377	-4.4990	0.5126	0.0111	0.0127	0.0066	0.519	0
30,000 yr Erzican	X and Z	0.0045	0.1486	-3.7084	0.5838	0.0245	0.0292	0.0189	0.647	0
PGA [±2σ (log Space), σ_{ln} = 0.2] and e variation [Median = 0.872, ±3σ, cov = 0.2]										
10,000 yr Chi-Chi	X and Z	0.0000	0.1305	-5.5175	2.4136	0.0040	0.0163	0.0210	1.290	0
30,000 yr Chi-Chi	X and Z	0.0028	0.6117	-2.7539	0.7288	0.0637	0.0802	0.0572	0.713	0.19
10,000 yr Erzican	X and Z	0.0006	0.0458	-4.4806	0.5215	0.0113	0.0129	0.0067	0.518	0
30,000 yr Erzican	X and Z	0.0046	0.1468	-3.7163	0.6022	0.0243	0.0293	0.0198	0.674	0
PGA [±2σ (log Space), σ_{ln} = 0.3] and e variation [Median = 0.872, ±3σ, cov = 0.2]										
10,000 yr Chi-Chi	X and Z	0.0000	0.6117	-5.9500	3.4670	0.0026	0.0241	0.0343	1.424	0.01
30,000 yr Chi-Chi	X and Z	0.0000	0.6117	-2.8963	1.1838	0.0552	0.0900	0.0903	1.003	0.96
10,000 yr Erzican	X and Z	0.0001	0.1432	-4.4619	0.8538	0.0115	0.0159	0.0142	0.891	0
30,000 yr Erzican	X and Z	0.0043	0.1906	-3.6097	0.8610	0.0271	0.0394	0.0373	0.947	0

Table C.6. Summary of SR-III (convolved soil motion)

Convolved Soil Motion	Excitation	Min.	Max	Log-normal Parameters			Normal Distribution			Overturn (%)
				$\mu_{\ln X}$	$\beta = \sigma_{\ln X}$	Median = $\exp(\mu_{\ln x})$	μ	σ	cov	
COR = 0.872; ±1% variation of COR, p, PGA; dt [10^{-3} to 10^{-4}]										
10,000 yr Chi-Chi	X and Z	0.0012	0.2856	-4.6058	1.3348	0.0100	0.0233	0.0315	1.350	0
30,000 yr Chi-Chi	X and Z	0.1667	0.6117	-1.3779	0.2636	0.2521	0.2632	0.0966	0.367	6.3
10,000 yr Erzican	X and Z	0.0060	0.0391	-4.4687	0.4156	0.0115	0.0127	0.0072	0.568	0
30,000 yr Erzican	X and Z	0.1506	0.1803	-1.8230	0.0341	0.1615	0.1616	0.0056	0.034	0
COR = 0.872; ±1% variation of COR, p, PGA; dt [10^{-3} to 10^{-4}]										
10,000 yr Chi-Chi	X Only	0.0023	0.1917	-5.1240	1.1362	0.0060	0.0145	0.0266	1.839	0
30,000 yr Chi-Chi	X Only	0.2322	0.2965	-1.3580	0.0597	0.2572	0.2576	0.0156	0.060	0
10,000 yr Erzican	X Only	0.0079	0.0364	-4.2941	0.3156	0.0136	0.0144	0.0052	0.363	0
30,000 yr Erzican	X Only	0.1373	0.1521	-1.9321	0.0178	0.1448	0.1449	0.0026	0.018	0
COR variation only : 0.872 ± 1%										
10,000 yr Chi-Chi	X and Z	0.0014	0.1483	-5.1175	1.0067	0.0060	0.0097	0.0116	1.198	0
30,000 yr Chi-Chi	X and Z	0.2062	0.6117	-1.4291	0.1958	0.2395	0.2456	0.0721	0.294	3.37
10,000 yr Erzican	X and Z	0.0079	0.0392	-4.7132	0.2957	0.0090	0.0096	0.0052	0.544	0
30,000 yr Erzican	X and Z	0.1543	0.1665	-1.8360	0.0204	0.1595	0.1595	0.0033	0.020	0
COR actual distribution (log-normal): Median = 0.872, ±3σ, cov = 0.2 (in normal space)										
10,000 yr Chi-Chi	X and Z	0.0014	0.6117	-4.9744	1.3013	0.0069	0.0192	0.0388	2.026	0.03
30,000 yr Chi-Chi	X and Z	0.1311	0.6117	-1.2912	0.4010	0.2749	0.3002	0.1394	0.464	14.39
10,000 yr Erzican	X and Z	0.0069	0.0603	-4.6572	0.3510	0.0095	0.0104	0.0063	0.609	0
30,000 yr Erzican	X and Z	0.1247	0.1982	-1.8296	0.0916	0.1605	0.1612	0.0148	0.092	0
PGA [±2σ (log Space), σ_{ln} = 0.3] and COR variation [Median = 0.872, ±3σ, cov = 0.2]										
10,000 yr Chi-Chi	X and Z	0.0000	0.6117	-6.6935	4.9308	0.0012	0.0631	0.0936	1.484	0.4
30,000 yr Chi-Chi	X and Z	0.0000	0.6117	-2.4639	2.4869	0.0851	0.2257	0.1755	0.778	11.24
10,000 yr Erzican	X and Z	0.0000	0.2346	-4.3286	2.2598	0.0132	0.0522	0.0646	1.239	0
30,000 yr Erzican	X and Z	0.0013	0.2453	-2.3550	1.1645	0.0949	0.1370	0.0690	0.504	0

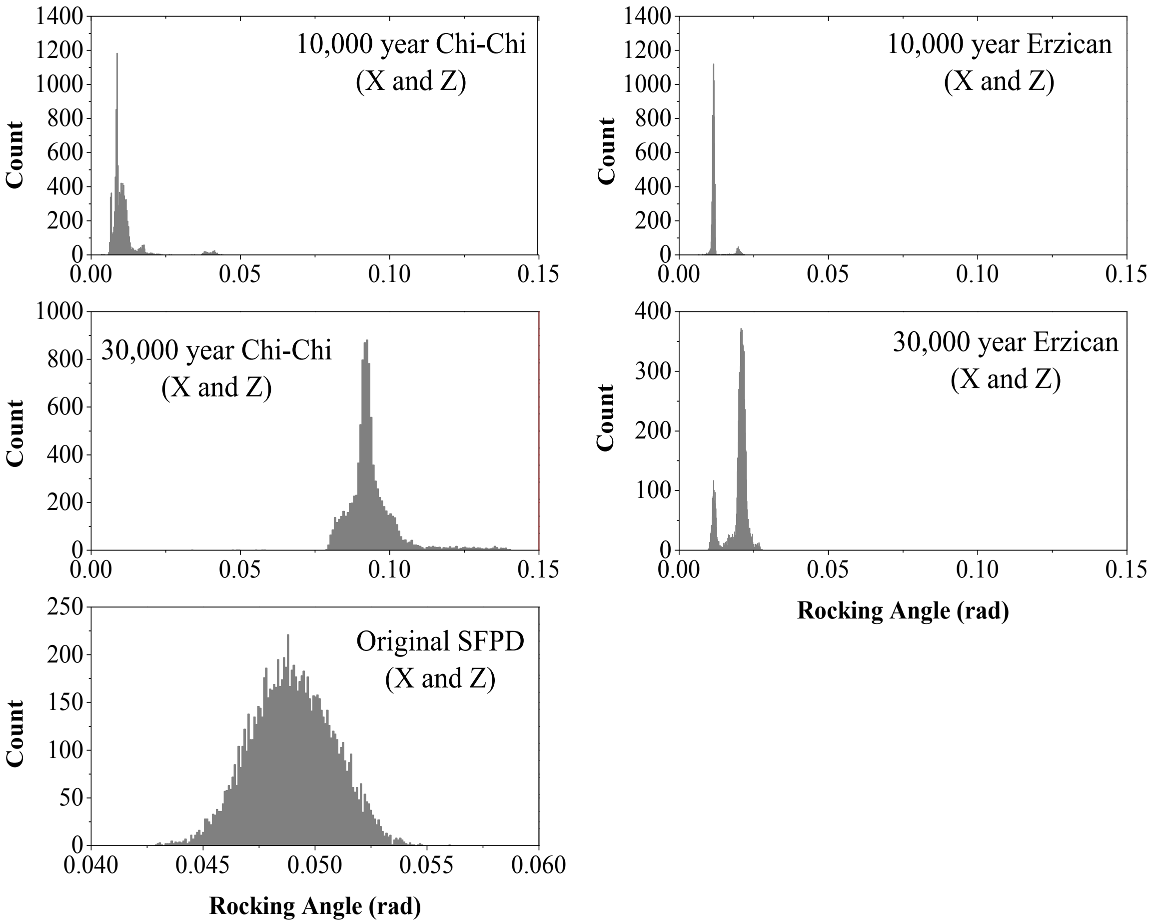

Figure C.1. Absolute maximum rocking angle distribution [FS.43, $e = 0.872 \pm 1\%$, $p = 2.37 \pm 1\%$, $dt = 10^{-3}$ to 10^{-4}, $\theta_0 = 0$, PGA ± 1% (X and Z acceleration)]

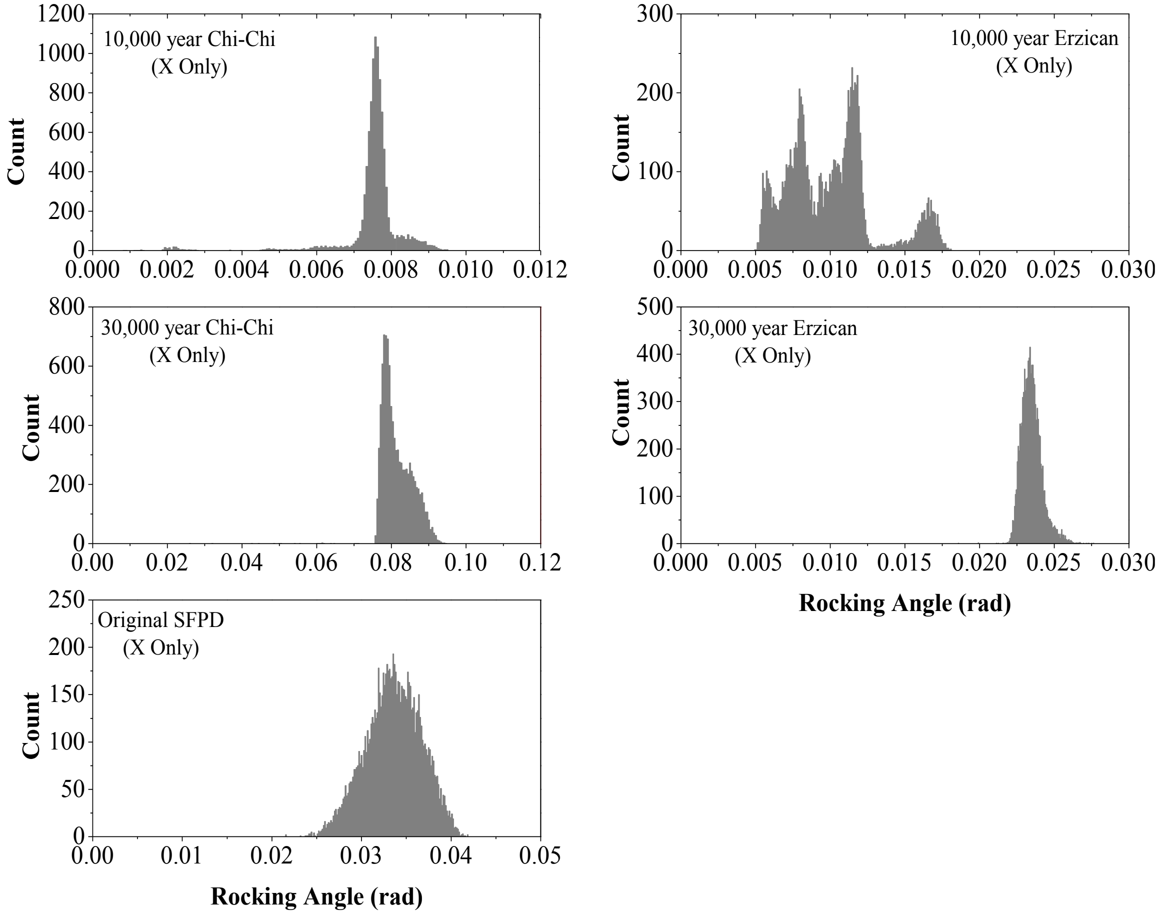

Figure C.2. Absolute maximum rocking angle distribution [FS.43, $e = 0.872 \pm 1\%$, $p = 2.37 \pm 1\%$, $dt = 10^{-3}$ to 10^{-4}, $\theta_0 = 0$, PGA ± 1% (X only)]

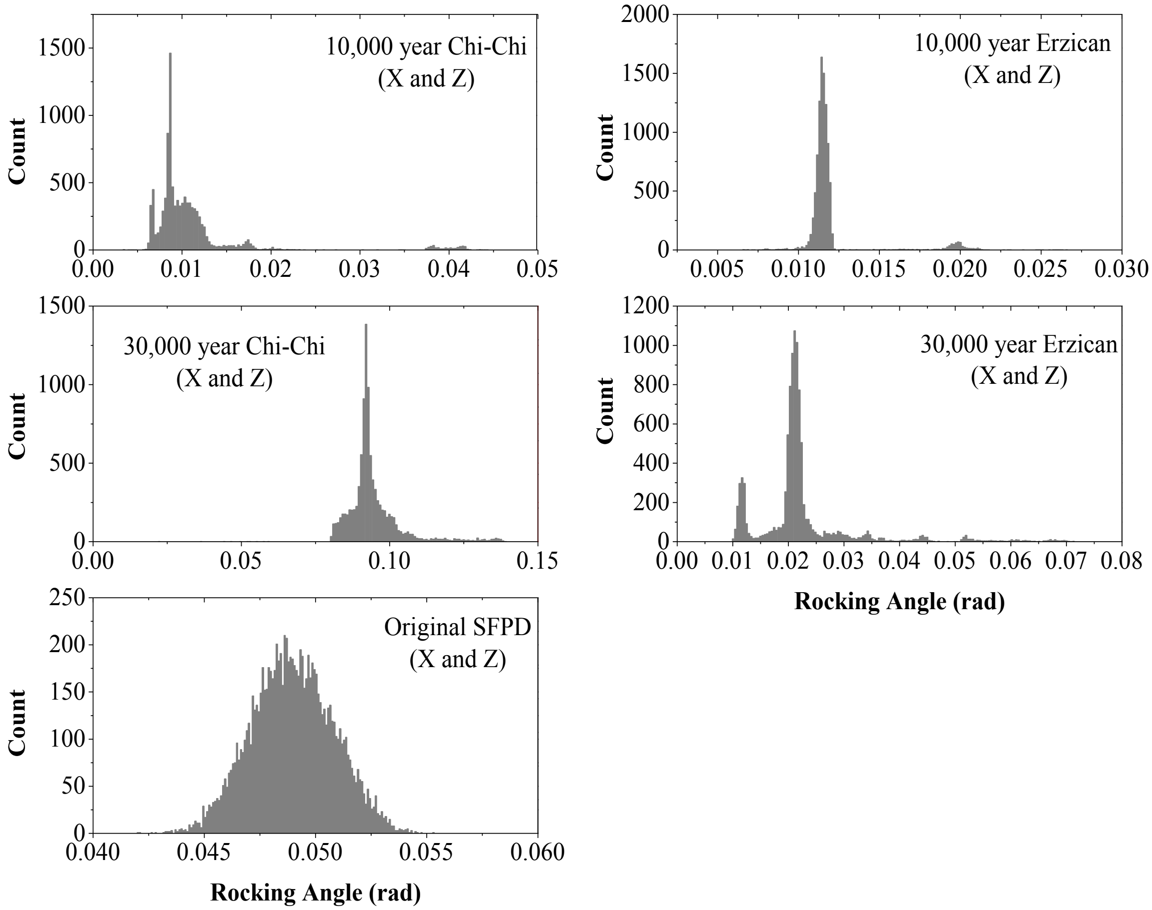

Figure C.3. Absolute maximum rocking angle distribution [FS.43, $e = 0.872 \pm 1\%$, $p = 2.37 \pm 1\%$, $dt = 10^{-3}$ to 10^{-4}, $\theta_0 = \pm 0.004$, PGA ± 1% (X and Z acceleration)]

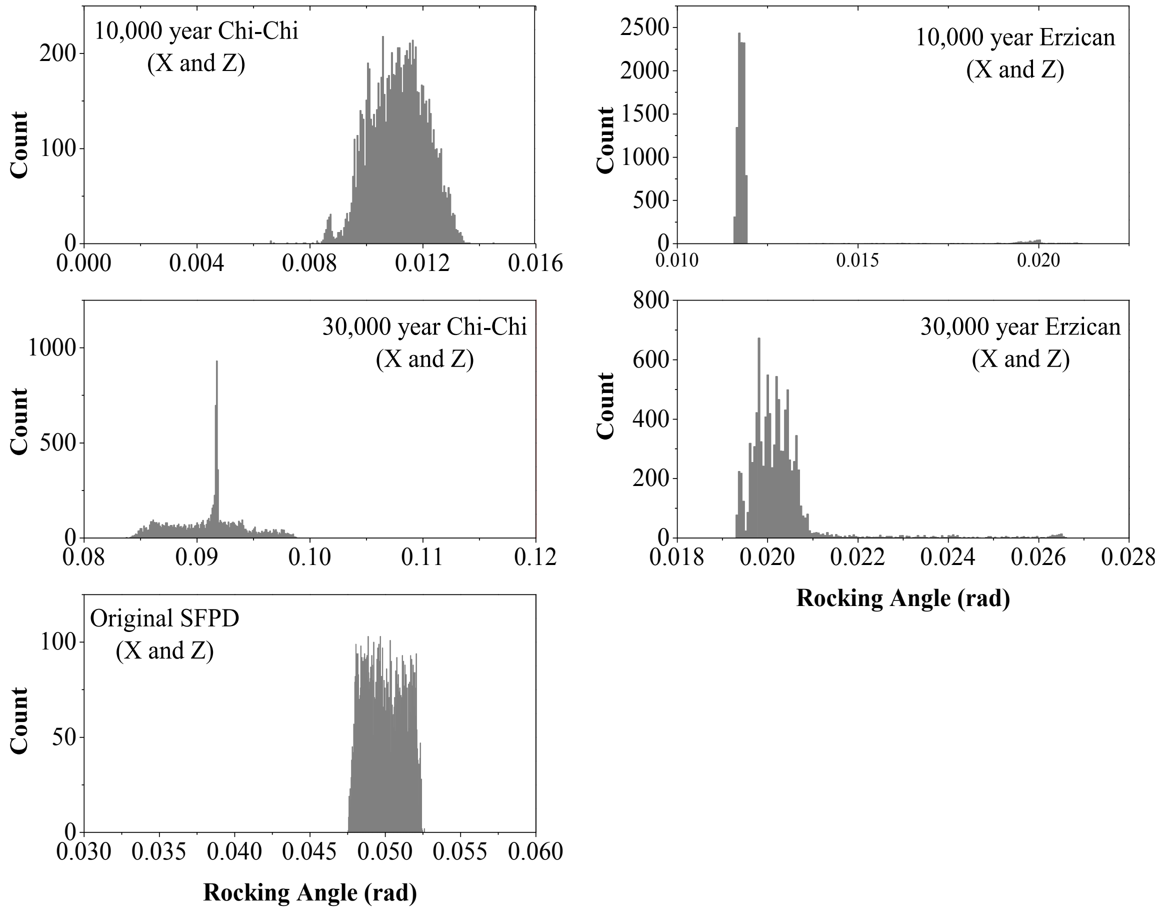

Figure C.4. Absolute maximum rocking angle distribution [FS.43, $e = 0.872 \pm 1\%$, $p = 2.37$, $dt = 10^{-4}$, $\theta_0 = 0$, no PGA variation (X and Z acceleration)]

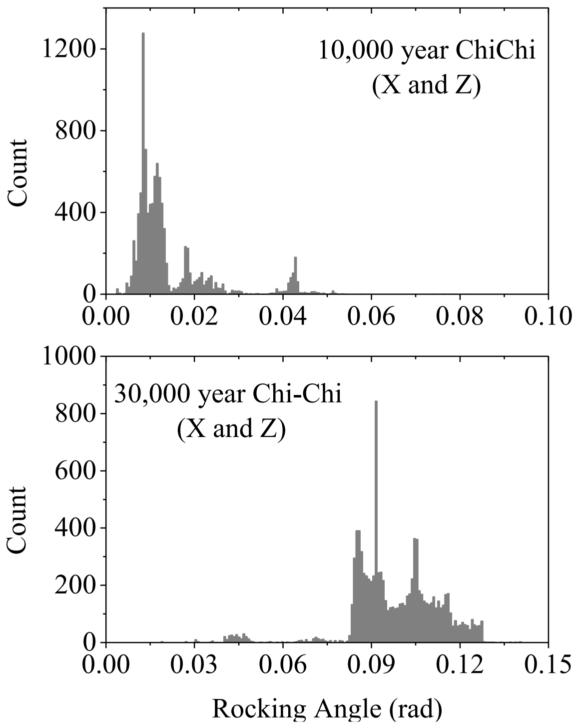

Figure C.5. Absolute maximum rocking angle distribution [FS.43, log-normal distribution $e = 0.872 \pm 3\,\sigma_{\ln}$; p=2.37, dt=10^{-4}, θ_0= 0 rad, (X and Z acceleration)]

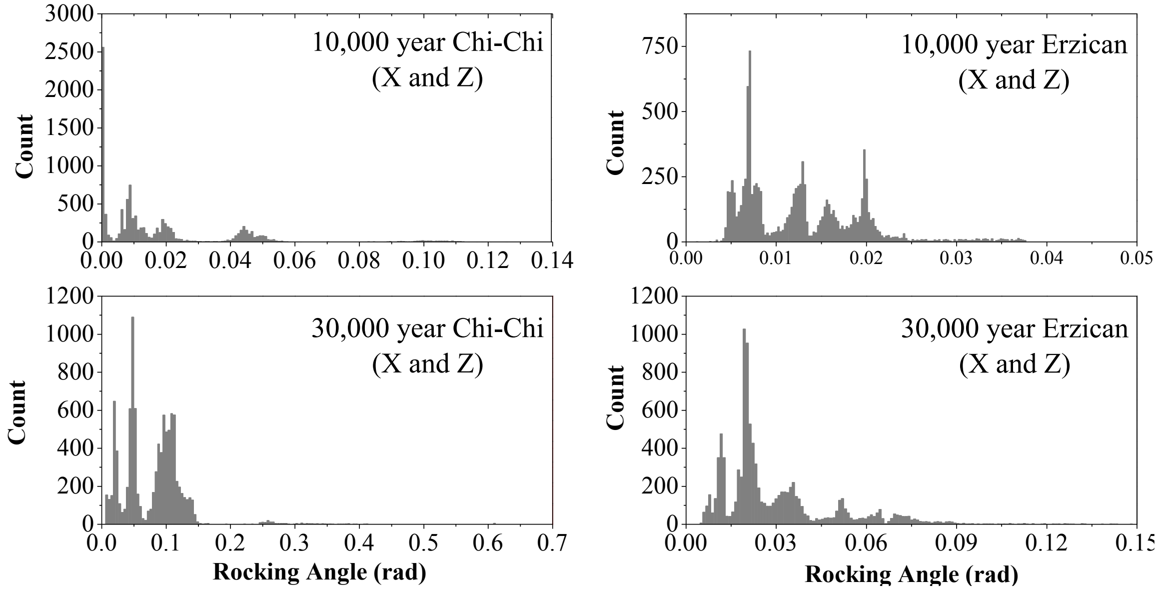

Figure C.6. Absolute maximum rocking angle distribution [FS.43, e = 0.872; p = 2.37, dt = 10^{-4}, θ_0 = 0 rad; PGA log-normal distribution $\pm 2\,\sigma_{\ln}$, $\sigma_{\ln}$ = 0.2 (X and Z acceleration) (X and Z acceleration)]

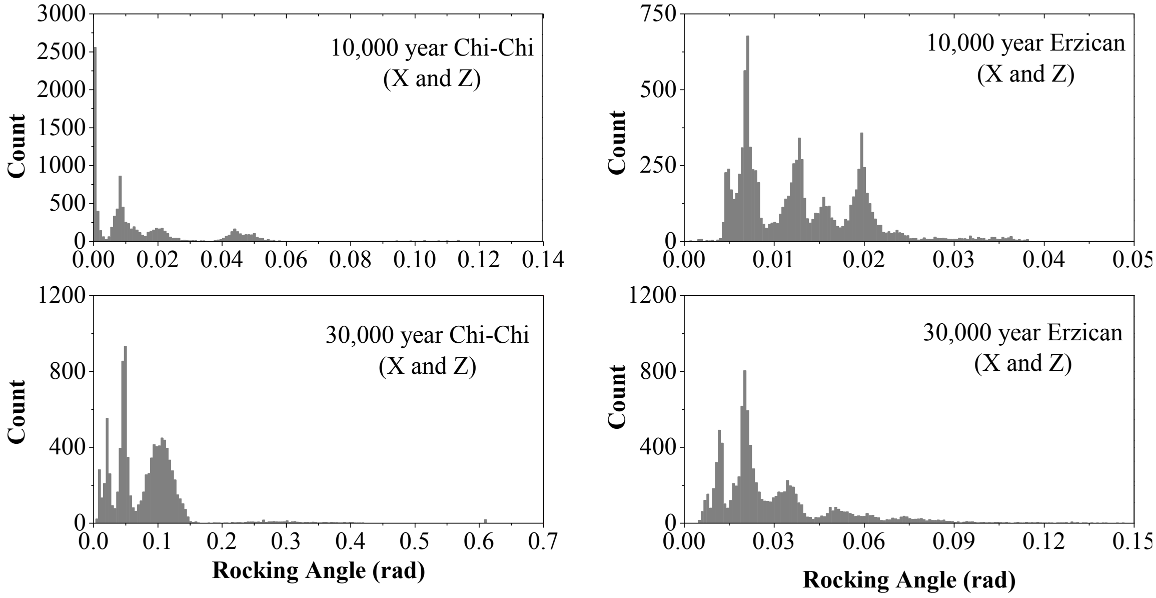

Figure C.7. Absolute maximum rocking angle distribution [FS.43, log-normal distribution e = 0.872 ± 3 $\sigma_{\ln}$; p=2.37, dt = 10^{-4}, θ_0= 0 rad; PGA log-normal distribution ± 2 $\sigma_{\ln}$, $\sigma_{\ln}$ = 0.2 (X and Z acceleration)]

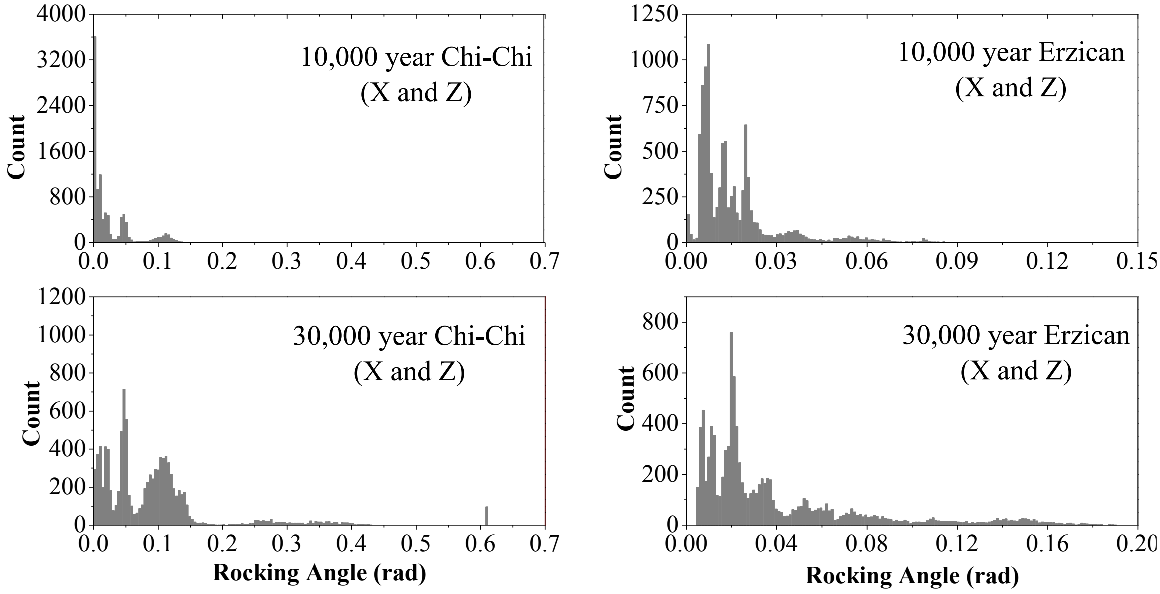

Figure C.8. Absolute maximum rocking angle distribution [FS.43, log-normal distribution e = 0.872 ± 3 $\sigma_{\ln}$; p=2.37, dt = 10^{-4}, θ_0= 0 rad; PGA log-normal distribution ± 2 $\sigma_{\ln}$, $\sigma_{\ln}$ = 0.3 (X and Z acceleration)]

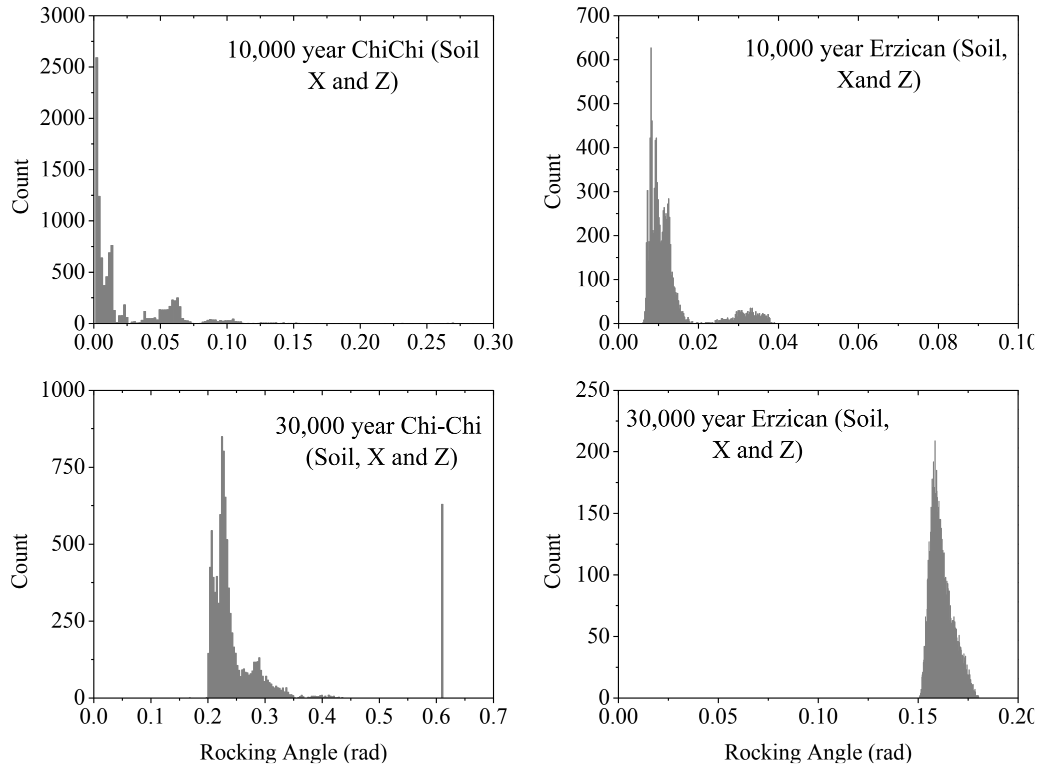

Figure C.9. Absolute maximum rocking angle distribution for soil motions [FS.43, e = 0.872 ± 1%; p=2.37± 1%, $dt = 10^{-3}$ to 10^{-4}, θ_0= 0 rad; PGA±1% (X and Z acceleration)]

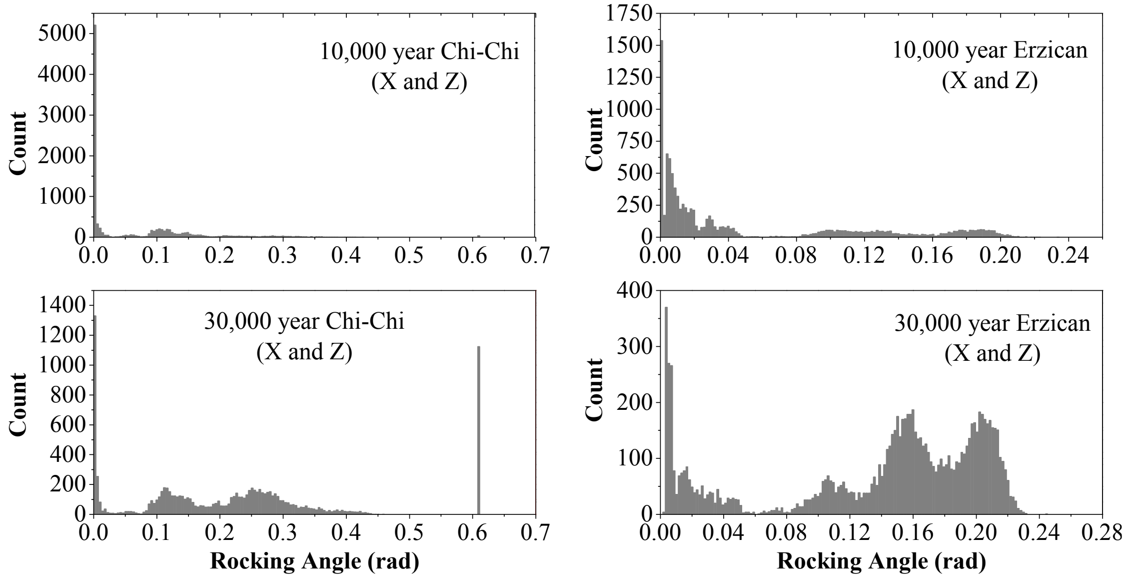

Figure C.10. Absolute maximum rocking angle distribution for soil motions [FS.43, e log-normal distribution = 0.872 ± $3\sigma_{\ln}$; p=2.37, $dt = 10^{-4}$, θ_0= 0 rad; PGA log-normal distribution ± $2\sigma_{\ln}$, $\sigma_{\ln} = 0.3$ (X and Z acceleration)]

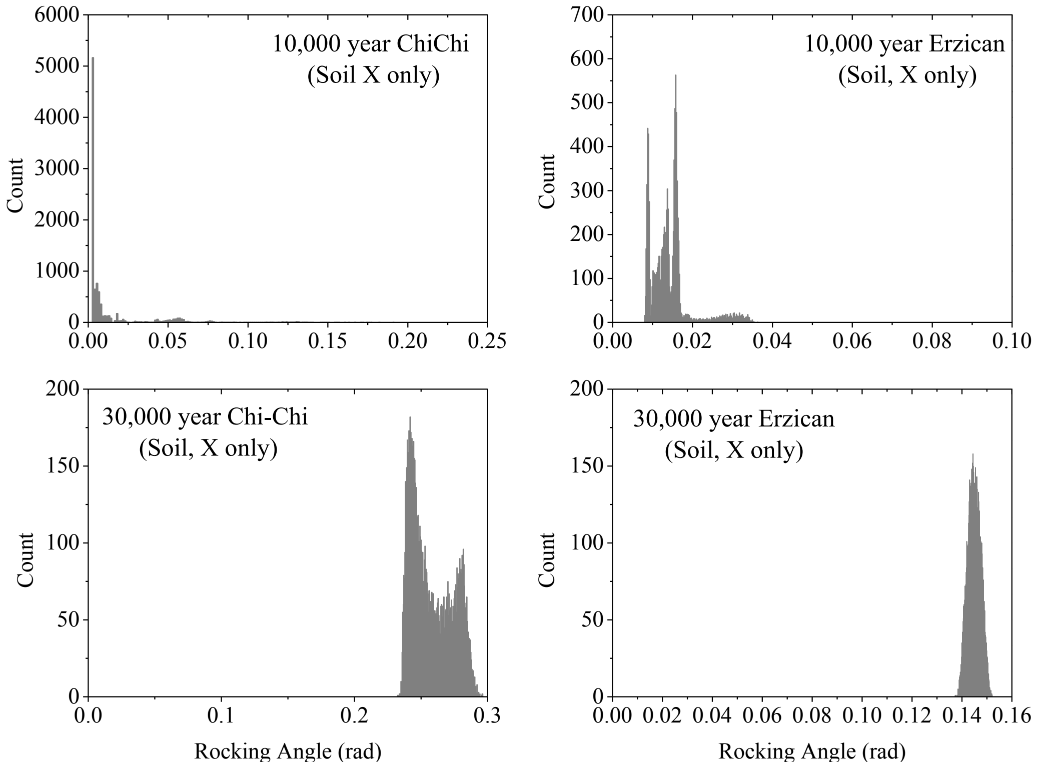

Figure C.11. Absolute maximum rocking angle distribution for soil motions [FS.43, *e* = 0.872 ± 1%; *p* = 2.37± 1%, *dt* = 10^{-3} to 10^{-4}, θ_0= 0 rad; PGA ±1% (X acceleration)]

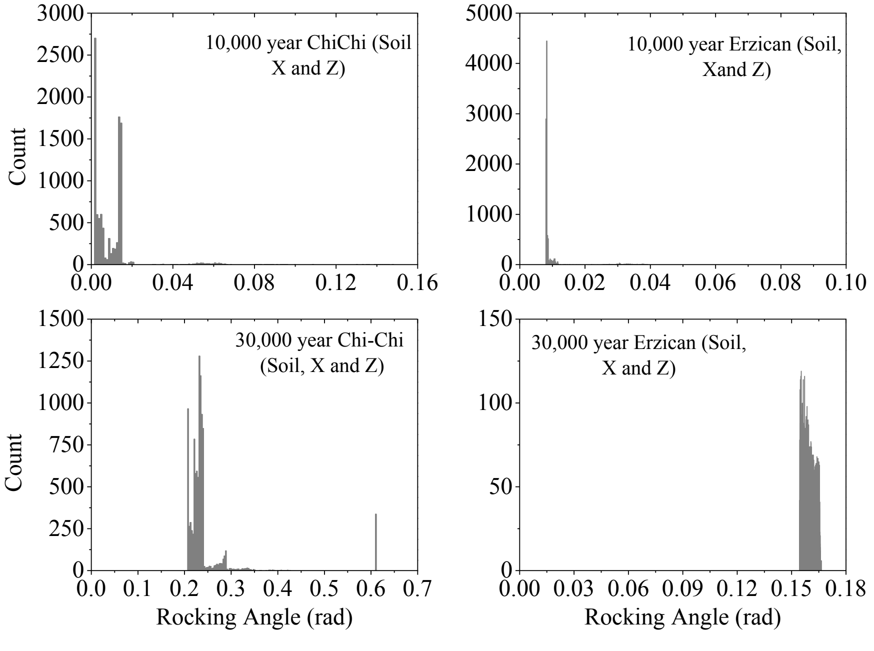

Figure C.12. Absolute maximum rocking angle distribution for soil motions [FS.43, *e* = 0.872 ± 1%; *p* = 2.37, *dt* = 10^{-4}, θ_0= 0 rad; no PGA variation (X and Z acceleration)]

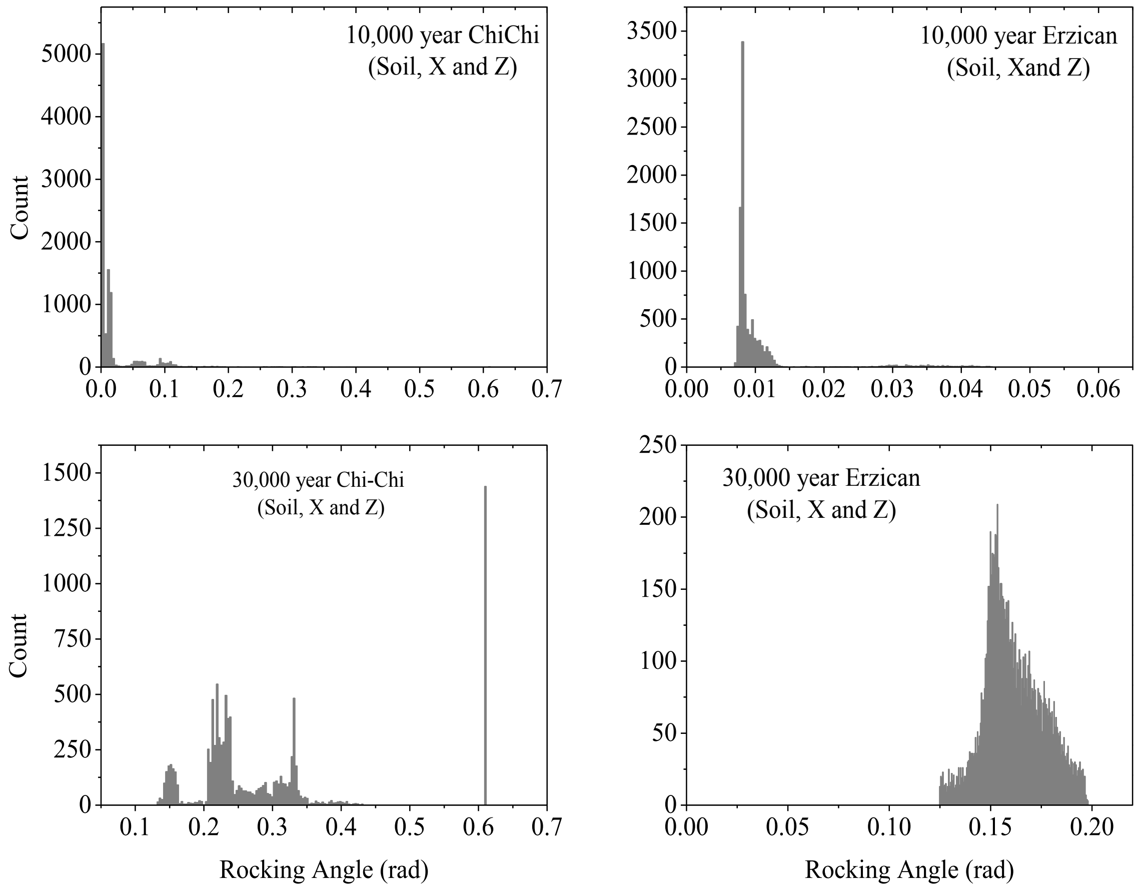

Figure C.13. Absolute maximum rocking angle distribution for soil motions [FS.43, *e* log-normal distribution 0.872 ± 3$\sigma_{\ln}$; p = 2.37, dt = 10^{-4}, θ_0= 0 rad; no PGA variation (X acceleration)]

REFERENCES

1. Code of Federal Regulations. *Title 10 Part 72*. 2004.

2. US NRC. Plan for the Long-Term Update to the Waste Confidence Rule and Integration with the Extended Storage and Transportation Initiative (SECY-11-0029). 2011.

3. LSTC. LS-DYNA 2012.

4. Tripathi BP, Hall JR. Seismic Slope Stability and Design/Analysis of an Independent Spent Fuel Storage Installation (ISFSI) Pads 2007, *SMiRT 19*, Toronto Canada: 2007.

5. Housner GW. The Behavior of Inverted Pendulum Structures during Earthquakes. *Bulletin of the Seismological Society of America* 1963; **53**(2): 403–417.

6. Ishiyama Y. Motions of Rigid Bodies and Criteria for Overturning By Earthquake Excitations. *Earthquake Engineering & Structural Dynamics* 1982; **10**: 635–650. DOI: 10.1002/eqe.4290100502.

7. Mostaghel N, Tanbakuchi J. Response of sliding structures to earthquake support motion. *Earthquake Engineering & Structural Dynamics* 1983; **11**(6): 729–748. DOI: 10.1002/eqe.4290110603.

8. Shenton III HW, Jones NP. Base Excitation of Rigid Bodies. I: Formulation. *Journal of Engineering Mechanics* 1991; **117**(10): 2286–2306. DOI: 10.1061/(ASCE)0733-9399(1991)117:10(2286).

9. Lipscombe PR, Pellegrino S. Free Rocking of Prismatic Blocks. *Journal of Engineering Mechanics* 1993; **119**(7): 1387–1410. DOI: 10.1061/(ASCE)0733-9399(1993)119:7(1387).

10. Zhang J, Makris N. Rocking Response of Free-Standing Blocks under Cycloidal Pulses. *Journal of Engineering Mechanics* 2001; **127**(5): 473–483. DOI: 10.1061/(ASCE)0733-9399(2001)127:5(473).

11. Lopez Garcia D, Soong TT. Sliding fragility of block-type non-structural components. Part 1: Unrestrained Components. *Earthquake Engineering & Structural Dynamics* 2003; **32**(1): 111–129. DOI: 10.1002/eqe.217.

12. Hao H, Zhou Y. Dynamic Response of Rigid Blocks to Simultaneous Horizontal and Vertical Ground Shock. *Advances in Structural Engineering* 2012; **15**(7): 1069–1082. DOI: 10.1260/1369-4332.15.7.1069.

13. Schau H, Johannes M. Rocking and Sliding of Unanchored Bodies Subjected to Seismic Load According to Conventional and Nuclear Rules. *Compdyn 2013*, Kos Island, Greece: 2013.

14. Jeong M, Suzuki K, Yim SCS. Chaotic Rocking Behavior of Freestanding Objects with Sliding Motion. *Journal of Sound and Vibration* 2003; **262**(5): 1091–1112. DOI: 10.1016/S0022-460X(02)01087-8.

15. Koh A siong, Mustafa G. Free Rocking of Cylindrical Structures. *Journal of Engineering Mechanics* 1990; **116**(1): 35–54. DOI: 10.1061/(ASCE)0733-9399(1990)116:1(35).

16. Koh A siong, Hsiung C min. Base Isolation Benefits of 3-D Rocking and Uplift. I: Theory. *Journal of Engineering Mechanics* 1991; **117**(1): 1–18.

17. Zulli D, Contento A, Di Egidio A. 3D Model of Rigid Block with a Rectangular Base Subject to Pulse-type Excitation. *International Journal of Non-Linear Mechanics* 2012; **47**(6): 679–687. DOI: 10.1016/j.ijnonlinmec.2011.11.004.

18. Chatzis MN, Smyth AW. Modeling of the 3D Rocking Problem. *International Journal of Non-Linear Mechanics* 2012; **47**(4): 85–98. DOI: 10.1016/j.ijnonlinmec.2012.02.004.

19. Luk VK, Spencer BW, Lam IP, Dameron RA. *Parametric Evaluation of Seismic Behavior of Freestanding Spent Fuel Dry Cask Storage Systems*. Prepared for the Nuclear Regulatory Commission, NUREG/CR-6865, Washington DC: 2005.

20. Ko YY, Hsu SY, Chen CH. Analysis for Seismic Response of Dry Storage Facility for Spent Fuel. *Nuclear Engineering and Design* 2009; **239**(1): 158–168. DOI: 10.1016/j.nucengdes.2008.09.006.

21. Ko Y, Yang H, Huang CC. An Investigation of the Seismic Response of a Free-Standing Dry Storage Cask for Spent Fuel using the Finite Element Method. *Nuclear Engineering and Design* 2013; **261**: 33–43. DOI: 10.1016/j.nucengdes.2013.03.021.

22. Ko Y yen, Yang H chih, Hsu Y han, Chang J ter. Seismic Analysis of Free-Standing Dry Storage Cask. *Smirt-22*, San Francisco: 2013.

23. Manos GC, Petalas A, Demosthenous M. Numerical and Experimental Study of the Rocking Response of Unanchored Body to Horizontal Base Excitation. *Compdyn 2013*, Kos Island: 2013.

24. Yang H, Ko Y. Analysis for the Influence of the Free-Standing Dry Storage Cask Seismic Response Subject to Retaining Bars. *SMiRT-23*, Manchester: 2015.

25. Gülerce Z, Abrahamson NA. Site-Specific Design Spectra for Vertical Ground Motion. *Earthquake Spectra* 2011; **27**(4): 1023–1047. DOI: 10.1193/1.3651317.

26. Shirai K, Hirata K, Saegusa T. Experimental Studies of Free-Standing Spent Fuel Storage Cask Subjected to Strong Earthquakes. *SMiRT 17*, Prague, Czech Republic: 2003.

27. Peña F, Prieto F, Lourenço P, Campos CA. Dynamical Behaviour of Rigid Block Structures Subjected to Earthquake Motion. *Structural Analysis of Historical Constructions*, New Delhi, India: 2006.

28. Peña F, Prieto F, Lorenço P, Campos CA, Lemos J. On the Dynamics of Rocking Motion of Single Rigid-Block Structures. *Earthquake Engineering and Structural Dynamics* 2007; **36**: 2382–2399. DOI: 10.1002/eqe.

29. Yim CS, Chopra AK, Penzien J. Rocking Response of Rigid Blocks to Earthquakes. *Earthquake Engineering & Structural Dynamics* 1980; **8**(6): 565–587. DOI: 10.1002/eqe.4290080606.

30. Aslam M, Scalise DT, Godden WG. Earthquake Rocking Response of Rigid Bodies. *Journal of the Structural Division* 1980; **106**(2): 377–392.

31. Hogan SJ. On the Dynamics of Rigid-Block Motion Under Harmonic Forcing. *Proceedings of the Royal Society of London. Series A, Mathematical and Physical Sciences* 1989; **425**(1869): 441–476. DOI: 10.1098/rspa.1989.0114.

32. Hogan SJ. The Many Steady State Responses of a Rigid Block under Harmonic Forcing. *Earthquake Engineering and Structural Dynamics* 1990; **19**(7): 1057–1071. DOI: 10.1002/eqe.4290190709.

33. Bruhn B, Koch BP. Heteroclinic Bifurcations and Invariant Manifolds in Rocking Block Dynamics. *Zeitschrift Für Naturforschung A* 1991; **46**(6): 481–490. DOI: 10.1515/zna-1991-0603.

34. Plaut RH, Fielder WT, Virgin LN. Fractal Behavior of an Asymmetric Rigid Block Overturning due to Harmonic Motion of a Tilted Foundation. *Chaos, Solitons & Fractals* 1996; **7**(2): 177–196. DOI: 10.1016/0960-0779(95)00059-3.

35. Bjorkman GS, Moore DP, Nolin JJ, Thomson VJ. Influence of ISFSI Design Parameters on the Seismic Response of Dry Storage Casks. *SMiRT 16*, Washington DC: 2001.

36. Callahan N, Papadelis C, Wilson P, Thomas GG, Bose M. Effects of ISFSI Pad Flexibility on Soil Structure (SSI) Analysis. *Smirt-22*, San Francisco: 2013.

37. Moncarz PD, Krawinkler H. Similitude Requirements for Dynamic Models. *ACI Special Publication* 1982; **73**. DOI: 10.14359/6771.

38. Moncarz PD, Krawinkler H. *Theory and Application of Experimental Model Analysis in Earthquake Engineering.* John A Blume Earthquake Engineering Center Techincal Report 50. 1981.

39. US NRC. Exemption to 10 CFR 72.102(f)(1) Seismic Design Requirement for Three Mile Island Unit 2 Independent Spent Fuel Storage installation (SECY-98-071) 1998.

40. Benjamin JR, Cornell CA. *Probality, Statistics and Decision for Civil Engineers*. New York: McGraw Hill, Inc.; 1970.

41. Dangol S, Ibarra L. Effect of Vertical Accelerations on Dry Storage Cask Seismic Performance. *Smirt-22*, San Francisco: 2013.

42. McGuire RK, Silva WJ, Costantino CJ. *Technical Basis for Revision of Regulatory Guidance on Design Ground Motions: Hazard- and Risk-consistent Ground Motion Spectra Guidelines*. Prepared for the Nuclear Regulatory Commission, NUREG/CR-6728, Washington DC: 2001.

43. Abrahamson NA. *Nonstationary Spectral Matching Program RSPMATCH.* PG&E Internal Report. 1993.

44. FEMA. *Qualification of Building Seismic Performance Factors - FEMA P695*. Prepared by Applied Technology Council for the Federal Emergency Management Agency, Washington, D.C.: 2009.

45. Alavi B, Krawinkler H. *Effects of Near-Fault Ground Motions on Frame Structures.* John A Blume Earthquake Engineering Center Technical Report 138. 2001.

46. PEER Ground Motion Database. 2014. http://peer.berkeley.edu/peer_ground_motion_database. [8 August 2014]

47. Bartlett SF. *Ground Response Analysis and Design Spectra for UDOT Bridges on Soft Soil Sites*. UDOT Research Report, University of Utah, Salt Lake City: 2004.

48. SEiSMOSOFT. SeismoSignal 2016.

49. ABAQUS Inc. ABAQUS User's Manual, Version 6.12 2012.

50. Maree AF, Nielsen T, Dangol S, Parks J, Sanders D, Ibarra LF, Pantelides CP. Shaking Table Experiments of Dry Storage Caks. *2015 Joint Conference AESE/ANCRiSST*, Urbana-Champaign: 2015.

51. Nielsen TM. Experimental Investigation into the Long-Term Seismic Performance of Dry Storage Casks. University of Nevada, Reno, 2016.

52. Maree AF, Nielsen T, Dangol S, Sanders D, Ibarra LF, Pantelides C. Sliding and Rocking of Free Standing Dry Storage Casks under Earthquake Excitation. *16th*

World Conference on Earthquake Engineering, Santiago, Chile: 2017.

53. Dangol S, Ibarra L, Maree A, Nielsen T, Sanders D, Pantelides C. Experimental Seismic Response of Scaled Storage Containments under Identical Loading Conditions. *WM2016 Conference*, Phoenix, Arizona: 2016.

54. Dangol S, Maree AF, Nielsen T, Ibarra LF, Sanders D, Pantelides C. Experimental Dynamic Response of Free-Standing Bodies under Near Field and Far Field Ground Motions. *16th World Conference on Earthquake Engineering*, Santiago, Chile: 2017.

55. Grigoriev IS, Meĭlikhov EZ, Radzig AA. *Handbook of Physical Quantities*. CRC; 1997.

56. Hashash YMA, Musgrove MI, Harmon JA, Groholski DR, Phillips CA, Park D. DEEPSOIL 6.1, Users Manual 2016.

57. Makris N, Zhang J. *Rocking Response and Overturning of Anchored Equipment under Seismic Excitations*. PEER Report 1999/06, University of California, Berkeley: 1999.

58. Kalliontzis D, Sritharan S, Schultz AE. Improving Accuracy of the Simple Rocking Model of Rigid Blocks. *16th World Conference on Earthquake Engineering*, Santiago, Chile: 2017.

59. Elgawady MA, Ma Q, Butterworth JW, Ingham J. Effects of Interface Material on the Performance of Free Rocking Blocks. *Earthquake Engineering & Structural Dynamics* 2011; **40**: 375–392.

60. Chatzis MN, Smyth AW. Robust Modeling of the Rocking Problem. *Journal of Engineering Mechanics* 2012; **138**(3): 247–262. DOI: 10.1061/(ASCE)EM.1943-7889.0000329.

61. American Society of Civil Engineers. *ASCE/SEI Standard 7-10 Minimum Design Loads for Building and Other Structres*. 2010.

62. EduPro Civil Services Inc. ProShake v1.12 2005.

63. Boore DM, Joyner WB. Site Amplification for Generic Rock Sites. *Bulletin of the Seismological Society of America* 1997; **87**(2).

64. Darendeli MB. Development of a New Family of Normalized Modulus Reduction and Material Damping Curves. University of Texas at Austin, 2001.

65. Ibarra L, Sanders D, Pantelides C, Yang H, Bartlett SF. *Unpublished NEUP Project Report*. 2016.

66. DeJong MJ. Amplification of Rocking Due to Horizontal Ground Motion.

Earthquake Spectra 2012; **28**(4): 1405–1421. DOI: 10.1193/1.4000085.

67. Moon FC. *Chaotic and Fractal Dynamics*. John Wiley & Sons, Inc; 1992.

68. Peña F, Lourenço P, Campos CA. Experimental Dynamic Behavior of Free-Standing Multi-Block Structures Under Seismic Loadings. *Journal of Earthquake Engineering* 2008; **12**: 953–979.

69. The MathWorks Inc. MATLAB v. 2013a 2013.

70. Parks JE, Pantelides CP, Ibarra LF, Sanders D. Siesmic Anchorage of Dry Storage Casks. *16th World Conference on Earthquake Engineering*, Santiago, Chile: 2017.